



HAL
open science

Novel Multifunctional Smart Textiles Application in Optoelectronic Devices

Fang-Cheng Liang

► **To cite this version:**

Fang-Cheng Liang. Novel Multifunctional Smart Textiles Application in Optoelectronic Devices. Organic chemistry. Université Grenoble Alpes; National Taiwan University (Taipei), 2019. English. NNT : 2019GREAV020 . tel-03348226

HAL Id: tel-03348226

<https://theses.hal.science/tel-03348226>

Submitted on 18 Sep 2021

HAL is a multi-disciplinary open access archive for the deposit and dissemination of scientific research documents, whether they are published or not. The documents may come from teaching and research institutions in France or abroad, or from public or private research centers.

L'archive ouverte pluridisciplinaire **HAL**, est destinée au dépôt et à la diffusion de documents scientifiques de niveau recherche, publiés ou non, émanant des établissements d'enseignement et de recherche français ou étrangers, des laboratoires publics ou privés.

THÈSE

Pour obtenir le grade de

**DOCTEUR DE LA COMMUNAUTE UNIVERSITE
GRENOBLE ALPES**

**DOCTEUR DE L'UNIVERSIT É NATIONALE DE
TECHNOLOGIE TAIPEI**

Spécialité : **Chimie Physique Moléculaire et Structurale**

Arrêté ministériel : le 6 janvier 2005 – 25 mai 2016

Présentée par

Fang-Cheng Liang

Thèse dirigée par « **Redouane BORSALI** »
codirigée par « **Chi-Ching Kuo** »

préparée au sein du **Centre de Recherche sur les
Macromolécules Végétales (CERMAV)** et du **Université
nationale de technologie Tapei (NTUT)**

dans **l'École Doctorale Chimie et Sciences du Vivant**

**Nouvelle application multifonctionnelle de
textiles intelligents dans les dispositifs
optoélectroniques**

Thèse soutenue publiquement le « **19 septembre 2019** »,
devant le jury composé de :

Mme Chao-Chin Su

UNIV. NATIONALE DE TECHNOLOGIE – TAIPEI (**Président**)

M. Syang-Peng Rwei

UNIV. NATIONALE DE TECHNOLOGIE – TAIPEI (**Examineur**)

M. Serge COSNIER

Directeur de Recherche au CNRS, DCM (**Examineur**)

M. Eric DROCKENMULLER

UNIVERSITE LYON 1 (**Rapporteur**)

M. Wen-Chang Chen

UNIVERSITE NATIONALE DE TAIWAN – NTU (**Rapporteur**)

M. Chi-Ching Kuo

UNIV. NATIONALE DE TECHNOLOGIE – TAIPEI (**Co-Directeur
de thèse**)

M. Redouane BORSALI

Directeur de Recherche au CNRS, CERMAV (**Directeur de thèse**)



中文摘要

論文名稱: 新穎性多功能智慧型紡織品在光電元件的應用

頁數: 159 頁

校所別: 國立台北科技大學分子科學與工程系有機高分子博士班

畢業時間: 一百零八學年度第一學期

學位: 博士

研究生: 梁芳誠

指導教授: 郭霽慶 博士

指導教授: Redouane Borsali 博士

關鍵詞: 自由基聚合、靜電紡絲纖維、智慧型紡織品、金屬離子與磁性螢光感測、轉印技術、奈米銀線、穿戴式感應裝置、電阻型壓力感測器、人造皮膚、健康監測。

近年來奈米科技發展日新月異，擬開發出低成本、高效率、柔性/可拉伸材料應用在智慧型紡織品備受重視，材料具有柔性、拉伸性、輕薄性是製作光電元件中不可或缺的一塊。其中靜電紡絲技術被譽為最符合經濟效益且具有製備智慧型紡織品的潛力。此方法簡單、製程溫度以及成本低，可以製備出比表面積高的高分子奈米纖維。藉由各種高分子材料混合以及靜電紡絲操控條件的搭配，可以調控出各式各樣具功能性之高分子奈米纖維型態。故本論文利用靜電紡絲技術開發出新穎性多功能智慧型紡織品運用於光電元件，主要應用能分成四個部分: (a)多變色兼pH感應型化學傳感器 (b)溫度與磁性環境感應型傳感器 (c)新穎性轉印技術應用於可拉伸電子器件(d)電阻型壓力感測器應用於穿戴式裝置。本博士論文可分為以下四個部分:

第一部分(第一章)-利用自由基聚合法(Free radical polymerization)合成出一系列新穎性螢光共聚高分子，結合靜電紡絲技術，成功製備具有感測 Hg^{2+} 離子及 pH 環境應答多功能之多變色螢光奈米纖維，探討不同濃度之 Hg^{2+} 離子與 pH 的

環境智慧應答所產生之光物理變化。本研究材料包括 Poly(MMA-co-RhBAM) (P1 具 pH 感測)、Poly(MMA-co-BNPTU) (P2 具 Hg²⁺ 離子感測)、Poly(MMA-co-BNPTU-co-RhBAM)含不同比例之 BNPTU:RhBAM (P3~P5 同時具 pH 與 Hg²⁺ 離子感測)，再利用靜電紡絲的技術，將上述材料製備成高孔隙度的奈米纖維，並探討不同材料感測 Hg²⁺ 離子的差異性。共聚高分子材料中導入兩種不同螢光基團，分別為可感測 Hg²⁺ 離子的綠色螢光單體 BNPTU(供體)，以及對 pH 值敏感的橘紅色螢光 RhBAM(受體)。其中 BNPTU 螯合 Hg²⁺ 離子，會從綠光轉移成藍光，而 RhBAM(受體)處於酸性環境下，會放出橘紅色螢光。藉由螢光能量共振轉移 (Fluorescence Resonance Energy Transfer)(FRET)的機制，調控 BNPTU(供體)與 RhBAM(受體)的鏈段比例，可達到多變色螢光放光現象，例如：在不同 Hg²⁺ 與酸性濃度下，能呈現如藍光、綠光、黃光、橘光、紫光、白光等多變色全彩的螢光奈米纖維。P5 於水溶液中的感測靈敏度的極限濃度可達 10⁻⁶~10⁻⁷ 莫耳濃度，實際應用在環檢檢測 Hg²⁺ 離子領域上，去除率能達到 92% 以上，歸功於材料特性與高比表面積的多孔型態奈米纖維。

第二部分(第二章)-合成具有磁性及多功能感測之螢光共聚合高分子 P(NIPAAm-co-NMA-co-AA)混摻Fe₃O₄ Nanoparticles 和 BNPTU，透過靜電紡絲技術製備成奈米纖維，應用於多功能感測系統中(可同時感測磁性與金屬汞離子)BNPTU具有感測汞(Hg²⁺)離子的能力；FeNPs具有磁性功能。實驗中透過自由基聚合法(Free Radical Polymerization)合成出不同比例的共聚高分子。藉由調控電紡參數製備成奈米纖維，以SEM觀察其奈米纖維型態；TEM和EDS鑑定Fe₃O₄尺寸大小與混摻含量，最後以PL、SQUID、強力磁鐵探討其光物理變化和磁性功能。研究結果顯示，奈米纖維透過熱交聯反應後能夠維持纖維型態，其P(NIPAAm-co-NMA-co-AA)混摻FeNPs和BNPTU具有感測汞(Hg²⁺)離子的能力，偵測範圍於 10⁻⁴~10⁻²M(或是更高濃度)。此多功能螢光奈米纖維，利用非接觸力(磁力)方式吸引已吸附金屬的奈米纖維，達到同時兼具磁性感測與金屬感測的功能。

第三部分(第三章)-藉由簡單的旋轉塗佈與噴塗披覆法，將奈米銀線塗佈在彈性高分子(PDMS)上，製作出具有良好導電度之透明貼覆膜，並且可藉由水轉印法貼覆在無規則的表面上(纖維織物、皮膚、玻璃基材...)，其電阻低($9\ \Omega \sim 200\ \Omega$)且透明度高(80 - 95%)，同時兼具以上兩種特性，使其可應用在各種透明的電子元件上。從SEM及EDS證實銀線可以均勻的分佈在所選用的彈性材料上。藉由Bending Test 與Expansion Test 試驗中，得知導電貼覆膜可應用在各種彎曲角度($45^\circ - 315^\circ$)的基材上，其電阻依然不受影響(可維持在 $11\ \Omega$)。本研究首次將導電薄膜貼覆在無規則球體上，藉由來回充放氣體(0ml - 30ml)，測量導電貼覆膜之電阻變化($145\ \Omega - 162\ \Omega$)，可以進一步估算球體體積的變化，屬於一種全新的量測手段，且其同時具有良好的循環再現性(在30次循環測試中，其電阻維持一樣)。貼覆膜體積輕薄不易影響到受測物體(增加準確性)，未來可以用於嬰兒呼吸的量測、老人健康照顧(呼吸長短快慢)以及動物情緒(導盲犬)的紀錄等等。並且將導電貼覆膜進一步製作成有機發光元件(LEC)，貼覆在纖維織物與皮膚表面上，形成新世代穿戴式LEC織物與電子皮膚。

第四部分(第四章)-在此篇研究中，我們以靜電紡絲奈米纖維結合銀奈米顆粒，製作出三明治結構的電阻型壓力感測器，整套系統成本低廉、製程簡單；藉由調控電紡奈米纖維的參數，可達到最小低於 $0.2\ \text{kPa}$ 的感測靈敏度，導通電阻值達到 $10\ \Omega$ 以下。並透過控制電紡奈米纖維的密度，得到數個不同範圍的壓力感測區間，在拉伸(應變 $\varepsilon=0.5$)和彎折(曲率 $1/3\ \text{mm}^{-1}$)的循環測試後，仍維持穩定的感測性能，本系統有良好的拉伸性、彎折性、可回復性、快速的反應時間、超高靈敏度與可微控感測區間的獨特特性，全織物型的精巧設計可以和貼身織物結合或直接與人體連結。我們已成功應用於智能開關和脈搏感測，智能開關與LED和衣物結合後，仍然可以維持其性能。脈搏感測可以即時監控正常成年人的心跳次數。未來可望廣泛應用和商業化在各種與人體互動的觸覺電子裝置上。

Abstract

Title: Novel Multifunctional Smart Textiles Application in Optoelectronic Devices

Pages: 159

University: National Taipei University of Technology

Department: Department of Molecular Science and Engineering, Institute of Organic and Polymeric Materials

Time: January, 2020

Degree: Ph.D.

Researcher: Fang-Cheng Liang

Advisor: Chi-Ching Kuo Ph.D.

Co-Advisor: Redouane Borsali Ph.D.

Keywords: Free Radical Polymerization, Electrospinning, Smart Textiles, pH and Magnetic Chemosensor, Transfer printing, Nanowires, Wearable Display, Resistive Pressure Sensor, Artificial Skins, Health-Monitoring.

To date, the development of smart textiles, artificial skins, environmental sensory devices, and flexible/stretchable optoelectronics involve the innovation of material synthesis, mechanical design, and fabrication strategies have attracted considerable attention in wearable displays. The mechanically flexible and stretchable functions with cost-effective, facile, lightweight, and large-area expandability are essential modules to fabricate the optoelectronic devices in various wearable display applications. Among them, electrospinning is an easy, versatile, and inexpensive technique enables flexible morphology tuning, assembling various functional nanofibers, and high-throughput continuous production has motivated extensive studies on wearable electronics applications. Therefore, it is necessary to develop innovative projects including the environment-sensing elements with pH-sensing dependency, temperature-sensitive,

full-color switchable chemosensors, stretchable electronics, and tactile sensors for various wearable electronics applications. The present PhD thesis can be categorized by four parts as below:

1. RGB-Switchable Porous Electrospun Nanofiber Chemoprobe-filter Prepared from Multifunctional Copolymers for Versatile Sensing of pH and Heavy Metals (Chapter 1): Novel red–green–blue (RGB) switchable probes based on fluorescent porous electrospun (ES) nanofibers exhibiting high sensitivity to pH and mercury ions (Hg^{2+}) were prepared with poly(MMA-co-BNPTU-co-RhBAM)) by using a single-capillary spinneret. The MMA, BNPTU, and RhBAM moieties were designed to (i) permit formation of porous fibers, (ii) fluoresce for Hg^{2+} detection, and (iii) fluoresce for pH, respectively. The fluorescence emission of BNPTU (fluorescence resonance energy transfer (FRET) donor) changed from green to blue as it detected Hg^{2+} . The fluorescence emission of RhBAM (FRET acceptor) was highly selective for pH, changing from nonfluorescent (pH 7) to exhibiting strong red fluorescence (pH 2). The full-color emission of the ES nanofibers included green, red, blue, purple, and white depending on the particular pH and Hg^{2+} -concentration combination of the solution. The porous ES nanofibers with 30-nm pores were fabricated using hydrophobic MMA, low-boiling-point solvent, and at a high relative humidity (80%). These porous ES nanofibers had a higher surface-to-volume ratio than did the corresponding thin films, which enhanced their performance.

2. Novel Magnet and Thermoresponsive Chemosensory Electrospinning Fluorescent Nanofibers and Their Sensing Capability for Metal Ions (Chapter 2): Novel multifunctional switchable chemosensors based on fluorescent electrospun (ES) nanofibers with sensitivity toward magnetism, temperature, and mercury ions (Hg^{2+}) were prepared using blends of poly(NIPAAm-co-NMA-co-AA), the fluorescent probe (BNPTU), and magnetite nanoparticles (NPs), and a single-capillary spinneret. The

moieties of *N*-isopropylacrylamide, *N*-methylolacrylamide, acrylic acid, BNPTU, and Iron oxide (Fe₃O₄) NPs were designed to provide thermoresponsiveness, chemical cross-linking, Fe₃O₄ NPs dispersion, Hg²⁺ sensing, and magnetism, respectively. The prepared nanofibers exhibited ultrasensitivity to Hg²⁺ (as low as 10⁻³ M) because of an 80-nm blueshift of the emission maximum (from green to blue) and 1.6-fold enhancement of the emission intensity, as well as substantial volume (or hydrophilic to hydrophobic) changes between 30 and 60 °C, attributed to the low critical solution temperature of the thermoresponsive *N*-isopropylacrylamide moiety. Such temperature-dependent variations in the presence of Hg²⁺ engendered distinct on–off switching of photoluminescence. The magnetic ES nanofibers can be collected using a magnet rather than being extracted through alternative methods.

3. Mechanically Robust Silver Nanowire–Polydimethylsiloxane Electrode Based on Facile Transfer Printing Techniques for Wearable Displays (Chapter 3): Silver nanowire (AgNW) networks have attracted considerable attention as transparent electrodes for emerging flexible optoelectronics. However, transference of such networks onto diverse arbitrary substrates with high conductivity remains a challenge because of the possibility of detaching and sliding occurring at the interface. Therefore, we developed a water-assisted transfer printing method for fabrication and transfer of an AgNW–polydimethylsiloxane (PDMS) electrode. The innovative approach exhibits a robust ability for thin film transfer onto arbitrary substrates and has highly controlled and nondestructive characteristics. The obtained electrodes exhibited high conductivity (9 Ω/sq, 82% at 550 nm, $\sigma_{DC}/\sigma_{Op} \approx 200$), tensile strain (0% to 50%), and flexibility (bending radius of less than 2 mm) without significant loss of conductivity compared with devices fabricated through conventional methods. Furthermore, we demonstrated novel textile-based flexible light-emitting electrochemical cell (PLECs) based on the stretchable AgNW-PDMS electrode and buckling concept, thereby realizing highly

stretchable PLECs with excellent performance and mechanical robustness. The strained device luminance intensity was optimized to 58 cd m⁻² at 7 V under 10% linear strain without damaging the electroluminescent properties. Notably, this effective and practical transfer method provides an approach for developing electronic nanowire devices with unique configurations and high performance.

4. Mechanically Robust and Ultra-Sensitive Skin-Inspired Nanofiber-based Resistive Pressure Sensor Based on Fibrous Interlocked Microstructures (Chapter 4):

To date, most of the skin-like pressure sensors largely depend on traditional lithography technique to fabricate the microstructures, limiting their wide practical applications due to the high-cost process and the redundant fabrication procedure. Herein, we present a cost-effective, lithographic-free, and large-area expandability to fabricate skin-inspired resistant-type pressure sensors with ultra-performance and lightweight based on fibrous interlocked-microstructures (FIM). The unique sandwich-structured conducting nanofiber (ESSCN) configuration is composed of poly(styrene-block-ethylene-ran-butylene-block-styrene) (SEBS) natural rubber and silver nanoparticles (AgNPs), whereas the dielectric SEBS nanofiber is employed as the middle layer, sandwiched by two SEBS/AgNPs electrodes at top and bottom for packaging. The FIM endows the obtained pressure sensors show superior performance, including ultra-high sensitivity of 71.07 kPa⁻¹ in a low-pressure regime (<0.06 kPa), rapid response time (<2 ms), highly reproducible stability (>100 cycles), mechanical stimuli sensing (pressure, strain, and curvature). As a proof-of-concept demonstration, the sensors have been used for integration with RGB-LED wristband and garments, monitoring human physiological signals, and detect spatial pressure distribution, thereby endowing our ESSCN has broader potential applications in versatile electronic skin and human machine interfaces.

In summary, based on electrospinning, spraying coating, transfer printing technology, we successfully prepared the ultra-sensitivity and full-color switchable functions smart textiles (part one), multifunctional magnetic and fluorescence chemosensor (part two), facile, inexpensive, and chemical free transfer printing technology (part three), skin-inspired resistive pressure sensors (part four). The present study demonstrated that full-color switchable and pH-sensing dependency chemosensors, temperature-sensitive and magnetic chemosensors, chemical free transfer printing technology, skin-inspired resistive pressure sensors have potential for diverse applications, such as water purification, sensing filters, environment-sensing devices, multifunctional smart textiles, wearable electronics, tactile sensors, and artificial skins.

Abstract-France

Mots clés : Polymérisation radicalaire, electrospinning, textiles intelligents, chemo-capteur de pH et/ou de champ magnétique, impression transfert, nanofils, prêt-à-porter connecté, capteur de pression résistif, peau artificielle, surveillance de la santé.

A ce jour, le développement de textiles intelligents, de peaux artificielles, de capteurs de paramètres environnementaux et de composés optoélectroniques souples ; qui nécessite des innovations à la fois dans la synthèse des matériaux, leur conception mécanique mais aussi, à l'échelle industrielle, en stratégie de production ; présente un intérêt majeur dans le domaine du prêt-à-porter connecté. D'un point de vue mécanique, l'obtention des propriétés de flexibilité et d'étirabilité à faible coût, via un procédé simple, au sein d'un matériau léger et capable de s'expandre sur de grandes surfaces est un prérequis essentiel pour incorporer des dispositifs optoélectroniques au sein des objets connectés portables. Parmi les différents procédés couramment utilisés, l'electrospinning est une technique simple, facilement adaptable et peu onéreuse qui permet un ajustement fin et flexible des morphologies de fibres, l'assemblage de plusieurs nanofibres fonctionnelles et une production en continue à haut débit. Ces multiples avantages sont à l'origine des nombreux travaux concernant l'utilisation de l'electrospinning dans le domaine du prêt-à-porter électronique et/ou connecté. Cependant, il est nécessaire de développer des projets innovants pour ce secteur qui incluent des capteurs détectant des paramètres environnementaux (pH, température), des chemo-capteurs colorimétriques à large spectre (full-color), des composantes électroniques étirables et capteurs tactiles. Cette thèse peut-être diviser en quatre parties présentées ci-dessous:

1. Membrane de filtration permettant une détection colorimétrique (RGB) versatile du pH/des métaux lourds et constituée de nanofibres poreuses obtenues à partir par électrospinning d'un copolymère multifonctionnel (chapitre 1): De nouvelles sondes colorimétriques RGB, basées sur des nanofibres poreuses fluorescentes obtenues par électrospinning (ES) et ayant une forte sensibilité au pH et aux ions mercures (Hg^{2+}), ont été préparés à partir du poly(MMA-co-BNPTU-co-RhBAM) en utilisant une filière simple réservoir. Les blocs MMA, BNPTU et RhBAM ont été respectivement sélectionnés pour (i) permet la formation de fibres poreuses, (ii) fluorescer en présence de Hg^{2+} et (iii) fluorescer en fonction du pH. Les photons de fluorescence émis par le bloc BNPTU (donneur FRET) sont passés du vert au bleu lorsqu'il interagit avec les ions Hg^{2+} . L'émission de photons de fluorescence par le bloc RhBAM (accepteur FRET) dépend fortement du pH environnant, passant d'une absence de fluorescence (pH 7) à l'émission de photons rouges en milieu acide (pH 2). Le spectre d'émission de ces nanofibres inclut le vert, le rouge, le bleu, le violet et le blanc en fonction du pH et de la concentration en ion Hg^{2+} . Les nanofibres poreuses (porosité 30 nm) ont été fabriquées à partir du bloc MMA hydrophobique, d'un solvant à basse température d'évaporation et dans des conditions de haut degré d'humidité relative (80%). Ces nanofibres ont un rapport surface/volume plus élevé que les films équivalents ce qui contribue à augmenter leur performance.
2. Nouvelles nanofibres obtenues par électrospinning, sensibles à la température et au magnétisme et utilisable pour détecter des ions métalliques (chapitre 2): De nouveaux chemo-senseurs multi-fonctionnels basés sur des nanofibres sensibles au magnétisme, à la température et aux ions mercure (Hg^{2+}) et obtenues

par ES en utilisant un mélange de poly(NIPAAm-co-NMA-co-AA), de BNPTU (une sonde fluorescente) de nanoparticules de magnétites (NPs) à travers une filière simple réservoir. Les blocs N-isopropylacrylamide, N-méthylacrylamide, acrylic acid ainsi que le BNPTU et les NPs ont été respectivement sélectionnés pour donner aux fibres une sensibilité à la température, une réticulation chimique, favoriser la dispersion de NPs, permettre la détection des ions Hg^{2+} ainsi que du magnétisme. Ces nanofibres montrent une sensibilité extrêmement haute aux ions Hg^{2+} (inférieur à 1 mM) à la fois à cause du décalage de 80 nm vers le bleu du maximum d'émission (du vert au bleu) accompagné d'un accroissement de 1,6 fois de l'intensité d'émission, mais également parce que le volume intrinsèque des fibres diminue fortement entre 30 et 60°C ce qui est attribué au comportement de LCST du bloc thermosensible N-isopropylacrylamide (comportement hydrophile vers hydrophobe). De tels variations, qui sont températures dépendantes, en présence de Hg^{2+} induit une transition nette et rapide (comportement on-off) des propriétés de photoluminescence des fibres. De plus, ces nanofibres magnétiques peuvent être facilement récupérés à l'aide d'un aimant plutôt qu'être extraites via une autre méthode.

3. Electrode mécaniquement renforcée, à base de nanofils d'argent et de polydimethylsiloxane, préparée à l'aide de techniques d'impression-transfert pour des applications en prêt-à-porter connecté (chapitre 3): Les réseaux de nanofils d'argent (AgNW) ont été extensivement étudiés comme électrodes transparentes afin de faire émerger des dispositifs optoélectroniques flexibles. Cependant, le transfert de ce type de réseaux sur n'importe quel substrat hautement conducteur reste un défi car l'adhérence à l'interface est très souvent

faible (possibilité de détachement et de glissement). Par conséquent, nous avons développé une méthode d'impression-transfert en milieu aqueux pour la fabrication et le transfert d'électrode d'AgNW-polydiméthylsiloxane (PDMS). Cette approche innovante permet un transfert fiable et robuste de films fins sur des substrats totalement différents tout en étant non-destructrice et hautement contrôlable. Les électrodes obtenues ont une haute conductivité ($9 \Omega/\text{sq}$, 82% à 500 nm, $\sigma_{\text{DC}}/\sigma_{\text{Op}} \approx 200$), un bon allongement (0% à 50%) et une bonne flexibilité (rayon de courbure inférieur à 2 mm) sans observer une diminution significative de la conductivité comparée aux autres dispositifs fabriqués à l'aide de méthodes conventionnelles. En outre, nous avons mis au point de nouvelles cellules électrochimiques souples et luminescentes (PLECs) incorporables aux textiles et basés sur des électrodes flexibles AgNW-PDMS et le concept de flambage, réalisant ainsi des PLECs hautement flexibles avec d'excellentes performances en termes de luminescence et de robustesse mécanique. L'intensité de luminescence du dispositif sous tension a été optimisée à $58 \text{ cd}\cdot\text{m}^{-2}$ à 7V pour un allongement linéaire de 10% sans nuire aux propriétés d'électroluminescence. Cette méthode pratique, simple et efficace de transfert est une approche très intéressante en vue de développer des appareils électroniques à hautes performances et configurations uniques à base de nanofils.

4. Capteur de pression résistif ultra-sensible, mécaniquement robuste, inspiré de la peau, constitué de nanofibres et basé sur une microstructure fibreuse interpénétrée (chapitre 4): A ce jour, la plupart des capteurs de pression inspirés de la peau sont fabriqués à l'aide des techniques classiques de lithographie afin de réaliser leur microstructuration ce qui limite leur développement à grande

échelle à cause du caractère onéreux et redondant de ce procédé. Nous proposons ici une méthode à faible coût, sans lithographie and utilisable sur de larges surfaces pour fabriquer des capteurs de pression inspirés de la peau qui présentent de hautes performances et sont basés sur une microstructure fibreuse interpénétrée (FIM) et légère. La structure-sandwich unique de nos nanofibres conductrices (ESSCN) est constituée de poly(styrene-block-éthyle-ran-butylène-block-styrene) ou SEBS, de caoutchouc naturel et de nanoparticules d'argent (AgNPs) : alors que les nanofibres diélectriques de SEBS sont utilisés comme couche intermédiaire, deux électrodes de SEBS/AgNPs sont placés au-dessus et en-dessous pour « l'enrober ». La structure FIM confère au capteur de pression des performances supérieures, y compris une ultra-haute sensibilité de $71,07 \text{ kPa}^{-1}$ en régime basse pression ($<0,06 \text{ kPa}$), un temps de réponse rapide ($<2\text{ms}$), une haute stabilité des performances aux cycles de reproductibilité (>100 cycles) et la possibilité de détecter des stimuli mécaniques variés (pression, allongement et courbure). Comme preuve de concept, les capteurs ont été intégrés à des bracelets et des vêtements afin d'enregistrer des signaux physiologiques humains mais aussi pour détecter la répartition spatiale de la pression démontrant ainsi que notre ESSCN a un potentiel d'application plus large dans le domaine des « peaux » électroniques et de l'interface machine/humain.

Pour résumer, en utilisant l'électrospinning, le revêtement par spray et les technologies d'impression-transfert, nous avons réussi à produire des textiles intelligents avec des fonctions de capteurs environnementaux (pH, métaux lourds) ultra-sensible et une transition colorimétrique à large spectre RGB (partie 1) ; un chemo-senseur multifonctionnel fluorescent et magnétique (partie 2) ; une technologie d'impression-transfert simple, peu coûteuse et sans substance chimique (partie 3) ; et un capteur de pression résistif inspiré de la peau (partie quatre). Les travaux effectués démontrent que les chemo-capteurs colorimétriques RGB pour la détection du pH, les chemo-senseurs sensible à la température et magnétique, les technologies d'impression-transfert sans substances chimiques ainsi que les capteurs de pressions résistif ont un fort potentiel pour diverses applications tel que la purification de l'eau, les filtres avec fonction de détection, les capteurs environnementaux, les textiles intelligents multifonctionnels, le prêt-à-porter connecté, les capteurs tactiles and les peaux artificielles.

致謝

博士生涯一轉眼就要結束了，能夠完成台北科大與法國格勒諾布爾的雙博士學位，我最要感謝的是我的指導教授兼亦師亦友-郭齊慶。感謝教授給予大量的資源投資在我的身上，並時常鼓勵與督促我，讓我可以順利完成博士班的目標。而在這段生涯裡我也接受了很多從未遇過的挑戰，這些挑戰可以說是在我人生中最大的幫助，因為能從中體驗未知的冒險以及接觸各國文化的洗禮，這當中涵蓋了自己獨立勇闖法國留學以及學習如何適應新的環境。這些無比的挑戰都是幫助我提前適應社會上的歷練。

在法國留學期間，特別感謝 Prof. Redouane Borsali 非常地關心我的生活起居，在我面臨法國文化上、住宿、電信及銀行等相關問題時，教授都會花很多心思及耐心幫助我度過難關。而在實驗和設備的建立上，教授都能給予我很大的空間發揮，並完全信任我的能力，讓我能有效率地為 CNRS-CERMAV lab 裡面建立”手套箱”和”蒸鍍機”等設備。此外，教授也授予我極大的職權，讓我能運用我所了解的電子元件專業知識，親自指導碩士生以及博士後研究生，而無形當中也培養了我的領導與管理能力。

特別感謝 Prof. Sami 在我不了解儀器如何安裝時，可以給我適時的協助；感謝 Prof. Issei 在我需要了解儀器的時候，可以有耐心和效率地為我分析；感謝 Postdoc Francois 可以提供額外的房間，解決了我後半年住宿上的問題，並時常利用假日帶我出去遊山玩水；感謝專業知識好夥伴 Postdoc Yoko，讓我有機會可以和妳交流 Solar Cell and LED 電子元件；感謝最好朋友兼夥伴 PhD. Rubal 時常幫助我解決法國文化上的問題，並總是為我準備了許多貼心小禮物；感謝我的吃飯好搭檔 PhD. Wei，讓我在法國可以不孤單還能一同分享法國的生活；感謝我的玩伴 Master JSB，時常帶我去品嚐不同品種的法國啤酒。最後感謝所有 CERMAV lab 的成員，非常感謝你們的幫助與支持，讓我能法國留學中可以進展順利。

特別感謝李文亞教授時常給予我很多專業上的知識，並且有細心和效率地為我解說專業問題，彌補了很多我知識上的不足。感謝台大孫翰笙學長給予我很多有機合成上的專業知識，讓我能更加了解每個合成機制。謝謝跟我同屆的好兄弟現為博士後家榮，這段期間內無論實驗或者各種大小事，我們都互相勉勵一起度過了種種難關，如今您貴為”博士後”了，希望您能可以繼續專研下去，繼續為實驗室發揚光大。也感謝所有現階段實驗室的成員們如:岱樺、富程、禎里、凱閔、威丞、權倫、依璇、苙君、蘋慧、俐媛、傳恩、菲比、翎雅、Logan 等，以及歷屆實驗室成員如: 士棟、以伶、皓仁、伯瑜、涵芳、婉玲、景誼、祐維等，這段期間給予我很多不同實質方面上的幫助，過程中也帶來了許多歡笑與打鬧，讓我在博师生涯裡可以更加豐富。

最後要感謝提拔我的父母，能尊重我的每項決定，並讓我能無憂無慮的專心讀書與研究，我會珍惜和你們相處的每一個日子，孝順你們。感謝我的哥哥，從小到大以來一直是我讀書的好榜樣，直到現在，我還是持續追隨你的每項豐功偉業。最後，要特別感謝我的女友，一路以來始終默默的支持我、包容我，總是不離不棄並時常鼓勵我，讓我有動力堅持下去。最後 感謝所有有幫助過我的貴人、老師、好兄弟和好朋友們，讓我能完成海外留學的夢想。

芳誠 謹致 於
國立臺北科技大學有機高分子博士班
中華民國一零八年九月十九日

Contents

中文摘要.....	i
Abstract.....	iv
France-Abstract.....	ix
致謝.....	xv
Contents.....	xvii
Figure Captions.....	xx
Table.....	xxx
Chapter 1、RGB-Switchable Porous Electrospun Nanofiber Chemoprobe-filter Prepared from Multifunctional Copolymers for Versatile Sensing of pH and Heavy Metals.....	1
1-1 Introduction.....	1
1-2 Motivation.....	3
1-3 Background and Review of literatures.....	7
1-3-1 Development of chemosensors for the detection of analytes.....	7
1-3-2 Electrospinning techniques for fabricating ENMs.....	13
1-3-3 Application of ENMs in optical chemosensors for heavy metal detection.....	15
1-4 Experimental Section.....	16
1-4-1 Material.....	16
1-4-2 Synthesis of 4-Bromo-N-allyl-1, 8-naphthalimide.....	17
1-4-3 Synthesis of 4-(Aminoethylene) amino-N-allyl-1, 8-naphthalimide.....	17
1-4-4 Synthesis of 1, 8-Naphthalimide-Based Monomer (BNPTU).....	18
1-4-5 Synthesis of RhB Hydrazide.....	19
1-4-6 Synthesis of RhBAM-Based Monomer.....	19
1-4-7 Synthesis of Poly(MMA-co-BNPTU-co-RhBAM).....	25
1-4-8 Synthesis of P1.....	26
1-4-9 Synthesis of P2.....	27
1-4-10 Synthesis of P5.....	29
1-5 Preparation of Copolymer Solutions with Different pH Values.....	30
1-6 Preparation of ES Nanofibers.....	30
1-7 Characterization.....	31
1-8 Results and Discussion.....	33
1-8-1 Characterization of BNPTU, RhBAM, Poly(MMA-co-BNPTU-co-RhBAM).....	33
1-8-2 Morphology of ES Nanofibers.....	37

1-8-3 pH Sensing of ES Nanofibers.....	39
1-8-4 Hg ²⁺ Sensing of ES Nanofibers.....	45
1-9 Conclusion.....	55

Chapter 2 、 Novel Magnet and Thermo-responsive Chemosensory

Electrospinning Fluorescent Nanofibers and Their Sensing Capability for Metal

Ions.....	57
2-1 Introduction.....	57
2-2 Motivation.....	59
2-3 Background and Review of literatures.....	62
2-3-1 Responsive Polymer-Based Temperature Sensors.....	62
2-3-2 Responsive Polymer-Based Magnetic Sensors.....	66
2-4 Experimental Section.....	69
2-4-1 Material.....	69
2-4-2 Synthesis of 4-Bromo-N-allyl-1,8-naphthalimide.....	70
2-4-3 Synthesis of 4-(Aminoethylene)amino-N-allyl-1,8-naphthalimide... ..	70
2-4-4 Synthesis of BNPTU.....	70
2-4-5 Synthesis of Magnetic Iron Oxide (Fe ₃ O ₄) Nanoparticles (NPs).....	71
2-4-6 Synthesis of Poly(NIPAAm-co-NMA-co-AA).....	72
2-4-7 Synthesis of Poly(NIPAAm-co-NMA) Random Copolymers (P1).....	73
2-4-8 Synthesis of Poly(NIPAAm-co-NMA-co-AA) Random Copolymers (P2).....	73
2-5 Preparation of Electrospun (ES) Nanofibers.....	74
2-6 Characterization.....	75
2-7 Results and Discussion.....	76
2-7-1 Characterization of BNPTU and Poly(NIPAAm-co-NMA-co-AA).....	76
2-7-2 Morphology and Characterization of ES Nanofibers.....	78
2-7-3 Hg ²⁺ Sensing, Thermo-responsiveness, Magnetic of Nanofibers.....	82
2-8 Conclusion.....	89

Chapter 3 、 Mechanically Robust Silver Nanowire–Polydimethylsiloxane

Electrode Based on Facile Transfer Printing Techniques for Wearable

Displays.....	90
3-1 Introduction.....	90
3-2 Motivation.....	91
3-3 Background and Review of literatures.....	94
3-3-1 Typical Transfer Printing Methods.....	94
3-3-2 Inorganic Semiconductors.....	96

3-4 Experimental Section.....	98
3-4-1 Material.....	98
3-4-2 Preparation of AgNW Dispersion.....	98
3-4-3 Fabrication of WTP Stretchable Conductive Electrodes.....	98
3-4-4 Stretchable Conductive Electrode Integrated with Textiles.....	99
3-4-5 Stretchable and Wearable Textiles in the PLEC Device.....	99
3-5 Device Characterization.....	100
3-6 Results and discussion.....	101
3-6-1 Designing New Transfer Methods by using WTP Technique.....	101
3-6-2 Electrical and Mechanical Properties of Conductive Electrode...	103
3-6-3 Textile-Based WTP PLEC Devices.....	115
3-7 Conclusion.....	120
Chapter 4 、 Mechanically Robust and Ultra-Sensitive Skin-Inspired Nanofiber-based Resistive Pressure Sensor Based on Fibrous Interlocked Microstructures.....	121
4-1 Introduction.....	121
4-2 Motivation.....	122
4-3 Background and Review of literatures.....	124
4-3-1 Strain and Pressure Sensors.....	124
4-3-2 Piezoresistive.....	126
4-4 Experimental Section.....	128
4-4-1 Materials.....	128
4-4-2 Preparation of SEBS fiber and silver nanoparticles.....	128
4-4-3 Design of the Skin-inspired ESSCN Pressure Sensor.....	129
4-5 Device Characterization.....	129
4-6 Results and discussion.....	130
4-7 Conclusion.....	144
Chapter 5 、 References and Notes.....	146
Chapter 6 、 Publication.....	158

Figure Captions

Chapter 1

Scheme 1	Design of multifunctional probe ES nanofibers synthesized from poly(MMA-co-BNPTU-co-RhBAM) and exhibiting various colors of fluorescence emission. (a) Polymerization and chemical structure of poly(MMA-co-BNPTU-co-RhBAM). (b) Fabrication of ES nanofibers. (c) Chemical structure of BNPTU in solutions with Hg ²⁺ and RhBAM in solutions with pH 2 or 12. (d) Effect of FRET on the fluorescence emission colors of multifunctional environment-sensing ES nanofibers.....	6
Figure 1.	Fluorescence (Forster) resonance energy transfer system.....	8
Figure 2.	Spectral overlap for FRET.....	9
Figure 3.	Schematic of the FRET process between the fluorescein and rhodamine.....	9
Figure 4.	The schematic of the molecular beacon-based FRET sensor; the presence of Hg ²⁺ ions brought the quenching of fluorescence emission.....	10
Figure 5.	Mechanism of ring-opening process of rhodamine derivative in the presence of a targeted metal ions or a Lewis acid.....	11
Figure 6.	The reaction scheme of rhodamine 6G derivative with Hg ²⁺ metal ions.....	11
Figure 7.	The Cu ²⁺ -induced FRET OFF/ON process.....	12
Figure 8.	The FRET system within the diblock copolymer for sensing ferric ion.....	13
Figure 9.	The scheme of pH and thermo-modulation of diblock copolymer.....	13
Figure 10.	Schematic illustration of the typical electrospinning setup.....	14
Figure 11.	(a) Polymerization and chemical structure of poly(MMA-co-NAAP). (b) Schematic illustration for poly (MMA-co-NAAP) nanofiber fluorescent sensors by electrospinning for Cu ²⁺ with enhanced detection sensitivity. (c) Fluorescent emission spectra of the ENM-based chemosensor in the presence of Cu ²⁺ (0–20 μM). Excitation wavelength was 400 nm, and emission wavelength was 439 and 487 nm.....	15
Scheme 2	Synthesis of (a) BNPTU fluorescent monomer (donor) and (b) RhBAM fluorescent probe (acceptor).....	20
Figure 12.	¹ H NMR spectra of (a) BN-Br in CDCl ₃ , (b) BN-NH ₂ in DMSO-d ₆ and (c) BNPTU monomer in DMSO-d ₆	21
Figure 13.	HRESI-MS spectra of (a) BN-Br, (b) BN-NH ₂ and (c) BNPTU.....	22
Figure 14.	IR spectrum of (a) BN-Br, (b) BN-NH ₂ and (c) BNPTU.....	23
Figure 15.	¹ H NMR spectra of (a) RhB hydrazide in CDCl ₃ and (b) RhBAM monomer in CDCl ₃	23
Figure 16.	HRESI-MS spectra of (a) RhB hydrazide and (b) RhBAM.....	24

Figure 17.	IR spectrum of (a) RhB hydrazide and RhBAM.....	25
Figure 18.	¹ H NMR spectra of (a) poly(MMA-co-RhBAM) in DMSO and (b) poly(MMA-co-BNPTU) in DMSO.....	28
Figure 19.	¹ H NMR spectrum of poly(MMA-co-BNPTU-co-RhBAM) in DMSO..	29
Figure 20.	ES fibers for pH and Hg ²⁺ sensing detector instrument.....	33
Figure 21.	TGA curves of P1–P5 copolymers when a heating rate of 10 °C/min was applied under a nitrogen atmosphere.....	34
Figure 22.	UV–Vis spectra of (a) RhBAM in CH ₃ CN solution (10 ⁻² M) under pH 2 conditions and (b) BNPTU in CH ₃ CN solution (10 ⁻⁵ M). (c) Variation in UV–Vis spectra of BNPTU CH ₃ CN solution (10 ⁻⁵ M, pH 7) containing different metal ions at 10 ⁻⁴ M. (d) PL spectrum of BNPTU under pH 2 and 7 conditions and UV–Vis absorption spectrum of RhBAM in CH ₃ CN solution under pH 2 conditions.....	36
Figure 23.	(a) FE-SEM image of the P5 porous ES nanofibers, with (b) an enlarged image, and (c) a cross-sectional image. (d) TEM image of the P5 ES nanofibers before (inset) and after absorption of Hg ²⁺ ions in aqueous solution (10 ⁻³ M, pH 7).....	38
Figure 24.	SEM images of P1–P4 ES nanofibers (a–d, Enlarged view (e–h)).	38
Figure 25.	(a) Variation in the PL spectra of the P5 ES nanofibers in aqueous solutions under pH 7 to pH 2 conditions. (b) Relative fluorescence intensity (I ₅₉₇ /I ₅₁₀) of the P5 ES nanofibers in aqueous solution under different pH conditions.....	40
Figure 26.	PL spectra of (a) P1 , (b) P2 , (c) P3 , (d) P4 , and (d) P5 ES nanofibers in aqueous solutions under pH 7 and pH 2 conditions.....	41
Figure 27.	Variation in the PL spectra of the P5 ES nanofibers in aqueous solutions under pH 7 to pH 14 conditions.....	41
Figure 28.	(a) Normalized PL spectra of the P1–P5 ES nanofibers in aqueous solutions under pH 2 conditions. CIE coordinates of the P2–P5 ES nanofibers in aqueous solutions under (b) pH 7 and (c) pH 2 conditions. (d) Confocal microscopy images of the ES nanofibers. (e) CIE coordinates of the P5 ES nanofibers in aqueous solutions under pH 7 to 2 conditions. (f) Reversibility of pH-dependent “on–off–on” fluorescence intensity profile of the P5 ES nanofibers. All of the inset figures are corresponding photographs taken under UV light.....	45
Figure 29.	(a) PL spectra of the P5 ES nanofibers in aqueous solution with Hg ²⁺ at 10 ⁻³ M and no Hg ²⁺ (blank) under neutral conditions. (b) PL spectra of the P5 ES nanofibers in Hg ²⁺ at 10 ⁻⁴ M in aqueous solution under pH 2 conditions and in aqueous solution without Hg ²⁺ under both pH 2 and 7	

	conditions. (c) PL spectra of the P5 ES nanofibers in aqueous solution with Hg^{2+} at 10^{-5} M under pH 2 conditions and in aqueous solution without Hg^{2+} under pH 2 and 7 conditions.....	46
Figure 30.	(a) CIE coordinates of the P5 ES nanofibers in aqueous solutions with different Hg^{2+} concentrations under pH 2 and pH 7 conditions. Blank refers to solution without Hg^{2+} at pH 7. (b) Confocal microscopy images of ES nanofibers. Inset: corresponding photographs taken under UV light.....	48
Figure 31.	(a) PL dependence on various concentrations of Hg^{2+} ($C(\text{Hg}^{2+})$) under neutral conditions: (a) P5 ES nanofibers and (b) P5 thin films. (c) Stern–Volmer plots (460/510) of the P5 nanofibers and thin films on $C(\text{Hg}^{2+})$ measured at λ_{ex} 380 nm. Inset of (c): enlarged Stern–Volmer plot of the P5 ES nanofibers on $C(\text{Hg}^{2+})$	50
Figure 32.	PL dependence on various concentrations of Hg^{2+} ($C(\text{Hg}^{2+})$) under neutral conditions: P5 solutions.....	51
Figure 33.	(a) Normalized PL spectra of the P5 ES nanofibers in aqueous solutions containing various metal ions (10^{-3} M, pH 7) and no cations (blank). (b) Fluorimetric response (I_{460}/I_{510}) of the P5 ES nanofibers to various cations at 10^{-3} M in aqueous solutions under neutral conditions, and corresponding photographs taken under UV light. Inset of (b): fluorimetric response of the P5 ES nanofibers to solutions containing various metal ions at 10^{-3} M (as in (b)) but when Hg^{2+} at 10^{-3} M is also present.....	52
Figure 34.	(a) Schematic illustration of a probe filter microfluidics system for real-time metal-ion sensing using an ES nanofiber membrane. (b) Relative conductivity versus time of the prepared Hg^{2+} solution in the microfluidics system.....	54

Chapter 2

- Figure 1.** Synthesis of BNPTU fluorescent monomer.....61
- Figure 2.** Design of multifunctional sensory electro spun (ES) nanofibers synthesized from poly(NIPAAm-co-NMA-co-AA), BNPTU, and Fe₃O₄ blends with magnetic fluorescence emission. (a) Polymerization and chemical structure of poly(NIPAAm-co-NMA-co-AA), BNPTU, and Fe₃O₄ particles. (b) Fabrication of ES nanofibers from the blends. (c) Change in the chemical structure of BNPTU in solutions containing Hg²⁺. The fluorescence emission from the ES nanofibers exhibited color changes. A magnet can directly attract the ES nanofibers because of the magnetism of Fe₃O₄ NPs.....62
- Figure 3.** Schematic Summary of Responsive Polymer-Based Sensors.....62
- Figure 4.** Chemical Structures of Monomers for Synthesis of Responsive Polymer...63
- Figure 5.** Chemical Structures of Functionalized Fluorescent Dyes.....64
- Figure 6.** Thermo-responsive P(DMAPAM-co-NTBAM-co-DBDAE) copolymer in aqueous solution serves as a fluorescent molecular thermometer..65
- Figure 7.** (a) Schematic for the Synthesis of Rhodamine B-Based Spirolactam Monomer (RhBHA) and (b) Proposed Ring-Opened Mechanism in the Presence of Hg²⁺ Ions or Acid Media.....65
- Figure 8.** NPTUA moieties enabling PNIPAM nanogel employed as a ratiometric fluorescent sensor of Hg²⁺ ions with enhanced detection sensitivity..66
- Figure 9.** Stimulus-responsive membrane triggering in vitro: schema of the proposed mechanism of membrane function.....68
- Figure 10.** Scheme of stimulus-magnetic-responsive membrane of PTMC-b-PGA polymersomes triggering in magnetic resonance imaging.....68
- Figure 11.** Schematic representation of (a) using PVA to stabilize the F127 to form a stable nanocarrier and (b) the structure of a thermosensitive nanocarrier (TSNC) composed of PVA and F127 with iron oxide nanoparticles and drug encapsulated.....69
- Figure 12.** ¹H-NMR spectra recorded for (a) BN-Br in CDCl₃, (b) BN-NH₂ in DMSO *d*₆ (c) BNPTU monomer in DMSO-*d*₆.....71
- Figure 13.** GPC profiles of P1 and P2 copolymers.....73
- Figure 14.** ¹H-NMR spectrum of poly(NIPAAm-co-NMA-co-AA) in DMSO.....74
- Figure 15.** TGA curves of **P1** and **P2** copolymers with a heating rate of 10 °C min⁻¹ in a nitrogen atmosphere.....77

- Figure 16.** Variations in optical transmittance of **P1** and **P2** in pH 7 water solutions with temperatures between 30 and 65 °C.....78
- Figure 17.** UV-Vis spectra of (a) BNPTU in CH₃CN solution (10⁻⁵ M) and (b) variation of UV-Vis spectra of BNPTU CH₃CN solution (10⁻⁵ M, pH 7) with different metal ions at 10⁻⁴ M. The corresponding inset figures show the color changes under visible light and 254-nm UV light...78
- Figure 18.** Field-emission scanning electron microscopy (FE-SEM) images of copolymers. (A) **P1** and (B) **P2** cross-linked nanofibers at 120 °C in a dry state and treated with water at 30 and 60 °C.....80
- Figure 19.** (a) FE-SEM and (b) Transmission electron microscopy (TEM) images of Fe₃O₄ NPs synthesized through coprecipitation. (c) Magnetic Fe₃O₄ NPs in the solution (left: Fe₃O₄ precipitated out of the solution and dropped to the bottom; right: Fe₃O₄ accumulated on the side of the bottle because of the magnet).....80
- Figure 20.** (a) SEM image of Fe₃O₄ NPs blended with nanofibers at a 5% weight ratio. (b) FE-SEM image of **P2-5%** cross-linked nanofibers in the presence of Fe³⁺. (c,d) Energy dispersive X-ray spectroscopy EDS maps of C and Fe within the confined area in (b). (e) EDS spectrum recorded within the region defined in (b).....81
- Figure 21.** TGA curves of **P2-5%** blended with 5 wt% Fe₃O₄ NP nanofibers with a heating rate of 10 °C min⁻¹ in a nitrogen atmosphere.....82
- Figure 22.** (a) Photoluminescence (PL) spectra of **P1** and **P2** nanofibers blended with 10 wt % BNPTU. (b) Comparison of **P2-5%** nanofibers with different Hg²⁺ concentrations between 10⁻², 10⁻³ and 10⁻⁴ M in aqueous solution. (c) Relative fluorescence intensity changes (*I*₄₅₀/*I*₅₃₀) of **P2-5%** ES nanofibers in aqueous solutions with various Hg²⁺ concentrations. (d) PL spectra of **P2-5%** ES nanofibers in 10⁻² M Hg²⁺ solution with a temperature increase from 30 to 60 °C.....84
- Figure 23.** PL intensity of pristine BNPTU compound under a temperature increase from 30 to 60 °C.....85
- Figure 24.** (a) Variation in the normalized PL spectra of **P2-5%** ES nanofibers in aqueous solutions with various metal ions (10⁻² M) and no cation (blank). (b) Fluorometric responses (*I*₄₅₀/*I*₅₃₀) of **P2-5%** ES nanofibers to various cations at 10⁻² M aqueous solutions. From left to right: Hg²⁺, Pb²⁺, Co²⁺, Cd²⁺, Mg²⁺, Ni²⁺, Zn²⁺, Fe²⁺, and Cu²⁺. All the inset figures show corresponding photographs recorded under UV light. Inset of (b): fluorimetric response of the **P2-5%** ES nanofibers to solutions containing various metal ions at 10⁻² M (as in (b)) when Hg²⁺ at 10⁻² M is present.....86

Figure 25. (a) CIE coordinates of **P2-5%** ES nanofibers in pH 7 aqueous solutions and after the detection of Hg^{2+} at 10^{-2} M aqueous solutions. (b) Confocal microscopy images of the ES nanofibers. All the inset figures show corresponding photographs recorded under UV light. (c) Schematic of a sensory filter microfluidics system for real-time metal ion sensing using an ES nanofiber membrane. (d) Relative conductivity versus time of the prepared Hg^{2+} solution in the microfluidics system.....**87**

Figure 26. (a) Hysteresis loops of **P2-5%** ES nanofibers (5 wt % Fe_3O_4 NPs) measured at 25 °C. (b) Schematic of a filter sensory membrane prepared from **P2-5%** ES nanofibers composed of poly(NIPAAm-*co*-NMA-*co*-AA)), BNPTU, and Fe_3O_4 NPs blends to simultaneously chelate and sense Hg^{2+} . A magnet can directly attract the **P2-5%** ES nanofibers because of the magnetism of Fe_3O_4 NPs.....**89**

Chapter 3

Figure 1. Schematics of the WTP process for AgNW TCEs. (a) (i) Prefabricated sacrificial layer (PVP) and flexible framework (PDMS); (ii) spraying of AgNWs on the top of PDMS after plasma treatment; (iii) transferred nanowire devices on a prehumidification target substrate with a sacrificial layer in between. (b) Corresponding photographs of various nonconventional substrates, including skin, a balloon, a round-bottomed flask, and an elastomeric textile.103

Figure 2. SEM images of (a) spraying AgNW on an untreated PDMS substrate and (b)–(d) spraying AgNW on a plasma-treated PDMS substrate from 5 to 30 s. The inset pictures (e)–(f) show the different contact angles before and after plasma treatment.....104

Figure 3. Visual transparency, electrical properties, and SEM characterization of electrodes. (a) Optical transmittance curves of the AgNW-PDMS electrode prepared with different spray durations as a function of the wavelength. The insets show the average sheet resistance for various spray durations. (b) SEM images of the AgNW-PDMS electrode prepared using various spray durations; the blue arrow indicates apparent welding between AgNWs. (c) σ_{DC}/σ_{Op} value plotted with sheet resistance and transmittance (at 550 nm). (d) Photographs of various AgNW-PDMS electrodes with corresponding transmittance values of 96%, 92%, and 82%.....107

Figure 4. Application of AgNW-PDMS electrodes in semitransparent and wearable LEDs under extreme deformation. (a) Schematics of bending test. (b) Relative change in the resistances of ITO (thickness 150 nm) on PET (thickness 150 μm), AgNW on PET (thickness 150 μm and 100 μm), and the AgNW-PDMS electrode (thickness 35 μm) with the WTP method as a function of the bending radius. The inset shows a photograph of a folded AgNW-PDMS flexible transparent electrode fabricated using the WTP method with a bending radius of 300 μm set for the bending test. (c) Relative change in the resistances of ITO (thickness 150 nm) on PET (thickness 150 μm), AgNW on PET (thickness 100 μm), and the AgNW-PDMS electrode (thickness 35 μm) with the WTP method as a function of bending cycles at a bending radius of 4 mm. (d) Plot of the sheet resistance of the AgNW-PDMS electrode (thickness 35 μm) and photographic image versus bending angles between 0° and 330°. (e) Schematics of the AgNW-PDMS electrode combined with a blue LED circuit on a plastic glove. The inset shows

photographs of the blue LED circuit in various folding states. (f) Detection of finger joint motion by the AgNW-PDMS electrode.....111

Figure 5. Demonstration of real-time conductivity monitor with the deformable AgNW-PDMS electrode. (a) Schematic of the prestretching and releasing strategy with the AgNW-PDMS electrode (prestretch: 20%) based on the WTP method. (b) SEM morphology of the AgNW-PDMS electrode under various strain stretched states from pristine to 20%, 40%, and 50%. (c) Strain-dependent electrical resistance of the AgNW-PDMS electrode with and without prestretching in various stretching tests. (d) Schematic of the deformable AgNW-PDMS electrode fabricated using the WTP method mounted on the dynamic surface of a balloon to realize the cycling test through expansion and contraction. (e) Cycle test of electrical resistance with the AgNW-PDMS electrode attached to the balloon through expansion and contraction. The insets show corresponding photographs of the expansion rate of the balloon from 112%.....114

Figure 6. Schematic of the fabrication process of stretchable textile-based PLECs. (a) Diagram of PLEC device structure based on AgNWs-PDMS electrodes with In-Ga cathodes. (b) Schematic of prestretching and releasing strategy based on the WTP method for integration on elastomeric textiles. (c) Current I–V–L responses of a PLEC device during the stretching and releasing cycle test. (d) EL spectra of the device versus various voltage bias levels. The inset contains a CIE 1931 x-y chromaticity diagram showing the brightness of PFO emission with blue color. (e) Photographs of a stretchable PLEC attached to a prestretched elastomer textile (20%); the images represent the buckle microstructure PLEC (unstrained elastomer) state being stretched to the flat PLEC (stretched elastomer) state119

Figure 7. Tapping mode AFM images with height line profiles of the (a) AgNW-PDMS electrode, (b) PEDOT:PSS-AgNW-PDMS electrode.....119

Chapter 4

Figure 1. Schematic diagrams illustration of a skin-like ESSCN resistive pressure sensors: (a) Schematic configuration of tactile sensors with interlocked fibrous structure. (b) SEM images of intermediate SEBS composites prepared with various electrospinning time. (c) Optical transmittance curves of the SEBS composites prepared with various electrospinning time, as a function of the wavelength, respectively. The inset figures show a linear decrease of transmittance at 550 nm with the increasing electrospinning time. (d) SEM images of the conductive composite uniformly with silver nanoparticles after chemical reduction of AgCF₃COO. (e) Energy dispersive X-ray spectroscopy EDS maps of Ag within the confined are in (inset). (f) EDS spectrum recorded within the region defined in (e). (g) Photograph of various SEBS composites with corresponding transmittance values of 91%, 74% and 56%.....**132**

Figure 2. FTIR analysis of the SEBS composite before and after absorption of silver trifluoroacetate (STA) as Ag precursors. Black and red lines indicate results of the pure SEBS and the SEBS-AgNPs absorbing the Ag precursors, respectively. Asymmetric stretching of C-F bonds of the Ag precursors (AgCF₃COO) is appeared in the two peaks at 1,126 cm⁻¹ and 1,184 cm⁻¹...**133**

Figure 3. XRD pattern of SEBS and SEBS-AgNPs.....**133**

Figure 4. SEM characterization of SEBS composites: (a) Schematic illustration of integrating the fibrous electrode with a dielectric layer forming a sandwich-type composites. (b) SEM images of bottom SEBS-AgNPs electrode was covered by different fiber diameter intervals. (c) Cross-sectional schematic view of laminated composites. (d) Cross-sectional SEM images of the top and side views of a dielectric layer sandwiched by two fibrous electrodes at top and bottom.....**134**

Figure 5. Pressure-sensing performance, durability and time-resolved responses: The pressure response for four consecutive measurements of (a) SEBS-1, (b) SEBS-2 and (c) SEBS-3. (d) The comparison of the resistance response and the threshold of resistance switching range of SEBS (second forward). (e) The stability test of the pressure sensor under a varied certain pressure range (0.16 to 0.176 kPa; 5.77 to 6.11 kPa; 22.02 to 25.69 kPa) over 100 loading-unloading cycles. (f) Response time of the SEBS-1 pressure sensor with an applied pressure of 0.18 kPa and exhibited instant response time within 2 ms. (the right

figure shows the magnified curve of the left one).....137

Figure 6. Response time of the SEBS-3 pressure sensor with an applied pressure of 25 kPa and exhibited instant response time within 10 ms. (the right figure shows the magnified curve of the left one).....138

Figure 7. Detection of various static mechanical stimuli: (a, c, e) Schematic illustration of the shape deformation of the SEBS-1 pressure sensor under press, stretching, and bending. (b, d, f) The plots of relative resistance change ($\Delta R/R_0$) of the sensors as a function of loading force under pressures, bending curvatures, and tensile strains, respectively.....143

Figure 8. The plots of relative resistance change ($\Delta R/R_0$) of the SEBS-3 pressure sensor as a function of loading force under pressures.....143

Figure 9. The sensitivities of the sensor under various tensile strain at stage I and stage II, which was obtained from the slopes of the curves in **Figure 7f**.....143

Figure 10. SEM image of the SEBS-1 and SEBS-3 composites before stretching (inset) and after 70% of the tensile strain.....144

Figure 11. Stress-strain curves of SEBS and SEBS-AgNPs composites.....144

Table

1-1 、 Standards and Guidelines for Selected Heavy Metals in Drinking Water Reported by the WHO and EPA.....	3
1-2 、 Polymerization conditions and molecular weights of random poly(MMA-co-BNPTU-co-RhBAM) copolymers.....	26
1-3 、 Time-dependent solution conductivity of the prepared Hg ²⁺ solution.....	55
2-1 、 Polymerization conditions and molecular weights of poly (NIPAAm-co-NMA-co- AA) random copolymers.....	72
2-2 、 Time-dependent solution conductivity of the prepared Hg ²⁺ solution.....	88
3-6 、 Comparison of the sheet resistance and the optical transmittance between the reported transparent AgNW films and the AgNW-PDMS composite films....	108.
4-6 、 The Comparison of this work and previous flexible pressure sensors.....	137

Chapter 1

RGB-Switchable Porous Electrospun Nanofiber Chemoprobe-filter Prepared from Multifunctional Copolymers for Versatile Sensing of pH and Heavy Metals

1-1 Introduction

Up to date, the heavy metals had been causing worldwide concern due to the rapid growth of industrialization. The heavy metals with the high density (above 5 g/cm³) and atomic weights between 63.5 and 200.6 are recognized as the metallic elements. Typical heavy metals such as cadmium (Cd), cobalt (Co), copper (Cu), mercury (Hg), potassium (K), Sodium (Na), aluminium (Al), manganese (Mn), magnesium (Mg), calcium (Ca), iron (Fe), zinc (Zn), nickel (Ni), and etc. A few of certain heavy metals (Fe, Mg, K, Zn, and etc.) are nutritionally essential for human health under low concentrations. They can be recognized as activators of enzyme reaction and playing critical roles in human physiology such as electron transfer, redox reaction, and structural functions in nucleic acid metabolism process. However, even at relatively low concentrations, heavy metals exhibit the potential ability to form complexes with biological molecules containing oxygen (O), nitrogen (N), and sulfur (S), which can transform structural change and break of hydrogen bonds, and therefore may cause the function of human organs including the central nervous system (Pb²⁺, Hg²⁺); skin, bones, or teeth (Cr³⁺, Cd²⁺, Cu²⁺), and the kidneys or livers (Cd²⁺, Pb²⁺, Hg²⁺)¹⁻³

The wastewater pollutions from various industrial activities such as metal plating, fertilizer, fossil fuel, tannery, battery manufacturing, and etc. is the main factor causing the serious environment contaminations.⁴ The heavy metals have non-biodegradable property and tend to accumulate in living organisms, which directly be uptake in human

body through the food chains or caused serious contaminations into the environment. For this reason, the international organizations have been defined the standards regulations concerning the safety limits or contaminant levels in drinking water. **Table 1** summarizes the standards and guidelines for the selected heavy metals in drinking water reported by Environmental Protection Agency (EPA) and World Health Organization (WHO) based on the scientific data.⁵ Furthermore, it is critical to classify and separate in the environment of wastewater, drinking water, food chain, ecological system, and biological fluids for global sustainability. Hence, the purpose of the present project is to provide an effective methods in the development of heavy-metal-detection devices and systems. The conventional methods based on real-time monitoring instruments to detect heavy metal contamination request sophisticated analytical techniques: atomic emission spectrometry (AES), atomic absorption spectroscopy (AAS), inductively coupled plasma mass spectrometry (ICPMS), X-ray fluorescence spectrometry, and etc.⁶⁻⁹ Although the aforementioned standard methods effectively exhibit high efficiency and sensitivity for trace heavy metals. Nevertheless, they require cumbersome instrumental setup, complex sample manipulation, and high cost, thus significantly limits its on-site potential as a practical devices with portable and light-weight characteristics. In contrast, rapid development of chemosensors based on nanotechnology platforms have intrinsic potential in high-throughput continuous detection of heavy metal contaminants on-site, thus improving the performance of sensors in terms of limit of detection, sensitivity, selectivity, reproducibility and also further enabled miniaturization and infield applications.

Table 1. Standards and Guidelines for Selected Heavy Metals in Drinking Water Reported by the WHO and EPA

Metal ⁺	WHO (mg/L) ⁺	EPA (mg/L) ⁺	⁺
Zn ⁺	3 ⁺	5 ⁺	⁺
Cu ⁺	2 ⁺	1.3 ⁺	⁺
Ni ⁺	0.07 ⁺	0.04 ⁺	⁺
Pb ⁺	0.01 ⁺	0.015 ⁺	⁺
As ⁺	0.01 ⁺	0.01 ⁺	⁺
Hg ⁺	0.001 ⁺	0.002 ⁺	⁺
Cd ⁺	0.003 ⁺	0.005 ⁺	⁺

1-2 Motivation

The development of sensitive and selective fluorescent chromogenic sensors composed of chelating ligands that are used to detect heavy-transition-metal (HTM) cations and pH in biological and environmental sensory devices has attracted extensive scientific interest because such cations can severely affect human health and the environment.¹⁰⁻¹² The HTM cation mercury Hg²⁺ and its derivatives are widely used in industry and have been demonstrated to cause environmental and health problems. Colorimetric-derivative sensors based on 1, 8-naphthalimide have been widely used in fluorescence detection of Hg²⁺, Cd²⁺, and Cu²⁺ because of their numerous excellent optical properties such as high quantum yields and favorable photostability.¹⁵⁻²¹ Liu reported the development of a new fluorescent chemodosimeter, namely a 1,8-naphthalimide-based colorimetric derivative (1-benzoyl-3-[2-(2-allyl-1,3-dioxo-2,3-dihydro-1Hbenzo[de]isoquinolin-6-ylamino)-ethyl]-thiourea (BNPTU) that exhibited high selectivity for Hg²⁺ in aqueous solutions and was based upon the reactivity of thiourea derivatives with Hg²⁺.¹⁵ A mercury-triggered intramolecular cyclization of

thiourea results in the formation of a highly blue fluorescent naphthalimide derivative, whereas the dosimeter itself fluoresces yellowish green. Rhodamine B and its derivatives (RhBs) are satisfactory fluorescent sensors for sensing pH because of their unique properties such as a high fluorescence quantum yield, long-wavelength emission, and high absorption coefficients.^{22–24} However, all of the aforementioned studies were based on solutions rather than nanofibers. The high surface-to-volume ratio of nanofibers facilitates responses in Hg²⁺-/pH-sensitive and multifunctional sensory materials.

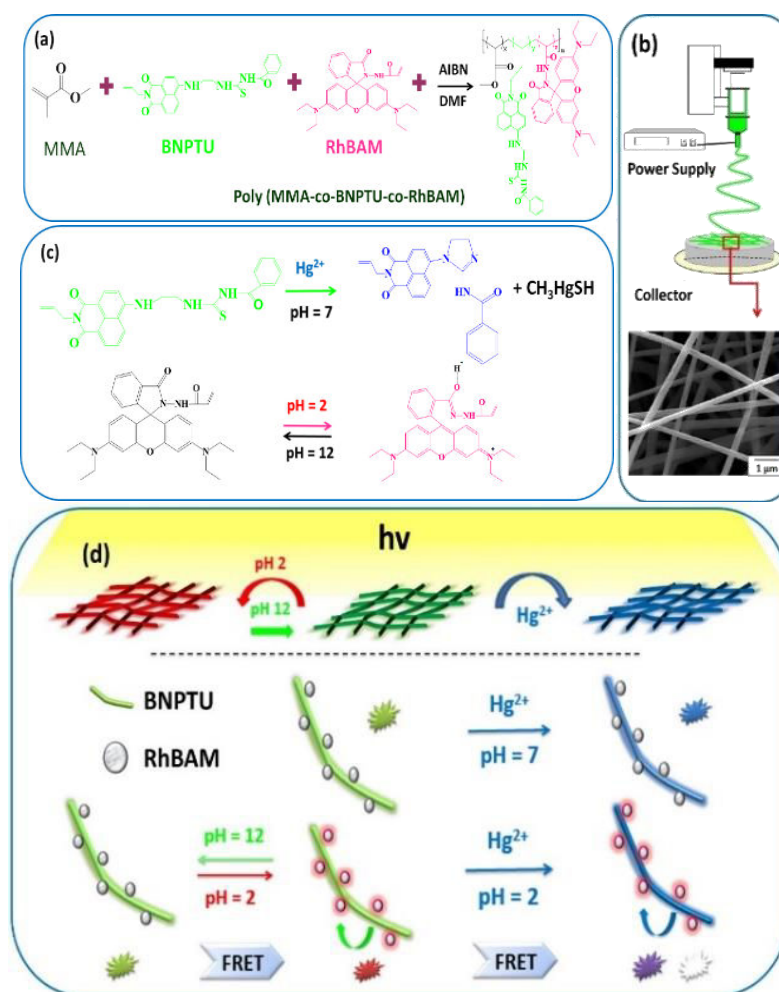
Electrospinning is an easy, versatile, and inexpensive technique for producing nanometer-scale fibers for assembling various functional nanofibers.^{25–28} The high surface-to-volume ratio of electrospun (ES) nanofibers has motivated extensive studies on sensory applications involving the sensing of pH levels,²⁹ temperatures^{30,31} NO gases³² and metal ions.^{33–37} Recently, various fluorescent sensor-based ES polymer nanofibers for sensing pH and metallic ions such as Hg²⁺, Fe³⁺, Zn²⁺, and Cu²⁺ were successfully prepared by our group.^{34–37} These prepared multifunctional fluorescent ES nanofibers exhibited distinct on-off switching such as quenching-enhancing photoluminescence (PL) intensity or changed-recovered PL colors for sensing various pH levels and metal ions.

Fluorescence resonance energy transfer (FRET)-based sensors for sensing specific HTM cations and pH values have attracted considerably more attention than quenching-enhancing PL intensity-based sensors because their color changes are easily observed by the naked eye. However, most of the developed FRET-based sensors were based on solutions^{38–41} rather than nanofibers.³⁵ We recently reported dual-ratiometric fluorescent chemosensory ES nanofibers that are able to detect pH and Fe³⁺ and were synthesized using binary blends of poly(2-hydroxyethyl methacrylate-co-N-methylolacrylamide-co-nitrobenzoxadiazolyl derivative) (poly(HEMA-co-NMA-co-

NBD), FRET donor) and a spiro lactam rhodamine derivative (SRhBOH, FRET acceptor).³⁵ In this paper, we report a full-color switchable fibrous probe that is not blended but is instead prepared from only one type of copolymer. This probe detected pH and Hg²⁺ simultaneously and exhibited full-wavelength-tuned fluorescence emission when solutions with different pH values and Hg²⁺ concentrations were tested. In addition, we would like to develop these ES nanofiber membranes into probe-filter membranes (nonwoven solid state with porous structures), which can assist future researchers in cleaning water while simultaneously chelating and sensing Hg²⁺.

The FRET-based fluorogenic probe ES nanofibers developed in this study were prepared using poly(methyl methacrylate-co-1, 8-naphthalimide derivatives-co-rhodamine derivative) (poly(MMA-co-BNPTU-co-RhBAM)) copolymers containing a naphthalimide derivative and a spiro lactam rhodamine derivative; the process involved combining synthesis, electrospinning, optical application, and analysis of morphological characteristics. The poly(MMA-co-BNPTU-co-RhBAM) was subjected to free-radical polymerization (Scheme 1(a)), with different ratios of its three components, and was then prepared for the formation of probe nanofibers using electrospinning (Scheme 1(b)). The fluorescence emission of BNPTU is highly selective for Hg²⁺, turning from green to blue in its presence (Scheme 1(c)). Furthermore, RhBAM exhibited reversible pH-sensing dependency; when it was used to detect acidic media, the spirocyclic form of RhBAM, which is colorless and nonfluorescent, transformed into the opened-cyclic form, which is pink and exhibits strong fluorescence emission (Scheme 1(c)). Thus, the fluorescence emission of the ES nanofibers change from green to red when they detect acidic media because of the energy transfer from the BNPTU (donor) to the RhBAM (acceptor) (Scheme 1(d)). More importantly, various emission colors—blue, green, yellow, red, and even white—can be observed by adjusting the various pH and Hg²⁺ combinations that are sensed.

Off-on switching of the FRET process can be easily modulated by simultaneously adjusting the concentrations of Hg^{2+} and the pH of the solution. The favorable detection of Hg^{2+} and pH demonstrated by the experimental results suggests that ES nanofibrous membranes, which can be used as naked eye probes, have potential applications in multifunctional environmental sensing devices.



Scheme 1 Design of multifunctional probe ES nanofibers synthesized from poly(MMA-co-BNPTU-co-RhBAM) and exhibiting various colors of fluorescence emission. (a) Polymerization and chemical structure of poly(MMA-co-BNPTU-co-RhBAM). (b) Fabrication of ES nanofibers. (c) Chemical structure of BNPTU in solutions with Hg^{2+} and RhBAM in solutions with pH 2 or 12. (d) Effect of FRET on the fluorescence emission colors of multifunctional environment-sensing ES nanofibers.

1-3 Background and review of literatures

1-3-1 Development of chemosensors for the detection of analytes

Fluorescent chemosensors is relatively facile technique which are rapidly performed, nondestructive and commonly used to multicomponent analysis due to their advantage of short-time detection, high selectivity and sensitivity, thus making its a desirably intrinsic technique among the researchers. Chemosensors can be classified by their signal transduction methods into three categories: (i) Fluorogenic sensors related to Fluorescence Resonance Energy Transfer (FRET), Photo-induce Electron Transfer (PET), Photo-induce Charge Transfer (PCT) Excited State Intramolecular Proton Transfer (ESIPT), Through Bond Energy Transfer (TBET), and etc. (ii) Colorimetric sensors related to intra/intermolecular Charge Transfer (ICT) (iii) Voltammetric sensors related to measure the variation of an electrical signal based on a redox reaction.⁴²⁻⁴⁹ The consist of sensing system have two essential features : the receptor and the immobilization/transducing. Generally, the receptors can specifically bind with the target chemical species and also responsible for the sensor selectivity and sensitivity. Typical interaction of heavy metals with the selected receptor involves noncovalent bonding, such as metal coordination, hydrogen bonding, $\pi - \pi$ interactions, van der Waals forces effects, and etc.⁵⁰ Those effects are originated from various types of recognition materials related to the specific ligand with different metal ions including alloys and amalgams, bismuth and antimony film electrode to form multicomponent alloys which can used in organic receptors (ionophores, crown ethers, and cyclodextrin)⁵¹ Transducers can trace the binding affinity between the receptors and the target chemical species through changes in the physicochemical properties. The charge transfer or energy transfer process can give rise to either a “turn-off” or a “turn-on” fluorescence response due to fluorescence quenching or enhancement. Among them, researchers have put a spotlight on the Forster resonance energy transfer (FRET) process when developing fluorescent sensors for heavy metal detection. FRET involves dipole-dipole coupling between an excited-state (donor) and an acceptor. This phenomenon was described as the donor return to its electronic ground state, and

emission may then occur from the acceptor center (**Figure 1**).⁵² The FRET efficiency is highly dependent several factors: the relative orientation of the transition dipoles (**Figure 2**), the distance between the donor and the acceptor, and the extent of spectral overlap between the donor emission and acceptor absorption spectrum. An intensive description of the physical basis of FRET are shown in **Figure 3**.⁵³ It indicated that the activation of FRET process can be switched on upon the sufficient excitation energy. The excited state donor molecule transfer the nonradiatively energy close to an acceptor molecule where located at distance r from the donor. The acceptor emits the energy either fluorescence or nonradiative pathways. The spectra of absorption (Abs) and emission (Em) show fluorescein (donor) exhibited efficiently excited at 480 nm and emits at around 520 nm. The spectral overlap between fluorescein emission and rhodamine absorption are observed at 500-600 nm. The Förster distance R_0 for this pair is 55 Å, thus result in significant FRET emission of the rhodamine above 600 nm.

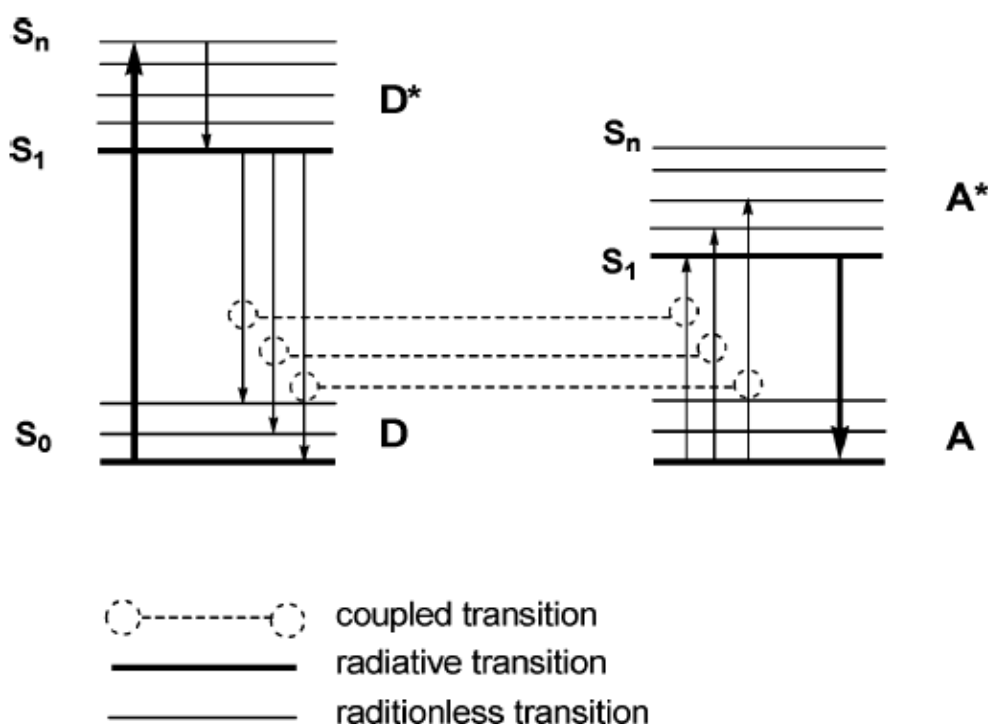


Figure 1. Fluorescence (Forster) resonance energy transfer system.

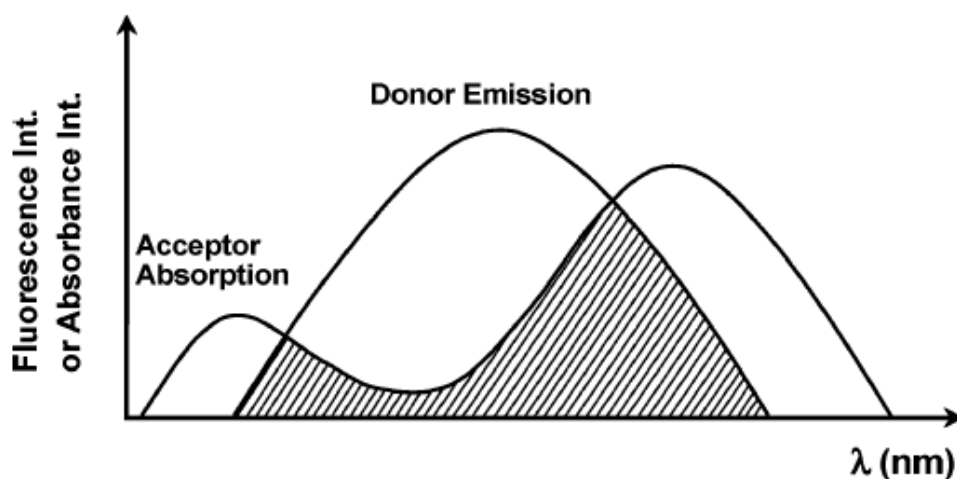


Figure 2. Spectral overlap for FRET.

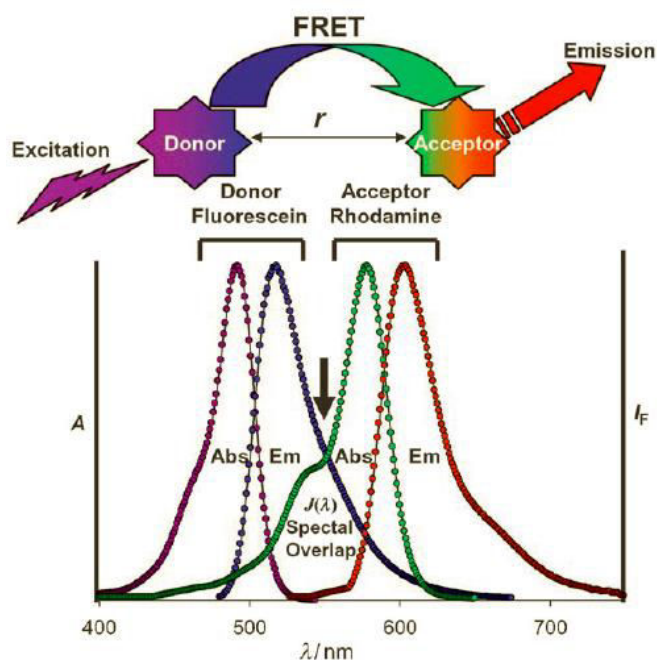


Figure 3. Schematic of the FRET process between the fluorescein and rhodamine.

The conventional FRET requires the overlap between the donor emission and acceptor absorption. Ono groups devoted to developing the FRET sensors for heavy metal detection.⁵⁴ The formation of FRET sensor has been linked with fluorophore and a quencher moieties in **Figure 4**. In the presence of Hg^{2+} ions, the hairpin structure can form by the T- Hg^{2+} -T sandwich structure upon the quencher close to the fluorophore, thus switched on the FRET process and results in significant fluorescence quenching. The limit of detection for this sensor can up to 40 nM toward Hg^{2+} in a buffer solution

and exhibit highly selectivity toward other common metal ions. The promising results from this groups had opened a new path for development of molecular chemosensors.

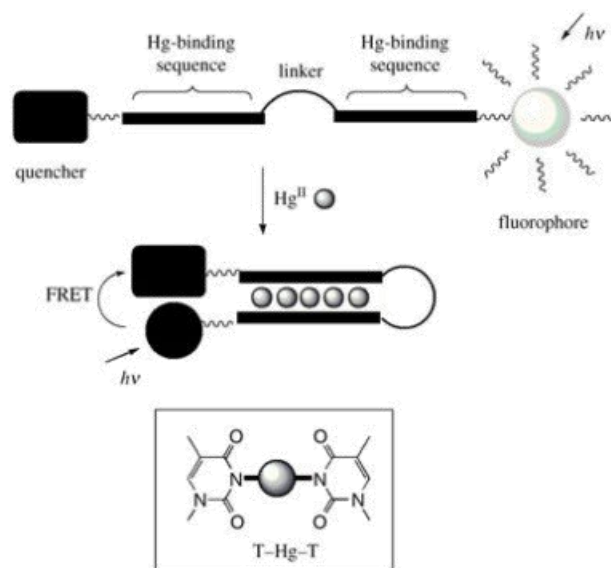


Figure 4. The schematic of the molecular beacon-based FRET sensor;

the presence of Hg^{2+} ions brought the quenching of fluorescence emission.

Organic dyes are generally used as the chromophore in FRET sensors due to the availability from commercial sources, their relatively inexpensive, and well established methods for labeling protocols.⁵⁵ Among the alternative chromophore sensors, the rhodamine fluorochrome has emerged as a quite promising candidate for fluorophore sensor because of its excellent photophysical property such as a high fluorescence quantum yield, long wavelength emission, high absorption coefficient, favorable photostability, and high sensitivity.²²⁻²⁴ Rhodamine derivatives are nonfluorescent and colorless, whereas addition of targeted metal ions or Lewis acid leads to ring opening of the corresponding spirolactam, giving rise to a strong fluorescence emission and a color change from colorless to pink. (**Figure 5**)⁵⁵ Tae groups reported that developed a promising system to achieve the highly selective and sensitivity for sensing Hg^{2+} in aqueous solution based on the rhodamine 6G derivative (**Figure 6**). They anticipated that the rhodamine 6G derivative coupling mechanism between the stoichiometric and irreversible Hg^{2+} induced the reaction of thiosemicarbazides to form 1,3,4-oxadiazoles.

This novel chemodosimeter exhibit highly limitation of detection, which is below 2 ppb in mercury aqueous solutions toward other common metal ions.⁵⁶

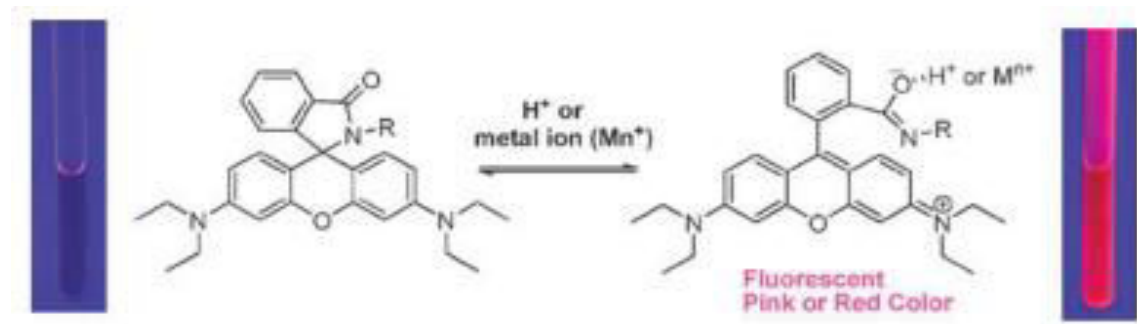


Figure 5. Mechanism of ring-opening process of rhodamine derivative in the presence of a targeted metal ions or a Lewis acid.

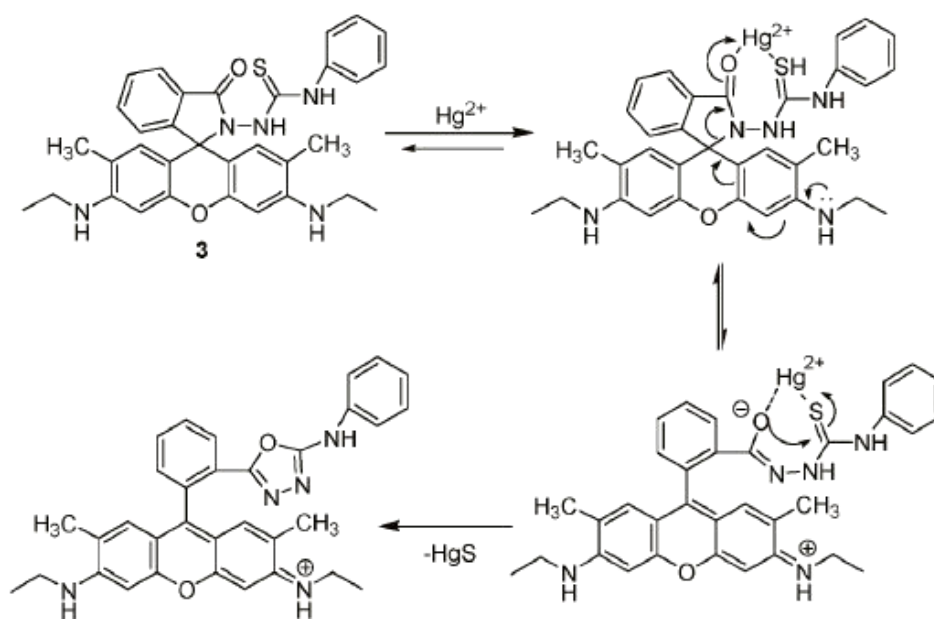


Figure 6. The reaction scheme of rhodamine 6G derivative with Hg^{2+} metal ions

Currently, the development of FRET-based sensor for detecting metal ions and pH have considerable attraction to broad audience due to their simplicity, color variation, and ratiometric detection capability.⁵⁷⁻⁶¹ Min groups firstly utilized the Rhodamine derivate fluorophores incorporated into tren moieties and measured their photophysical property upon addition the metal cations (**Figure 7**).The off/on switching of the FRET process can be modulated by adjusting the concentrations of Cu^{2+} ions to achieve the spirolactam ring of the rhodamine, whereas exhibit the various fluorescence change. ⁶²

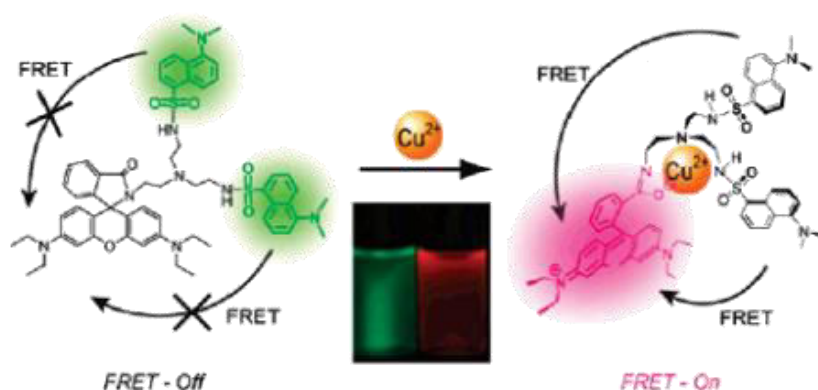


Figure 7. The Cu^{2+} -induced FRET OFF/ON process

Ma reported that using a two fluorescent dye to detect Fe^{3+} in aqueous solution containing a nitrobenzoxadiazolyl derivative (NBD) (donor), and RhB (acceptor) for fulfill the FRET-based system (**Figure 8**).⁶⁰ Liu groups proposed that fabricate the diblock copolymer with dual-ratiometric fluorescent probes through FRET donor (NBD) and acceptor moieties (RhBs) at the chain middle and terminals (**Figure 9**).⁶¹ However, all of the aforementioned studies were focused on solutions, it is necessary to develop the new platforms such as using the micro/nano materials with the high surface-to-volume property to improve the sensitivities.

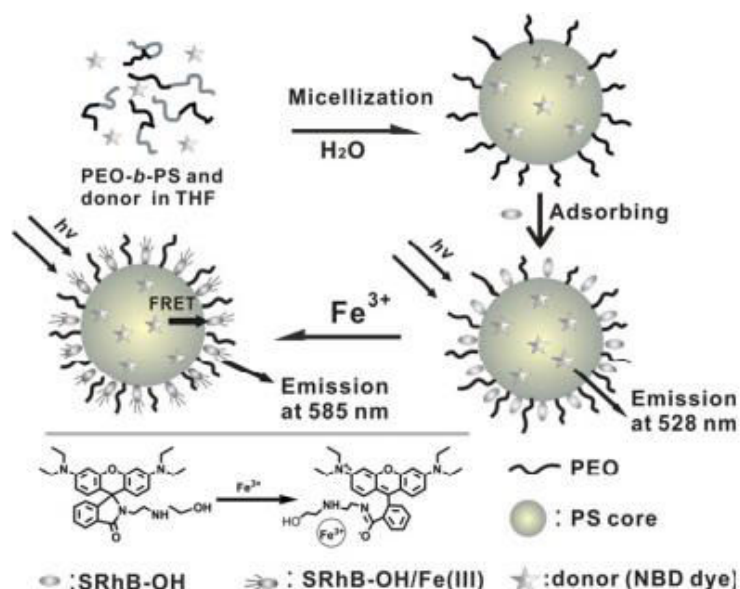


Figure 8. The FRET system within the diblock copolymer for sensing ferric ion.

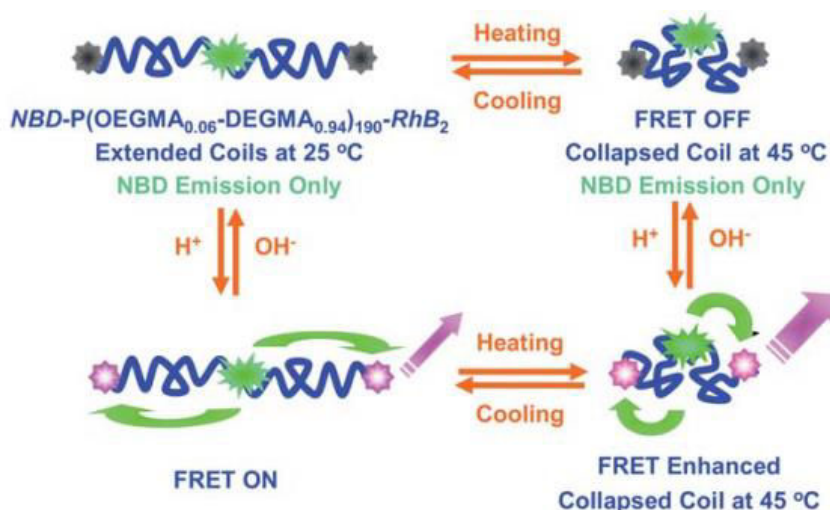


Figure 9. The scheme of pH and thermo-modulation of diblock copolymer.

1-3-2 Electrospinning techniques for fabricating ENMs

Electrospinning is an easy, versatile, and inexpensive technique for producing nanometer-scale fibers for assembling various functional nanofibers. The electrospinning technique consists of three major components: a high-voltage power supply, a spinneret (a metallic needle), and a collector (a ground conductor) (**Figure 10**). During the electrospinning process, a high voltage is applied to generate the droplet from a polymer solution at the tip of the spinneret. The droplet will begin to elongate into a conical shape commonly known as “Taylor cone” as the high voltage continuously increased.⁶³ The steady charged jet will be ejected from the bottom of the

Taylor cone until the electrostatic force overcomes the surface tension of the droplet. Subsequently, the electrostatic field jet undergoes a series of stretching and whipping process, resulting in randomly oriented nanosized fibers by a fast evaporation of the solvent. In some of case, the jet will be broken into droplet as the applied external electrostatic force is quite small than the voltage, which is called “Plateau-Rayleigh instability”⁶⁴⁻⁶⁶ On the contrary, if the applied external electrostatic force exceeds the range of voltage and much bigger than the surface tension, thus forming several of electrospinning jets from only one droplet in the same time. The fiber morphology and diameter are affected by several electrospinning parameters and conditions. 1) set up parameter from electrospinning process including feeding rate, the shape of spinneret, the distance between the collector and the spinneret tip; 2) Polymer properties such as molecular weight, polymer architecture; 3) solution properties such as boiling point, rheological behavior, polymer concentration, viscosity, conductivity, and electric potential; 4) ambient parameters such as the relative humidity, temperature, and the air velocity in the chamber. So far, based on this relatively facile and straightforward technique, more than 100 various types of polymers have already been fabricated as fibers with diameters ranging from tens of nano-meters to a few micrometers.

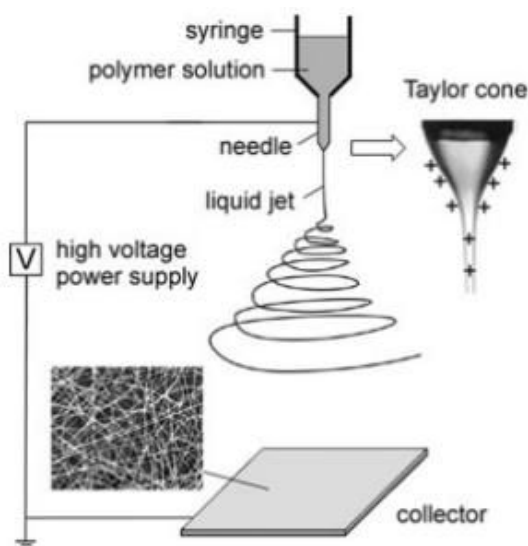


Figure 10. Schematic illustration of the typical electrospinning setup

1-3-3 Application of ENMs in optical chemosensors for heavy metal detection

Electrospun membranes with chelating agents are used as the tool for the removal of organic impurities and heavy metal ions in wastewater. Due to the advantages of ENMs, a large number of scientists have been widely investigated the fabrication methods in many fields by using functionalized polymer into nanofibers. Those composite nanofibers can provide high aspect ratio with porous structure, excellent mechanical and reinforcements properties, such as high modulus and strength to weight ratio compare to the conventional material. All of characteristics make electrospun polymer nanofibers have considerable attention applications in the filtration and water treatment. Wang reported the development of polymer-based chemical synthesis method for fabrication of ENM-immobilized optical chemosensors to detect Cu^{2+} in aqueous solution (**Figure 11**)⁶⁷ The fluorescent chemodosimeter, namely, N-allyl-4, 5-di [(2-picolyl) amino]-1, 8-naphthalimide (NAAP) was designing for ratiometric metal ions based on intermolecular charge transfer (ICT) process. The fluorescence emission of ICT-based fluorophores can shift remarkably when it binds with target metal ions. The poly (MMA-co-NAAP) was copolymerized with methyl methacrylate (MMA) and naphthalimide derivative (NAAP) via a free-radical polymerization process. Afterwards, poly (MMA-co-NAAP) was used to fabricate ENMs (ENM-immobilized optical chemosensors) based on electrospinning technique. As the fabricated ENM-immobilized optical chemosensors were immerse into Cu^{2+} solution, the copper ions can bind with the fluoorphore on the surface of electrospun nanofibers to form a 1:1 metal-ligand complex, which ICT-induced a 48 nm blue shift from 487 nm to 439 nm in fluorescence spectra. Because of high surface area-to-volume ratio of the nanofibrous film structures, the results revealed that the ENM-immobilized chemosensors exhibited a high sensitivity for copper metal ions and achieve the detection limit of 20×10^{-6} M at the nanomolar level. Moreover, the specificity of detection selectivity of the ENM-

immobilized chemosensors showed a higher selectivity toward Cu^{2+} as distinct from toward other common metal ions. This working revealed that polymer-based chemical synthesis methods are suitable methods to prepare ENM-immobilized optical chemosensors application in the filtration, water treatment, and heavy metal detection.

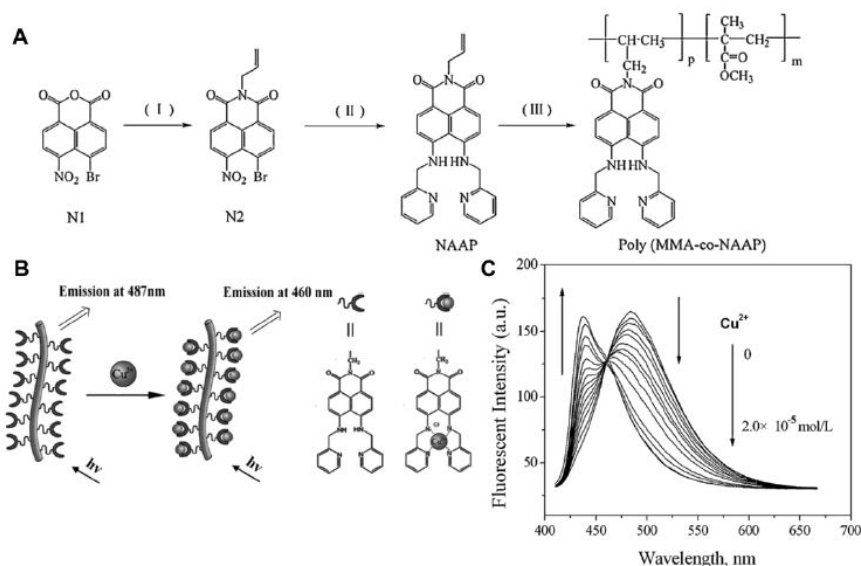


Figure 11. (A) Polymerization and chemical structure of poly(MMA-co-NAAP). (B) Schematic illustration for poly (MMA-co-NAAP) nanofiber fluorescent sensors by electrospinning for Cu^{2+} with enhanced detection sensitivity.

1-4 Experimental Section

1-4-1 Materials

Methyl methacrylate (MMA, Aldrich, 99%) was dried over CaH_2 to distill in a round-bottomed flask overnight, then purified by passing it through a short aluminum-oxide column (50–200 μm), and stored at 4 °C prior to use. The radical initiator 2,2'-azobis(2-methylpropionitrile) (AIBN) was purchased from UniRegion Bio-Tech and was recrystallized twice in ethanol prior to use. Rhodamine B (Acros, GR (guaranteed reagent)); acryloyl chloride (Alfa Aesar, 97%); dichloromethane (Tedia, 99.9%); methanol (Tedia, HPLC/SPECTRO); calcium hydride (reagent grade 95%); 4-bromo-1, 8-naphthalic anhydride (95%); benzoyl isothiocyanate (98%); allylamine (98%);

1, 2-ethylenediamine (99%); chloroform (anhydrous, 99%); N,N-dimethylformamide (99%); 1, 4-dioxane (99.5%); acetonitrile (99%); hydrochloric acid (reagent grade 37%); ethanol (99.8%); and hydrazine hydrate (reagent grade, N₂H₄ 50–60 %) were used as received. Perchlorate salts of metal ions (Co²⁺, Cu²⁺, Ca²⁺, Fe²⁺, Mg²⁺, Na⁺, Hg²⁺, Pb²⁺, Zn²⁺, Cd²⁺, K⁺, Ni²⁺, Mn²⁺, Pd²⁺, Fe³⁺) were purchased from Sigma-Aldrich.

1-4-2 Synthesis of 4-Bromo-N-allyl-1, 8-naphthalimide

Fluorescent BNPTU was prepared according to a previously reported method.¹⁸ The process of its synthesis is illustrated in (**Scheme 2(a)**). A 50-mL round-bottomed flask was charged with 4-bromo-1, 8-naphthalic anhydride (1.385 g, 5 mM), allylamine (0.317 g, 5.18 mM), and 20 mL of 1, 4-dioxane. The reaction mixture was stirred at reflux for 8 h. After cooling to room temperature, the suspension was poured into 600 mL of ice water and then filtrated. After drying in a vacuum oven overnight at room temperature, 4-bromo-N-allyl-1, 8-naphthalimide (BN-Br) was obtained as a slightly gray solid (1.24 g, yield: 89%). ¹HNMR (300 MHz, CDCl₃, **Figure 12(a)**): δ = 5.35 (a, 2H, -CH₂CHCH₂-); δ = 5.93 (b, 1H, -CH₂CHCH₂-); δ = 4.6 (c, 2H, -CH₂CHCH₂-); δ = 8.07 (d, 1H, 3-CH); δ = 7.96 (e, 1H, 6-CH); δ = 8.47 (f, 1H, 2-CH); δ = 8.58 (g, 1H, 7-CH); δ = 8.66 (h, 1H, 5-CH). HRESI-MS (**Figure 13(a)**): m/z calcd C₁₅H₁₀BrNO₂, C₁₅H₁₀⁸¹BrNO₂ +H⁺([M+H⁺]) 314.99, 316.99; found, 314.99, 316.99. FT-IR (Film, cm⁻¹, **Figure 14(a)**): 2949, 3084 (C-H stretch), 1655 (C=O stretch), 1588 (C=C stretch), 1234 (C-H stretch).

1-4-3 Synthesis of 4-(Aminoethylene) amino-N-allyl-1, 8-naphthalimide

A 25-mL round-bottomed flask was charged with NP-Br (500 mg, 1.57 mM) and an excess of 1, 2-ethylenediamine (8 mL). The reaction mixture was stirred at reflux for 6 h. The residues were dissolved in CH₂Cl₂ (200 mL) and extracted with water. Finally,

4-(aminoethylene) amino-N-allyl-1, 8-naphthalimide (NP-NH₂) was obtained as an orange crystal (420 mg, yield: 84%). ¹H NMR (300 MHz, DMSO-d₆, **Figure 12(b)**): δ = 5.35 (a, 2H, -CH₂CHCH₂-); δ = 5.93 (b, 1H, -CH₂CHCH₂-); δ = 4.6 (c, 2H, -CH₂CHCH₂-); δ = 7.68 (d, 1H, 6-CH); δ = 6.8 (e, 1H, 3-CH); δ = 8.27 (f, 1H, 2-CH); δ = 8.42 (g, 1H, 7-CH); δ = 8.71 (h, 1H, 5-CH); δ = 2.87 (i, 2H, -CH₂NH₂). HRESI-MS (**Figure 13(b)**): m/z calcd C₁₇H₁₇N₃O₂ + H⁺ ([M+H⁺]) 295.13; found, 295.13. FT-IR (Film, cm⁻¹, **Figure 14(b)**): 3383 (N-H stretch), 2924, 3200 (C-H stretch), 1634 (C=O stretch), 1513, 1539 (C-N stretch).

1-4-4 Synthesis of 1, 8-Naphthalimide-Based Monomer (BNPTU)

A 25-mL round-bottomed flask was charged with NP-NH₂ (400 mg, 1.36 mM), benzoyl isothiocyanate (0.22 g, 1.36 mM), and 12 mL of acetone. The reaction mixture was stirred at reflux for 1 h. After cooling to room temperature, the solution was filtrated and washed with ethanol. The product was purified using chromatography with CH₂Cl₂ (320 mg, yield: 80%). ¹H NMR (300 MHz, DMSO-d₆, **Figure 12(c)**): δ = 5.35 (a, 2H, -CH₂CHCH₂-); δ = 5.93 (b, 1H, -CH₂CHCH₂-); δ = 4.6 (c, 2H, -CH₂CHCH₂-); δ = 4.03 (d, 2H, -NCH₂CH₂N-); δ = 3.97 (e, 2H, -NCH₂CH₂N-); δ = 11.09 (f, 1H, -CSNH-); δ = 11.42 (g, 1H, -CONH-); δ = 8.28 (h, 1H, 2-CH); δ = 7.03 (i, 1H, 3-CH); δ = 8.73 (j, 1H, 5-CH); δ = 8.43 (k, 1H, 7-CH); δ = 7.62-7.88 (l + m, 3H, 6-CH; -COCCHCHCHCH-); δ = 7.49 (n, 1H, -COCCHCH-); δ = 7.93 (o, 2H, -COCCH-; -COC(CH)₄CH-). HRESI-MS (**Figure 13(c)**): m/z calcd C₂₅H₂₂N₄O₃S + H⁺ ([M+H⁺]) 458.14; found, 458.14. FT-IR (Film, cm⁻¹, **Figure 14(c)**): 3380 (N-H stretch), 2946, 3183 (C-H stretch), 1636, 1685 (C=O stretch), 1514, 1540 (C-N stretch), 1145, 1235 (C-H stretch).

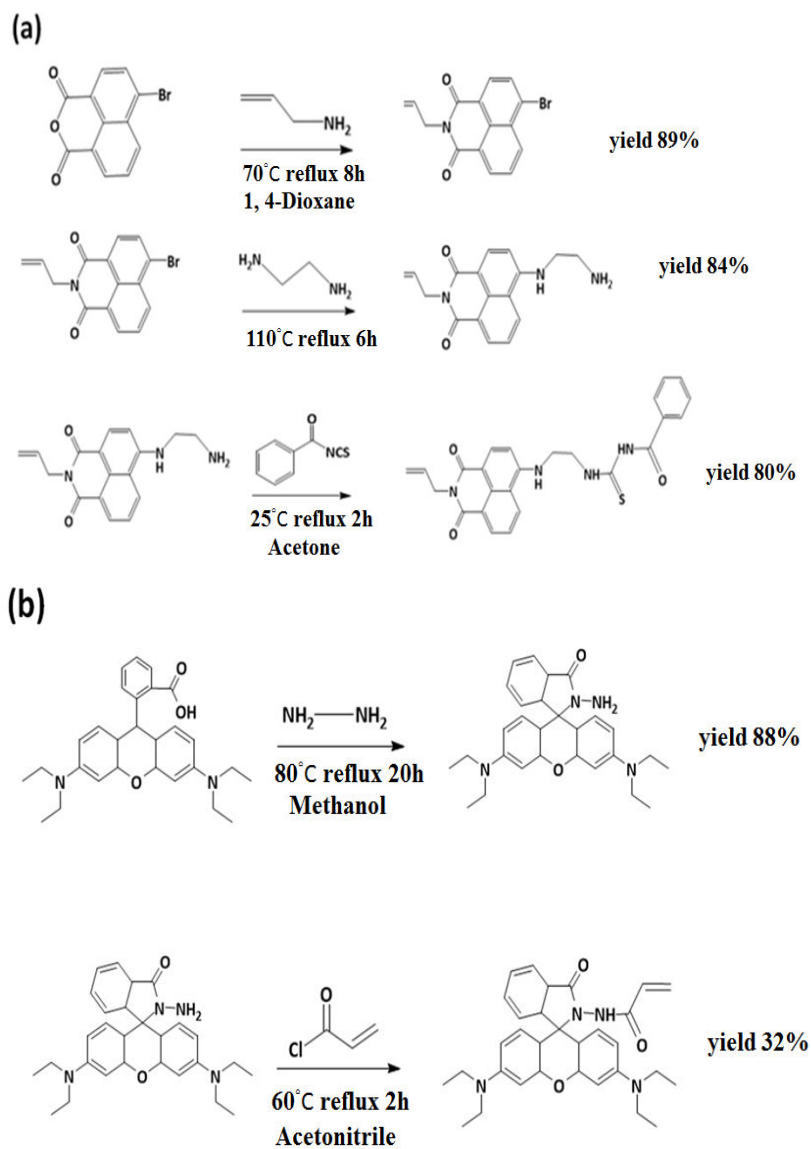
1-4-5 Synthesis of RhB Hydrazide

The RhB hydrazide synthesis scheme is shown in (**Scheme 2(b)**). The fluorescent probe, RhBAM, was synthesized according to a previously reported method.⁶⁸ Rhodamine B (4.8 g, 10 mM) and an excess of hydrazine hydrate (85%, 8 mL, 150 mM) were dissolved in 80 mL of methanol. The reaction mixture was stirred at 80 °C and refluxed for 20 h until the solution changed from dark purple to light orange and became transparent. After cooling to room temperature, the solvent was removed under decreased pressure. CH₂Cl₂ (200 mL) was then added, and the solvent was washed with water several times and dried over anhydrous sodium sulfate. RhB hydrazide was obtained as a pink solid (4.2 g, yield: 88%). ¹H NMR (300 MHz, CDCl₃, **Figure 15(a)**): δ = 3.62 (a, 2H, -CONNH₂); δ = 3.33 (b, 8H, Ar-N(CH₂)₄-); δ = 1.2 (c, 12H, Ar-NCH₂(CH₃)₄); δ = 6.2–7.88 (aromatic hydrogen, 10H). HRESI-MS (**Figure 16(a)**): m/z calcd C₂₈H₃₂N₄O₂ +H⁺([M+H⁺]) 456.25; found, 456.25. FT-IR (Film, cm⁻¹, **Figure 17(a)**): 3229, 3348 (N-H stretch), 2968 (C-H stretch), 1721 (C=O stretch), 1616 (C=C stretch), 1508 (Ar-H stretch), 1113 (C-O-C stretch).

1-4-6 Synthesis of RhBAM-Based Monomer

RhB hydrazide (1.5 g, 3.3 mM) was dissolved in 80 mL of dry MeCN, and dropwise addition of acryloyl chloride (8 mL, 99 mM) was performed. The reaction solution was stirred at 60 °C and refluxed for 2 h. The precipitates were collected through filtration and washed with dry CH₃CN three times. The crude product was dissolved in CH₂Cl₂ (200 mL) and washed with saturated NaHCO₃ aqueous solution several times. The organic phase was dried over anhydrous Na₂SO₄ and filtrated. After removal of all the solvents, the product obtained was a violet solid (480 mg, yield: 32%). ¹H NMR (300 MHz, CDCl₃, **Figure 15(b)**): δ = 1.21 (a, 12H, Ar-NCH₂(CH₃)₄); δ = 3.32 (b, 8H, Ar-N(CH₂)₄-); δ = 5.91 (c, 1H, -COCH-); δ = 5.32–5.63 (d, 2H, -COCHCH₂); δ = 6.2–

7.89 (aromatic hydrogen, 10H). HRESI-MS (**Figure 16(b)**): m/z calcd $C_{31}H_{34}N_4O_3 + H^+([M+H^+])$ 510.26; found, 510.27. FT-IR (Film, cm^{-1} , **Figure 17(b)**): 3210 (N-H stretch), 2970 (C-H stretch), 1729 (C=O stretch), 1615 (C=C stretch), 1515 (Ar-H stretch), 1112 (C-O-C stretch).



Scheme 2 Synthesis of (a) BNPTU fluorescent monomer (donor) and (b) RhBAM fluorescent probe (acceptor).

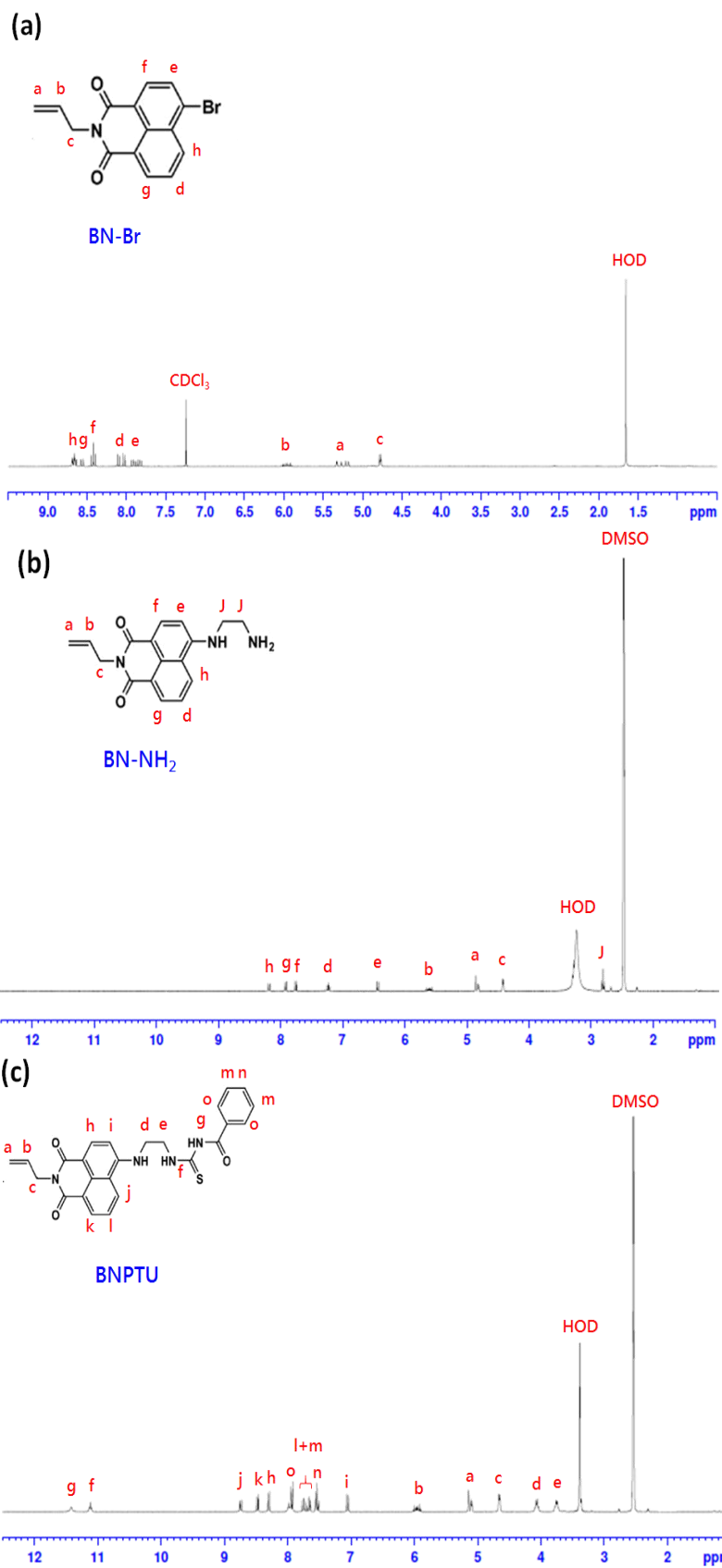


Figure 12. ¹H NMR spectra of (a) BN-Br in CDCl₃, (b) BN-NH₂ in DMSO-d₆ and (c) BNPTU monomer in DMSO-d₆.

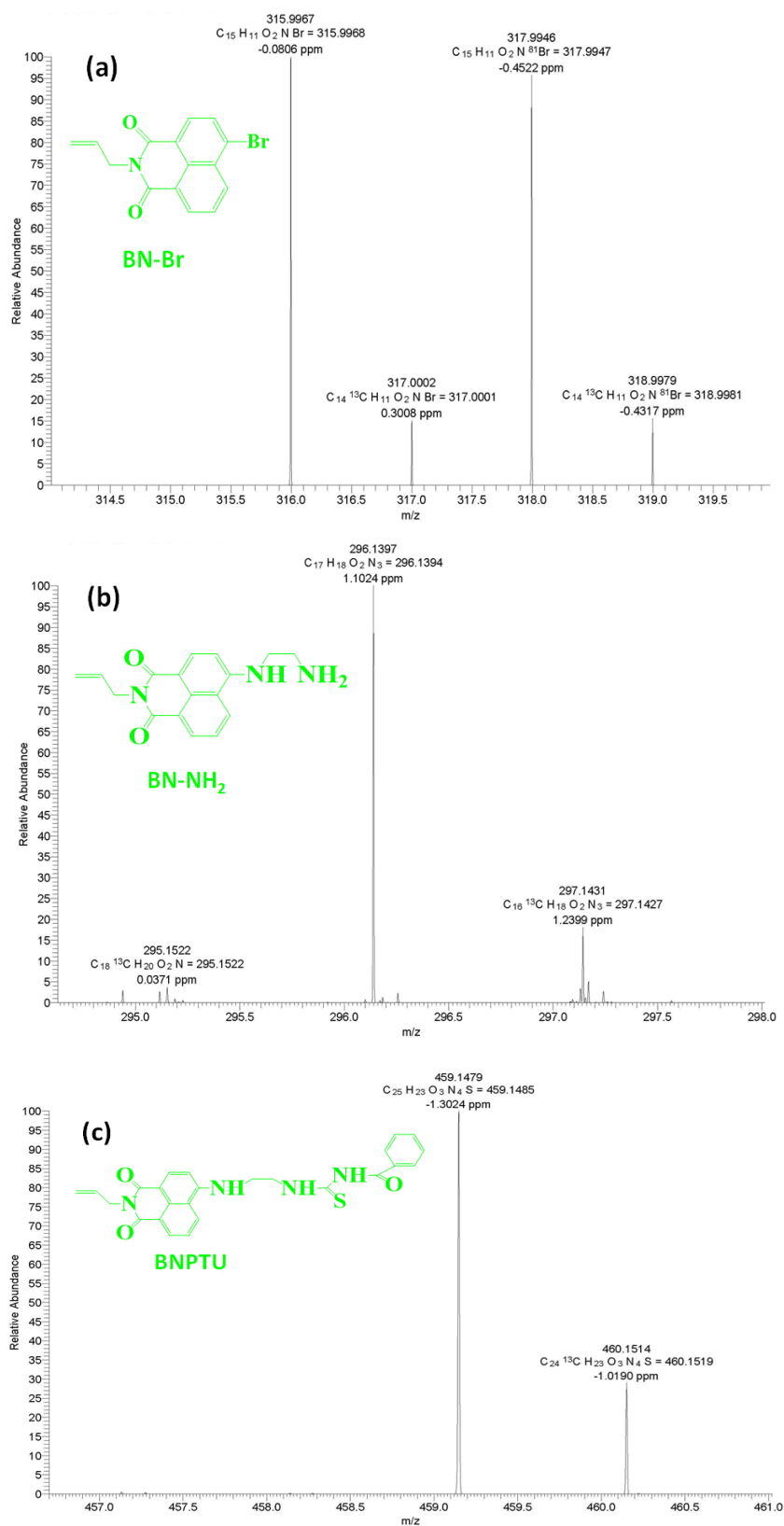


Figure 13. HRESI-MS spectra of (a) BN-Br, (b) BN-NH₂ and (c) BNPTU.

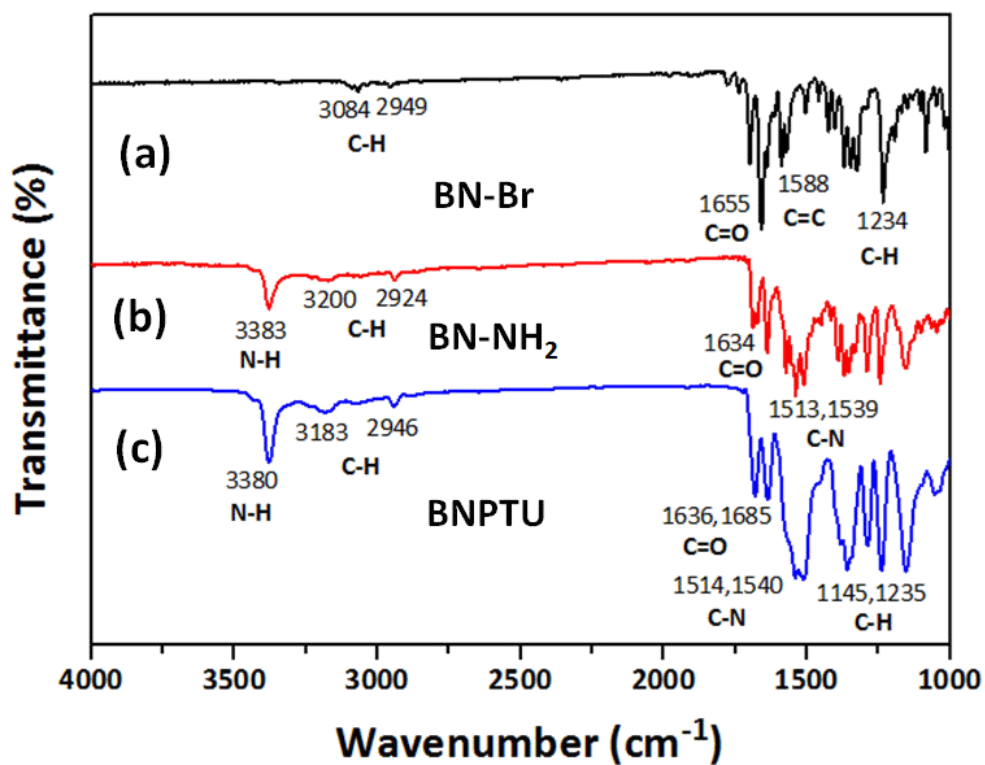
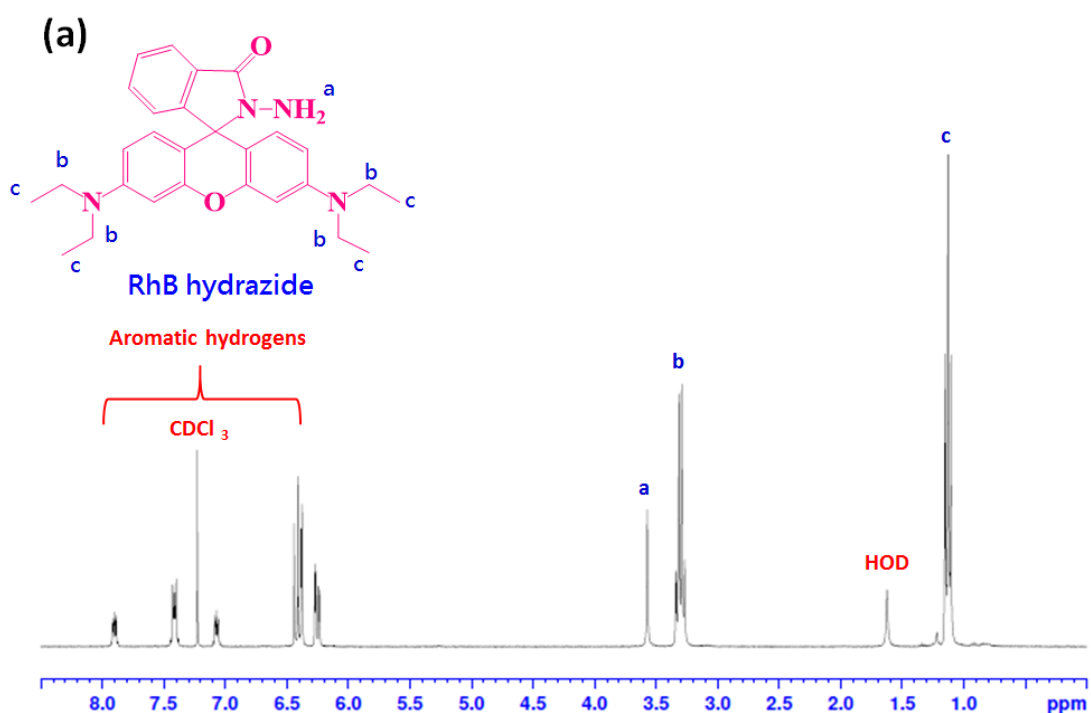


Figure 14. IR spectrum of (a) BN-Br, (b) BN-NH₂ and (c) BNPTU.



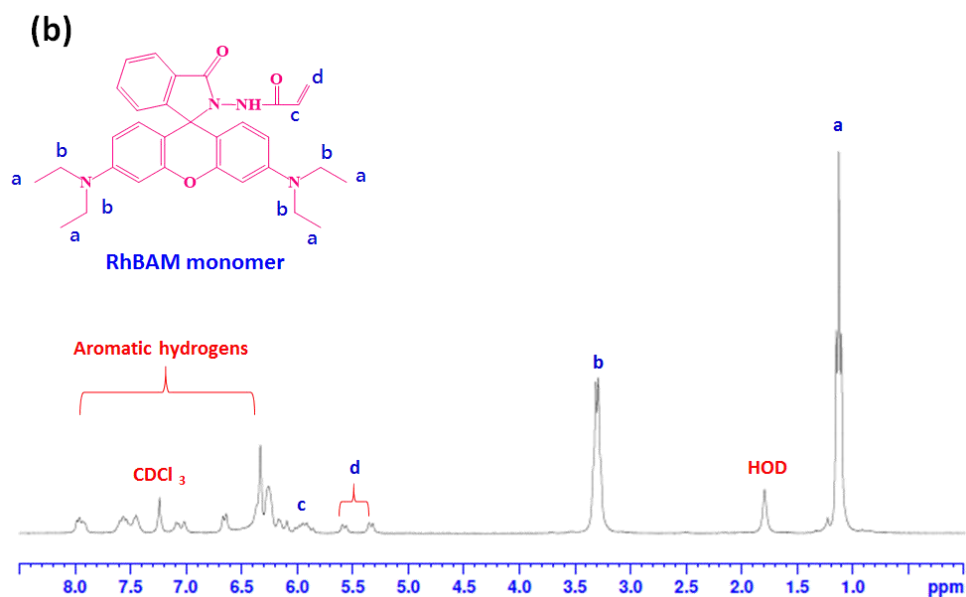


Figure 15. ¹H NMR spectra of (a) RhB hydrazide in CDCl₃ and (b) RhBAM monomer in CDCl₃.

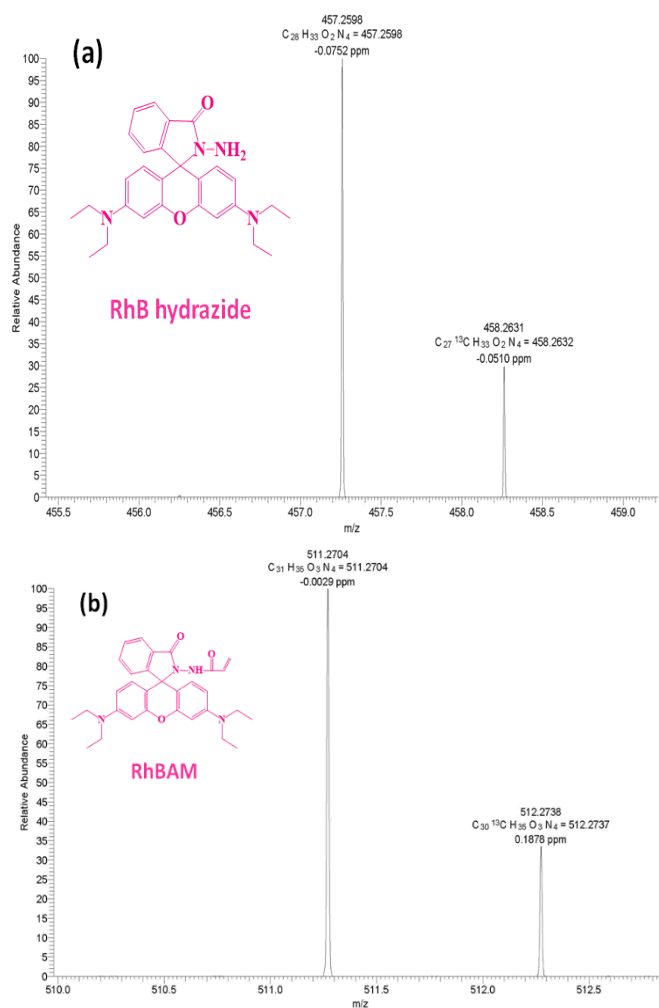


Figure 16. HRESI-MS spectra of (a) RhB hydrazide and (b) RhBAM.

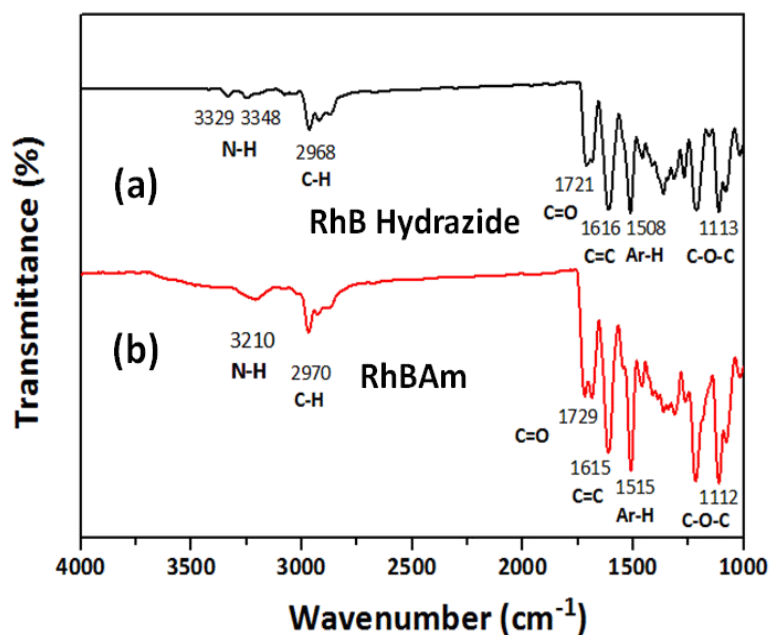


Figure 17. IR spectrum of (a) RhB hydrazide and RhBAM.

1-4-7 Synthesis of Poly(MMA-co-BNPTU-co-RhBAM)

Poly(MMA-co-BNPTU-co-RhBAM) was synthesized through free-radical copolymerization of the following three monomers: MMA, BNPTU, and RhBAM (**Scheme 1**). Poly(MMA-co-RhBAM), poly(MMA-co-BNPTU), and poly(MMA-co-BNPTU-co-RhBAM) with different monomer ratios were denoted **P1–P5**, as listed in **Table 2**. The concentration of AIBN used as the initiator was 0.004 M. The reaction mixture, containing dimethylformamide (DMF) and monomers, was degassed by first bubbling nitrogen for 30 min and then left to react at 70 °C for 24 h. The reaction mixture was subsequently poured into methanol, precipitated, filtered, and dried at room temperature under vacuum to obtain the polymer. The synthesis and characterization of **P5** are described in the following sections, and those of the other

four polymers are described in the supporting information. The number-averaged molecular weight (M_n) and polydispersity index (PDI) estimated from gel permeation chromatography (GPC) (DMF eluent) are listed in **Table 2**.

Polymer	Feed molar ratio MMA:BN:Rh	Experimental ratio ^a	M_n ^b	PDI	Td(°C)
P1	99 : 0 : 1	99.4 : 0 : 0.6	31000	1.45	278
P2	99 : 1 : 0	99.5 : 0.5 : 0	29300	1.42	274
P3	96.5 : 3 : 0.5	95 : 4.6 : 0.4	32500	1.35	276
P4	95.5 : 3 : 1.5	94.6 : 4.4 : 1	29500	1.33	282
P5	92.5 : 3 : 4.5	93.4 : 4.2 : 2.4	29250	1.36	294

Table 2. Polymerization conditions and molecular weights of random poly(MMA-co-BNPTU-co-RhBAM) copolymers.

^a Molar ratio (%), estimated from ¹H NMR spectra.

^b Determined using the DMF eluent.

1-4-8 Synthesis of P1

A reaction mixture of 1219.4 mg (12.17 mM) of MMA, 62.14 mg (0.12 mM) of RhBAM, 5 mg (0.03 mM) of AIBN, and 12.4 mL of DMF was used to produce a pink solid (yield: 60%). **Figure 18(a)** and **Table 2** present the molecular weight and chemical structure characterization of poly(MMA-co-RhBAM) obtained using GPC with DMF as the eluent and ¹H NMR, respectively. The estimated copolymer ratio of poly(MMA-co-RhBAM) based on the NMR spectrum was 99.4:0.6, and the number-averaged

molecular weight and PDI estimated using GPC were 31,000 g mol⁻¹ and 1.45, respectively. ¹H NMR (300 MHz, DMSO-d₆, **Figure 18(a)**): δ = 3.56 (a+e, 7 11H, -COOCH₃, -Ar-NCH₂(CH₃)₄); δ = 0.8–1.8 (b+c+d, 16H, -CH₂CH-, -CH₂CH-, Ar-NCH₂(CH₃)₄); δ = 1.8–2.1 (b+c, 2H, -CH₂CH-, -CH₂CH-); and δ = 6.2–7.89 (aromatic hydrogen, 10H).

1-4-9 Synthesis of P2

A reaction mixture of 1219.4 mg (12.17 mM) of MMA, 55.92 mg (0.12 mM) of BNPTU, 5 mg (0.03 mM) of AIBN, and 12.4 mL DMF was used to produce a light green solid (yield: 62%). **Figure 18(b)** and **Table 2** present the molecular weight and chemical structure characterization of poly(MMA-co-BNPTU) obtained using GPC with DMF as the eluent and ¹H NMR, respectively. The copolymer composition, estimated by performing peak integration, was consistent with the proposed structure. The estimated copolymer ratio of poly(MMA-co-BNPTU) based on the NMR spectrum was 99.5:0.5, and the number-averaged molecular weight and PDI estimated using GPC were 29,300 g mol⁻¹ and 1.42, respectively. ¹H NMR (300 MHz, DMSO-d₆, **Figure 18(b)**): δ = 3.56 (a, 3H, -COOCH₃); 0.8–1.8 (b+c, 4H, -CH₂CH-, -CH₂CH-); δ = 1.8–2.1 (b+c, 2H, -CH₂CH-, -CH₂CH-); δ = 5.92 (d, 2H, -CHCH₂-); δ = 4.61 (e, 2H, -NCH₂-); δ = 3.96 (f, 2H, -ArCH₂); δ = 11.01 (g, 1H, -CSNH); δ = 11.26 (h, 1H, -CONH); and δ = 6.96–8.68 (aromatic hydrogen, 10H).

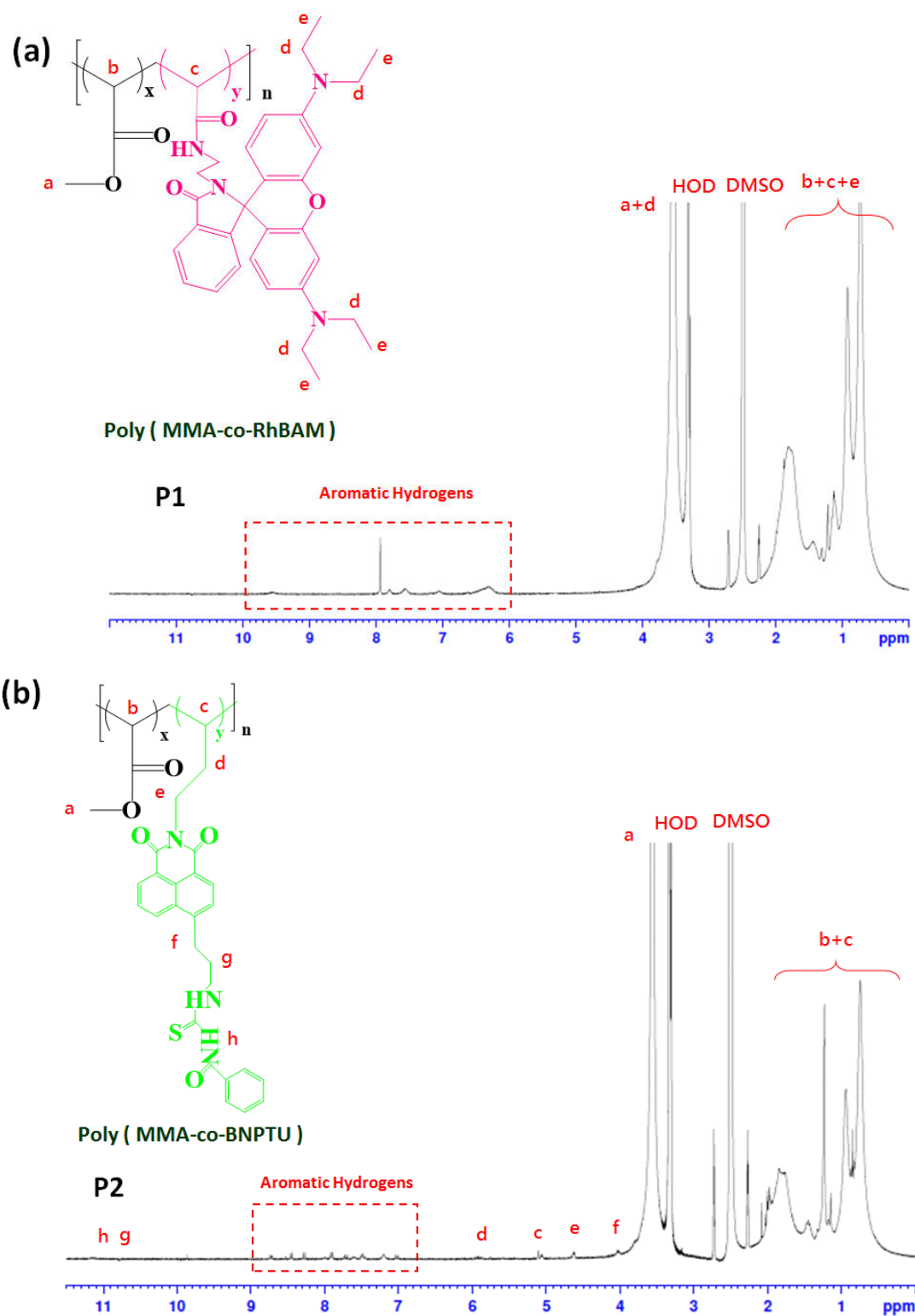


Figure 18. ^1H NMR spectra of (a) poly(MMA-co-RhBAM) in DMSO and (b) poly(MMA-co-BNPTU) in DMSO.

1-4-10 Synthesis of P5

A reaction mixture of 1219.4 mg (12.17 mM) of MMA, 167.78 mg (0.36 mM) of BNPTU, 93.22 mg (0.18 mM) of RhBAM, 5 mg (0.03 mM) of AIBN, and 12.4 mL of DMF was used to produce an orange solid (yield: 64%). **Figure 19** and **Table 2** present the molecular weight and chemical structure characterization of poly(MMA-co-BNPTU-co-RhBAM) obtained using GPC with DMF as the eluent and ^1H NMR, respectively. The copolymer composition, estimated by performing peak integration, was consistent with the proposed structure. The estimated copolymer ratio of poly(MMA-co-BNPTU-co-RhBAM) based on the NMR spectrum was 93.4:4.2:2.4, and the number-averaged molecular weight M_n and PDI estimated using GPC were 29,250 g M^{-1} and 1.36, respectively. ^1H NMR (300 MHz, DMSO- d_6 , **Figure 19**): $\delta = 3.56$ (a+h, 11H, $-\text{COOCH}_3$, $\text{Ar}-\text{N}(\text{CH}_2)_4-$); $\delta = 0.8-1.8$ (b+c+d+i, 18H, $-\text{CH}_2\text{CH}-$, $-\text{CH}_2\text{CH}-$, $-\text{CH}_2\text{CH}-$, $\text{Ar}-\text{NCH}_2(\text{CH}_3)_4$); $\delta = 1.8-2.1$ (b+c+d, 3H, $-\text{CH}_2\text{CH}-$, $-\text{CH}_2\text{CH}-$, $-\text{CH}_2\text{CH}-$); $\delta = 5.08$ (c, 1H, $-\text{CH}_2\text{CHCH}_2-$); $\delta = 5.92$ (e, 2H, $-\text{CHCH}_2-$); $\delta = 4.61$ (f, 2H, $-\text{NCH}_2-$); $\delta = 3.96$ (g, 2H, $-\text{ArCH}_2-$); $\delta = 11.01$ (j, 1H, $-\text{CSNH}-$); $\delta = 11.26$ (k, 1H, $-\text{CONH}-$); and $\delta = 6.32-8.68$ (aromatic hydrogen, 20H).

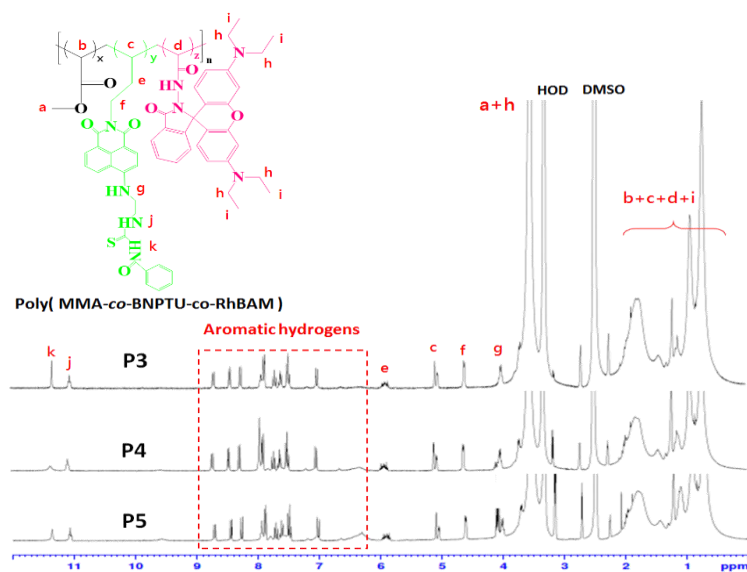


Figure 19. ^1H NMR spectrum of poly(MMA-co-BNPTU-co-RhBAM) in DMSO.

1-5 Preparation of Copolymer Solutions with Different pH Values

Preparation of a pH 2 copolymer solution was performed by mixing 7 mL 10^{-2} M probe in CH_3CN solution and 3 mL 4×10^{-2} M H^+ water solution (prepared using HCl). After preparation, we double checked with a pH meter to ensure the pH values of the prepared copolymer solutions were correct. The preparation of the other pH value copolymer solutions followed a similar method, as is also described in our earlier report.³⁵

1-6 Preparation of ES Nanofibers

As shown in Scheme 1(b), the ES nanofibers were prepared using a single-capillary spinneret in a procedure similar to that described in our previous reports.^{29–32,34–37} Poly(MMA-co-BNPTU-co-RhBAM) (250 mg mL^{-1}) was dissolved in a chloroform and dimethylformamide (CHCl_3/DMF) solvent and stirred overnight. The polymer solution was fed into a metallic needle using syringe pumps (KD Scientific Model 100, USA) with a feed rate of $0.8\text{--}1.0 \text{ mL h}^{-1}$. The tip of the metallic needle was connected to a high-voltage power supply (Chargemaster CH30P SIMCO, USA) that was set at 13.4 kV during electrospinning. A piece of aluminum foil or quartz was placed 15 cm below the tip of the needle for 30 min to collect the ES nanofibers. All experiments were performed at room temperature and a relative humidity of approximately 80%. Polymer films equivalent to the ES nanofibers were prepared using drop-casting of the same solution on a quartz substrate and then dried in an airflow hood. The properties of the thin films were compared with those of the ES nanofibers.

1-7 Characterization

^1H NMR data were recorded at room temperature using a Bruker AM 300 (300 MHz) spectrometer and the residual proton resonance of deuterated chloroform and deuterated dimethyl sulfoxide. High-resolution electrospray ionization mass spectrometry (HRESI-MS) spectra were recorded using a Shimadzu LCMS-IT-TOF mass spectrometer. GPC analysis was performed using a Lab Alliance RI2000 instrument (two-column, MIXED-C and -D from Polymer Laboratories) connected to a refractive index detector from Schambeck SFD GmbH. All GPC analyses were performed using a polymer/DMF solution at a flow rate of 1 mL min^{-1} at $40\text{ }^\circ\text{C}$ and were calibrated with polystyrene. The thermal decomposition temperature was determined using a thermal gravimetric analyzer (TGA) from TA Instruments (TGA Q50) over a heating range of $100\text{ to }800\text{ }^\circ\text{C}$ at a heating rate of $10\text{ }^\circ\text{C min}^{-1}$ in a nitrogen atmosphere. The Fourier transform infrared (FT-IR) spectra were recorded using a Bio-Rad 155 FT-IR spectrometer at ambient temperature in the range of $650\text{--}4000\text{ cm}^{-1}$.

The morphologies of ES nanofibers were characterized using scanning electron microscopy (SEM, Hitachi S-520). Samples were coated with platinum prior to the SEM characterization, and analysis was performed at an acceleration of 15 kV. Transmission electron microscopy (TEM) images were taken using a transmission electron microscope operated at 100 kV. Fluorescence optical microscopy images were taken using a two-photon laser confocal microscope (Leica LCS SP5). The morphologies of the ES nanofibers were similar to those reported in our previous studies.^{26,31,35}

To determine the surface area of the **P5** ES fiber membranes, an ASAP 2010 Accelerated Surface Area and Porosimetry Analyzer (Micromeritics; Norcross, GA) was used. **P5** ES fiber membranes can adsorb nitrogen gas. The specific surface area of a fiber membrane can be determined according to the adsorbed amount of nitrogen and

the size of nitrogen molecules by using the Brunauer–Emmett–Teller (BET) methodology. A 50- μm -thick **P5** ES fiber membranes was cut into a rectangular shape (1 \times 2 cm) and weighed. The sample was then placed in the sample container of the ASAP 2010 for the determination of nitrogen adsorption at various nitrogen pressures. BET surface areas were determined according to nitrogen adsorption in a relative pressure (p/p_0) range of 0.05–0.25 according to the BET method.⁶⁹ The mechanical properties of the **P5** ES nanofibers were determined using Dynamic Mechanical Analysis (DMA; Perkin Elmer, USA). The specimens, which were 10 mm wide and 30 mm long, were subjected to a tensile test with a crosshead speed of 10 mm/min. Young's modulus was calculated using the stress/strain curves, as described in our previous studies.⁷⁰⁻⁷¹

Ultraviolet–visible (UV–Vis) absorption and PL spectra were measured to study photophysical properties, and were recorded using a Shimadzu UV–Vis spectrophotometer and a Fluorolog-3 spectrofluorometer (Horiba Jobin Yvon), respectively. Variations in the optical absorption and PL of the prepared ES nanofibers (**P1–P5**) at different pH and metal-ion concentrations are described as follows. As shown in **Figure 20**, to ensure that the beam excited the same point on the prepared samples during each measurement, the ES nanofibers or films were fixed in cuvettes using adhesive tape and the cuvette was filled with an acidic or basic aqueous or metal-ion solution at 10^{-8} to 10^{-2} M. Each measurement was taken for 15 min to ensure that the chelating reaction reached equilibrium. All PL spectra of the ES fibers were recorded using the Fluorolog-3 spectrofluorometer, and the samples were excited at a suitable wavelength, as described in our previous studies.^{29-31,34-37}

P5 ES nanofibers

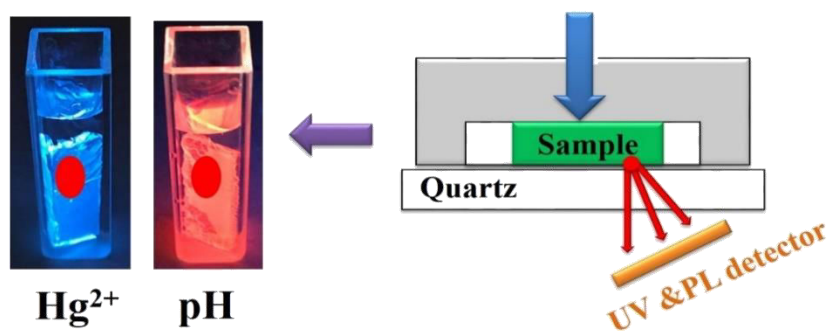


Figure 20. ES fibers for pH and Hg²⁺ sensing detector instrument.

1-8 Results and Discussion

1-8-1 Characterization of BNPTU, RhBAM, and Poly(MMA-co-BNPTU-co-RhBAM)

The chemical structures of BNPTU and RhBAM were characterized using ¹H NMR, HRESI-MS, and FT-IR as illustrated in **Figures 12–17**. The synthesis routes of BNPTU and RhBAM are shown in **Scheme 2** and are similar to those previously reported.^{18,68} **Scheme 1(a)** shows the route through which poly(MMA-co-BNPTU-co-RhBAM) copolymers were synthesized using free-radical polymerization. The five types of copolymers (**P1–P5**) synthesized and their composites are listed in **Table 2**. **Figure 19** shows the ¹H NMR spectrum of poly(MMA-co-BNPTU-co-RhBAM) (**P3–P5**), which was composed of MMA, BNPTU, and RhBAM in DMSO in ratios of 96.5:3:0.5, 95.5:3:1.5, and 92.5:3:4.5, respectively. The DMSO proton peak is marked in Figure 1. Proton signals from the phenyl group and an aromatic ring on the BNPTU and RhBAM moiety were discovered in the range 6.32–8.68 ppm. The proton peaks at 3.96 ppm (Peak g), 4.61 ppm (Peak f), 5.92 ppm (Peak e), 11.01 ppm (Peak j), and 11.26 ppm (Peak k) correspond to the methylene neighbors of the aromatic ring, nitrogen, alkyl chains on the polymer, nitrogen, and sulfur on BNPTU, respectively. The proton peaks at 3.56 ppm (Peak h) and 0.8–1.8 ppm (Peak i) correspond to the methylene neighbors of methyl and methylene groups on RhBAM, respectively. The proton peaks at 3.56 ppm (Peak a) correspond to the methylene neighbor of oxygen on

MMA. One peak at 0.8–1.8 ppm and the peaks at 5.08 ppm (Peaks b, c, d) correspond to the alkyl chains on the copolymers. The chemical structures of the other two copolymers (**P1** and **P2**) are revealed by their ^1H NMR spectra in **Figure 18**. The copolymer ratios of poly(MMA-co-RhBAM) and poly(MMA-co-BNPTU), estimated from NMR spectra, were 99.4:0.6 and 99.5:0.5 for copolymers **P1** and **P2**, respectively. The favorable agreement between the feeding ratio and experimental composition suggests the preparation of the target copolymers was successful. The molecular weights and thermal properties of the five copolymers, **P1–P5**, are listed in **Table 2**. The number-averaged molecular weight and PDI of **P1–P5** were 31,000 g M^{-1} and 1.45, 29,300 g M^{-1} and 1.42, 32,500 g M^{-1} and 1.35, 29,500 g M^{-1} and 1.33, and 29,250 g M^{-1} and 1.36, respectively. The thermal decomposition curves of the prepared polymers are presented in **Figure 21**. The decomposition temperature was higher when there were more phenyl groups and aromatic rings in the RhBAM moiety. All decomposition temperatures for **P1–P5** were higher than 270 $^{\circ}\text{C}$, and thus they exhibited favorable and stable thermal properties.

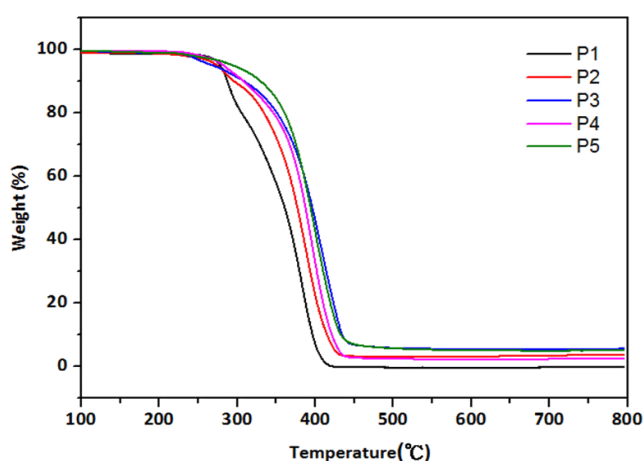


Figure 21. TGA curves of **P1–P5** copolymers when a heating rate of 10 $^{\circ}\text{C}/\text{min}$ was applied under a nitrogen atmosphere.

Figure 22(a) presents the changes in the UV–Vis absorption of RhBAM during pH sensing in a CH_3CN solution. As the pH of the solution decreased from 7 to 2, an

absorption peak maximum ($\lambda_{\text{max}}^{\text{abs}}$) at 558 nm emerged, and the solution's color changed from transparent to orange under 254-nm UV light (inset). Therefore, when RhBAM was used to detect H^+ , the spirocyclic form of RhBAM (which is colorless and nonfluorescent) transformed into the opened-cyclic form (which is pink and has a strong orange fluorescence), as shown in Scheme 1(c). **Figure 22(b)** illustrates that BNPTU in CH_3CN had a $\lambda_{\text{max}}^{\text{abs}}$ of 430 nm at pH 7 and emitted green fluorescence under UV light (inset) because it is a fluorescent dye. **Figure 22(c)** shows the variations in the UV–Vis spectra of BNPTU in a CH_3CN solution containing various metal ions at a concentration of 10^{-5} M (pH 7). The absorption maximum of BNPTU blue-shifted from 430 to 350 nm when the Hg^{2+} ion was added. Therefore, the Hg^{2+} ion transformed the thiourea unit of the BNPTU under aqueous conditions into an imidazoline moiety with considerably weakened electron-donating ability,^{15,72-74} as indicated in Scheme 1(c). However, no change in the absorption peak was observed when other metal ions, such as Co^{2+} , Cu^{2+} , Ca^{2+} , Fe^{2+} , Mg^{2+} , Na^+ , Pb^{2+} , Zn^{2+} , Cd^{2+} , K^+ , Ni^{2+} , Mn^{2+} , Pd^{2+} and Fe^{3+} , were added. This suggested that BNPTU exhibited high selectivity and sensitivity for Hg^{2+} .

Figure 22(d) shows the PL spectrum of BNPTU in CH_3CN solution under pH 7 (blank, without Hg^{2+}) and pH 7 (with Hg^{2+}) conditions, as well as the UV–vis absorption spectrum of RhBAM in CH_3CN solution under pH 2 conditions. The PL spectra of BNPTU (blank) subjected to 430-nm excitation displayed an emission peak maximum ($\lambda_{\text{max}}^{\text{PL}}$) at 510 nm, but BNPTU (with Hg^{2+}) exhibited a significant blue-shift with a $\lambda_{\text{max}}^{\text{PL}}$ of 460 nm. The overlap between the PL spectra of BNPTU (with or without Hg^{2+}) and the optical absorption spectra of RhBAM (in acidic media) was substantial, as shown in the shadowed area of **Figure 22(d)**. Therefore, FRET is efficient when interchain interaction is high. Thus, the ES nanofibers of poly(MMA-co-BNPTU-co-RhBAM) may have exhibited different degrees of FRET when they

were used to sense different pH values and Hg^{2+} concentrations simultaneously. This difference in the degree of FRET results in substantial variation in the photophysical properties of ES nanofibers, as discussed in the following sections.

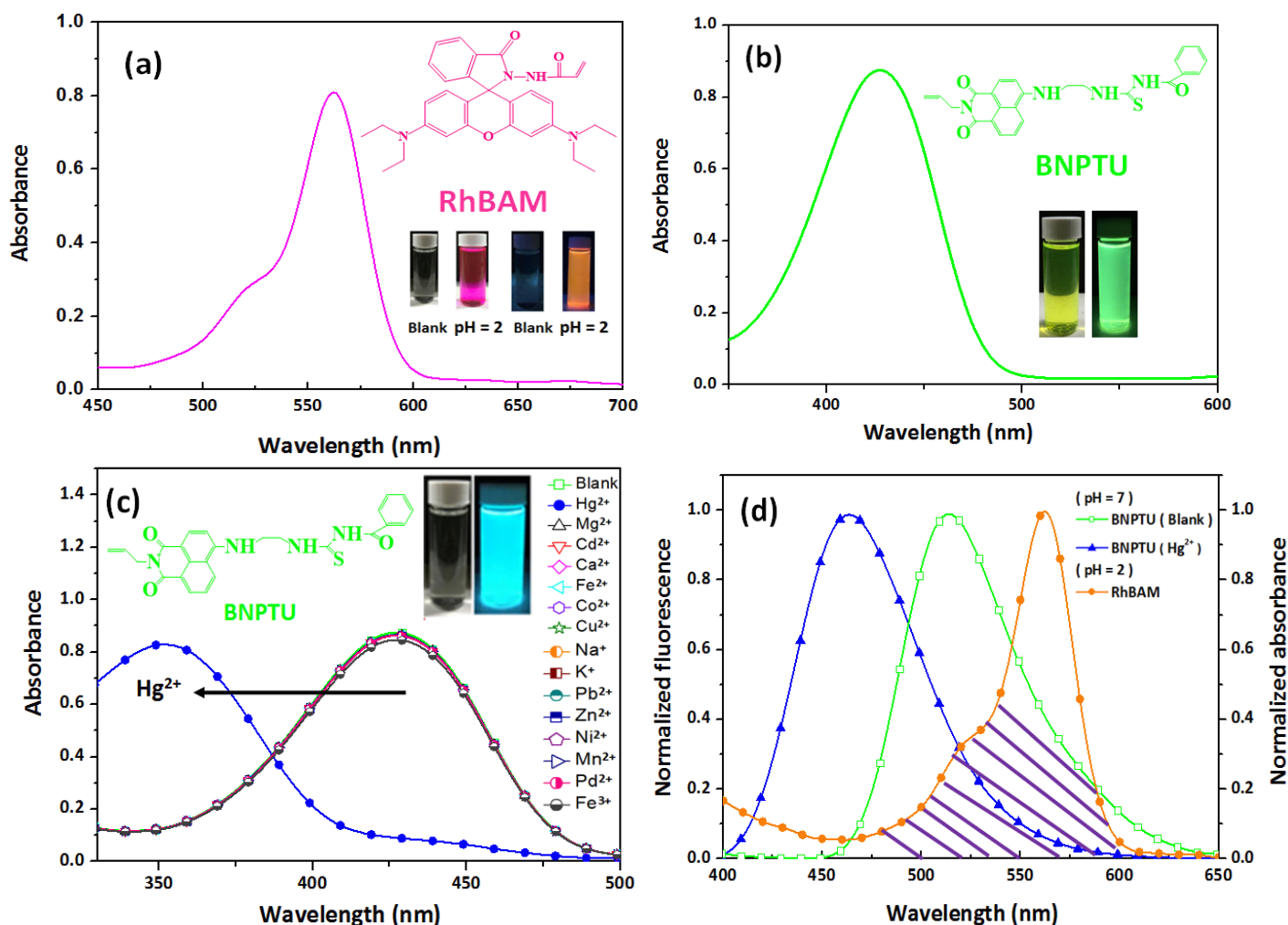


Figure 22 UV-Vis spectra of (a) RhBAM in CH_3CN solution (10^{-2} M) under pH 2 conditions and (b) BNPTU in CH_3CN solution (10^{-5} M). (c) Variation in UV-Vis spectra of BNPTU CH_3CN solution (10^{-5} M, pH 7) containing different metal ions at 10^{-4} M. (d) PL spectrum of BNPTU under pH 2 and 7 conditions and UV-Vis absorption spectrum of RhBAM in CH_3CN solution under pH 2 conditions.

1-8-2 Morphology of ES Nanofibers

Figure 23 presents FE-SEM and TEM images of the ES nanofibers prepared using poly(MMA-co-BNPTU-co-RhBAM) (**P5**) at a solution concentration of 250 mg mL^{-1} with a CHCl_3/DMF volume ratio of 15:1. The **P5** porous ES nanofibers prepared using CHCl_3/DMF had an average diameter and pore size of 410 ± 45 and 34.2 ± 6.2 nm, as shown in **Figure 23(a) and 23(b)**, respectively. The strong stretching force associated with electrospinning induces orientation of these pores along the axis of the fiber. The average diameter was a statistical average of 50 fibers for each sample. **P1, P2, P3, and P4** had the same average fiber diameter of approximately 400 nm (**Figure 24**). The porous structures located within the fiber are clear from the cross-sectional fiber morphology displayed in **Figure 23(c)**. The porous structure probably resulted from the rapid evaporation of the low-boiling-point solvent CHCl_3 and its subsequent rapid solidification at a high relative humidity (80%) during electrospinning, as was noted in our previous studies.^{75,76} The ES nanofiber surfaces contained a variety of broadly distributed pores that were elongated along the fiber axis and were approximately 30 nm in size. These porous ES fibers might have increased surface-to-volume ratios and thus have potential applications in photonics and probes.

A TEM image of the **P5** ES nanofibers before (inset) and after Hg^{2+} absorption is presented in **Figure 23(d)**. The **P5** ES nanofibers were completely black and substantially darker than before they sensed Hg^{2+} ; this was because Hg^{2+} has a high electronic density. Therefore, the **P5** ES nanofibers absorbed a substantial amount of Hg^{2+} because of the BNPTU segment's efficient absorption. Such absorption of Hg^{2+} by BNPTU within ES nanofibers resulted in substantial variations in the photophysical properties of ES nanofibers. Similar results were demonstrated in our previous studies.^{26,35,77}

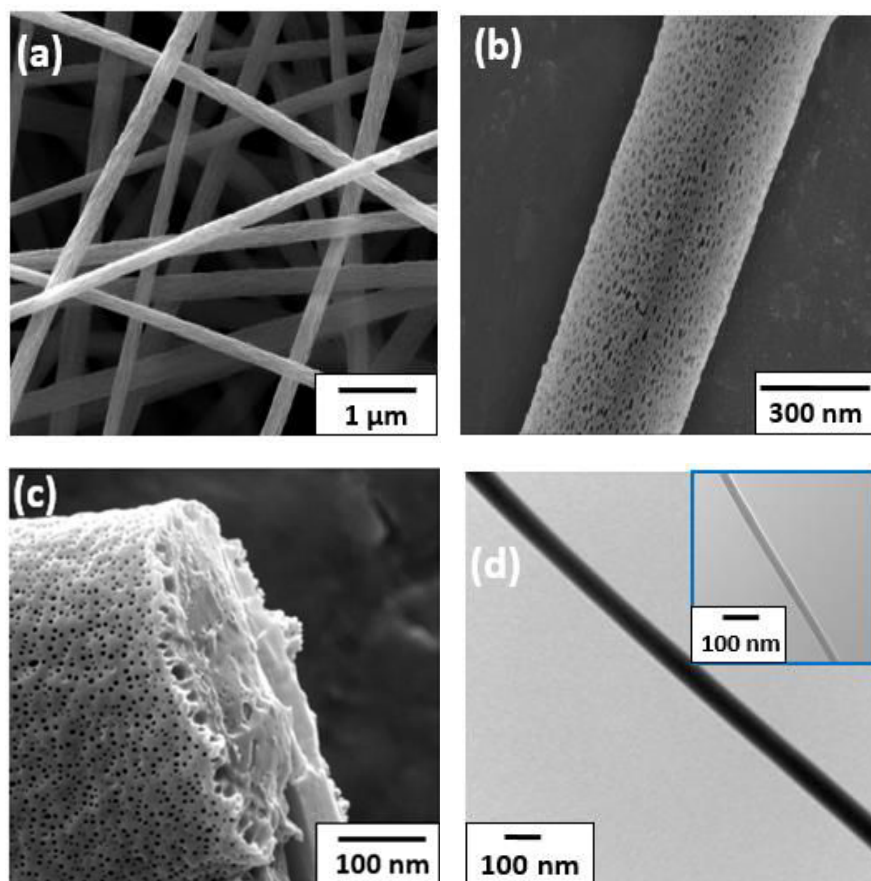


Figure 23 (a) FE-SEM image of the **P5** porous ES nanofibers, with (b) an enlarged image, and (c) a cross-sectional image. (d) TEM image of the **P5** ES nanofibers before (inset) and after absorption of Hg^{2+} ions in aqueous solution (10^{-3} M, pH 7).

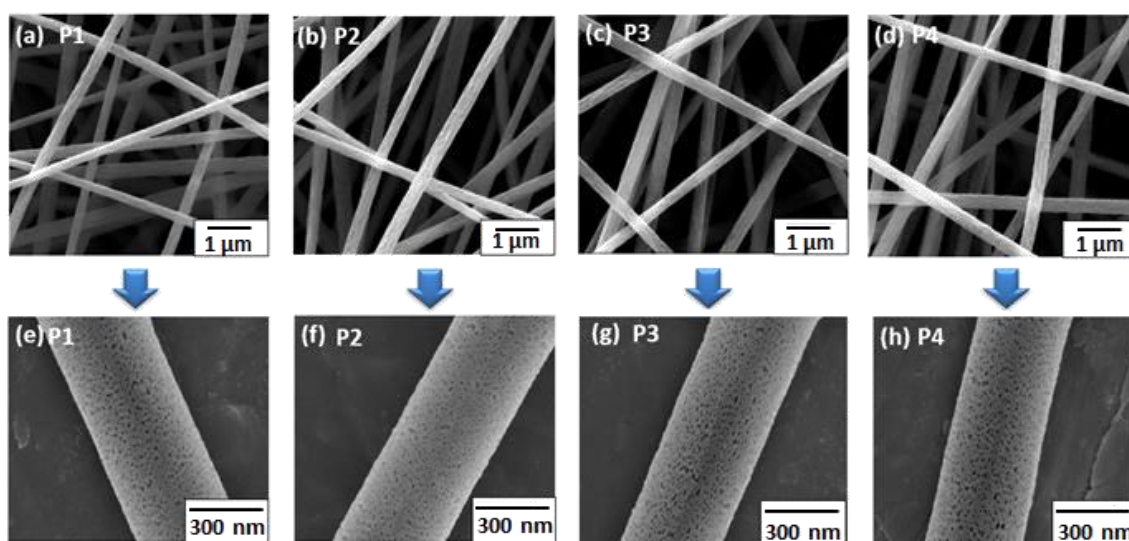


Figure 24 SEM images of P1–P4 ES nanofibers (a–d, Enlarged view (e–h).)

1-8-3 pH Sensing of ES Nanofibers

Figure 25(a) depicts the PL spectra of poly(MMA-co-BNPTU-co-RhBAM) ES nanofibers in aqueous solutions under different pH conditions, ranging from pH 7 to 2. The **P5** ES nanofibers had a $\lambda_{\text{max}}^{\text{PL}}$ at 510 nm (pH 7) and 597 nm (pH 2). A marked redshift of $\lambda_{\text{max}}^{\text{PL}}$ from 510 nm to 597 nm was thus observed as the pH changed from 7 to 2; this shift was caused by energy transfer between the BNPTU and RhBAM moieties. When RhBAM detected H^+ , the nonfluorescent spirocyclic form of RhBAM transformed into the opened-cyclic form, which was strongly fluorescent at 597 nm. Such substantial energy transfer can be explained by the overlapping of the emission of poly(MMA-co-BNPTU-co-RhBAM) and the absorption of RhBAM in the acidic aqueous solution (**Figure 22(d)**). Similar energy transfer was observed in the PL spectra of **P1** to **P5** under acidic conditions (**Figure 26**). Although a lightly decreased intensity of $\lambda_{\text{max}}^{\text{PL}}$ at 510 nm was observed from pH 5 to 7, very significant changes occurred on the PL curves for pH ranging from 4 to 2 (i.e., an acidic environment). Thus, the **P5** ES nanofibers are particularly suitable as pH probes for acidic environments. Note that there is no sensitivity for pH 7 to 14 (i.e., alkaline environments) (**Figure 27**), indicating that RhBAM is sensitive for environments ranging from pH 2 to 7, and particularly for conditions under pH 5 (**Figure 25a**)

Figure 25(b) illustrates the relative fluorescence intensity changes (I_{597}/I_{510}) of the **P5** ES nanofibers in aqueous solution under different pH conditions during H^+ absorption. (I_{510} is the fluorescence intensity of BNPTU emission at 510 nm; I_{597} is the fluorescence intensity of RhBAM emission at 597 nm.) When the pH was reduced from 7 to 5, I_{597}/I_{510} did not change. However, I_{597}/I_{510} significantly increased from approximately 0.25 to 3.5 when the pH was decreased from 5 to 2. These changes corresponded to the fluorescence of RhBAM chelated with sufficient H^+ ions. The **P5** ES nanofibers exhibited significant pH sensing performance in the range pH 5–2.

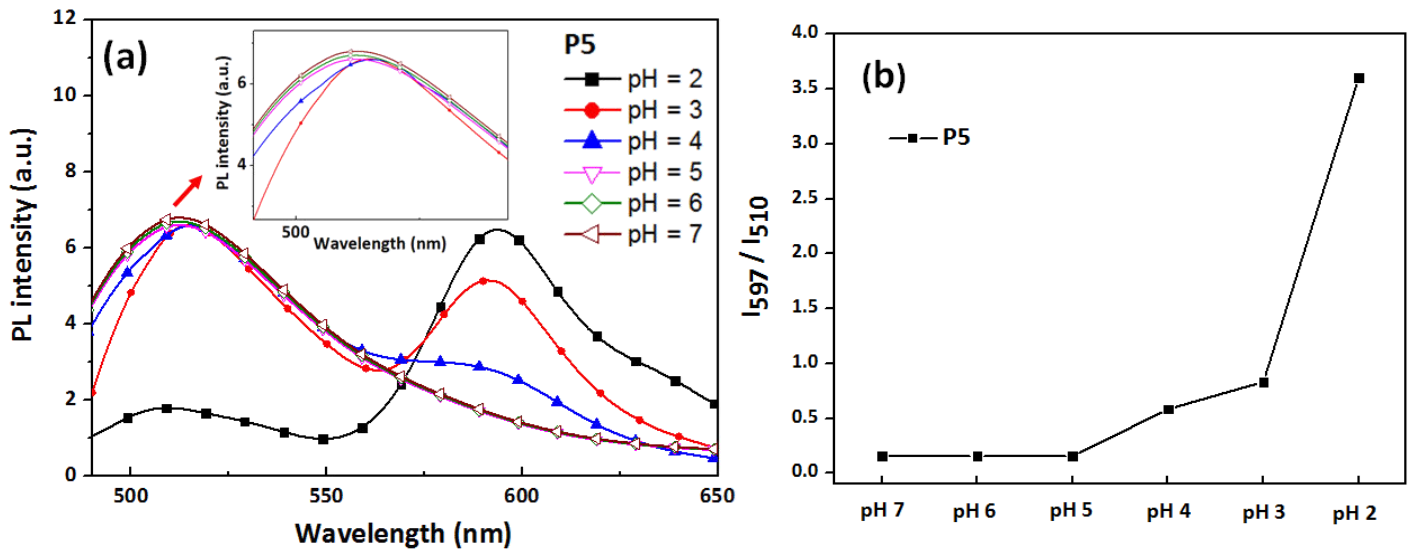
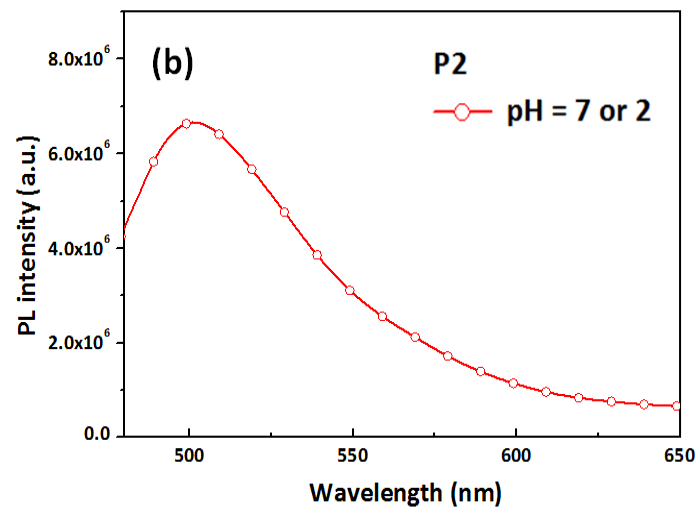
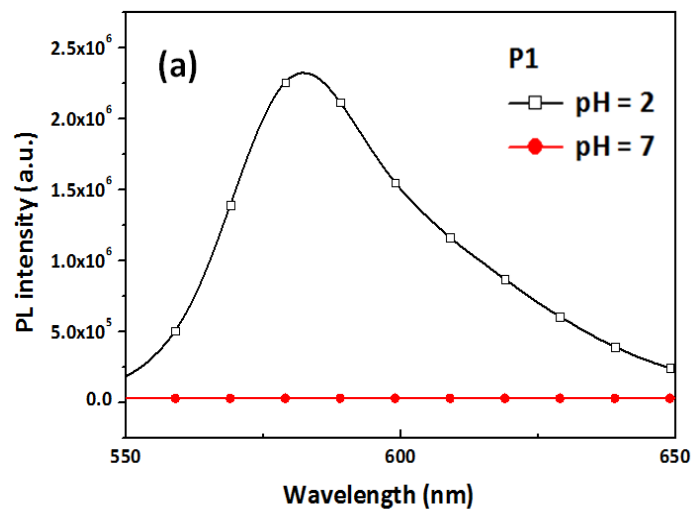


Figure 25. (a) Variation in the PL spectra of the **P5** ES nanofibers in aqueous solutions under pH 7 to pH 2 conditions. (b) Relative fluorescence intensity (I_{597}/I_{510}) of the **P5** ES nanofibers in aqueous solution under different pH conditions.



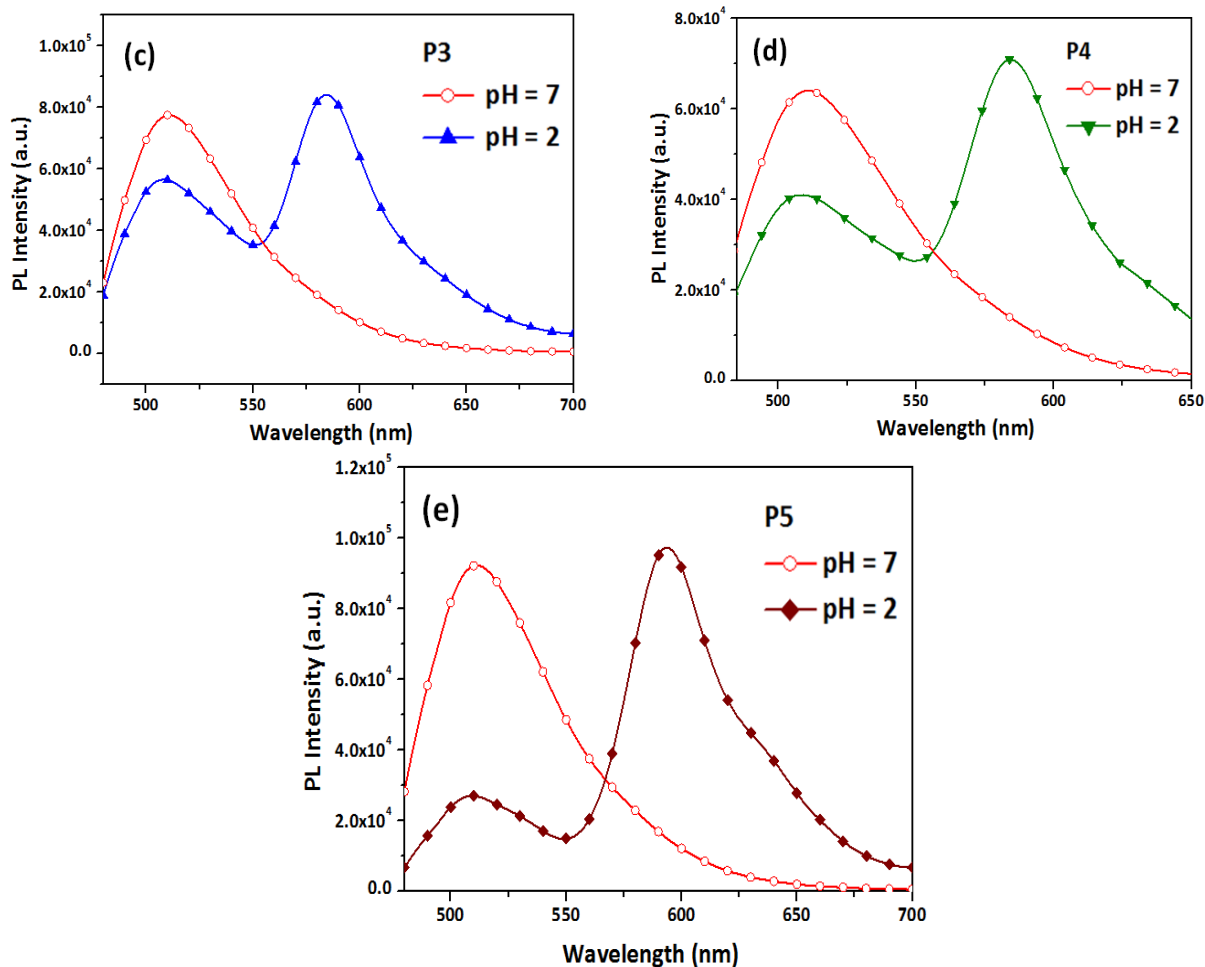


Figure 26. PL spectra of (a) P1, (b) P2, (c) P3, (d) P4, and (e) P5 ES nanofibers in aqueous solutions under pH 7 and pH 2 conditions.

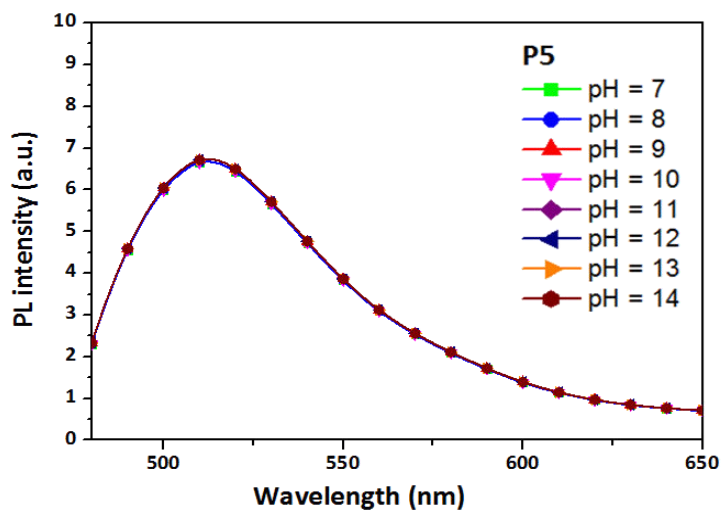


Figure 27. Variation in the PL spectra of the P5 ES nanofibers in aqueous solutions under pH 7 to pH 14 conditions.

Figure 28(a) depicts the normalized PL spectra of the **P1–P5** ES nanofibers in an acidic aqueous solution (pH 2). For high ratios of RhBAM composition, the BNPTU emission intensity at approximately 510 nm was low, and the RhBAM emission peak at approximately 586–597 nm was high. **P5** had the largest emission maximum shift $\Delta\lambda_{\max}$ (87 nm) and demonstrated a luminescence color change between green (510 nm) and red (597 nm), indicating that energy transfer from BNPTU to RhBAM occurred.⁷⁷ Green emission bands at approximately 510 nm were also found for the **P2–P4** ES nanofibers but were almost completely absent for the **P5** ES nanofibers. This suggested that the **P5** ES nanofibers had more RhBAM segments, which can enhance interchain interactions between BNPTU and RhBAM. The energy transfer and shifts are also more efficient.

The Commission Internationale de L'Eclairage (CIE) coordinates^{78,79} of the **P2–P5** ES nanofibers in neutral (pH 7) and acidic (pH 2) aqueous solutions are illustrated in **Figure 28(b) and 28(c)**, respectively, and are summarized in Table 2. All ES nanofibers in a neutral aqueous solution (pH 7) with green-light emission had similar CIE coordinates (0.24, 0.61). For nanofibers in acidic solutions, however, the CIE coordinates substantially red shifted when the ratio of RhBAM composition increased. Furthermore, as demonstrated in the confocal microscopy images in **Figure 28(d)**, the emission of the **P2–P5** ES nanofibers became green (**P2**), yellow (**P3**), orange (**P4**), and red (**P5**). This suggested that energy transfer between BNPTU (donor) and RhBAM (acceptor) occurred in the fibers, and the different degrees of energy transfer achieved by adjusting the RhBAM composition ratio yielded various CIE coordinates.

We investigated the FRET efficiency of **P3**, **P4**, and **P5** ES nanofibers under pH 7 and pH 2 conditions, as shown in Figure S11. The FRET efficiency can be calculated by measuring the fluorescence intensity of the donor in the cassette (in the presence of the acceptor) (pH 2 condition) and the fluorescence intensity of the free donor (in the

absence of the acceptor) (pH 7 condition).⁸⁰⁻⁸² Thus, the FRET efficiency can be established according to following equation (1):

$$\text{FRET efficiency} = \{ 100 \times [1 - (\text{fluorescence intensity of donor in cassette}) / (\text{fluorescence intensity of free donor})] \% \} \quad (1)$$

In our system, BNPTU and RhBAM fluorophores were chosen as the donor and acceptor units, respectively. Consequently, the FRET efficiencies of **P3**, **P4**, and **P5** were calculated to be 28%, 41%, and 72%, respectively (raw data is shown in Figure S11). This result indicates that **P5** ES nanofiber has higher energy transfer than **P3** and **P4** owing to its higher RhBAM composition ratio resulting in largely red-shifted performance.

A similar trend of red-shifted CIE coordinates was observed for the **P5** ES nanofibers under pH 7–2 conditions (**Figure 28(e)**), indicating that the **P5** ES nanofibers possessed significant pH sensing ability owing to their fluorescence color changes. As the pH changed from 7 to 2, the color changed from green to red ($\lambda^{\text{PL}}_{\text{max}}$ at 597 nm) due to energy transfer between the BNPTU moiety and the fluorescent opened-cyclic RhBAM. The FRET efficiency, color, and concentration of the analytes can correlated, as follows. The increased addition of acidic solution caused further color changes: CIE coordinates redshifted from (0.24, 0.61) (deep-green) (pH 7–5), to (0.28, 0.58) (light-green; pH 4), to (0.35, 0.52) (yellow-green; pH 3), and to (0.52, 0.41) (red; pH 2). This indicates that the enhanced FRET efficiency produced by increasing acid concentration caused a large red-shifted color change.

Moreover, the **P5** ES nanofibers exhibited reversible off–on (green–red) switchable fluorescence emission at pH 12 and pH 2, and the switching process could be repeated at least five times (**Figure 28(f)**). At pH 12, the **P5** ES nanofibers exhibited green emission ($\lambda^{\text{PL}}_{\text{max}}$ at 510 nm) because of the BNPTU moiety and nonfluorescent spirocyclic RhBAM. As the pH changed from 12 to 2, the color changed from green to

red ($\lambda_{\text{max}}^{\text{PL}}$ at 597 nm) because of energy transfer between the BNPTU moiety and the fluorescent opened-cyclic RhBAM. Finally, the color changed back to green when the structure of the RhBAM changed from opened-cyclic to spirocyclic because the energy transfer had stopped. Thus, the **P5** ES nanofibers had excellent pH sensitivity for various pH stimuli and high reversibility.

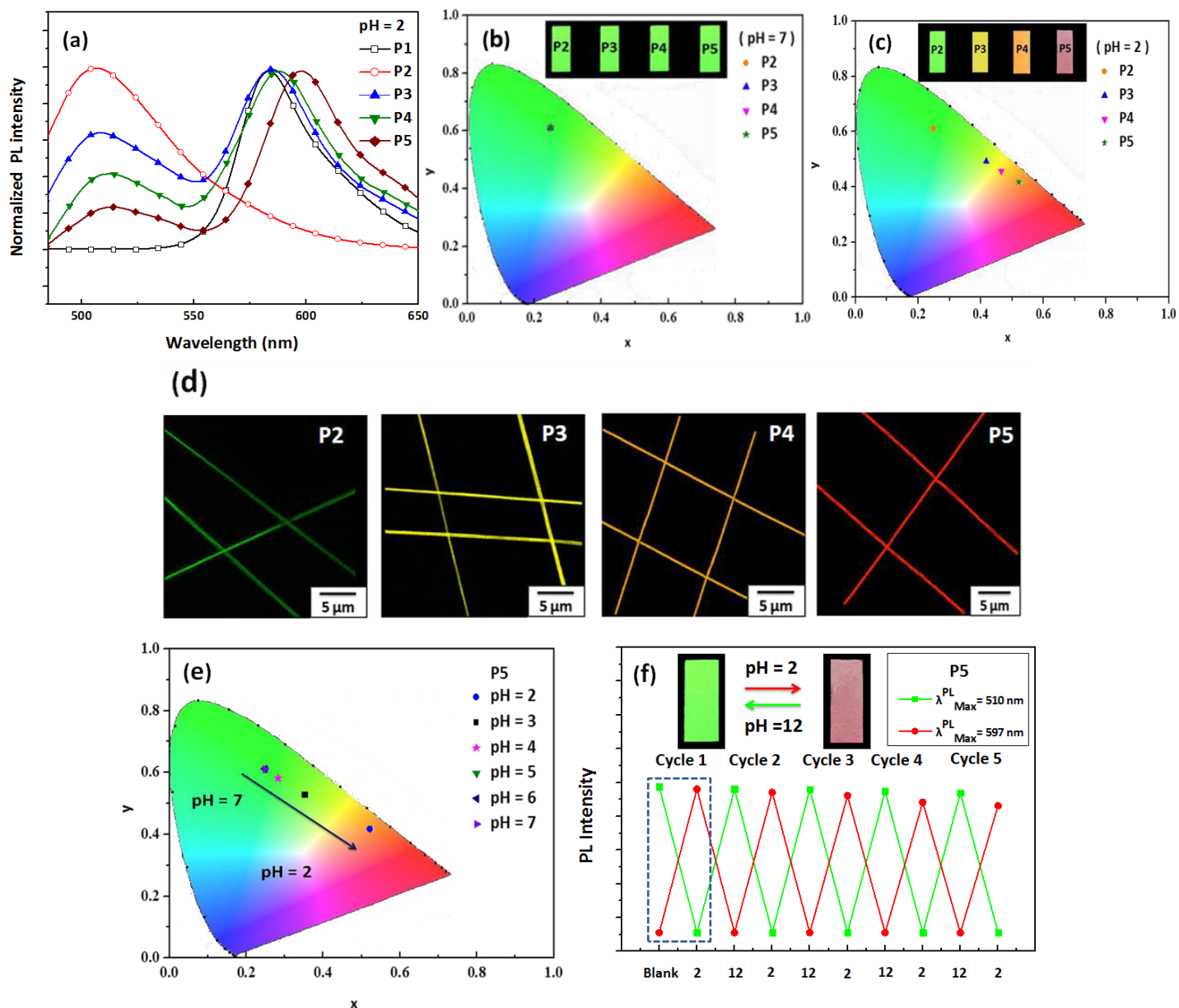


Figure 28. (a) Normalized PL spectra of the **P1–P5** ES nanofibers in aqueous solutions under pH 2 conditions. CIE coordinates of the **P2–P5** ES nanofibers in aqueous solutions under (b) pH 7 and (c) pH 2 conditions. (d) Confocal microscopy images of the ES nanofibers. (e) CIE coordinates of the **P5** ES nanofibers in aqueous solutions under pH 7 to 2 conditions. (f) Reversibility of pH-dependent “on–off–on” fluorescence intensity profile of the **P5** ES nanofibers. All of the inset figures are corresponding photographs taken under UV light.

1-8-4 Hg²⁺ Sensing of ES Nanofibers

The aforementioned results demonstrated that the **P5** ES nanofibers had excellent pH sensitivity for various pH stimuli, as well as high reversibility. Therefore, we decided to study the **P5** ES nanofibers further. **Figure 29(a)** illustrates the PL spectra of the **P5** ES nanofibers when no Hg²⁺ ions were present in an aqueous solution under neutral conditions, and when Hg²⁺ at 10⁻³ M was present. High Hg²⁺ concentration led to a $\lambda^{\text{PL}}_{\text{max}}$ blue shift from 510 to 460 nm in the emission spectra. This change was due to the thiourea unit of the BNPTU transforming the imidazoline moiety, resulting in a significant decrease in electron delocalization within the fluorophores. BNPTU is a favorable fluorescent for sensing Hg²⁺ ions, and RhBAM is sensitive to pH. Thus, we designed two-step switchable emission colors for simultaneous Hg²⁺ and pH level detection. **Figure 29(b) and 29(c)** illustrate the fluorescence response of the **P5** ES nanofibers for various concentrations of Hg²⁺ aqueous solutions—but at a constant pH of 2. When the **P5** ES nanofibers were in an acidic aqueous solution (pH 2), the energy transfer process was activated and the BNPTU (FRET donor) emission at 510 nm gradually decreased, while the RhBAM (FRET acceptor) emission at 597 nm increased. These fluorescence intensity changes were due to the ring opening of spiro lactam rhodamine. The second emission color switch observed entailed decreased emission at

510 nm and enhanced emission at 460 nm and was due to blue shifted emission when BNPTU detected Hg^{2+} . This switch was considerably more significant in the aqueous solution containing a high concentration of Hg^{2+} (10^{-4} M) (**Figure 29(b)**) than in that containing a low concentration (10^{-5} M) (**Figure 29(c)**). Hence, changes in the intensity of the PL of the **P5** ES nanofibers resulted in variation in the luminescence color.

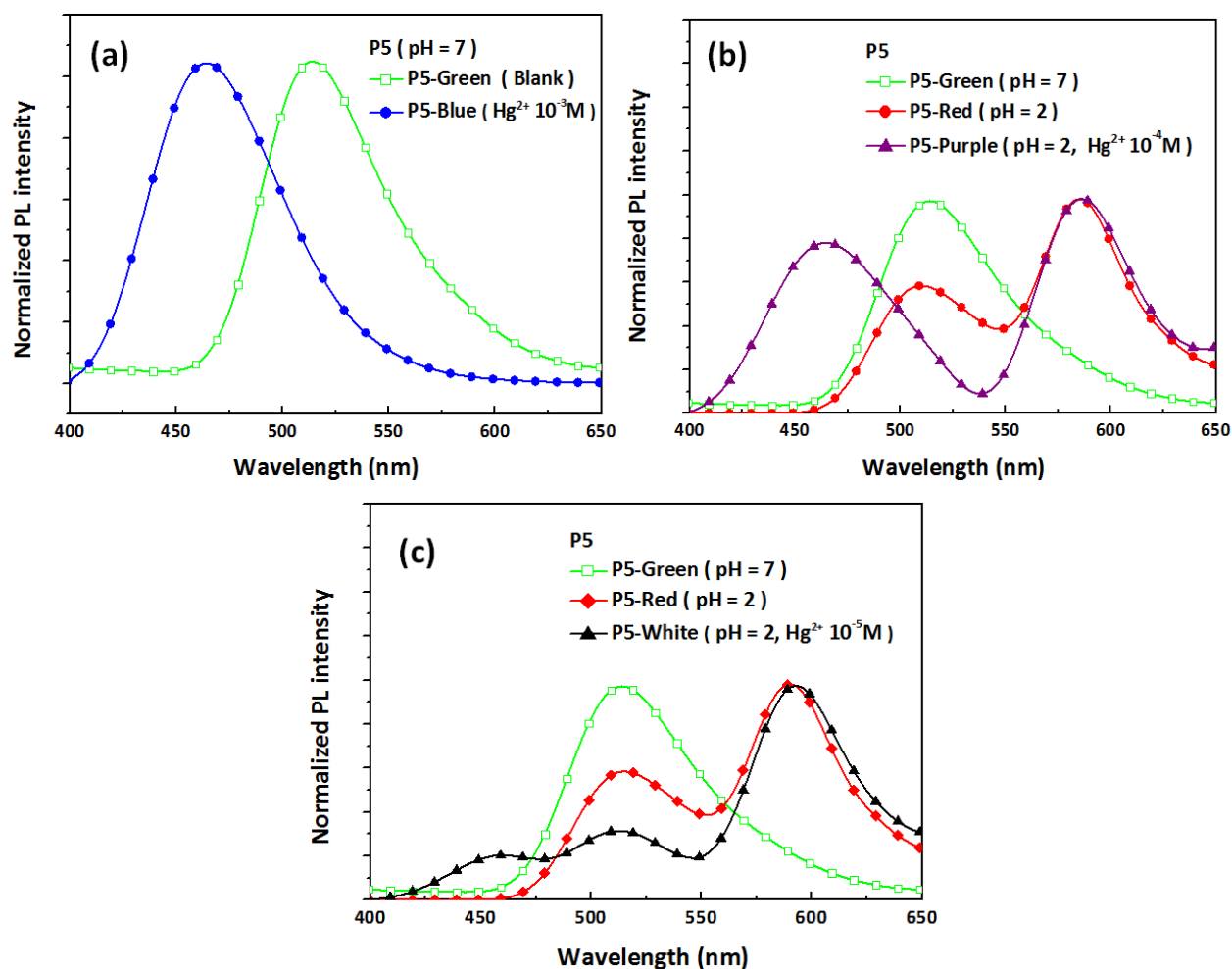


Figure 29. (a) PL spectra of the **P5** ES nanofibers in aqueous solution with Hg^{2+} at 10^{-3} M and no Hg^{2+} (blank) under neutral conditions. (b) PL spectra of the **P5** ES nanofibers in Hg^{2+} at 10^{-4} M in aqueous solution under pH 2 conditions and in aqueous solution without Hg^{2+} under both pH 2 and 7 conditions. (c) PL spectra of the **P5** ES nanofibers in aqueous solution with Hg^{2+} at 10^{-5} M under pH 2 conditions and in aqueous solution without Hg^{2+} under pH 2 and 7 conditions.

Figure 30(a) and Table 2 present the CIE coordinates of **P5** ES nanofibers in pH 7 and pH 2 aqueous solutions containing $0\text{--}10^{-3}$ M Hg^{2+} . All the inset figures in **Figure 30(a)** are corresponding photographs taken under UV light. The CIE coordinate strongly blue-shifted from (0.24, 0.61) to (0.16, 0.08) when the concentration of Hg^{2+} was increased from 0 to 10^{-3} M under neutral conditions. This was due to the detection of Hg^{2+} by BNPTU and resulted in the colors of the **P5** ES fibers changing from green to blue. However, the CIE coordinates red-shifted from (0.24, 0.61) to (0.54, 0.41) when the Hg^{2+} concentration was 0 M and the solution became acidic; this was due to energy transfer and resulted in a color change from green to red. The addition of Hg^{2+} to this acidic solution caused further color changes: CIE coordinates blue-shifted from (0.24, 0.61) (green) to (0.31, 0.26) (purple) for 10^{-4} M Hg^{2+} , and from (0.24, 0.61) (green) to (0.36, 0.37) (white) for 10^{-5} M Hg^{2+} aqueous solutions. Visible changes in the fluorescence colors of the **P5** ES nanofibers after they were used to absorb Hg^{2+} are shown in the inset of **Figure 30(a)**. The confocal microscopy images in **Figure 30(b)** illustrate the RGB (red–green–blue) full-color emission of the **P5** ES nanofibers as different pH values and concentrations of Hg^{2+} were considered: green for pH 7 and 0 M Hg^{2+} , red for pH 2 and 0 M Hg^{2+} , blue for pH 7 and 10^{-3} M Hg^{2+} , purple for pH 2 and 10^{-4} M Hg^{2+} , and white for pH 2 and 10^{-5} M Hg^{2+} (**Figure 30(b)**). This suggested that an effective switch in the FRET process between the BNPTU (donor) and ring-opening RhBAM (acceptor) moieties occurred in the fibers and demonstrated the metal-ion sensing ability of BNPTU. The tuned and switchable RGB emission of the **P5** ES nanofibers enabled them to simultaneously detect pH and Hg^{2+} concentration in complete environments.

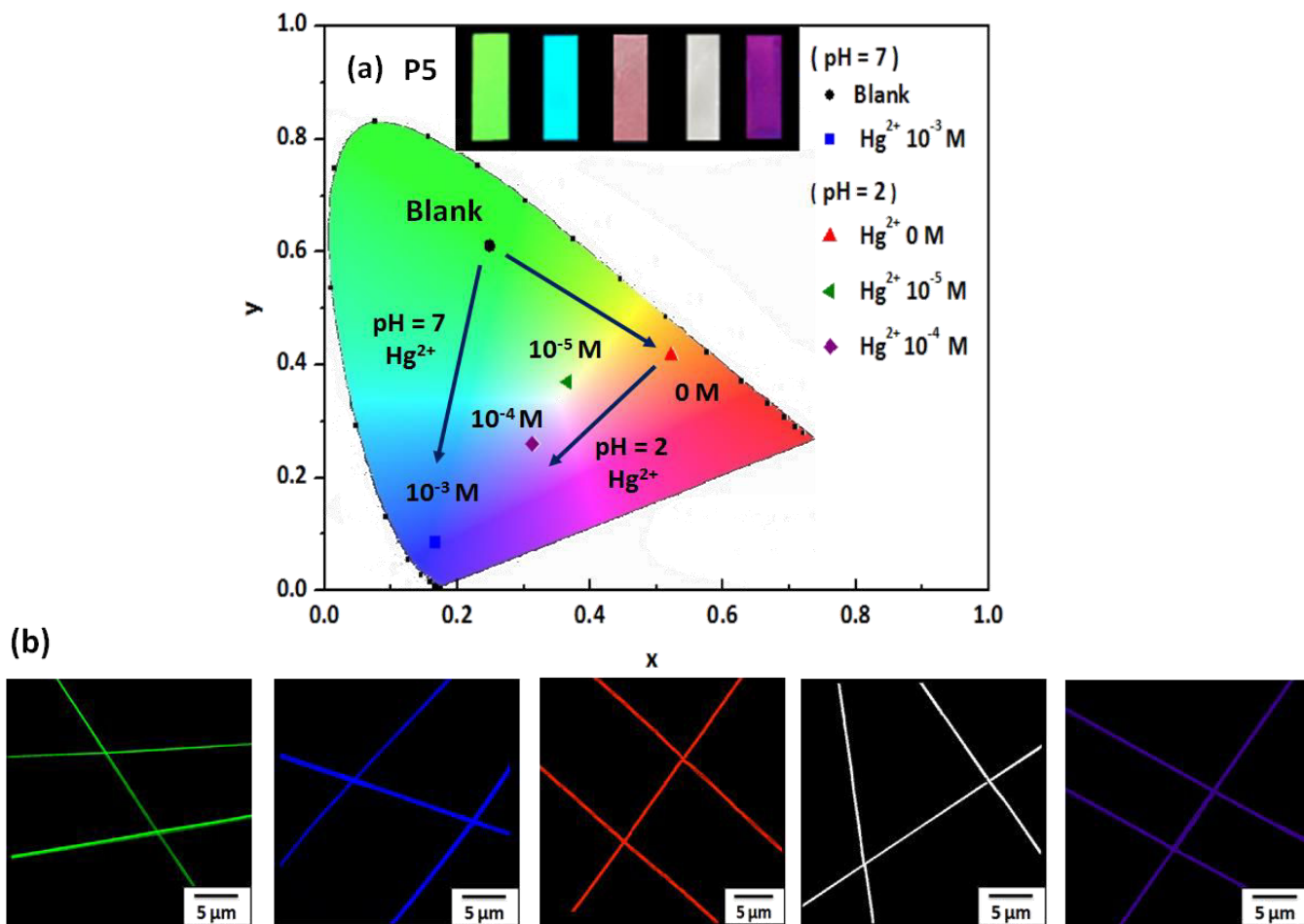
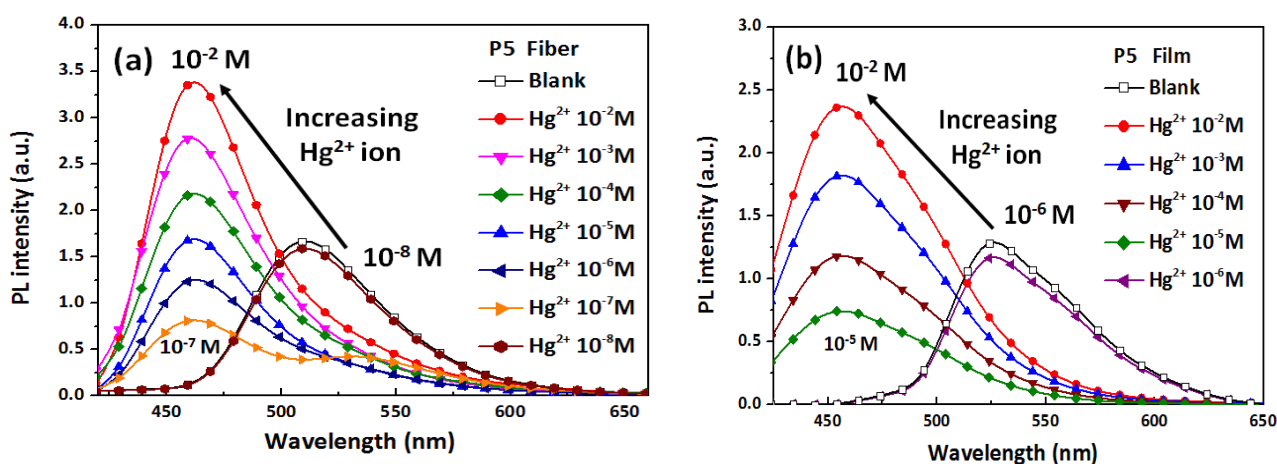


Figure 30 (a) CIE coordinates of the **P5** ES nanofibers in aqueous solutions with different Hg^{2+} concentrations under pH 2 and pH 7 conditions. Blank refers to solution without Hg^{2+} at pH 7. (b) Confocal microscopy images of ES nanofibers. Inset: corresponding photographs taken under UV light.

Figure 31(a) and 31(b) show the PL spectra of the **P5** ES nanofibers and thin films used to sense various concentrations of Hg^{2+} in water solutions, respectively. High Hg^{2+} concentrations resulted in a blue shifted spectrum from 510 to 460 nm for both the ES nanofibers and thin films. The lowest detectable Hg^{2+} concentrations for the thin films and ES nanofibers were 10^{-5} M and 10^{-7} M, respectively, suggesting that the ES nanofibers were more sensitive to Hg^{2+} . Note that the improved sensitivity for Hg^{2+}

detection of ES nanofibers is defined on the basis of how low the concentrations of Hg^{2+} is that results in the first blue-shifted spectrum, by contrast with the response of thin films. We also measured the nanofibers' and films' Hg^{2+} concentration sensing limit, as shown in **Figure 31(c)**, which illustrates changes in the fluorescence intensity ratio for very low Hg^{2+} concentrations. I_{460}/I_{510} is the ratio of the original PL intensity at 510 nm of $\lambda^{\text{PL}}_{\text{max}}$ to the PL intensity at 460 nm of $\lambda^{\text{PL}}_{\text{max}}$ for the material in an Hg^{2+} aqueous solution. The inset figure of **Figure 31(c)** exhibits a gradual increase in I_{460}/I_{510} for the **P5** ES fibers from 0.23 to 3.2 as the Hg^{2+} concentration increases from 2×10^{-8} to 1×10^{-7} M. Thus, the nanofibers' Hg^{2+} concentration sensing limit is 2×10^{-8} M. I_{460}/I_{510} for the **P5** thin film, however, begins to gradually increase at 2×10^{-6} M Hg^{2+} , a substantially higher concentration than that for the ES fibers. Additionally, the PL intensity I_{460}/I_{510} at 10^{-7} M Hg^{2+} was 3.25 for the **P5** ES fibers, whereas I_{460}/I_{510} for the **P5** thin film was only 2.5 at a much higher concentration of 10^{-5} M Hg^{2+} . Thus, our prepared porous ES nanofibers had a higher surface-to-volume ratio than that of the thin films because of their distinctive structure, and this led to higher performance even in low Hg^{2+} concentrations. BET methodology indicates that the surface area of **P5** ES nanofibers is $3.68 \text{ m}^2\text{g}^{-1}$; numerous research groups have reported that electrospun nanofibrous membranes can exhibit approximately 1 to 2 orders of magnitude more surface area than that found in continuous thin film.⁸³



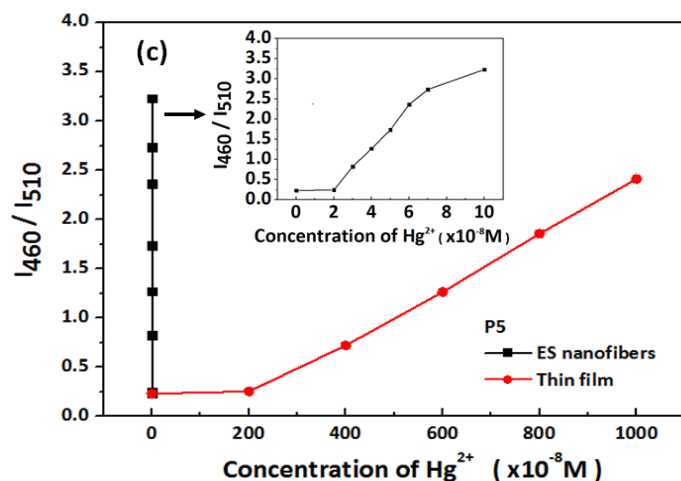


Figure 31 (a) PL dependence on various concentrations of Hg^{2+} ($C(Hg^{2+})$) under neutral conditions: (a) **P5** ES nanofibers and (b) **P5** thin films. (c) Stern–Volmer plots (460/510) of the **P5** nanofibers and thin films on $C(Hg^{2+})$ measured at λ_{ex} 380 nm. Inset of (c): enlarged Stern–Volmer plot of the **P5** ES nanofibers on $C(Hg^{2+})$.

The variation in the PL spectra of **P5** in CH_3CN solutions at different Hg^{2+} concentrations were also explored, as shown in **Figure 32**. Similarly, increasing the concentration of Hg^{2+} from 10^{-7} to 10^{-2} M resulted in a clear blue shift in the emission peak from 510 to 460 nm. However, the first blue shift occurred at 10^{-6} M, which differs from **P5** for the ES nanofiber and thin film types. Thus, the sensitivity to Hg^{2+} can be ranked in the following order, based on the lowest concentration of Hg^{2+} that resulted in an initial blue shift: **P5** ES nanofibers (10^{-7} M) > **P5** solution (10^{-6} M) > **P5** thin films (10^{-5} M), as shown in **Figures 31(a), 32, and 31(b)**. The results are similar to those of our previous report.³⁵

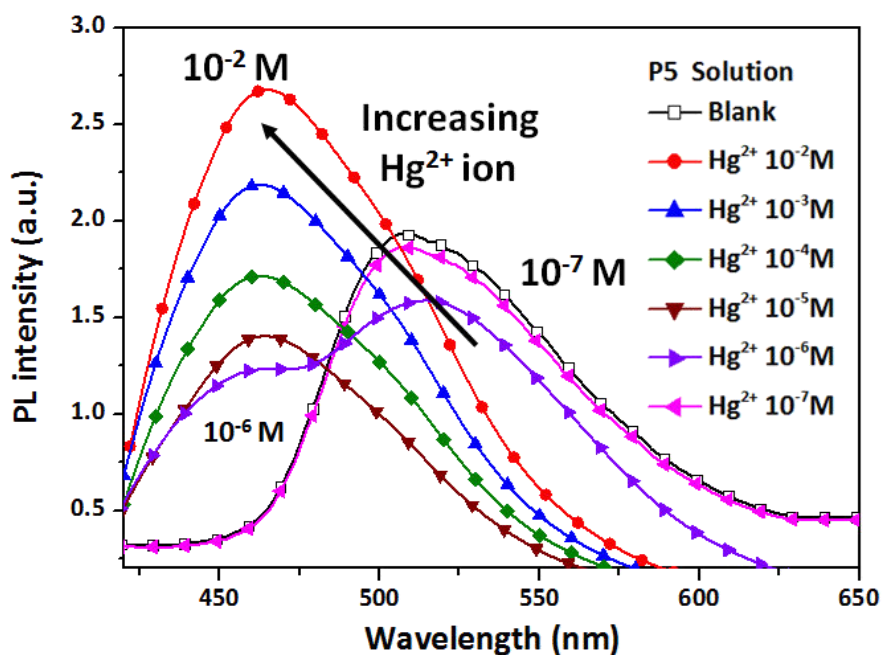


Figure 32. PL dependence on various concentrations of Hg²⁺ (C (Hg²⁺)) under neutral conditions: **P5** solutions.

The specificity of the detection selectivity of the **P5** ES nanofibers toward Hg²⁺ as distinct from toward other common metal ions was also studied. **Figure 33(a)** illustrates that, among all the tested metal ions (Hg²⁺, Co²⁺, Zn²⁺, Cd²⁺, Mg²⁺, Pb²⁺, Ni²⁺, Na⁺, K⁺, Fe²⁺, Cu²⁺, Ca²⁺, Mn²⁺, Pd²⁺ and Fe³⁺; 10⁻³ M; pH 7), only the presence of Hg²⁺ resulted in substantially blue shifted PL. The pH of the Hg²⁺ and other metal-ion test solutions was controlled at 7. The presence of Hg²⁺ induced the most prominent I₄₆₀/I₅₁₀ enhancement (a factor of 3), resulting in blue emission, whereas the presence of any other metal ions led to decreased I₄₆₀/I₅₁₀ (a factor of 0.1), resulting in green emission (**Figure 33(b)**). Additionally, the fluorescence spectra recorded when both Hg²⁺ ions and other competing metal ions were present in the solution revealed that the Hg²⁺-ion-induced fluorescence enhancement was unaffected by the presence of other metal ions (inset of Figure 9(b)). The sensing of Hg²⁺ by the **P5** ES nanofibers was thus almost unaffected by a range of ions with which Hg²⁺ commonly coexists. In this study, we observed that the **P5** ES nanofibers specifically sensed Hg²⁺ (**Figure 33(b)**) and

were colorable (**Figure 30(b)**). On the basis of the demonstrated advantages of the **P5** ES nanofibers, we designed a microfluidics system to measure solution conductivity.

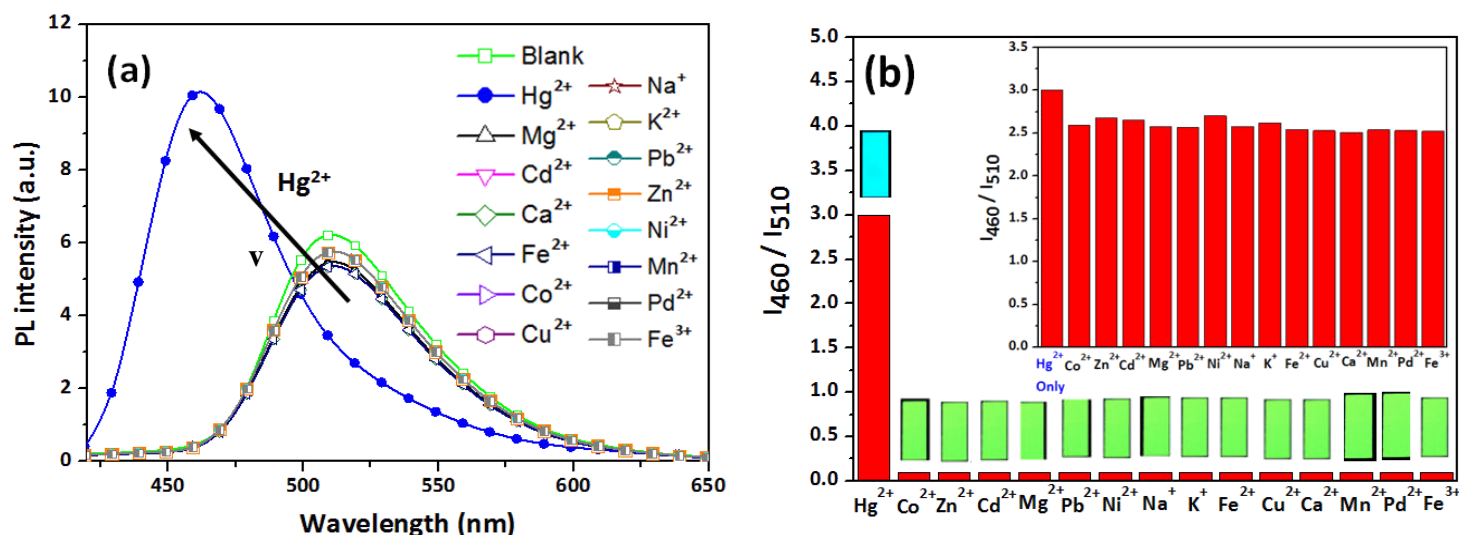


Figure 33. (a) Normalized PL spectra of the **P5** ES nanofibers in aqueous solutions containing various metal ions (10^{-3} M, pH 7) and no cations (blank). (b) Fluorimetric response (I_{460}/I_{510}) of the **P5** ES nanofibers to various cations at 10^{-3} M in aqueous solutions under neutral conditions, and corresponding photographs taken under UV light. Inset of (b): fluorimetric response of the **P5** ES nanofibers to solutions containing various metal ions at 10^{-3} M (as in (b)) but when Hg^{2+} at 10^{-3} M is also present.

A microfluidics system was constructed in which a **P5** ES nanofiber filter membrane with an area of 16 cm^2 placed in the middle of a tube was used to rapidly absorb and sense Hg^{2+} in a solution flowing through the tube (**Figure 34(a)**). **Figure 34(b)** depicts the measured time-dependent variation of the solution conductivity. The prepared Hg^{2+} solution contained 1 ppm Hg^{2+} (7.5×10^{-3} M Hg^{2+} in 0.5 L of water), and the conductivity of the Hg^{2+} solution in the initial state (0 min) was $132.7 \mu\text{S cm}^{-1}$. With time, the solution conductivity decreased to 77.1 uS cm^{-1} . **Table S1** contains raw

data on the entire change in conductivity over 50 min, and **Figure 34(b)** depicts C_t/C_0 (%) versus time (C_0 denotes the original conductivity at 0 min, and C_t denotes the conductivity at time t). The solution conductivity decreased as the flow time increased, indicating that an increasing number of Hg^{2+} ions were absorbed by the **P5** ES nanofiber membrane, causing less Hg^{2+} to be present in the solution. Thus, the 100% conductivity of the solution in the initial state (0 min) decreased to 58.1% after 50 min. The rapid change in conductivity was caused by the high surface-to-volume ratio of the porous **P5** ES nanofibers. This probe filter membrane based on the porous **P5** ES nanofibers specifically absorbed Hg^{2+} in an aqueous solution that contained a variety of metal ions and had a dual fluorescent chemoprobe function for Hg^{2+} . The Young's modulus of the porous **P5** ES nanofibers is 0.85 MPa, similar to that reported previously,⁸⁴ and their filter membrane structure can be maintained after operating the microfluidics system, instead of resulting in a broken morphology (**Figure 34**). This indicates that the **P5** ES nanofibers have suitable mechanical properties. Thus, the porous ES nanofibers prepared from poly(MMA-co-BNPTU-co-RhBAM) have potential for application in multifunctional probe filter membrane devices that sense pH and metal ions. The nanofibers have multiple functions: chelation detection for heavy metal ions and a chemoprobe function for pH detection. Consequently, both pH and metal ions can be detected simultaneously, which can protect our environment.

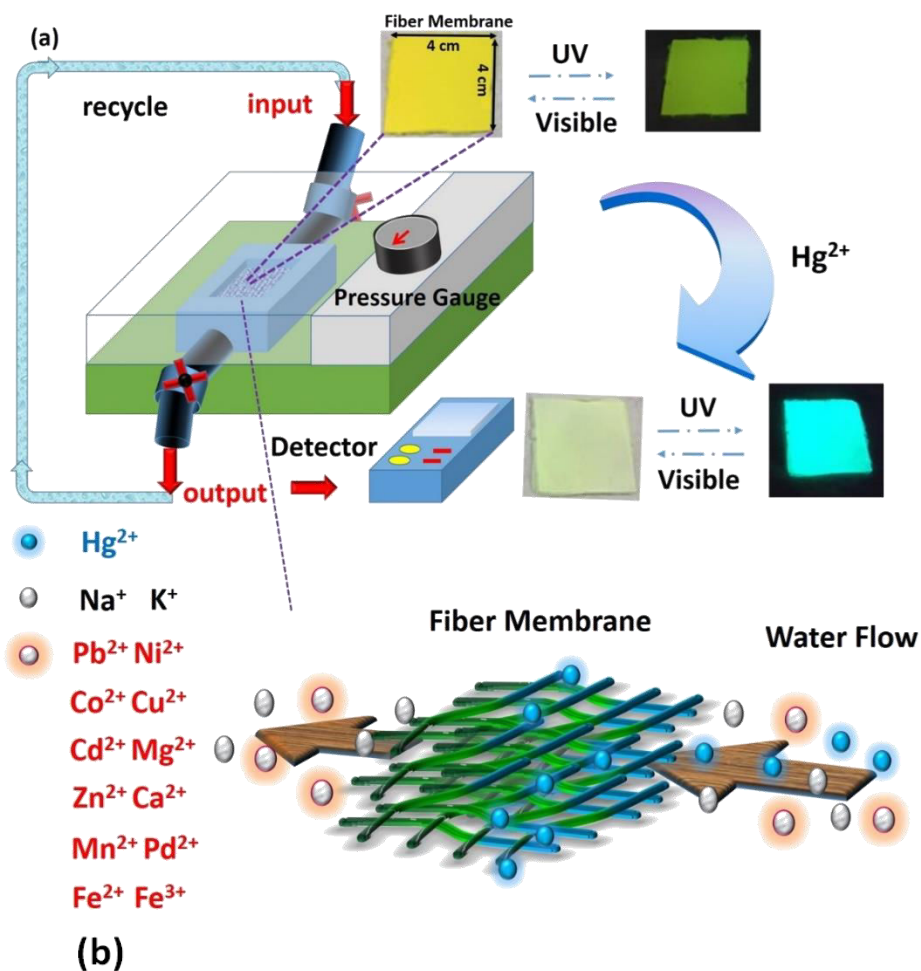


Figure 34. (a) Schematic illustration of a probe filter microfluidics system for real-time metal-ion sensing using an ES nanofiber membrane. (b) Relative conductivity versus time of the prepared Hg^{2+} solution in the microfluidics system.

Time (min)	Conductivity ($\mu\text{S/cm}$)
0	132.7
5	112.4
10	102.1
15	97.1
20	93.4
25	88.2
30	85.3
35	82.1
40	79.6
45	77.8
50	77.1

Table 3. Time-dependent solution conductivity of the prepared Hg^{2+} solution.

1-9 Conclusions

Novel FRET-based RGB full-color-switchable chemoprobes that are able to simultaneously detect pH and Hg^{2+} and are based on highly porous fluorescent ES nanofibers were prepared from random synthesized copolymers of poly(MMA-co-BNPTU-co-RhBAM) by using a single-capillary spinneret. The MMA, BNPTU, and RhBAM moieties were designed to have one function each: to be the primary material and maintain the fiber's structure in water; to detect Hg^{2+} (FRET donor); and to be pH responsive (FRET acceptor), respectively. The fluorescence emission of BNPTU (FRET donor) within the ES nanofibers was highly selective for Hg^{2+} (with green emission in aqueous solutions without Hg^{2+} (thiourea-derived) shifting to blue emission in aqueous solutions containing Hg^{2+} (imidazoline-derived)). The fluorescence emission of RhBAM (FRET acceptor) within the ES nanofibers was highly selective for pH (nonfluorescent in neutral and alkaline media (spirolactam form) and highly fluorescent with red emission in acidic media (ring-opened acyclic form)). Thus, the off-on FRET switching is easily modulated by adjusting the pH and Hg^{2+} concentration of the aqueous solution tested. In an acidic aqueous solution, the emission of the **P2**–**P5** ES nanofibers was green (**P2**), yellow (**P3**), orange (**P4**), and red (**P5**), where **P2**–

P5 denotes an increasing RhBAM composition ratio. The **P5** ES nanofibers exhibited the largest red-shifted $\Delta\lambda_{\max}$ of 87 nm owing to their having the highest RhBAM content, resulting in the largest FRET. Furthermore, we varied the pH and Hg^{2+} concentration of the aqueous solutions and discovered the RGB full-color emission of the **P5** ES nanofibers, which varied between green, red, blue, purple, and white depending on the particular pH/ Hg^{2+} -concentration combination. The tuned and switchable RGB emission of the **P5** ES nanofibers indicated that they can detect complete environments and sense pH and Hg^{2+} concentration simultaneously. Furthermore, the **P5** porous ES nanofiber had a higher surface-to-volume ratio than corresponding thin films, which resulted in higher performance. Experimental results obtained using a microfluidics system demonstrated that solution conductivity decreased as flow time increased, indicating that an increasing number of Hg^{2+} ions in the solution were absorbed by the **P5** porous ES nanofiber membrane. The present study demonstrated that the on–off switching FRET-based full-color-fluorescence porous nanofibrous membranes, which can be used as naked eye probes, have potential for application in multifunctional environment-sensing devices.

Chapter 2

Novel Magnet and Thermoresponsive Chemosensory Electrospinning Fluorescent Nanofibers and Their Sensing Capability for Metal Ions

2-1 Introduction

Over the past decades, polymeric-inorganic hybrid membranes have considerable attention in drug delivery systems owing to their drug loading capacity and biocompatibility for targeting therapy.⁸⁵ As drug carriers, polymeric-inorganic hybrid membranes were able to load therapeutic agents, such as hydrophobic drugs in the hydrophobic core region, while the hydrophilic shell region provided good dispersion in water and reduced the toxicity.⁸⁶ Polymer polymeric-inorganic hybrid membranes also have shown prolonged-circulation characteristics and great accumulation properties in tumor tissue due to the inefficient drainage by the lymph system, the so-called enhanced permeation and retention (EPR) effect.⁸⁷ Moreover, polymer-inorganic hybrid membranes provide the promising solution to overcoming the limitation of the trade-off between permeability and selectivity in polymeric membranes.^{88,89} Thus, several researches have been devoted to developing the multifunctional stimuli-responsive polymer application in sensory device, which could undergo a tremendous and reversible transition of morphology and dominate the precise controlled release. Moreover, the photophysical properties could be significantly tuned by external stimuli to the various environmental stimuli, like temperature,⁹⁰ pH,⁹¹ metal ionic,⁹² and magnetic field.⁹³

Environmental-stimulus polymers were widely investigated since the temperature was easy to control and could provide several advantages for in vitro treatments. Among the reported environmental-stimulus polymers, poly(N-isopropylacrylamide)

(PNIPAAm) exhibited the characteristic of lower critical solution temperature (LCST) at 32°C closely to the human body temperature. It preserved the considerable phase transition from hydrophilic (below the LCST) to hydrophobic (above the LCST).⁹⁴

Since the LCST was close to the human body temperature, hydrophilic-segments, like acrylic acid (AA), were introduced into PNIPAAm for LCST tuning by copolymerization and surface modification in order to fabricate hollow structured nanoparticles via thermo-triggered self-assembling. Moreover, the spherical sub-micron particle with empty core region provide various advantages, such as higher drug loading content.⁹⁵ However, the practical controlled release was still interrupted in vivo colloidal stability,⁹⁶ thus got lower therapeutic efficiency and caused side effects.⁹⁷

The practical development of drug carriers are designed with responsive and stimuli characteristics in real-time for disease control. Recently, the promising magnetic materials were widely used as nanocarriers platform due to the non-contact magnetic field force method, which provided magnetically triggered release and remote treatment for drug delivery in therapy applications.⁹⁸⁻¹⁰³ In spite of the magnetic materials show the good benefits for drug delivery, the magnetic field treatment with a non-contact method, which significantly permits the rapid trigger of the drug release behavior due to the heat generated by magnetic nanoparticles in comparison to those require physical or chemical contact. The release rate of pure iron oxide (Fe_3O_4) by magnetic field were still limited because of its poor water dispersion. Thus, the incorporation or the surface modification of magnetic iron oxide with thermo-sensitive polymers has been employed to promote the biocompatibility and the drug delivery capability.

2-2 Motivation

In recent years, identifying the presence and concentration of heavy metal ions has received gradually increasing levels of attention because of emerging environmental and human health issues.¹⁰⁻¹² Heavy transition metal (HTM) cations and their derivatives are used extensively in the industrial sector, and can cause adverse environment and health problems;¹³⁻¹⁴ thus, developing sensitive and selective fluorescent chromogenic probes composed of chelating ligands that are used to detect HTM cations in biological and environmental sensory devices is crucial. Colorimetric derivative probes based on 1,8-naphthalimide have been used extensively in fluorescence detection for HTMs such as Hg^{2+} , Cd^{2+} , and Cu^{2+} because of their many excellent optical properties such as high quantum yields and high photo stability.¹⁵⁻²¹ A new fluorescent chemodosimeter, namely a 1,8-naphthalimide-based colorimetric derivative, 1-benzoyl-3-[2-(2-allyl-1,3-dioxo-2,3-dihydro-1Hbenzo[de]isoquinolin-6-ylamino)-ethyl]-thiourea (BNPTU), with high selectivity for Hg^{2+} in aqueous solutions and based on the reactivity of thiourea derivatives toward Hg^{2+} was reported by Liu et al.¹⁴ Mercury-triggered intramolecular cyclization of thiourea results in the formation of a highly blue fluorescent naphthalimide derivative, whereas the dosimeter itself fluoresces yellowish green.

Poly(*N*-isopropyl acrylamide) (PNIPAM) is a well-known thermosensitive polymer that exhibits a low critical solution temperature (LCST) of 32 °C, close to the healthy human body temperature. PNIPAM exhibits a hydrophilic extended structure below its LCST, whereas above its LCST, it dehydrates and exhibits a compact structure.¹⁰⁴ Chen reported that introducing hydrophilic acrylic acid (AA) monomers with different compositions can change the thermal responses of PNIPAM microgels. Furthermore, the AA content of poly(NIPAM-*co*-AA) can be adjusted to change the LCST, with the hydrogen bonding interaction being the fundamental cause of the change.¹⁰⁵ However, all of the aforementioned studies adopted solutions and polymer composites rather than nanofibers in sensory applications. The high surface-to-volume ratio of nanofibers could induce responses in metal ions-sensitive, temperature-sensitive, and multifunctional sensory materials.

Electrospinning is an easy, versatile, and inexpensive technique that enables the assembly of various functional nanofibers.²⁵⁻²⁸ The high surface-to-volume ratio of electrospun (ES) nanofibers has encouraged extensive research on sensory applications

including sensors for pH levels,²⁹ temperatures,^{30,31} nitric oxide,³² and metal ions.³³⁻³⁷ Recently, various fluorescent sensor-based ES polymer nanofibers for sensing pH or different metal ions such as Hg²⁺, Fe³⁺, Zn²⁺, and Cu²⁺ were successfully prepared by our research group.³³⁻³⁵ These multifunctional fluorescent ES nanofibers exhibited distinct on–off switching capabilities such as quenching–enhancing photoluminescence (PL) intensity and changed–recovered PL colors for sensing various pH levels or metal ions.

Poly(acrylic acid) (PAA) is a weak polyelectrolyte often used to change the surface properties of inorganic particles, because of the strong chelation of its numerous carboxyl groups with metal ions. Iron oxide (Fe₃O₄) nanoparticles (NPs) obtained through a one-pot method with PAA can solve the agglomeration problem.¹⁰⁶⁻¹⁰⁹ Recently, Liu reported the fabrication of Fe₃O₄ NP, PAA, and polyvinyl alcohol composite ES nanofibers with a homogeneous dispersion of Fe₃O₄ NPs and high water resistance.¹¹⁰ In addition, Xu et al. developed a material for industrial wastewater treatment combining polydopamine-coated mesh with PAA. This material not only selectively detects Hg²⁺ but also effectively separates oil and water, a process attributed to the hydrophilicity of PAA and the change in mesh wettability based on the chelation between Hg²⁺ and PAA.¹¹¹ However, most studies on polymer-inorganic composites have focused on exploring their physical properties, which have seldom been studied in terms of their combination with metal ions, temperature, and magnetic multifunctional materials in sensory applications. This paper reports the production of novel multifunctional switchable ES nanofiber sensors from blends of multifunctional copolymers and Fe₃O₄ NPs. Comprising traditional polymer-inorganic composite ES nanofibers, our chemosensors can simultaneously detect metal ions, temperature, and magnetism.

In this study, we developed magnetic fluorescent sensory ES nanofibers by using blends of poly(*N*-isopropylacrylamide)-*co*-(*N*-methylolacrylamide)-*co*-(acrylic acid) (poly(NIPAAm-*co*-NMA-*co*-AA)), fluorescent BNPTU, and Fe₃O₄ NPs and a single-capillary spinneret. The nanofibers, which can sense Hg²⁺, temperature, and magnetism simultaneously, were prepared by combining synthesis and electrospinning, and their optical applications and morphological characteristics were analyzed. The process for synthesizing fluorescent BNPTU probes is shown in **Figure 1**. The poly(NIPAAm-*co*-NMA-*co*-AA) was synthesized through free radical polymerization (**Figure 2a**). The moieties of *N*-isopropylacrylamide (NIPAAm), *N*-methylolacrylamide (NMA), AA,

BNPTU, and Fe₃O₄ NPs were designed to achieve thermoresponsiveness, chemical cross-linking, hydrophilicity, Hg²⁺ sensing, and magnetism, respectively. A single-capillary spinneret was used to fabricate ES nanofibers from poly(NIPAAm-*co*-NMA-*co*-AA) blended with BNPTU (10%) and Fe₃O₄ NPs (5%). The nanofibers were then post-treated through chemical cross-linking to enhance their stability in water (**Figure 2b**). The fluorescence emission of BNPTU is highly selective and Hg²⁺ dependent. When BNPTU is used to detect Hg²⁺, its fluorescence emission changes from green to blue, and the NIPAAm and Fe₃O₄ NPs exhibit thermoresponsive magnetic properties, respectively (**Figure 2c**). The relationship between the morphology of the ES nanofibers and their photophysical properties together with their sensing behavior in aqueous solutions was systematically investigated. The favorable detection of Hg²⁺, temperature, and magnetism demonstrated by the experimental results suggests that ES nanofibrous membranes can be used as naked eye sensors, and have the potential for application in multifunctional environmental sensing devices.

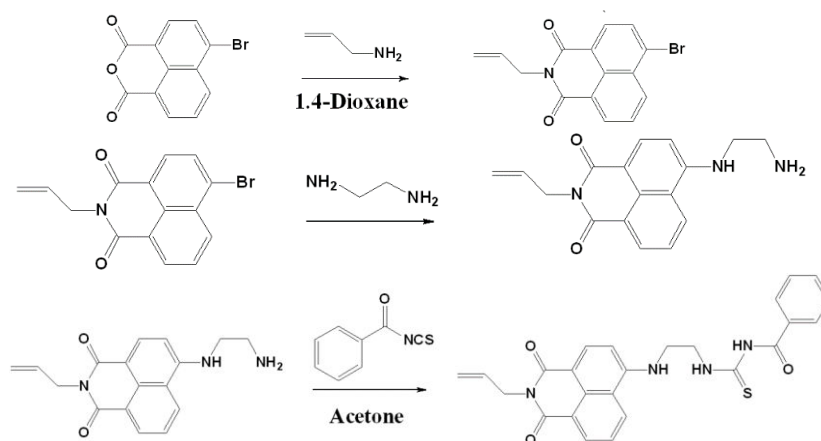


Figure 1. Synthesis of BNPTU fluorescent monomer.

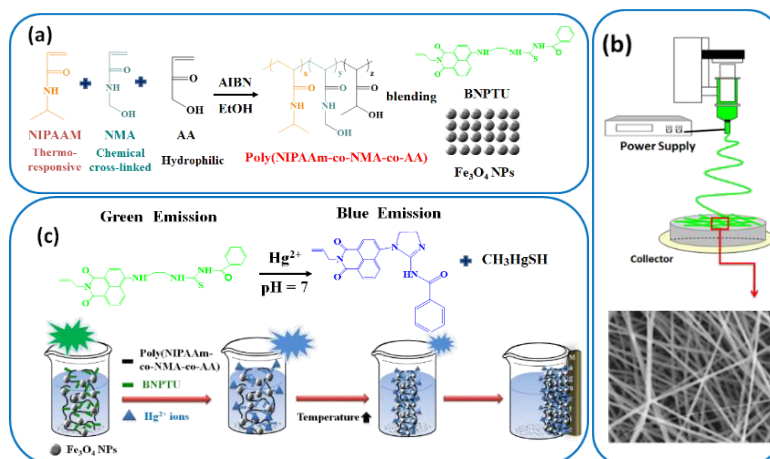


Figure 2. Design of multifunctional sensory electro spun (ES) nanofibers synthesized from poly(NIPAAm-co-NMA-co-AA), BNPTU, and Fe₃O₄ blends with magnetic fluorescence emission. (a) Polymerization and chemical structure of poly(NIPAAm-co-NMA-co-AA), BNPTU, and Fe₃O₄ particles. (b) Fabrication of ES nanofibers from the blends. (c) Change in the chemical structure of BNPTU in solutions containing Hg²⁺. The fluorescence emission from the ES nanofibers exhibited color changes. A magnet can directly attract the ES nanofibers because of the magnetism of Fe₃O₄ NPs.

2-3 Background and review of literatures

2-3-1 Responsive Polymer-Based Temperature Sensors

The development of responsive polymer-based sensors has been considerable attention in different research field. It can be categorized into three subjects: (a) development of sensors by utilizing intrinsic characteristics of responsive polymers; (b) the incorporation of molecular dye acts as sensing elements into responsive polymers, enabling improved sensing performance; (c) the realization of novel detecting concepts into responsive polymer-based sensors to fulfil high selectivity and sensitivity (**Figure 3**). Among the research directions, we devoted to developing of responsive polymer-based chemosensors with selected literature researches. For instance, the advantage of functional polymer materials show prominent property such as structural stability, biocompatibility, and facile integration into detection elements compared to conventional small molecular dye.¹¹²

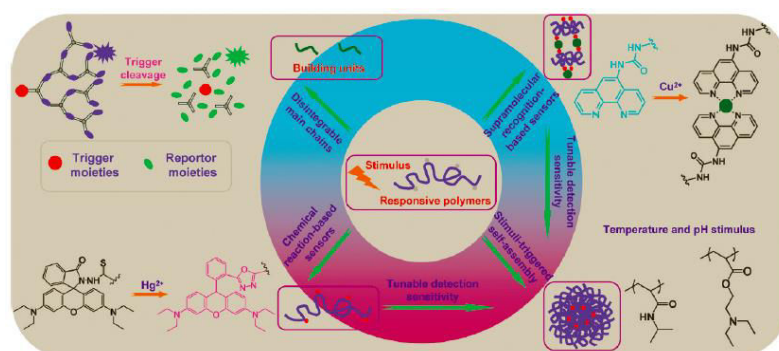


Figure 3. Schematic Summary of Responsive Polymer-Based Sensors.

Most of pH- and thermo-responsive polymers are generally dissolved in aqueous solution under certain conditions; however, the various critical pH (pKa) or temperature can directly altered either the chain collapse or aggregation in aqueous solution, enabling transformed the chain conformations and hydrophobic domains. By incorporating fluorescent receptors into responsive polymers, the variations of pH and temperature can be changed in fluorescence signal intensities due to the phase separation between hydrophilicity and hydrophobicity. Thermo-responsive polymers in aqueous solution generally form aggregates with low polarity above their lower critical solution temperatures (LCSTs). A diverse of thermo-responsive polymers with various LCSTs characteristics have been employed for fabricated the polymer-based thermometers, such as homopolymers or copolymers of N-isopropylacrylamide (NIPAM), N-isopropylmethacrylamide (NIPMAM), N-n-propylacrylamide (NNPAM), and N-tertbutylacrylamide (NTBAM). Typical polymerizable fluorescent reporters employed by Uchiyama et al.⁴⁶⁻⁵³ contain benzoxadiazole motifs, such as 4-N-(2-acryloyloxyethyl)-N-methylamino-7-(N,N-dimethylamino)sulfonyl-2,1,3-benzoxadiazole (DBDAE) and 4-(2-acryloyloxyethylamino)-7-nitro-2,1,3-benzoxadiazole (NBDAE) (Figure 4 and 5).¹¹²

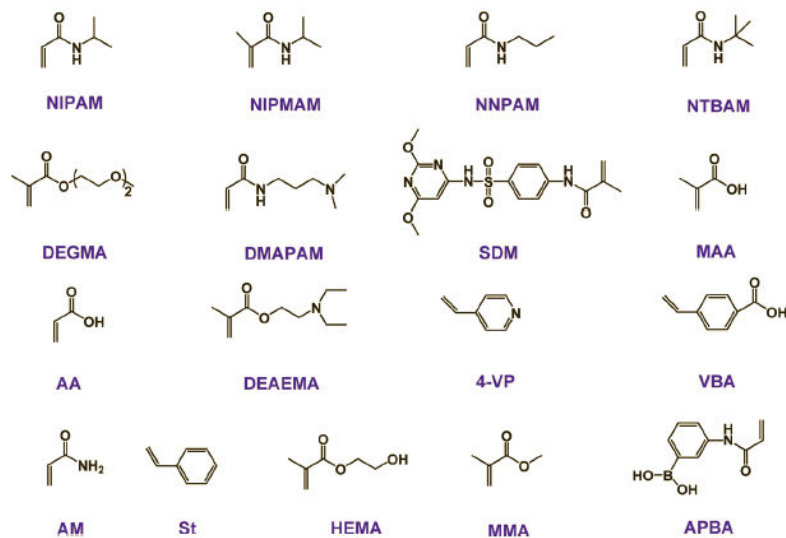


Figure 4. Chemical Structures of Monomers for Synthesis of Responsive Polymers.

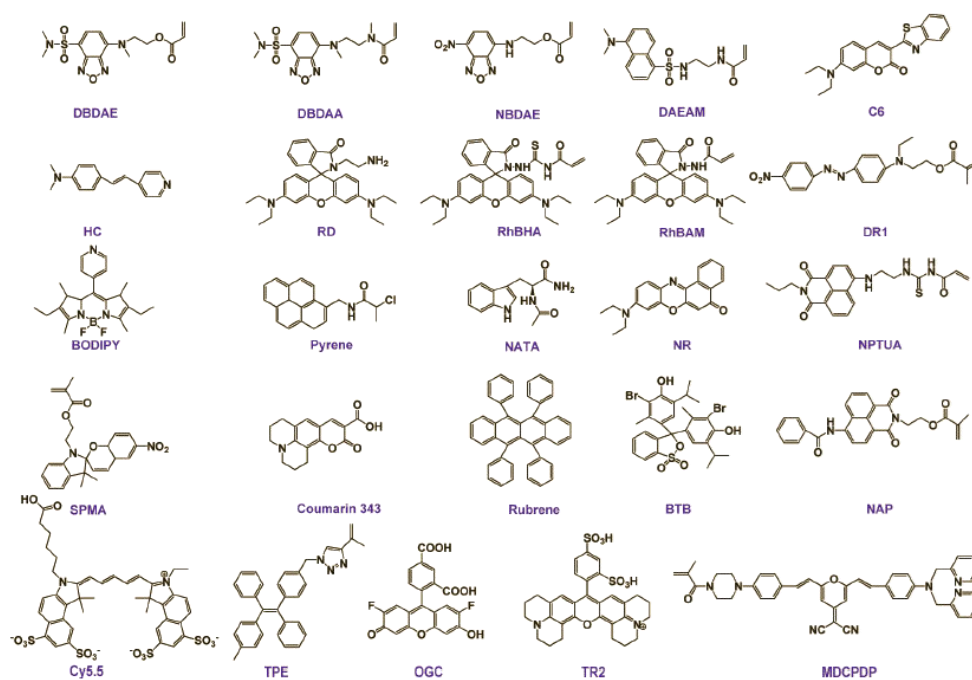


Figure 5. Chemical Structures of Functionalized Fluorescent Dyes

Recently, Seiichi groups reported that using DBDAE monomer copolymerized with the thermo-responsive polymer. The P(DMAPAM-co-NTBAM-co-DBDAE) exhibits significantly increase in fluorescence emission intensity in a aqueous solution as the temperature above the LCST. Thermal annealing induced the phase transition from the collapse and aggregation of polymer chains, and further alter the DBD dyes moieties from being hydrophilic to hydrophobic, which caused considerable increase in quantum yields. Since the presence of pH-sensitive DMAPAM moieties ($pK_a \sim 9.8$), the P(DMAPAM-co-NTBAM-co-DBDAE) copolymer can be utilized as a pH probe.¹¹³ **(Figure 6)** Moreover, the incorporation of DBDAA dyes copolymerizing with thermo-responsive PNIPAM microgels, which enhanced the fluorescence intensity performance above the LCST. Hence, the promising results successfully demonstrated that the novel microgel-based thermometer can be integrated for intracellular thermometry.

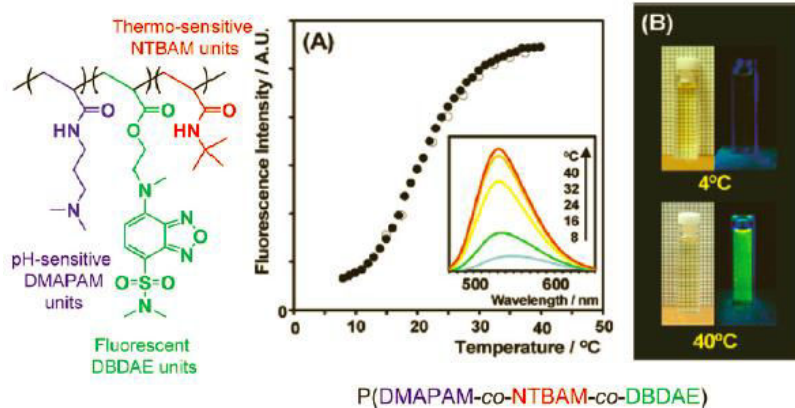


Figure 6. Thermo-responsive P(DMAPAM-co-NTBAM-co-DBDAE) copolymer in aqueous solution serves as a fluorescent molecular thermometer.

The strategy for using chemical reaction-based small molecular probes can be associated with conventional stimuli-responsive polymers. Hu et al.¹¹⁴ synthesized double hydrophilic block copolymers (DHBCs), PEO-*b*-P(NIPAM-co-RhBHA) (**Figure 7**). In this system, the RhBHA is designed by detecting Hg²⁺ ions. In the absence of Hg²⁺, RhBHA is nonfluorescent in the spirolactam form, whereas addition of Hg²⁺ ions leads to ring opening of the corresponding RhBHA, giving rise to a highly fluorescent acyclic form and a color change from colorless to pink. Furthermore, the thermo-responsive property of PNIPAM moiety and the pH-dependent of RhBHA enable PEO-*b*-P(NIPAM-co-RhBHA) diblock copolymer to serve as multifunctional probes to pH, temperature, and Hg²⁺ ions.

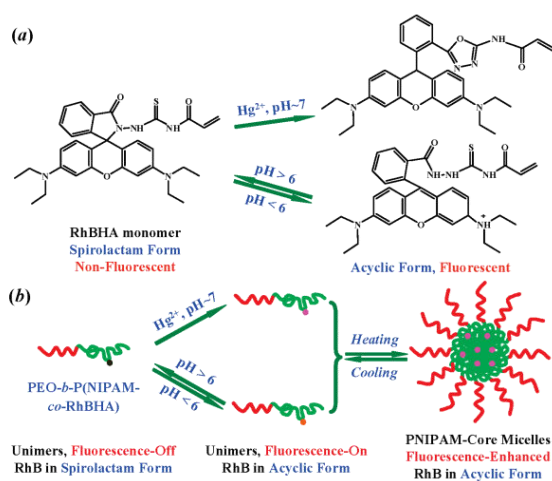


Figure 7. (a) Schematic for the Synthesis of Rhodamine B-Based Spirolactam Monomer (RhBHA) and (b) Proposed Ring-Opened Mechanism in the Presence of Hg²⁺ Ions or Acid Media

Li et al.¹¹⁵ utilized the thermo-responsive nanogels via emulsion polymerization of NIPAM and a novel 1,8-naphthalimide-based dye. The moiety of fluorescent monomer (NPTUA) are sensitive to detecting the Hg²⁺ ions. (**Figure 8**) When the annealing above the VPT temperature, the fluorescence intensity of NPTUA-based nanogels in the absence of Hg²⁺ ions, thus exhibiting ~3.4-fold increase performance because of the NPTUA moieties are loaded at hydrophobic microenvironment. Furthermore, the detection sensitivity for Hg²⁺ ions can be significantly improved as the annealing temperature above the nanogel LCST. Since the high selectivity of reaction-based detection method. It is quite anticipated that the promising concepts have potential applications in multifunctional environmental sensing devices.

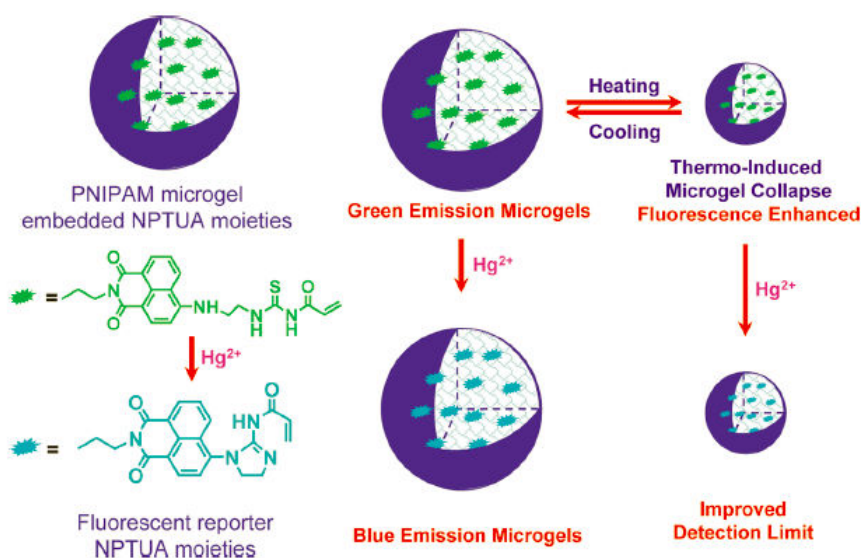


Figure 8. NPTUA moieties enabling PNIPAM nanogel employed as a ratiometric fluorescent sensor of Hg²⁺ ions with enhanced detection sensitivity.

2-3-2 Responsive Polymer-Based Magnetic Sensors

Considerable attention has been focused on magnetic biosensors composed of magnetite (Fe₃O₄) nanoparticles for several promising applications, such as magnetic fluids, biotechnology, magnetic resonance imaging (MRI), tumor hyperthermia, and membrane separation due to their excellent technological and fundamental scientific

importance.¹¹⁶⁻¹¹⁸ The well-organized and size-controlled synthesis of nanomagnetite without particle aggregation are considerable attention for the preparation of environmental sensory device applications. There are several facile approaches can achieved the 100 nm Fe₃O₄ nanoparticles, such as hydrothermal reaction, chemical coprecipitation, and sol-gel synthesis.¹¹⁹⁻¹²⁰ The efficiency modification strategy is added diverse stabilizers, such as surfactant or polymers to prevent the coalescence and stabilize Fe₃O₄ nanoparticles. Moreover, the functionalities hybrid membranes can assisted Fe₃O₄ nanoparticles well-dispersed toward the polymeric matrix and intended to eliminate the defects at the interface between the polymeric matrix and particles.

Recently, Hoare et al.¹²¹ fabricated magnetically triggered nanocomposite membranes based on thermosensitive, poly(N-isopropylacrylamide)-based nanogels and magnetite nanoparticles to fulfil “on-demand” drug delivery application of an external oscillating magnetic field (**Figure 9**). In spite of PNIPAM-based hydrogel induced the phase transition with a swell-deswell response process, enabling reduces drug flux from the hydrogel. The drug release rate still too slow to apply to cure disease due to it is dependent on diffusion consistent. Sanson et al.¹²² demonstrated that utilizing the radio frequency magnetic hyperthermia for realization of controlled drug release (**Figure 10**). The promising results presented a novel multifunctional nanocarriers platform based on magneto-chemotherapy strategy have potential applications for magnetic resonance imaging.

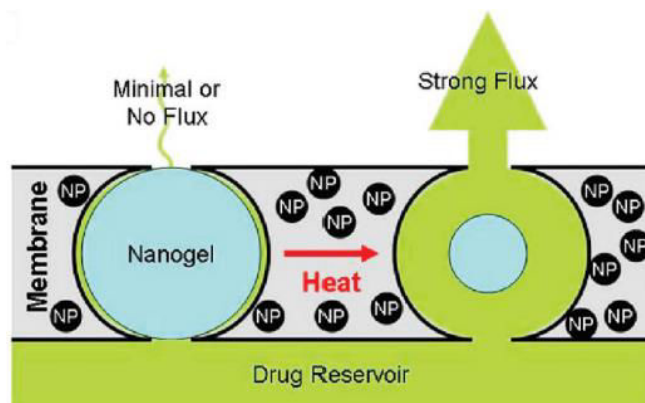


Figure 9. Stimulus-responsive membrane triggering in vitro: schema of the proposed mechanism of membrane function.

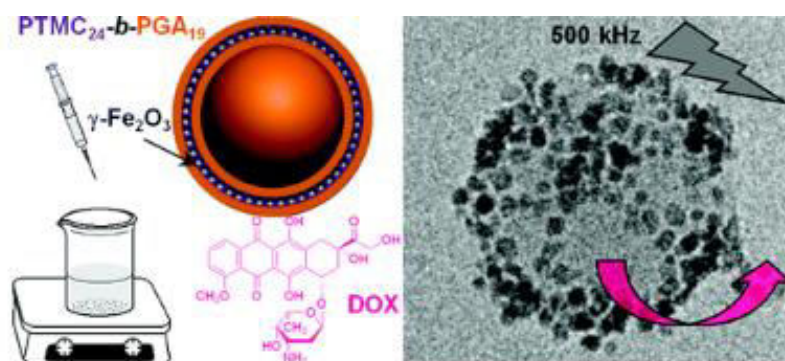


Figure 10. Scheme of stimulus-magnetic-responsive membrane of PTMC-b-PGA polymersomes triggering in magnetic resonance imaging.

Huang et al were synthesized the self-assembling, crosslinker-free, and thermo-sensitive nanocarriers (TSNCs) composed of thermo-sensitive (PEO-PPO-PEO) and polyvinyl alcohol (PVA) block copolymers by the addition of iron oxide nanoparticles and hydrophobic drug molecules via a mini-emulsion process. **(Figure 11)** The promising results show the magnetic field can induced a temperature change between the 40 °C to 50°C and improved the triggering size contraction and shrinkage from the inner cores, enabling make the nanocarriers collapse. This present working demonstrated that a novel multifunctional nanocarrier exhibited high magnetization behavior, long-circulating and non-cytotoxic efficiency for magnetic resonance imaging (MRI), enabling have a potential to instantly release an anti-epileptic agent under remote control.¹²²



Figure 11. Schematic representation of (a) using PVA to stabilize the F127 to form a stable nanocarrier and (b) the structure of a thermosensitive nanocarrier (TSNC) composed of PVA and F127 with iron oxide nanoparticles and drug encapsulated.

2-4 Experimental Section

2-4-1 Materials

N-Isopropylacrylamide (NIPAAm) and *N*-methylolacrylamide (NMA) were provided by Tokyo Chemical Industry Co. Japan. NIPAAm was re-crystallized three times from hexane–toluene (10/1, v/v) prior to use. Acrylic acid (AA, Aldrich, Saint Louis, USAcity, country, 99%) was dried over CaH_2 to distill in a round-bottomed flask overnight, then purified by passing it through a short aluminum-oxide column (50–200 μm), and stored at 4 °C prior to use. The radical initiator 2,2'-azobis(2-methylpropionitrile) (AIBN) was purchased from UniRegion Bio-Tech and was recrystallized twice in ethanol prior to use. Iron (II) ($\text{FeCl}_2 \cdot 4\text{H}_2\text{O}$) and Iron (III) ($\text{FeCl}_3 \cdot 6\text{H}_2\text{O}$) chloride hexahydrate (Aldrich, 99%), dichloromethane (Tedia, Fairfield, USAcity, country, 99.9%); methanol (Tedia, HPLC/SPECTRO); NH_4OH (Alfa, 28%); anhydrous tetrahydrofuran (99.9%); acetone (99.8%); calcium hydride (reagent grade 95%); diethyl ether (99%); 4-bromo-1,8-naphthalic anhydride (95%); benzoyl isothiocyanate (98%); allylamine (98%); 1,2-ethylenediamine (99%); chloroform (anhydrous, 99%); *N,N*-dimethylformamide (99%); 1,4-dioxane (99.5%); acetonitrile (99%); ethanol (99.8%); and hydrazine hydrate (reagent grade, N_2H_4 50%–60%) were used as received. Perchlorate salts of metal ions (Co^{2+} , Cu^{2+} , Fe^{2+} , Mg^{2+} , Hg^{2+} , Pb^{2+} , Zn^{2+} , Cd^{2+} , Ni^{2+}) were purchased from Sigma-Aldrich (Saint Louis, USAcity, country).

2-4-2 Synthesis of 4-Bromo-N-allyl-1,8-naphthalimide

Fluorescent BNPTU was prepared according to a previously reported method.¹⁸ The process of its synthesis is illustrated in **Figure 1**. A 50-mL round-bottomed flask was charged with 4-bromo-1,8-naphthalic anhydride (1.385 g, 5 mmol), allylamine (0.317 g, 5.18 mmol), and 20 mL of 1,4-dioxane. The reaction mixture was stirred at reflux for 8 h. After cooling to room temperature, the suspension was poured into 600 mL of ice water and then filtrated. After drying in a vacuum oven overnight at room temperature, 4-bromo-N-allyl-1,8-naphthalimide (BN-Br) was obtained as a slightly gray solid (1.12 g, yield: 85%). ¹H-NMR (300 MHz, CDCl₃, TMS, **Figure 12a**): $\delta = 5.33$ (a, 2H, $-\text{CH}_2\text{CHCH}_2-$); $\delta = 5.91$ (b, 1H, $-\text{CH}_2\text{CHCH}_2-$); $\delta = 4.58$ (c, 2H, $-\text{CH}_2\text{CHCH}_2-$); $\delta = 8.56$ (d, 1H, 7-CH); $\delta = 8.03$ (e, 1H, 3-CH); $\delta = 8.64$ (f, 1H, 5-CH); $\delta = 7.94$ (g, 1H, 6-CH); $\delta = 8.45$ (h, 1H, 2-CH).

2-4-3 Synthesis of 4-(Aminoethylene)amino-N-allyl-1,8-naphthalimide

A 25-mL round-bottomed flask was charged with NP-Br (500 mg, 1.57 mmol) and an excess of 1,2-ethylenediamine (8 mL). The reaction mixture was stirred at reflux for 6 h. The residues were dissolved in CH₂Cl₂ (200 mL) and extracted with water. Finally, 4-(aminoethylene) amino-N-allyl-1,8-naphthalimide (NP-NH₂) was obtained as an orange crystal (400 mg, yield: 80%). ¹H-NMR (300 MHz, DMSO-*d*₆, TMS, **Figure 12b**): $\delta = 5.33$ (a, 2H, $-\text{CH}_2\text{CHCH}_2-$); $\delta = 5.91$ (b, 1H, $-\text{CH}_2\text{CHCH}_2-$); $\delta = 4.58$ (c, 2H, $-\text{CH}_2\text{CHCH}_2-$); $\delta = 8.56$ (d, 1H, 7-CH); $\delta = 8.03$ (e, 1H, 3-CH); $\delta = 8.64$ (f, 1H, 5-CH); $\delta = 7.94$ (g, 1H, 6-CH); $\delta = 8.45$ (h, 1H, 2-CH); $\delta = 2.85$ (i, 2H, $-\text{CH}_2\text{NH}_2$).

2-4-4 Synthesis of BNPTU

A 25-mL round-bottomed flask was charged with NP-NH₂ (400 mg, 1.36 mmol), benzoyl isothiocyanate (0.22 g, 1.36 mmol), and 12 mL of acetone. The reaction mixture was stirred at reflux for 1 h. After cooling to room temperature, the solution was filtrated and washed with ethanol. The product was purified using chromatography with CH₂Cl₂ (320 mg, yield: 80%). ¹H-NMR (300 MHz, DMSO-*d*₆, TMS, **Figure 12c**): $\delta = 5.33$ (a, 2H, $-\text{CH}_2\text{CHCH}_2-$); $\delta = 5.91$ (b, 1H, $-\text{CH}_2\text{CHCH}_2-$); $\delta = 4.58$ (c, 2H, $-\text{CH}_2\text{CHCH}_2-$); $\delta = 8.41$ (d, 1H, 7-CH); $\delta = 7.62-7.88$ (e + n, 3H, 6-CH; $-\text{COCCHCHCHCH}-$); $\delta = 8.72$ (f, 1H, 5-CH); $\delta = 7.03$ (g, 1H, 3-CH); $\delta = 8.26$ (h, 1H, 2-CH); $\delta = 4.02$ (i, 2H, $-\text{NCH}_2\text{CH}_2\text{N}-$); $\delta = 3.95$ (j, 2H, $-\text{NCH}_2\text{CH}_2\text{N}-$); $\delta = 11.08$ (k,

ammonium hydroxide (8 mL) was added dropwise under mechanical stirring at 60 °C for 30 min under N₂. Then, the magnetic iron oxides were isolated from the solution by a magnet bar and dried in a vacuum oven at 40 °C for 24 h.

2-4-6 Synthesis of Poly(NIPAAm-co-NMA-co-AA)

Poly(NIPAAm-co-NMA-co-AA) was synthesized through free-radical copolymerization of the following three monomers: NIPAAm, NMA, and AA (**Figure 2**) Poly(NIPAAm-co-NMA-co-AA) with different monomer ratios were denoted **P1–P2**, as listed in **Table 1**. The concentration of AIBN used as the initiator was 0.004 M. The reaction mixture, containing dimethylformamide (DMF) and monomers, was degassed by first bubbling nitrogen through for 30 min and then left to react at 70 °C for 24 h. The reaction mixture was quenched by exposure to air. The mixture was diluted with methanol to remove the unreacted monomers. The light white filtrate was concentrated, re-precipitated from diethyl ether, collected by filtration, and dried under vacuum to obtain the polymer product. The synthesis and characterization of **P1–P2** are described in the following sections. The number-averaged molecular weight (M_n) and polydispersity index (PDI) estimated from gel permeation chromatography (GPC) (THF eluent) are listed in **Table 1** and **Figure 13**.

Table 1. Polymerization conditions and molecular weights of poly(NIPAAm-co-NMA-co-AA) random copolymers.

Polymer No.	Composition ^a	M_n ^b	PDI	T_d (°C)	LCST (°C) (in pH = 7)
	NIPAAm:NMA:AA				
P1	10:5:0	26,856	2.01	375	54.5
P2	10:5:3	18,041	1.76	374	58.1

^a Molar ratio (%) estimated from ¹H-NMR spectra. ^b Determined using THF eluent.

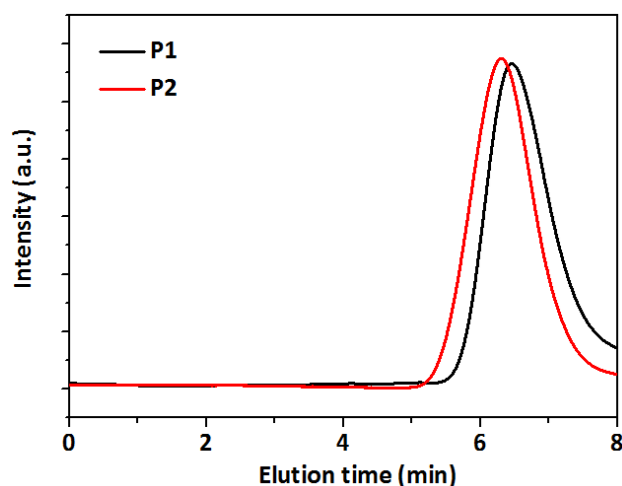


Figure 13. GPC profiles of **P1** and **P2** copolymers.

2-4-7 Synthesis of Poly(NIPAAm-co-NMA) Random Copolymers (P1)

A reaction mixture of 1.131 g (9.99 mmol) of NIPAAm, 505 mg (4.99 mmol) of NMA, 5 mg (0.03 mmol) of AIBN, and 7.5 mL of EtOH was used to produce an orange solid (yield: 86%). Figure 4 and Table 1 present the molecular weight and chemical structure characterization of poly(NIPAAm-co-NMA) obtained using GPC with THF as the eluent and $^1\text{H-NMR}$, respectively. The copolymer composition, estimated by performing peak integration, was consistent with the proposed structure. The estimated copolymer ratio of poly(NIPAAm-co-NMA) based on the NMR spectrum was 81:19, and the number-averaged molecular weight M_n and PDI estimated using GPC were 26856 and 2.01, respectively. $^1\text{H-NMR}$ (300 MHz, $\text{DMSO-}d_6$, TMS, **Figure 14**): $\delta = 0.82\text{--}1.12$ (a, 6H, $-\text{CH}(\text{CH}_3)_2$); $1.23\text{--}1.46$ (h + i, 4H, $-\text{CH}_2\text{CH}-$, $-\text{CH}_2\text{CH}-$); $1.84\text{--}2.10$ (h + i, 2H, $-\text{CH}_2\text{CH}-$, $-\text{CH}_2\text{CH}-$); $5.34\text{--}5.53$ (b, 1H, $-\text{NHCH}_2\text{OH}$); $3.71\text{--}3.82$ (c, 1H, $-\text{CH}(\text{CH}_3)_2$); $7.23\text{--}7.59$ (e, 1H, $-\text{CONHCH}-$); $7.92\text{--}8.14$ (f, 1H, $-\text{NHCH}_2\text{OH}$); $4.36\text{--}4.65$ (g, 2H, $-\text{NHCH}_2\text{OH}-$).

2-4-8 Synthesis of Poly(NIPAAm-co-NMA-co-AA) Random Copolymers (P2)

A reaction mixture of 1.131 g (9.99 mmol) of NIPAAm, 505 mg (4.99 mmol) of NMA, 0.204 ml (0.0029 mmol) of AA, 5 mg (0.03 mmol) of AIBN, and 9 mL of EtOH was used to produce an orange solid (yield: 82%). **Figure 14** and **Table 1** present the molecular weight and chemical structure characterization of poly(NIPAAm-co-NMA-co-AA) obtained using GPC with THF as the eluent and $^1\text{H NMR}$, respectively. The copolymer composition, estimated by performing peak integration, was consistent with the proposed structure. The copolymer ratio of poly(NIPAAm-co-NMA-co-AA) based

on the NMR spectrum was 72:15:13, and the number-averaged molecular weight M_n and PDI estimated using GPC were 18041 and 1.76, respectively. $^1\text{H-NMR}$ (300 MHz, $\text{DMSO-}d_6$, TMS, **Figure 14**): $\delta = 0.82\text{--}1.12$ (a, 6H, $-\text{CH}(\text{CH}_3)_2$); $1.23\text{--}1.46$ (h + i + j, 6H, $-\text{CH}_2\text{CH-}$, $-\text{CH}_2\text{CH-}$, $-\text{CH}_2\text{CH-}$); $1.84\text{--}2.10$ (h + i + j, 3H, $-\text{CH}_2\text{CH-}$, $-\text{CH}_2\text{CH-}$, $-\text{CH}_2\text{CH-}$); $5.34\text{--}5.53$ (b, 1H, $-\text{NHCH}_2\text{OH}$); $3.71\text{--}3.82$ (c, 1H, $-\text{CH}(\text{CH}_3)_2$); $11.92\text{--}12.05$ (d, 1H, $-\text{COCH}_2\text{OH}$); $7.23\text{--}7.59$ (e, 1H, $-\text{CONHCH-}$); $7.92\text{--}8.14$ (f, 1H, $-\text{NHCH}_2\text{OH}$); $4.36\text{--}4.65$ (g, 2H, $-\text{NHCH}_2\text{OH-}$).

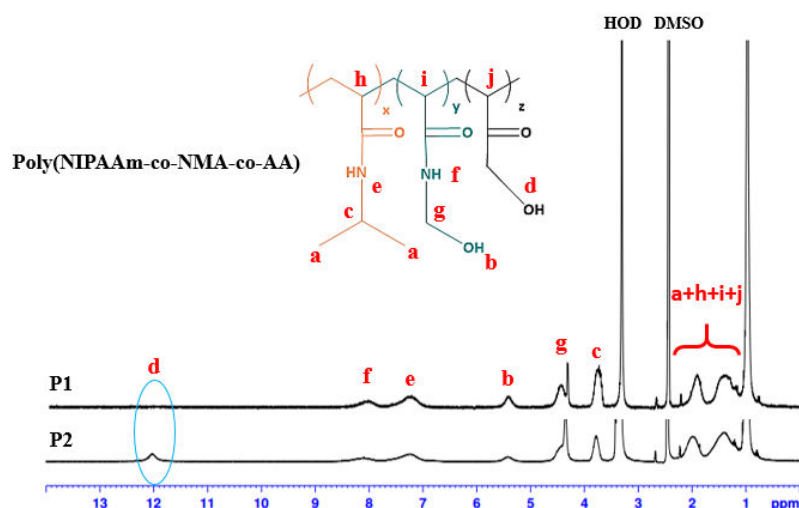


Figure 14. $^1\text{H-NMR}$ spectrum of poly(NIPAAm-*co*-NMA-*co*-AA) in DMSO.

2-5 Preparation of Electrospun (ES) Nanofibers

As shown in **Figure 2b**, the ES nanofibers were prepared using a single-capillary spinneret in a procedure similar to that described in our previous papers.²⁵⁻³³ The poly(NIPAAm-*co*-NMA) (**P1**), poly(NIPAAm-*co*-NMA-*co*-AA) (**P2**), BNPTU, and Fe_3O_4 NPs blend was dissolved in methanol (MeOH) as solvent at 250 mL h^{-1} and stirred overnight. The blend composition (wt %) of (**P1** or **P2**), BNPTU, and Fe_3O_4 NPs for preparing the ES nanofibers was 85/10/5. The polymer solution was fed into a metallic needle using syringe pumps (Model 100, KD Scientific, Holliston, MA city, state abbreviation, USA) at a feed rate of $0.8\text{--}1.0 \text{ mL h}^{-1}$. The tip of the needle was connected to a Chargemaster CH30P high voltage power supply (Simco, Hatfield, PA city, state abbreviation, USA) set at 13.4 kV during electrospinning. A piece of aluminum foil or quartz was placed 15 cm below the tip of the needle for 30 min to collect the ES nanofibers. All experiments were performed at room temperature and a relative humidity of approximately 30%. **P1** and **P2** blended with the Fe_3O_4 NPs at a 5

wt % ratio are denoted by **P1-5%** and **P2-5%**. The ES nanofibers were annealed at 100 °C for 24 h in an oven for chemical cross-linking.

2-6 Characterization

¹H-NMR data were recorded at room temperature using an AM 300 (300 MHz) spectrometer (Bruker, Billerica, MA city, state abbreviation, USA) and the residual proton resonance of deuterated chloroform and deuterated dimethyl sulfoxide. High resolution electrospray ionization mass spectrometry spectra were recorded using an ion-trap time-of-flight liquid chromatograph mass spectrometer (Shimadzu, Kyoto city, Japan). Gel permeation chromatography (GPC) analysis was performed using a Lab Alliance RI2000 instrument (two-column, MIXED-C and MIXED-D from Polymer Laboratories, Theale city, UK) connected to a refractive index detector (Schambeck SFD GmbH, Bad Honnef city, Germany). All GPC analyses were performed using a polymer and THF solution at a flow rate of 1 mL min⁻¹ at 40 °C and calibrated with methyl methacrylate. The thermal decomposition temperature was determined using a Q50 thermal gravimetric analyzer (TGA) (TA Instruments, Lukens Drive, New Castle city, state abbreviation, USA) over a heating range of 100–800 °C at a heating rate of 10 °C min⁻¹ in a nitrogen atmosphere. The LCST of the prepared copolymer solution was recorded by monitoring the transmittance of a 520 nm light beam on Shimadzu UV–Vis spectrophotometer. The copolymer concentration in water was 1 wt %, and the temperature was raised from 10 to 70 °C in 2.5 °C increments every 10 min. A plot of the changes in optical transmittance as a function of temperature for polymers in water was made, the LCST corresponds to the first turning point of the transition curve.³² Magnetic properties of Fe₃O₄ nanoparticles or ES nanofibers were measured on a Lake Shore VSM-7407 instrument (MPMS (SQUID) VSM, Quantum Design, San Diego, CA city, state abbreviation, USA). The magnetization hysteresis loops were measured at 300 K.¹⁰⁸

The morphologies of ES nanofibers were characterized using an S-520 scanning electron microscope (Hitachi, Tokyo, Japan) equipped with X-ray microanalysis capability. Samples were coated with platinum prior to scanning electron microscopy (SEM) characterization, and analysis was conducted at an increased voltage of 10 kV. Fluorescence optical microscopy images were captured using an LCS SP5 two-photon

laser confocal microscope (Leica, Mannheim city, Germany). The morphologies of the ES nanofibers were similar to those reported in our previous studies.^{26,31,35}

Ultraviolet–visible (UV–Vis) absorption and PL spectra were measured to examine photophysical properties and recorded using a UV–Vis spectrophotometer (Shimadzu) and a Fluorolog-3 spectrofluorometer (Horiba Jobin Yvon, Edison, NJ city, state abbreviation, USA), respectively. Variations in the optical absorption and PL of the prepared ES nanofibers with different metal ion concentrations are described as follows. To ensure that the beam excited the same point on the prepared samples during each measurement, the ES nanofibers were fixed in cuvettes with adhesive tape, and the cuvette was filled with a basic aqueous metal ion solution at 10^{-4} – 10^{-2} M. Each measurement was maintained for 15 min to ensure that the chelating reaction reached equilibrium. All PL spectra of the ES nanofibers were recorded using the spectrofluorometer, and the samples were excited at a suitable wavelength, as described in our previous studies.²⁵⁻³³

2-7 Results and Discussion

2-7-1 Characterization of BNPTU and Poly(NIPAAm-co-NMA-co-AA)

The chemical structure of BNPTU was characterized using ¹H-NMR (**Figure 12**). The synthesis routes of BNPTU (**Figure 1**) are similar to those reported in a previous study.¹⁸ **Figure 2a** shows the route by which poly(NIPAAm-co-NMA-co-AA) copolymers were synthesized through free radical polymerization. The two types of copolymers (**P1** and **P2**) were synthesized and their composites are listed in **Table 1**. **Figure 14** shows the ¹H-NMR spectrum of poly(NIPAAm-co-NMA) (**P1**) and poly(NIPAAm-co-NMA-co-AA) (**P2**). The proton peaks at 7.23–7.59 ppm (Peak e) and 3.71–3.82 ppm (Peak c) correspond to the methylene neighbors of the secondary amine moiety and the alkyl chains on NIPAAm, respectively. The proton peaks at 5.34–5.53 ppm (Peak b), 7.92–8.14 ppm (Peak f), and 4.36–4.65 ppm (Peak g) correspond to the methylene neighbors of the hydroxyl, secondary amine moiety, and alkyl chains on NMA, respectively. The proton peak at 11.92–12.05 ppm (Peak d) corresponds to the methylene neighbor of hydroxyl on the AA in **P2**. The peak at 0.82–1.12 ppm (Peak a) and those at 1.23–2.1 ppm (Peaks h, i, and j) correspond to the alkyl chains on the copolymers. The copolymer ratios of **P1** and **P2** were estimated from NMR spectra, and were 81:19 and 72:15:13, respectively. The favorable agreement between the

feeding ratio and experimental composition suggests the successful preparation of the target copolymers. The molecular weights, thermal properties, and LCSTs of **P1** and **P2** are listed in **Table 1**. The number-averaged molecular weights and polydispersity indices (PDIs) of **P1** and **P2** were 26,856 and 2.01, and 18,041 and 1.76, respectively. Notably, **Figure 14** shows that the accurate PDI (M_n/M_w) data of **P1** were 26,856/53,980 equal to 2.01 and that of **P2** was 18,041/31,752 equal to 1.76. The thermal decomposition curves of the prepared polymers are presented in **Figure 15**. The identical thermal decomposition temperature of 210 °C for **P1** and **P2** is attributable to their similar NIPAAm compositions. All decomposition temperatures for **P1** and **P2** were higher than 270 °C, and thus, they exhibited favorable and stable thermal properties. **Figure 16** shows the typical optical transmittance (520 nm) versus temperature curves of **P1** and **P2**, which exhibit thermoresponsive soluble-to-insoluble phase transitions in an aqueous medium. The copolymers are soluble in water below their LCSTs. The LCSTs of **P1** and **P2** are both approximately 55 °C, slightly higher than that of PNIPAM (32 °C) because of the hydrophilic characteristics of the NMA and AA compounds, as stated in our previous study³⁴ and one other study.¹²³

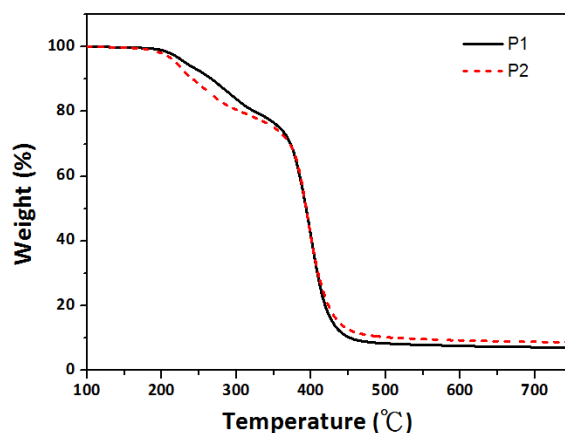


Figure 15. TGA curves of **P1** and **P2** copolymers with a heating rate of 10 °C min⁻¹ in a nitrogen atmosphere.

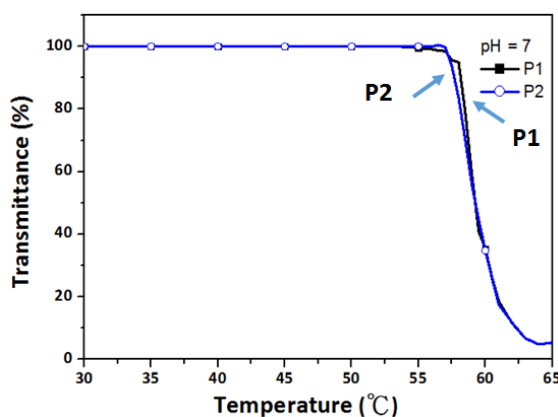


Figure 16. Variations in optical transmittance of **P1** and **P2** in pH 7 water solutions with temperatures between 30 and 65 °C.

Figure 17a illustrates that BNPTU in CH₃CN had a maximum in the UV–Vis absorption peak ($\lambda^{\text{abs}}_{\text{max}}$) of 430 nm at pH 7 and emitted green fluorescence under UV light (inset) as it is a fluorescent dye. **Figure 17b** shows variations in the UV–Vis spectra of BNPTU in a CH₃CN solution containing various metal ions at a concentration of 10⁻⁵ M (pH 7). The $\lambda^{\text{abs}}_{\text{max}}$ of BNPTU was blueshifted from 430 to 350 nm when the Hg²⁺ ion was added. The Hg²⁺ ion transformed the thiourea unit of BNPTU under aqueous conditions into an imidazoline moiety with considerably weakened electron-donating ability (**Figure 2c**) [5,35–37]. However, no change in the absorption peak was observed when other metal ions such as Co²⁺, Ni²⁺, Pb²⁺, Zn²⁺, Mg²⁺, Cu²⁺, Fe²⁺, and Cd²⁺ were added, suggesting that BNPTU exhibited high selectivity and sensitivity toward Hg²⁺.

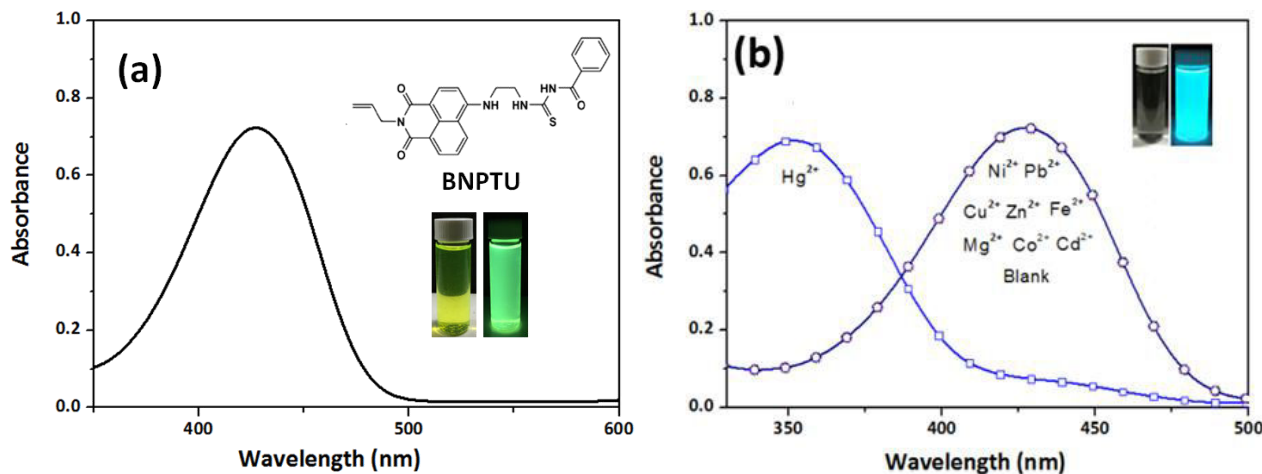


Figure 17. UV-Vis spectra of (a) BNPTU in CH₃CN solution (10⁻⁵ M) and (b) variation of UV–Vis spectra of BNPTU CH₃CN solution (10⁻⁵ M, pH 7) with different metal ions at 10⁻⁴ M. The corresponding inset figures show the color changes under visible light and 254-nm UV light.

2-7-2 Morphology and Characterization of ES Nanofibers

Figure 18 presents field-emission SEM (FE-SEM) images of the ES nanofibers prepared using **P1** and **P2** at a solution concentration of 250 mg mL⁻¹ with MeOH.

When dry, the **P1** and **P2** ES nanofibers had average diameters of 416 ± 31 and 437 ± 42 nm, respectively. The recorded average diameter was a statistical average of 50 fibers from each sample. Moreover, all of the ES nanofibers from pure MeOH solvent were smooth and nonporous. The diameters of the **P1** and **P2** ES nanofibers were similar when they were dry because the concentration of the ES solution was fixed and the molar ratios of the NMA and AA moieties in the copolymers were lower than that of NIPAAm. To observe the morphologies of the cross-linked **P1** and **P2** ES nanofibers in pure water at various temperatures, the fibers were collected on a small piece of aluminum foil and immersed in water at 30 °C or 60 °C. After 10 min, the samples were solidified by placing in a flask containing liquid nitrogen, and the residual water was removed using a vacuum for 30 min to retain the original morphology. **Figure 18** shows the FE-SEM images of the **P1** and **P2** ES nanofibers in a wet state after they were immersed in water at 30 or 60 °C. As shown in **Figure 18** (wet state), the **P1** and **P2** fibers exhibited diameters of 1250 ± 205 and 1420 ± 282 nm at 25 °C and 830 ± 124 and 920 ± 138 nm at 60 °C, respectively. The diameters were substantially enlarged after the nanofibers were immersed in water (416 ± 31 , 437 ± 42 nm, respectively; **Figure 18**) because the hydrophilic NIPAAm chain swelled in the water. However, these swollen fibers maintained their cylindrical shape and did not dissolve in water, a phenomenon attributed to the efficient chemical cross-linking of the NMA moiety.³⁴ Furthermore, the fiber diameters at 30 °C were greater than those at 60 °C because of the hydrophilic NIPAAm chain, the temperature of which was below the LCST. By contrast, the nanofiber diameters decreased from approximately 1.5 μm to 1.0 μm as the temperature increased from 30 to 60 °C, due to the temperature of which was above the LCST resulting in the hydrophobic NIPAAm chain.

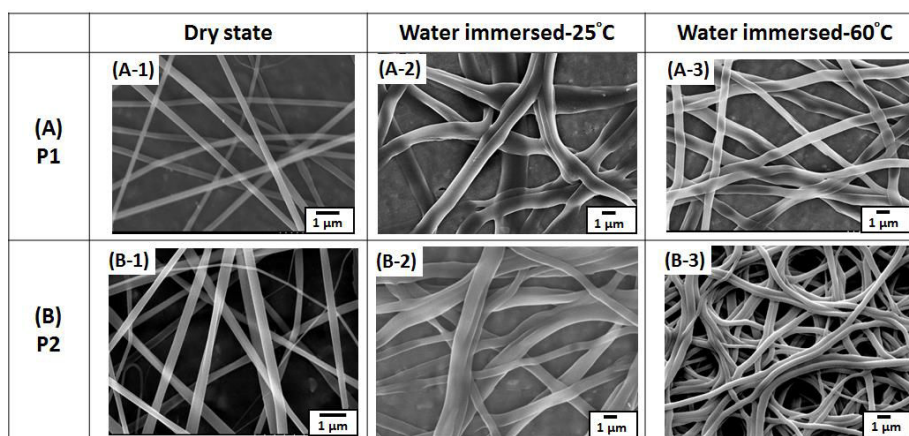


Figure 18. Field-emission scanning electron microscopy (FE-SEM) images of copolymers. (A) **P1** and (B) **P2** cross-linked nanofibers at 120 °C in a dry state and treated with water at 30 and 60 °C.

Figure 19a and b shows FE-SEM images and transmission electron microscopy images of the Fe_3O_4 NPs, respectively. The diameters of the nanoparticles were monodispersed within the range 15–25 nm. **Figure 19c** shows that the Fe_3O_4 NPs precipitated out of the solution and dropped to the bottom because of higher density (left image) and then accumulated on the side of the bottle because of a magnetic bar placed next to the bottle (right image), indicating that magnetic Fe_3O_4 NPs can be absorbed using a magnet.¹²⁷

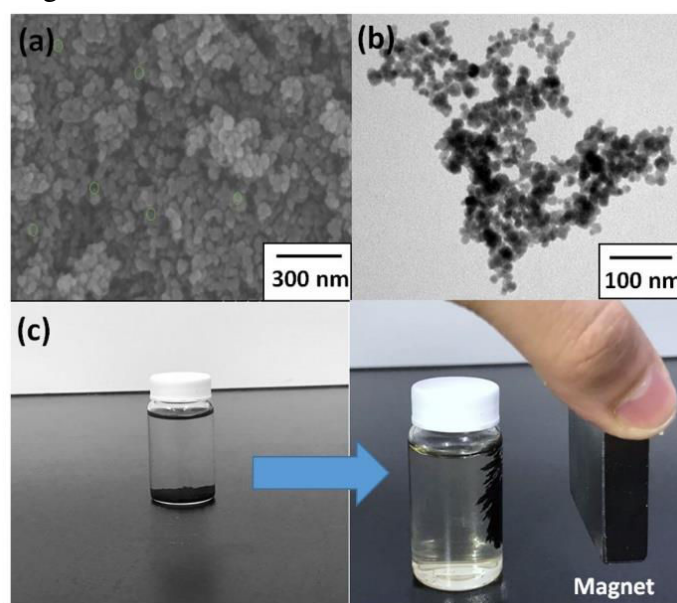


Figure 19. (a) FE-SEM and (b) Transmission electron microscopy (TEM) images of Fe_3O_4 NPs synthesized through coprecipitation. (c) Magnetic Fe_3O_4 NPs in the solution (left: Fe_3O_4 precipitated out of the solution and dropped to the bottom; right: Fe_3O_4 accumulated on the side of the bottle because of the magnet).

Figure 20a presents an SEM image of **P2-5%** ES nanofibers prepared from **P2** copolymers blended with Fe_3O_4 NPs at a 5% weight ratio. The strong stretching force associated with electrospinning induces orientation of these Fe_3O_4 NPs along the axis of the fiber. The numerous carboxyl groups of PAA in **P2** inhibited the aggregation of Fe_3O_4 NPs, a result similar to those of several previous studies.¹⁰⁶⁻¹¹¹ The result can be attributed to **P2-5%** containing carboxyl groups of PAA that interact with the Fe_3O_4 NPs, thereby enabling the PAA to be easily adsorbed by Fe_3O_4 NPs. **Figure 20b** shows

an SEM image of **P2-5%** ES nanofibers before elemental mapping, and **Figure 20c and d** shows the corresponding SEM images of **P2-5%** ES nanofibers after carbon (C) and iron (Fe) elemental mapping, respectively, by using energy dispersive X-ray spectroscopy (EDS). Notably, the C and Fe are contributed by the **P2** and Fe₃O₄ NPs, respectively. The C and Fe mapping images in **Figure 20b–d** indicate that Fe₃O₄ NPs were present within the **P2-5%** ES nanofibers because no Fe species remained on the substrate, as shown by the dark region. The Fe content within the **P2-5%** ES nanofibers was 14.54 wt% as estimated according to the EDS spectrum (**Figure 20e**). Furthermore, the amounts of Fe₃O₄ NPs within the **P2-5%** ES nanofibers were confirmed through TGA in an oxygen atmosphere (**Figure 21**). **Figure 21** shows the stages within the temperature range 100–750 °C, including the decomposition of poly(*N*-methylolacrylamide)(PNMA) and PAA, and the oxidation of the Fe₃O₄ NPs. Weight loss initially occurred below 300 °C, and originated from either the decomposition of noncoordinated carboxyls or the evaporation of trace water. Weight loss that occurred between 300 and 450 °C was caused by the cleaving of PNIPAM chains.¹⁰⁹ Finally, the copolymers were degraded and Fe₃O₄ was completely transformed into Fe₂O₃ at 700 °C.¹⁰⁹ The calculated weight percentage of the remaining content, consisting of carbon residue and Fe₂O₃, was approximately 14 wt %.

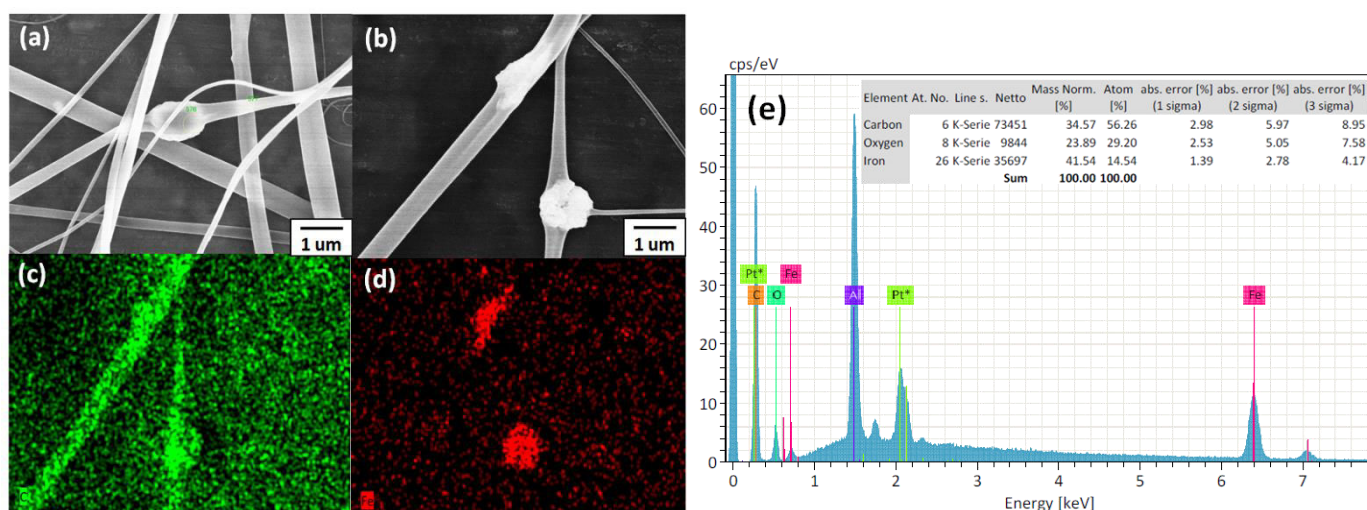


Figure 20. (a) SEM image of Fe₃O₄ NPs blended with nanofibers at a 5% weight ratio. (b) FE-SEM image of **P2-5%** cross-linked nanofibers in the presence of Fe³⁺. (c,d) Energy dispersive X-ray spectroscopy EDS maps of C and Fe within the confined area in (b). (e) EDS spectrum recorded within the region defined in (b).

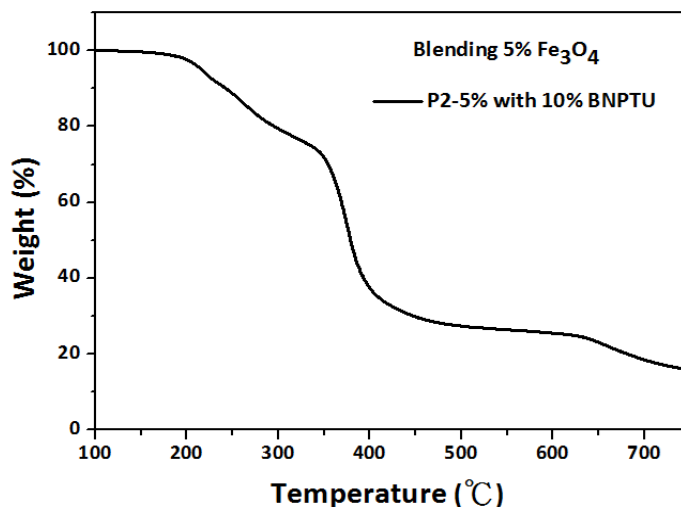


Figure 21. TGA curves of **P2-5%** blended with 5 wt% Fe_3O_4 NP nanofibers with a heating rate of $10\text{ }^\circ\text{C min}^{-1}$ in a nitrogen atmosphere.

2-7-3 Hg^{2+} Sensing, Thermoresponsiveness, and Magnetic Properties of ES Nanofibers

P1 or **P2** blended with 10% BNPTU and 5% Fe_3O_4 NP ES nanofibers, which can sense metal ions because of the ability of PAA and BNPTU to adsorb Hg^{2+} , was systematically explored.^{18,111} **Figure 22a** shows the PL spectra of ES nanofibers prepared from **P1** and **P2** blended with 10% BNPTU in an aqueous solution without Hg^{2+} (blank) or with Hg^{2+} at 10^{-2} M and subjected to 430-nm excitation. The maximum emission peak ($\lambda^{\text{PL}_{\text{max}}}$) of the **P1** and **P2** ES nanofibers blueshifted substantially from 530 nm in a non- Hg^{2+} aqueous solution to 450 nm in an Hg^{2+} aqueous solution. This change corresponded to the thiourea unit of BNPTU, which transformed the imidazoline moiety (with the Hg^{2+} ion), thereby causing a significant reduction in electron delocalization within the fluorophore (**Figure 2c**).^{14,124-126} Moreover, the PL intensity of the **P2** ES nanofibers was 1.3 times that of **P1** ES nanofibers, indicating that the AA moiety of **P2** enhances the adsorption of mercury ions, similar to one report.¹¹¹

Figure 22b shows the PL spectra of ES nanofibers prepared from **P2** blended with 10% BNPTU and 5% Fe_3O_4 NPs. **P2-5%** was placed in aqueous solutions without Hg^{2+} (blank), with Hg^{2+} at 10^{-4} , 10^{-3} , and 10^{-2} M, and under neutral conditions at 430-nm excitation. The presence of the highest Hg^{2+} concentration (10^{-2} M) led to a $\lambda^{\text{PL}_{\text{max}}}$

blueshift from 530 nm to 450 nm in the emission spectra, similar to that of the **P2** ES nanofibers without Fe₃O₄ NPs, indicating that the metal ion sensing ability was unaffected by Fe₃O₄ NPs. As shown in the figure, the concentration of Hg²⁺ increasing from 0 (blank) to 10⁻⁴, 10⁻³, and 10⁻² M resulted in clear blueshifts in the $\lambda_{\text{max}}^{\text{PL}}$ from 530–500 nm, 450, and 450 nm, respectively. Furthermore, when the mercury ion concentration was at the extremely dilute level of 10⁻³ M, the emission maximum shift $\Delta\lambda_{\text{max}}$ was observed to be as high as 80 nm, resulting in a color change easily observable by the naked eye. Moreover, the lowest detectable Hg²⁺ concentration for the ES nanofibers was 10⁻⁴ M, suggesting that the **P2-5%** ES nanofibers were highly sensitive to Hg²⁺ but not to general ions, even when the system contained Fe₃O₄ NPs.

Figure 22c shows the changes of the fluorescence intensity ratio, I_{450}/I_{530} (I_{450} is the fluorescence intensity of BNPTU after the detection of Hg²⁺ emission at 537 nm, whereas I_{530} is the fluorescence intensity of BNPTU before the detection of Hg²⁺ emission at 530 nm) of the **P2-5%** ES nanofibers when subjected to Hg²⁺. As the concentration of Hg²⁺ was increased, BNPTU emission at 530 nm gradually decreased, and BNPTU-Hg²⁺ emission at 450 nm gradually increased. These changes corresponded to the fluorescence of BNPTU chelated with Hg²⁺ ions, causing the I_{450}/I_{530} to increase from approximately 0.1 to 1.2 as the Hg²⁺ ion concentration increased from 0 to 10⁻² M. The **P2-5%** ES nanofibers exhibited high sensitivity to Hg²⁺ ions between 10⁻⁴ and 10⁻² M. Moreover, the titration data of **Figure 22c** show that the K_d was calculated as 1.58 mM.³⁵

Figure 22d shows fluorescence variations in the **P2-5%** ES nanofibers in a 10⁻² M Hg²⁺ environment as the temperature was varied from 30 to 60 °C. At 30 °C, the temperature at which the ES nanofibers chelate Hg²⁺, the $\lambda_{\text{max}}^{\text{PL}}$ was blue shifted substantially from 530 nm (blank, green emission) to 450 nm (blue emission) in the emission spectra. When the temperature was increased from 30 to 45 °C, only a mild decrease in PL intensity at 450 nm ($\lambda_{\text{max}}^{\text{PL}}$) was observed, exhibiting almost no change, as shown in the enlarged inset image. However, when the temperature was increased from 45 to 50 °C, a dramatic quenching of the PL intensity of the ES nanofibers was observed. The PL intensity decreased as the temperature increased from 50 to 60 °C, reaching its lowest point at 60 °C. Notably, **Figure 23** shows no changes in the PL intensity of the pristine BNPTU compound as the temperature was increased from 30 to 60 °C because the chemical stability of BNPTU is favorable at room temperature or

higher temperatures (e.g., 60 °C), indicating that the quenching of the PL intensity of the ES nanofibers (**Figure 22d**) was not caused by the pristine BNPTU compound.

The aforementioned thermoreversible luminescence characteristics are explained as follows. As shown in **Figure 18**, compared with those in the dry state, the ES fibers soaked in water (wet state) underwent morphological change at 30 °C (below the LCST). At 30 °C, the hydrophilic groups in the PNIPAM interacted easily with water molecules to form intermolecular hydrogen bonds. However, the swollen ES fibers were insoluble in water because of the chemically cross-linked NMA segment. When the temperature was raised to 60 °C (above the LCST), the intermolecular hydrogen bonds between the PNIPAM and water were broken, leading to the release of water molecules from the fibers. However, Hg^{2+} was still present within the fibers. Furthermore, as the temperature was 60 °C (above the LCST), the PNIPAM was collapsed and densely packed, potentially suppressing absorption of incident light by the BNPTU moiety with Hg^{2+} , resulting in a reduction of the PL intensity. Thus, the prepared ES fibers exhibited an on–off PL intensity profile with temperature variation (**Figure 22d**), indicating that the ES nanofibers have thermoresponsive properties.

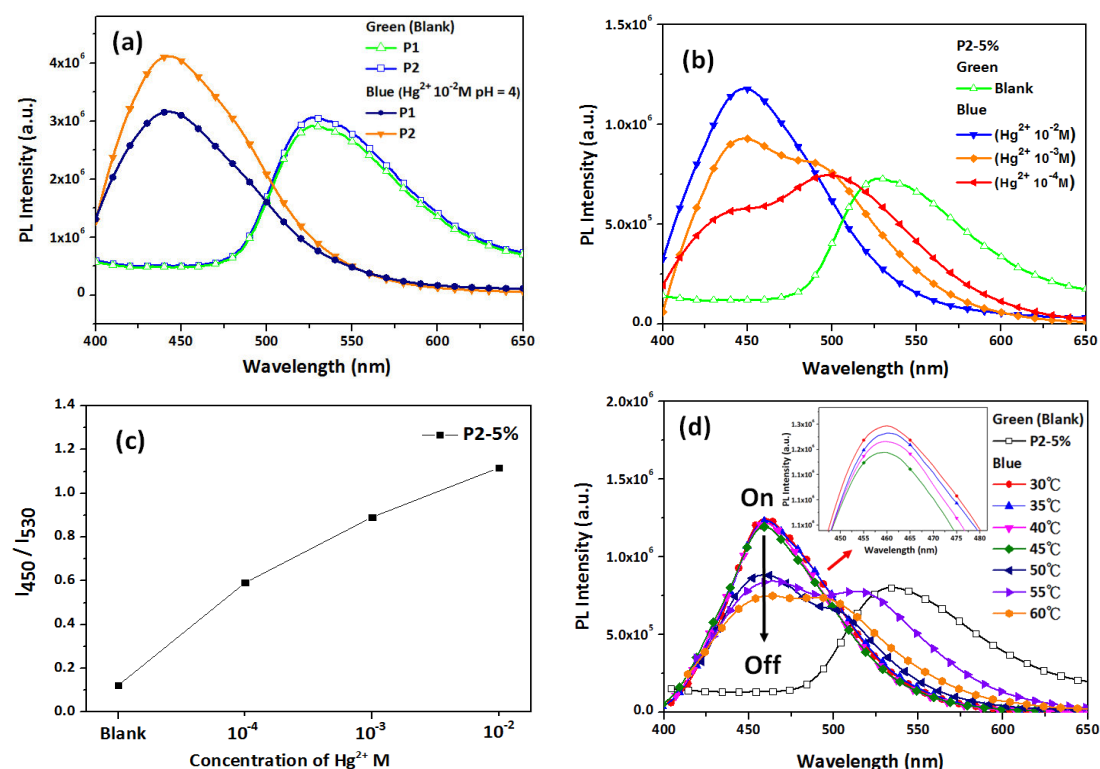


Figure 22. (a) Photoluminescence (PL) spectra of **P1** and **P2** nanofibers blended with 10 wt % BNPTU. (b) Comparison of **P2-5%** nanofibers with different Hg^{2+} concentrations between 10⁻², 10⁻³ and 10⁻⁴ M in aqueous solution. (c) Relative fluorescence intensity changes (I_{450}/I_{530})

of **P2-5%** ES nanofibers in aqueous solutions with various Hg^{2+} concentrations. **(d)** PL spectra of **P2-5%** ES nanofibers in 10^{-2} M Hg^{2+} solution with a temperature increase from 30 to 60 °C.

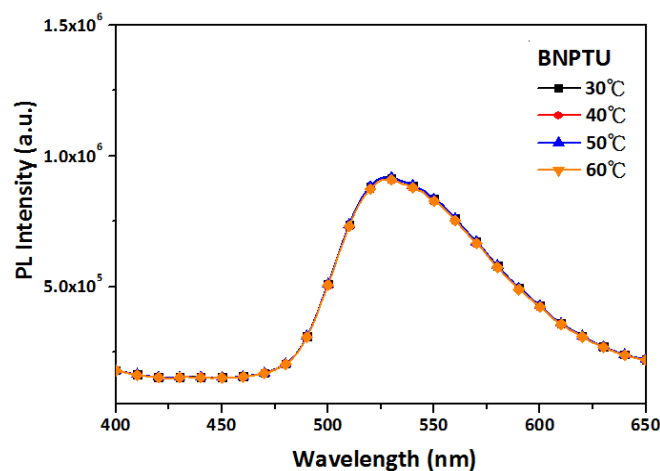


Figure 23. PL intensity of pristine BNPTU compound under a temperature increase from 30 to 60 °C.

The selectivity of **P2-5%** ES nanofibers toward Hg^{2+} over other common metal ions was also studied (**Figure 24**). **Figure 24a** shows that among all tested metal ions, namely Hg^{2+} , Pb^{2+} , Co^{2+} , Cd^{2+} , Mg^{2+} , Ni^{2+} , Zn^{2+} , Fe^{2+} , and Cu^{2+} (10^{-2} M; all metal ion test solutions were controlled at pH 4), a substantial blue shift in PL was observed only in the presence of Hg^{2+} . In Figure 8b, I_{450}/I_{530} indicates the ratio of a PL intensity of 530 nm ($\lambda_{\text{PL, max}}$), corresponding to other metal ions (Hg^{2+} , Pb^{2+} , Co^{2+} , Cd^{2+} , Mg^{2+} , Ni^{2+} , Zn^{2+} , Fe^{2+} , and Cu^{2+}), to a PL intensity of 450 nm ($\lambda_{\text{PL, max}}$), corresponding to Hg^{2+} . The presence of Hg^{2+} induced the most prominent I_{450}/I_{530} enhancement (approximately 2.5-fold), resulting in blue emission. For all of the other metal ions, the nanofibers exhibited reduced I_{460}/I_{510} values (approximately 0.1-fold), resulting in green emission (**Figure 24b**). In addition, the fluorescence spectra recorded in the presence of Hg^{2+} ions and the other metal ions revealed that none of the other metal ions interfered with the Hg^{2+} ion-induced fluorescence enhancement (inset **Figure 24b**), indicating that the sensing of Hg^{2+} by the **P2-5%** ES nanofibers was virtually unaffected by commonly coexisting ions.

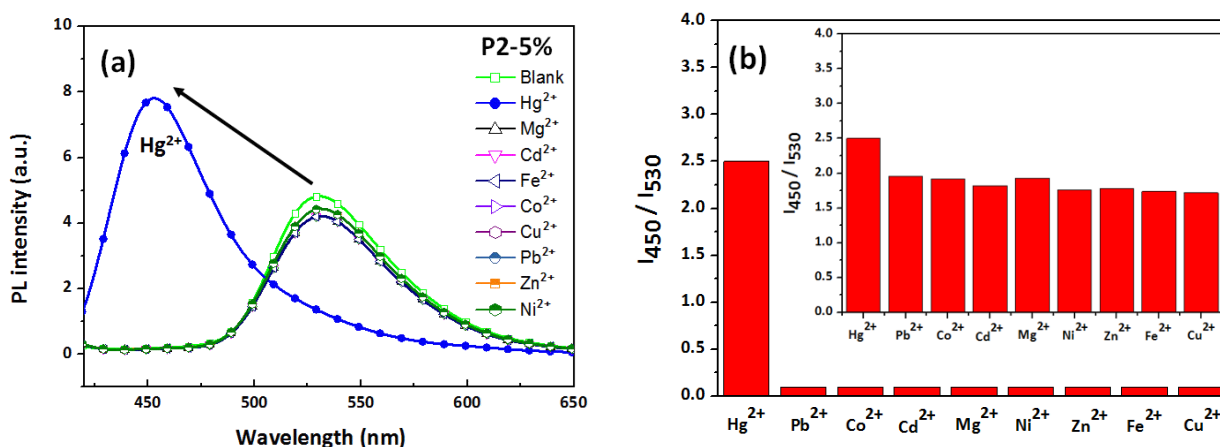


Figure 24. (a) Variation in the normalized PL spectra of **P2-5%** ES nanofibers in aqueous solutions with various metal ions (10^{-2} M) and no cation (blank). (b) Fluorimetric responses (I_{450}/I_{530}) of **P2-5%** ES nanofibers to various cations at 10^{-2} M aqueous solutions. From left to right: Hg²⁺, Pb²⁺, Co²⁺, Cd²⁺, Mg²⁺, Ni²⁺, Zn²⁺, Fe²⁺, and Cu²⁺. All the inset figures show corresponding photographs recorded under UV light. Inset of (b): fluorimetric response of the **P2-5%** ES nanofibers to solutions containing various metal ions at 10^{-2} M (as in (b)) when Hg²⁺ at 10^{-2} M is present.

Figure 25a shows the CIE coordinates of the **P2-5%** ES nanofibers in 0– 10^{-2} M Hg²⁺ aqueous solutions. All of the inset figures show corresponding photographs captured under UV light. The CIE coordinates show a strong blueshift from (0.24, 0.61) (blank) to (0.16, 0.08) (pH 4, Hg²⁺ 10^{-2} M) as the concentration of Hg²⁺ was varied from 0 to 10^{-2} M because of the detection of BNPTU by Hg²⁺, resulting in a color change from green to blue in the **P2-5%** ES nanofibers. Furthermore, as shown in the confocal microscopy images in **Figure 25b**, the color emission of the **P2-5%** ES nanofibers varied from green to blue as the concentration of Hg²⁺ was increased. A microfluidics system was constructed, in which a **P2-5%** ES nanofiber filter membrane with an area of 3 cm² placed in the middle of a tube was used to rapidly absorb and sense Hg²⁺ in a solution flowing through the tube (**Figure 25c**). **Figure 25d** depicts the measured time-dependent variation in the solution conductivity. The prepared Hg²⁺ solution contained 1 ppm Hg²⁺ (6.3×10^{-3} M Hg²⁺ in 0.5 L of water) and the conductivity of the Hg²⁺ solution in its initial state (0 min) was 131.2 $\mu\text{S cm}^{-1}$. The

solution conductivity gradually decreased to 101.4 uS cm^{-1} . **Table 2** contains raw data on the conductivity changes over 20 min, and **Figure 25d** depicts C_t/C_0 (%) versus time (C_0 : original conductivity at 0 min; C_t : conductivity at time t). The solution conductivity decreased as the flow time increased, indicating that an increasing number of Hg^{2+} ions was absorbed by the **P2-5%** ES nanofiber membrane, yielding less Hg^{2+} in the solution. Thus, the 100% conductivity of the solution in its initial state (0 min) had decreased to 77.2% after 20 min. This rapid change in conductivity was caused by the high surface-to-volume ratio of the **P2-5%** ES nanofibers. The sensory filter membrane based on the **P2-5%** ES nanofibers specifically absorbed Hg^{2+} in an aqueous solution that contained a variety of metal ions and had a dual fluorescent chemosensory function for Hg^{2+} .

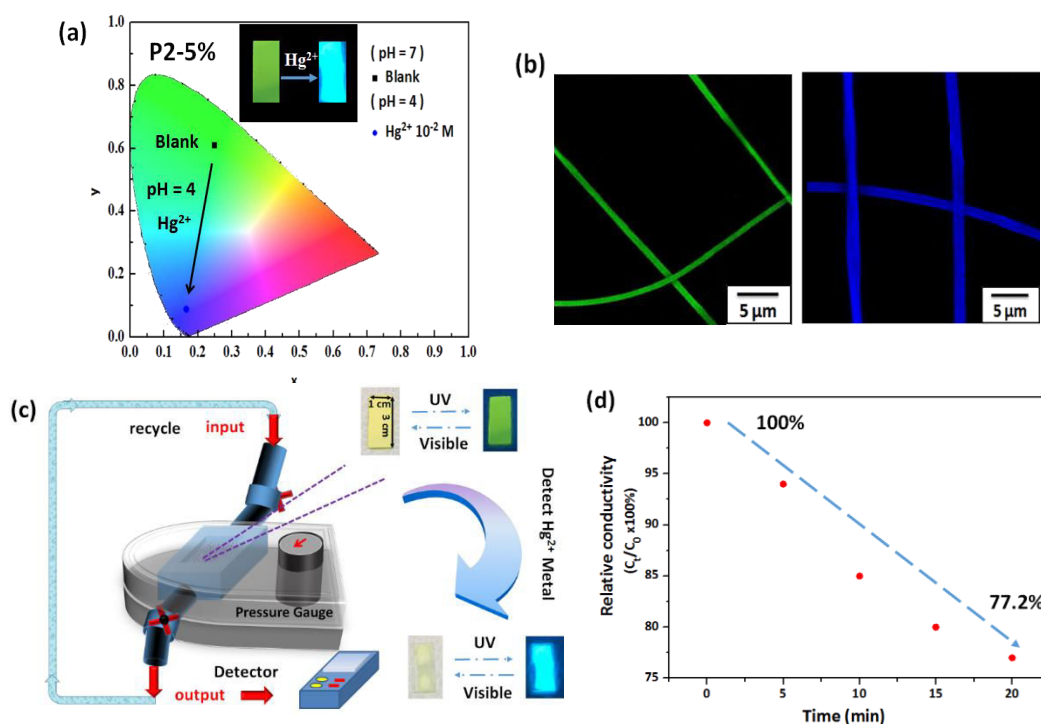


Figure 25. (a) CIE coordinates of **P2-5%** ES nanofibers in pH 7 aqueous solutions and after the detection of Hg^{2+} at 10^{-2} M aqueous solutions. (b) Confocal microscopy images of the ES nanofibers. All the inset figures show corresponding photographs recorded under UV light. (c) Schematic of a sensory filter microfluidics system for real-time metal ion sensing using an ES nanofiber membrane. (d) Relative conductivity versus time of the prepared Hg^{2+} solution in the microfluidics system.

Time (min)	Conductivity ($\mu\text{S}/\text{cm}$)
0	131.2
5	124.5
10	112.8
15	118.3
20	101.4

Table 2. Time-dependent solution conductivity of the prepared Hg^{2+} solution.

Figure 26a shows the saturation magnetization and coercivity of the **P2-5%** ES nanofibers-nanocomposite, which were determined using a vibrating sample magnetometer in the field range of $\pm 20,000$ Oe at 300 K. The results indicate that the **P2-5%** ES nanofibers exhibited magnetic properties, and the saturation magnetization was 4.8 emu g^{-1} . Moreover, the magnetic **P2-5%** ES nanofibers specifically adsorbed Hg^{2+} in an aqueous solution containing a variety of metal ions and had a fluorescent chemosensory response to Hg^{2+} (**Figure 25**). Thus, filter membranes based on the **P2-5%** ES nanofibers with porous architectures can specifically chelate with Hg^{2+} in an aqueous solution containing many types of metal ion and serve as fluorescent chemosensors for Hg^{2+} . These results could assist researchers in cleaning water while simultaneously chelating and sensing Hg^{2+} . In addition, rather than removal through alternative methods, a magnet can directly attract the **P2-5%** ES nanofibers because of the magnetism of the Fe_3O_4 NPs. The results in **Figure 26b** and **Figure 2c** indicate that **P2-5%** ES nanofibers have the potential for application in multifunctional sensory filter membrane devices for HTM ion chelation, temperature sensing, and magnetism. In conclusion, these copolymer inorganic NP-based sensory fibers have considerable potential for application in water purification sensing filters for the filtration of industrial wastewater with HTM, and may assist researchers in purifying water while simultaneously chelating and sensing Hg^{2+} ; moreover, used magnetic fluorescent switchable chemosensors can be collected using magnets (noncontact force).

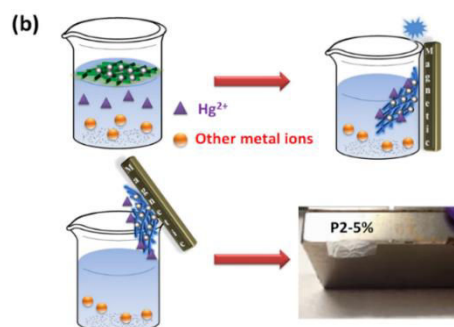
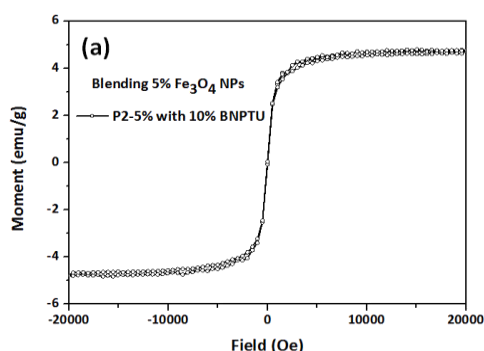


Figure 26. (a) Hysteresis loops of **P2-5%** ES nanofibers (5 wt % Fe₃O₄ NPs) measured at 25 °C. (b) Schematic of a filter sensory membrane prepared from **P2-5%** ES nanofibers composed of poly(NIPAAm-*co*-NMA-*co*-AA)), BNPTU, and Fe₃O₄ NPs blends to simultaneously chelate and sense Hg²⁺. A magnet can directly attract the **P2-5%** ES nanofibers because of the magnetism of Fe₃O₄ NPs.

2-8 Conclusions

Novel magnetic fluorescent switchable chemosensors for the simultaneous detection of temperature, magnetism, and Hg²⁺ based on fluorescent ES nanofibers were prepared using blends of poly(NIPAAm-*co*-NMA-*co*-AA), BNPTU, and Fe₃O₄ NPs by employing a single-capillary spinneret. The NIPAAm, NMA, AA, BNPTU, Fe₃O₄ NPs moieties were designed to provide thermoresponsiveness, chemical cross-linking, dispersion of Fe₃O₄ NPs, sensing of Hg²⁺, and magnetism, respectively. Cross-linked ES nanofibers maintained their structure in water and exhibited sensitivity toward temperature variations and Hg²⁺ because of the sufficient NMA composition. The fluorescence emission of BNPTU within the ES nanofibers exhibited strong selectivity toward Hg²⁺ with green emission in aqueous solutions without Hg²⁺ (thiourea-derived), shifting to blue emission in aqueous solutions with Hg²⁺ (imidazoline-derived)). The **P2-5%** ES nanofibers exhibited considerable blueshifts in photoluminescence spectra and enhanced emission intensity for detecting an extremely dilute concentration of Hg²⁺ (10⁻³ M). Furthermore, the LCST of the NIPAAm moiety in the **P2-5%** nanofibers showed a significant temperature-dependent variation in PL intensity due to fiber volume change (or hydrophilic to hydrophobic change), engendering distinct on–off switching of photoluminescence when the nanofibers were exposed to Hg²⁺. Furthermore, a magnet can directly attract the **P2-5%** ES nanofibers because of the magnetism of the Fe₃O₄ NPs, which serves as a substitute for removal through other methods. The present study demonstrated that the prepared magnetic fluorescent ES nanofibers can be used as naked eye sensors and have potential for application in multifunctional environmental sensing devices.

Chapter 3

Mechanically Robust Silver Nanowire–Polydimethylsiloxane Electrode Based on Facile Transfer Printing Techniques for Wearable Displays

3-1 Introduction

Transparent conducting electrodes (TCEs) are essential components and play a pivotal role in various optoelectronic devices such as solar cells, organic light emitting diodes, wearable displays, touch screens.^{128, 129} To date, the most of scientists are search for the suitable strategy using the transparent conductive materials instead of the indium tin oxide (ITO) since the poor mechanical flexibility, limited supply, high vacuum process of the ITO, which has been restricted its applications in electronics.¹³⁰ Several alternative nanostructured transparent conducting materials has been thoroughly explored and have attracted much attention in the past few years, such as graphene,¹³¹ carbon nanotubes (CNTs),¹³² and metallic nanowires.¹³³ In particular, metallic nanowire (MNW) possess high electrical conductivity, superior flexibility, and high optical transparency based on percolating networks characteristics, which can exhibit optoelectronic performances similar to the ITO-based electrodes. Thanks to the superior performance, the AgNWs are widely considered to be the optimal material for application in flexible electronics.

Transfer printing technology (TPT) provides a potentially promising platform for developing the materials assembly and micro-/nanofabrication applications in various optoelectronic devices through the transformational approach. The rapid progress in the recently has expanded the TPT capability in the range of materials for patterning and scope of applications enabled. Since the simplified processing steps, low fabrication costs, and simple patterning procedures enable achieved the various forms of

commercial printing and soft lithography with cost-effective manufacturing.¹³⁴⁻¹³⁶ The typical transfer printing has evolved promising approach to device fabrication from complex molecular scale materials, such as self-assembled thin films,¹³⁴⁻¹³⁶ nanotube and graphene,^{137, 138} functional polymer,^{139,140} and photoresists,¹⁴¹ to integrate the device structures (light emitting diodes (LEDs),^{142,143} solar cells,^{144,145} and complementary metal oxide semiconductor (CMOS) circuits.^{146,147} Based on the above examples, the new fabrication routes for the transfer printing can be illustrated including the multidimensional assembly,¹⁴⁸ large-scale of nanostructure materials,¹⁴⁹ and the active devices with flexible and lightweight characteristics.¹⁵⁰

3-2 Motivation

Transparent conductive electrodes (TCEs) are an essential component of various optoelectronic devices such as touch panels, flat panel displays, organic light-emitting diodes (OLEDs), and solar cells¹⁵¹⁻¹⁵⁶. Indium tin oxide (ITO) electrodes are widely used in a variety of applications; however, these electrodes are not cost-effective because of the high price of indium, and they exhibit limited flexibility (brittleness). To address these drawbacks, several alternative materials have been developed to replace ITO, including carbon nanotubes (CNTs),¹⁵⁷⁻¹⁵⁹ conductive polymers,^{158,159} graphene,¹⁵⁷⁻¹⁶⁰ metal nanowires,^{157,158,160} and hybrid electrodes.^{158,160,161} Among alternative electrodes, silver nanowires (AgNWs) have emerged as a quite promising candidate for flexible TCEs because of their excellent opto-electrical properties and outstanding mechanical flexibility.^{162,163} Recently, AgNWs have been adopted as components in various applications such as displays,¹⁶⁴ thin film transistors (TFTs),^{157,165} solar cells,¹⁶⁶ light-emitting diodes (LEDs),¹⁶⁷ touch panels,¹⁶⁸ and pressure sensors,¹⁶⁹ suggesting the advent of new flexible electrodes that are superior to ITO electrodes.

Stretchable electronics are evolving from a concept into a key branch of modern electronics. Polydimethylsiloxane (PDMS) is one of the most promising materials for

stretchable electronics because of its high biocompatibility, high ductility, and strong opto-electrical properties.¹⁷⁰ Stretchable conductors based on PDMS and conductive fillers (e.g., AgNWs) have been adopted as stretchable electric connectors.^{171,172} The vacuum filtration,^{173,174} and patterned PDMS stamp,¹⁷⁵⁻¹⁷⁷ are well-known effective methods for transferring AgNW TCEs on various flexible substrates. However, some methods can damage substrates or have poor feasibility on some substrates, whereas others exhibit low-quality AgNW patterns in uniformity or fidelity. Furthermore, such approaches must overcome the common difficulty of transference onto various arbitrary substrates, including hole structures and curved surfaces; this difficulty restricts the application of such approaches in high-performance structures and devices. Consequently, proposing a scalable and facile transfer method through which AgNW TCEs can be fabricated on planar and curved substrates without loss of electrical or mechanical properties while overcoming the aforementioned difficulty is a substantial challenge.

One development strategy for intrinsically stretchable electronics is fabrication on flexible substrates based on the prestretched method. Previous studies have employed this strategy to fabricate stretchable supercapacitors and organic solar cells.^{178,179} In each of these studies, organic device materials were deposited on a prestretched PDMS substrate. Releasing the prestrain induces compressive forces on films, thereby producing sinusoidal buckles that can accommodate the subsequent application of uniaxial tensile stress in the direction of the prestrain. However, despite these advances, developing an intrinsically stretchable electronic device that can be deposited onto diverse arbitrary substrates—thereby enabling the fabrication of the large-area, illuminated, conformable panels required for lighting applications—remains a challenge.

The schematic in **Figure 1** illustrates the attachment of a device to diverse nonconventional substrates (e.g., e-skins, balloons, round-bottomed flasks, and elastomeric textiles) while achieving high transference efficiency and protecting the device from delamination. We propose a novel concept with a sacrificial polymer material deposited on top of an AgNW electronic device based on water-assisted transferring printing technology, which can prevent looseness and detachment of AgNWs and sliding at the interface during the transfer process. Furthermore, the fabrication procedure is facile, inexpensive, and chemical free and uses commercially available materials; these factors render the coatings easily accessible as transparent electrodes for flexible device testing. By using this strategy, we optimized stretchable AgNW-PDMS electrodes that exhibited excellent opto-electrical ($9 \Omega/\text{sq}$, 82% at 550 nm, $\sigma_{\text{DC}}/\sigma_{\text{Op}} \approx 200$) and mechanical performance (tensile strain: 0% to 50%; flexibility: bending radius of less than 2 mm) compared with conventional methods. Moreover, we demonstrated the use of these electrodes for development of flexible textile-based light-emitting electrochemical cell (PLEC) electronics. The highest optimized luminance intensity of the textile-based PLECs was 58 cd m^{-2} at 7 V under 10% linear strain without damage to the electroluminescent properties. Thus, the innovative approach based on the water transfer printing (WTP) technique paves the way for practical applications of AgNWs in various arbitrary substrates, thereby further developing their potential for integration in novel textile-based PLEC systems. This research represents a major step toward the realization of flexible stretchable applications in wearable electronics.

3-3 Background and review of literatures

3-3-1 Typical Transfer Printing Methods

To date, the conventional transfer printing can be distinct categories by three parts as shown in **Figure 1**: I. Additive transfer II. Substrate transfer III. Deterministic assembly, respectively. All printing techniques utilize their own specific methods in order to achieve the highest efficiency performance. **I.** The **Figure 1(a)** illustrated using the patterned way to control adhesion between two intrinsically different substrates through the mold stamp with the surface chemistry. The many types of organic and inorganic materials can be effectively manipulated with various modality via the additive transfer. The transfer generally occurs between the entire ink layer and selected parts of it, which has been deposited on the surface of a stamp and target substrate. Inking of the stamp can be accomplished through a variety of methods from solution casting to physical vapor deposition as discussed on previous researches.^{180,181} The additive techniques endow a different functions on layers printed, such as the integrated device assembly or serving as etch masks for substrate processing.^{182,183} **II.** The **Figure 1(b)** are schematically shown the “subtractive transfer” methods for utilizing a stamp to retrieve the regions of the thin films. This promising printing modality directly employed the pattern an active layer or to open windows in etch mask, enabling access to underlying layers of materials for subsequent fabrication.¹⁸⁴ The first method of additive printing, chemical modification of the target substrate or the middle polymeric adhesion can assist the transfer efficiency between the stamp and ink.¹⁸⁵ In comparison with the additive printing, the “substrate transfer” methods have considered the additional engineering design on the cohesive fracture of the ink layer. In some instance, the subtractive transfer represents the linking step for the additive transfer process. The combination of the first and second methods can be developed and re-defined structures on a donor substrate for utilizing in deterministic assembly techniques, as shown in **III.**

Figure 1(c). This protocol is particularly powerful and valuable since its natural compatibility and dramatically expands the possibilities of the material in fabrication by separating growth and the inks procedure from the stamp and the target substrates. These methods provide a high-resolution large-area assembly technique with capabilities in two or three-dimensional layouts and in the integration of the material beyond the competency of other methods.

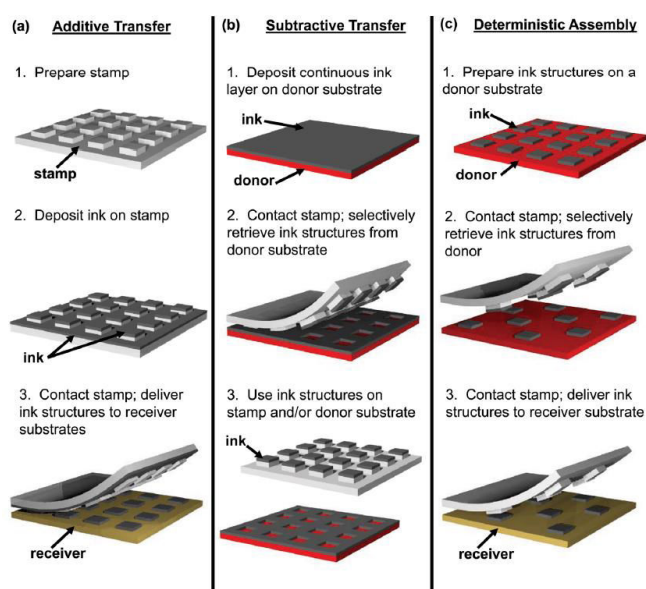


Figure 1. Schematic illustrations of three protocols for transfer printing. **(a)** Additive transfer demonstrate a stamp with “inked” material or physical transfer. Contacting such an inked stamp to a target substrate followed by peel-back effects transfer of material. **(b)** Subtractive transfer begins with a continuous thin films deposited on a donor substrate. A stamp brought into contact with the film selectively removes material in the areas of contact, leaving behind a patterned film on the donor and transferred material on the stamp. **(c)** Deterministic assembly involves the stamp contact between the donor substrate and pre-fabricated micro or nanostructures. Peeling the stamp away leads to removal of selected structures from the donor substrate and transfer to the target substrate. In all three cases, chemical, thermal, and mechanical strategies promote the inking and printing processes, thereby enabling the highly effective procedure.

3-3-2 Inorganic Semiconductors

The one-dimensional metal nanowire have recently been used to fabricate TCEs and provide an interesting promising properties in electronic and optoelectronic. The possibility of techniques to manipulate the size, structure, and nanowire networks morphology enable serve as building blocks for various applications in the fields of electronics,^{186,187} sensors,^{188,189} and energy conversion.^{190,191} Although those superior features can integrate the precise control the nanowires over size and position in their configurations. An alternative approaches facilitated the well-organized assembly with separate steps of synthesis. The CVD growth with ordered catalyst arrays approach can be prepared by different techniques such as electron-beam lithography, nanosphere lithography, AFM lithography, nanoimprint lithography, and self-assembled templates.¹⁹²⁻¹⁹⁴ Xiao and De et al reported that using the " subtractive transfer" enable transfer of silver nanowire films to flexible substrates based on the vacuum filtration as shown in the **Figure 2**.^{173,174} Madaria and Choil reported that using a dry-removal soft lithography based on the patterned PDMS stamp to retrieve porous silicon microstructures from a donor substrates as shown in the **Figure 3**.¹⁷⁵⁻¹⁷⁷ However, some methods not only suffers from a long fabrication time and are inherently chemical-intensive process but also request careful and exhaustive transfer techniques, whereas others exhibit low-quality AgNW patterns in uniformity or fidelity. Furthermore, such approaches must overcome the common difficulty of transference onto various arbitrary substrates, including hole structures and curved surfaces; this difficulty restricts the application of such approaches in high-performance structures and devices. Consequently, proposing a scalable and facile transfer method through which AgNW TCEs can be fabricated on planar and curved substrates without loss of electrical or mechanical properties while overcoming the aforementioned difficulty is a substantial challenge.

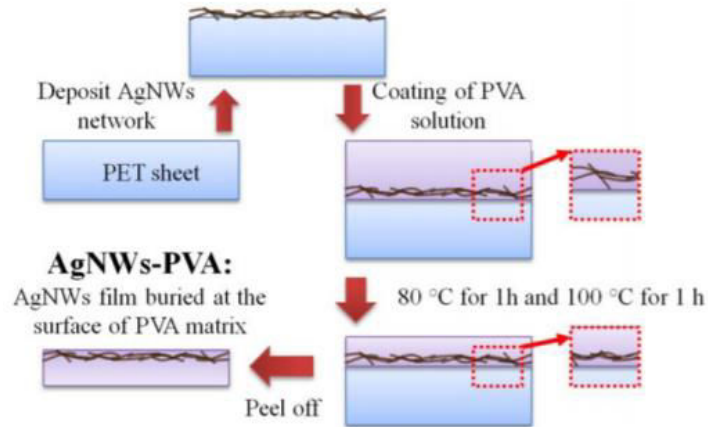


Figure 2. The Schematic Diagram of fabricating AgNWs film buried at the surface of PVA matrix. The incompact AgNWs network is consolidated as the PVA is dried.

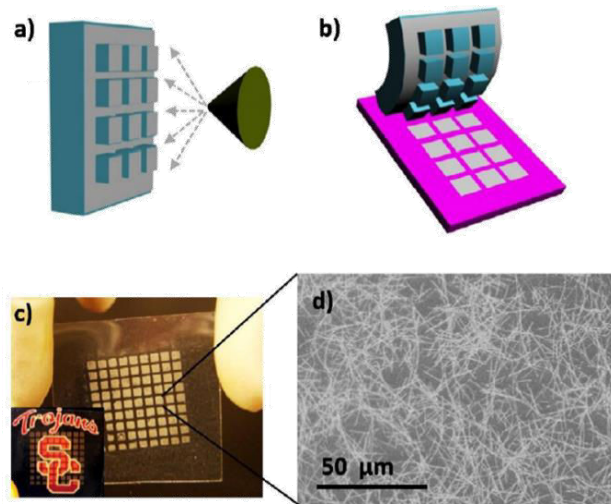


Figure 3. The fabrication of patterned transfer of silver nanowire film. (a) Ag nanowire solution was sprayed uniformly on the patterned PDMS stamp. (b) Schematic diagram of the transfer of Ag nanowire from the patterned PDMS stamp to the target substrate. (c) Photograph of a patterned nanowire film transferred on the PET substrate. The size of each pixel is 1 mm × 1 mm with a spacing of 0.5 mm. Inset shows that the patterned nanowire film is highly transparent on pixel. (d) SEM image of the nanowire network from one pixel.

3-4 Experimental section

3-4-1 Materials

Polydimethylsiloxane (PDMS; DOW-CORNING, SYGARD-184AB), polyvinylpyrrolidone (PVP; Alfa Aesar, Mw \approx 1,300,000), silver nanowire (AgNW; diameter: 55–75 nm, length: 10–20 μ m; Zhejiang Kechuang, AW060), poly(3,4-ethylenedioxythiophene):polystyrene sulfonate (PEDOT:PSS; UniRegion Bio-Tech, UR-PH1000) were stored at 4 °C prior to use. Poly[9,9-dioctylfluorenyl-2,7-diyl] (PFO; American Dye Source, ADS129BE) and lithium trifluoromethanesulfonate (LiTf; 99.995%) were stored in a vacuum prior to use. Isopropyl alcohol (IPA; anhydrous, 99.5%), zonyl fluorosurfactant (Zonyl FS-300; Fluka), chlorobenzene (CB; anhydrous, 99.8%), methanol (HPLC, 99.9%), dimethyl sulfoxide (DMSO; anhydrous, 99.9%), and eutectic gallium-indium (EGaIn; 99.99%), were purchased from Sigma-Aldrich. ITO films (thickness 150 nm, 15 Ω /sq) sputtered onto PET substrate with a thickness of 150 μ m. All materials were used as received.

3-4-2 Preparation of AgNW Dispersion

AgNWs suspended in IPA at a concentration of 0.66wt% were purchased from Zhejiang Kechuang Inc. Each nanowire was 10–20 μ m in length and 55–75 nm in diameter, as provided by the supplier. The AgNW solution was diluted with IPA to a concentration of 0.066 mg mL⁻¹ and sonicated for a further 30 min before use.

3-4-3 Fabrication of WTP Stretchable Conductive Electrodes

The PVP (200 mg mL⁻¹) was dissolved in methanol and stirred overnight. The polymer solution was deposited on the PET substrate by a spin-coater at 2000 rpm for 30 s. The PDMS solution was mixed with a curing agent at a ratio of 10:1 and stirred for 15 min. To avoid air bubbles in the solution, the solution was placed in a vacuum

chamber for 10 min prior to use. Subsequently, the PDMS solution was coated on the top of the PVP surface and cured for 1 h at 70 °C. Before the AgNWs were sprayed, the cured PDMS was treated with oxygen plasma for 60 s. The AgNWs (0.066%) were then dispersed in isopropanol and added to the container. The air brush of a spray gun (FUSO SEIKI, 033G-Double Action) was set at 45 psi with a spraying distance of 10 cm from the surface of the PDMS membrane. Dispersion of the AgNWs was distributed over different durations (5, 15, and 30 s). The surfaces of target substrates, including skin, a balloon, a round-bottomed flask, and an elastomeric textile, were moistened with DI water to enable the water surface tension to stretch the sacrificial layer flat on the moist surface during the WTP process.

3-4-4 WTP Stretchable Conductive Electrode Integrated with Wearable Textiles

The integration process of a wearable PLEC device with elastomeric textiles (Fig. 5). Elastomer adhesive tape [3M VHB 4905 tape (3M elastomer)] and elastomeric textiles provided by Taiwan textile research institute were used as received. 3M elastomer was used to seal the device. Subsequently, the device was reversed to adhere to the elastomeric textiles.

3-4-5 Stretchable and Wearable Textiles in the PLEC Device

The PEDOT:PSS (UR-PH1000 with 5% DMSO mixed with 1 vol% Zonyl FS-300 fluorosurfactant) was filtered using a 0.45- μ m polytetrafluoroethylene (PTFE) syringe filter prior to use. The PEDOT:PSS was spin-coated on the AgNWs-PDMS electrode through a consecutive two-step process at 1000 and 2000 rpm each for 60 s and then annealed at 70 °C for 30 min in air. After cooling, the chlorobenzene solution containing the mixture of PFO, LiTf, and PEO at a total concentration of 16 mg/mL was spin-coated onto the PEDOT:PSS layer at 2000 rpm for 30 s to form the emitting layer. The

textile was prestretched by 20% using a fixture. Meanwhile, the buckle of the device was generated against the deformation by stretching. Subsequently, an EGaIn cathode was deposited onto the surface of the emitting layer by using a syringe. 3M elastomer was used to seal the device through attachment to the prestretched elastomeric textiles. The elastomeric textiles were further measured using a PR-670 spectroradiometer and Keithley 2400 source meter.

3-5 Device Characterization

Transmittance spectra were recorded using a Shimadzu ultraviolet–visible spectrophotometer. The morphologies of the membrane and the distribution of the nanowires were characterized using scanning electron microscopy (SEM; Hitachi S-520). Samples were coated with platinum prior to SEM characterization, and analysis was performed at an acceleration rate of 15 kV. The surface roughness was measured by atomic force microscopy (AFM, Park Systems, XE-100TM, USA). The contact angle was measured using an FTA125 contact angle analysis system (FTA, America). Water droplets (approximately 2 mL) were dropped onto the samples. The average contact angle of each sample was calculated by measuring five positions on the same sample. The nanowires on the PDMS membrane were annealed in air on a hot plate at 100 °C for 10 min with various spray durations between 5 and 30 s after plasma treatment (NELTA, TPO4). The sheet resistance of the AgNW-PDMS electrode was measured using a four-point probe technique and a Keithley 2400 source meter. Bending and strain sensor tests were conducted using lab-made apparatus and software to record film resistance and the number of cycles. Sheet resistance measurements were conducted at various bending angles (30° to 330°) by attaching four probes at the corners of the films with copper tape (Supplementary Movie S1 in the ESI†). The volume of the balloon shrink–expand cycle apparatus was customized (Fig. 4d), and the sheet resistance of the AgNWs-PDMS electrode was measured using a four-point

probe technique and a Keithley 2400 source meter. The AgNWs-PDMS electrode was attached to the plastic glove by using the WTP method and the circuit was completed using a blue-colored LED (Supplementary Movie S2 in the ESI†). The PLEC devices were characterized using a Keithley 2400 source meter and a silicon photodiode to measure the current–voltage and luminance–voltage characteristics. The silicon photodiode was further calibrated using a photo research PR-670 spectroradiometer. The external quantum efficiency (EQE) was calculated using a Lambertian emission profile. EL spectra were collected using the PR-670 with neutral density filters, which provided attenuation down to 3% within the visible wavelength region.

3-6 Results and discussion

3-6-1 Designing New Transfer Methods by using WTP Technique

The WTP technique and fabrication procedure are schematically illustrated (**Figure 1**). The technology was designed with an ultrathin polymer film as the sacrificial layer for transfer onto various arbitrary substrates based on the hydrophilic characteristic. The key feature of the layer is the ease with which it can be wrapped around the membrane formed on the surface of the target substrate. The interfacial adhesion between the donor, sacrificial layer, and receiver requires strength for fabrication but weakness for the release process. The substrate release process should be carefully performed in a stable manner to protect the device from damage and maximize transfer efficiency. Notably, we developed a novel green chemical transfer process that, in contrast to the solvent etchable-organic transfer process, does not require an organic solvent and applies negligible mechanical and thermal stress to the target substrate^{173,196}. Notable methods with high reliability and high efficiency (**Figure 1a**). In our design, polyvinylpyrrolidone (PVP) is used as the sacrificial layer that can be transferred onto the target substrate through dissolution in deionized (DI) water.

PDMS serves as a flexible framework between the PVP and AgNWs because of its flexibility, robustness, and transparency property, and it is highly desirable for gripping surface, from polished smooth surfaces to highly rough substrates. Notably, the transfer yield is nearly 100%, regardless of feature geometries and materials. Furthermore, when the WTP method is used to transfer the AgNW-PDMS electrode, the electrical properties of the electrode are preserved owing to the flexible PDMS framework between the substrate after the transfer. In addition, the WTP method is rapid; an AgNW-PDMS electrode can be separated from a donor substrate in 3–4 s in water at room temperature. Finally, we successfully developed a new transfer process that is simple and yields high adhesion to any nonconventional substrate, (**Figure 1b**). The stretchable conductive electrode was transferred to various target substrates, namely skin, a balloon round-bottomed flask, and an elastomeric textile.

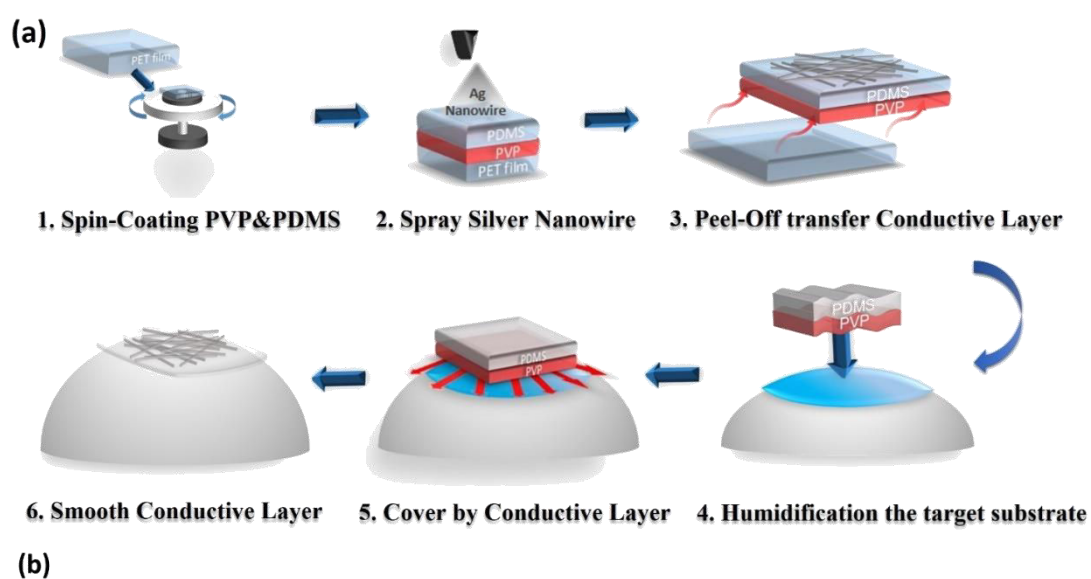


Figure 1. Schematics of the WTP process for AgNW TCEs. (a) (i) Prefabricated sacrificial layer (PVP) and flexible framework (PDMS); (ii) spraying of AgNWs on the top of PDMS after plasma treatment; (iii) transferred nanowire devices on a prehumidification target substrate with a sacrificial layer in between. (b) Corresponding photographs of various nonconventional substrates, including skin, a balloon, a round-bottomed flask, and an elastomeric textile.

3-6-2 Electrical and Mechanical Properties of Conductive Electrode

The developed transfer process for AgNWs is closely related to the surface characteristics and morphologies of a substrate. The nanowire densities were controlled by varying the spray time between 5, 15, and 30 s after plasma treatment. Through application of the plasma technique, the adjacent AgNWs are well-dispersed, and homogenous random distribution is achieved, in contrast to the pristine AgNW-PDMS (**Figure 2a, b, c and d**). Furthermore, the rapid increase in the density of the AgNW can be attributed to the interface between the nanowires and PDMS surface (**Figure 2 e and f**). The contact angle for pristine AgNW-PDMS was 98° , and this decreased to 8° after plasma treatment; this marked decrease illustrated that plasma treatment extensively changed the surface energy of the PDMS from a hydrophobic to a hydrophilic surface owing to the silanol group¹⁹⁷. Conventional fabrication methods that use the vacuum filtration process suffer from long fabrication times and are inherently chemical-intensive processes that require extremely careful and exhaustive transfer techniques.^{160, 173,176,198,199} By contrast, the flexible conductive membrane fabricated using an all-spray-coating process alongside the WTP concept has the advantage of an extended integration environment. First, fabrication can be conducted on arbitrary areas and various geometrical features in a selective manner. Second, no additional process is required between the chemical surfactant and nanowires. Third,

spray coating for a short period reduces the fabrication time and minimizes any possible damage to the substrate.

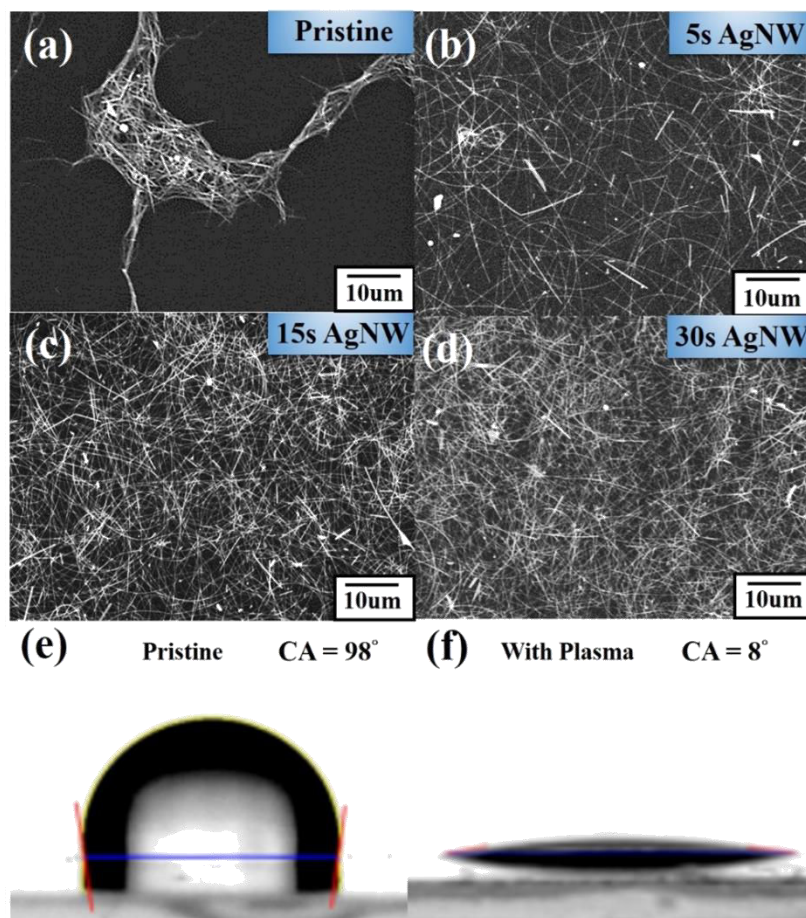


Figure 2. SEM images of (a) spraying AgNW on an untreated PDMS substrate and (b)–(d) spraying AgNW on a plasma-treated PDMS substrate from 5 to 30 s. The inset pictures (e)–(f) show the different contact angles before and after plasma treatment.

In this study, various AgNW films were deposited to analyze sheet resistance behavior with transmittance. **Figure 3a** shows the relationship between transmittance and sheet resistance with respect to variation in the AgNW-deposited electrodes; the figure inset plots optical transmittance as a function of the sheet resistance for each spray time. As expected, AgNW-PDMS-30 (i.e., note that AgNW-PDMS-30, is designated as prepared silver nanowire by spraying 30s onto the PDMS flexible

framework after plasma treatment) with a higher nanowire density yielded higher optical transmittance and lower sheet resistance. The optimized values for sheet resistance and transmittance were $9 \Omega/\text{sq}$ and 82% at 550 nm, respectively; these values represent a significant improvement in sheet resistance compared with previous AgNW-based electrodes on PDMS (T~80%, $35 \Omega/\text{sq}$),²⁰⁰ (T~80%, $19 \Omega/\text{sq}$),²⁰¹ and (T~80%, $20 \Omega/\text{sq}$).²⁰² To optimize the highly conductive ultrathin AgNW films, we fixed the back pressure at 45 psi as the optimal parameter for increasing drop across the nozzle; this resulted in high fluid velocity with the airbrush nozzle. These effects should help the liquid dispersion to break into smaller ligaments and droplets.²⁰³ By contrast, we attribute the increase in conductivity after annealing to the favorable contact and fusion between the nanowires. The scanning electron microscopy (SEM) image (**Figure 3b**) shows the AgNW films on PDMS with multiple spray times between 5 and 30 s. The estimated numbers of AgNWs in the $2.4 \text{ cm} \times 1.4 \text{ cm}$ PDMS film regions were counted as 12.4 ± 1.8 ($0.002 \text{ mg}/\text{cm}^2$), 548.2 ± 12.3 ($0.055 \text{ mg}/\text{cm}^2$), and 1160.5 ± 42.8 ($0.11 \text{ mg}/\text{cm}^2$). In addition, the observed melting and fusion of nanowires led to superior contact between them, which further reduced the contact resistance between them, resulting in highly conductive nanowire films. The image (**Figure 3d**) shows that the nanowires formed a percolated network that became denser with increasing spray time, thereby demonstrating the application of this method for obtaining AgNW films of various transmittances for various applications. In general, the transparent conducting films are related with the transmittance and sheet resistance by using figures of merit (FoM). The FoM is often calculated related by the equation as following:²⁰⁴

$$T(\lambda) = \left(1 + \frac{Z_0}{2R_s} \frac{\sigma_{Op}}{\sigma_{DC}}\right)^{-2} \quad (1)$$

Where Z_0 is the impedance of free space (377Ω), σ_{Op} is the optical conductivity and σ_{DC} is the DC conductivity of the films, respectively (note that in this expression the DC conductivity, σ_{DC} , is taken to be the bulk conductivity, i.e., that of a thick film/network) Generally, transmittance of at least 80% in the visible light range is necessary for a conductor to function with the present electronic device requirements. Therefore, σ_{DC}/σ_{Op} at high transmittance is particularly crucial, and corresponds to films with high σ_{DC} and low σ_{Op} (**Figure 3c**). The optimum value of σ_{DC}/σ_{Op} approached as high as 200 for $T \approx 82\%$. Notably, the transmittance and sheet resistance result was far superior to corresponding results for other reported transparent conductors (**Table 1**). Moreover, previous reports have suggested that networks of AgNWs yield a value of $\sigma_{DC}/\sigma_{Op} \approx 75$.¹⁷⁵ However, such studies have been restricted from optimizing the high value of σ_{DC}/σ_{Op} by the PDMS stamp transfer method. We speculate that in each such study, the transfer process has a few drawbacks owing to the mechanical and adhesive problem between the AgNWs and polyethylene terephthalate (PET) substrate. By contrast, our spray coating AgNW fabrication technique based on the WTP method not only directly overcame the AgNW adhesion problem but also further optimized the ultrathin diameter with a high aspect ratio and facilitated formation of uniformly interconnected nanowire networks.

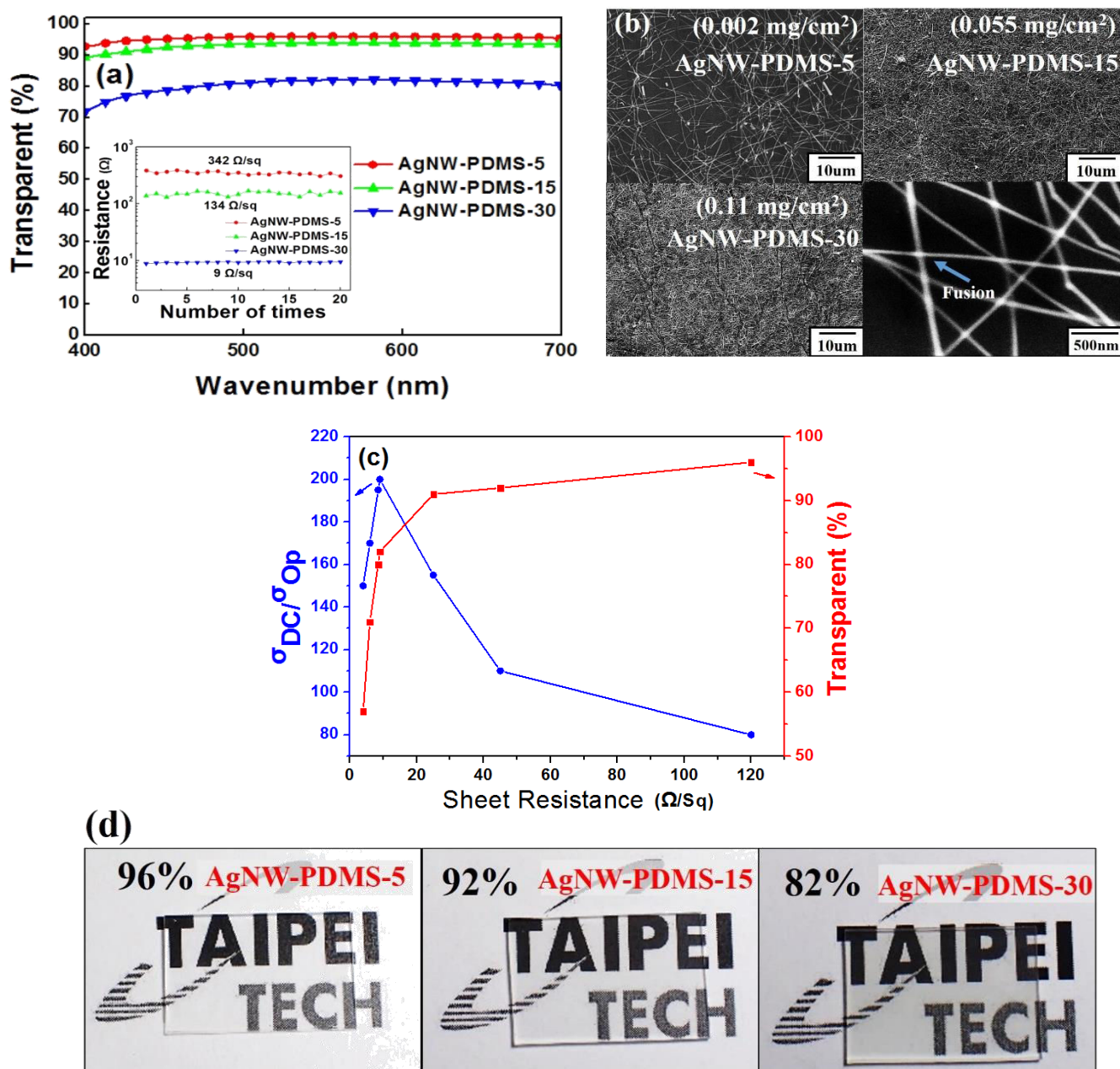


Figure 3. Visual transparency, electrical properties, and SEM characterization of electrodes. (a) Optical transmittance curves of the AgNW-PDMS electrode prepared with different spray durations as a function of the wavelength. The insets show the average sheet resistance for various spray durations. (b) SEM images of the AgNW-PDMS electrode prepared using various spray durations; the blue arrow indicates apparent welding between AgNWs. (c) σ_{DC}/σ_{OP} value plotted with sheet resistance and transmittance (at 550 nm). (d) Photographs of various AgNW-PDMS electrodes with corresponding transmittance values of 96%, 92%, and 82%.

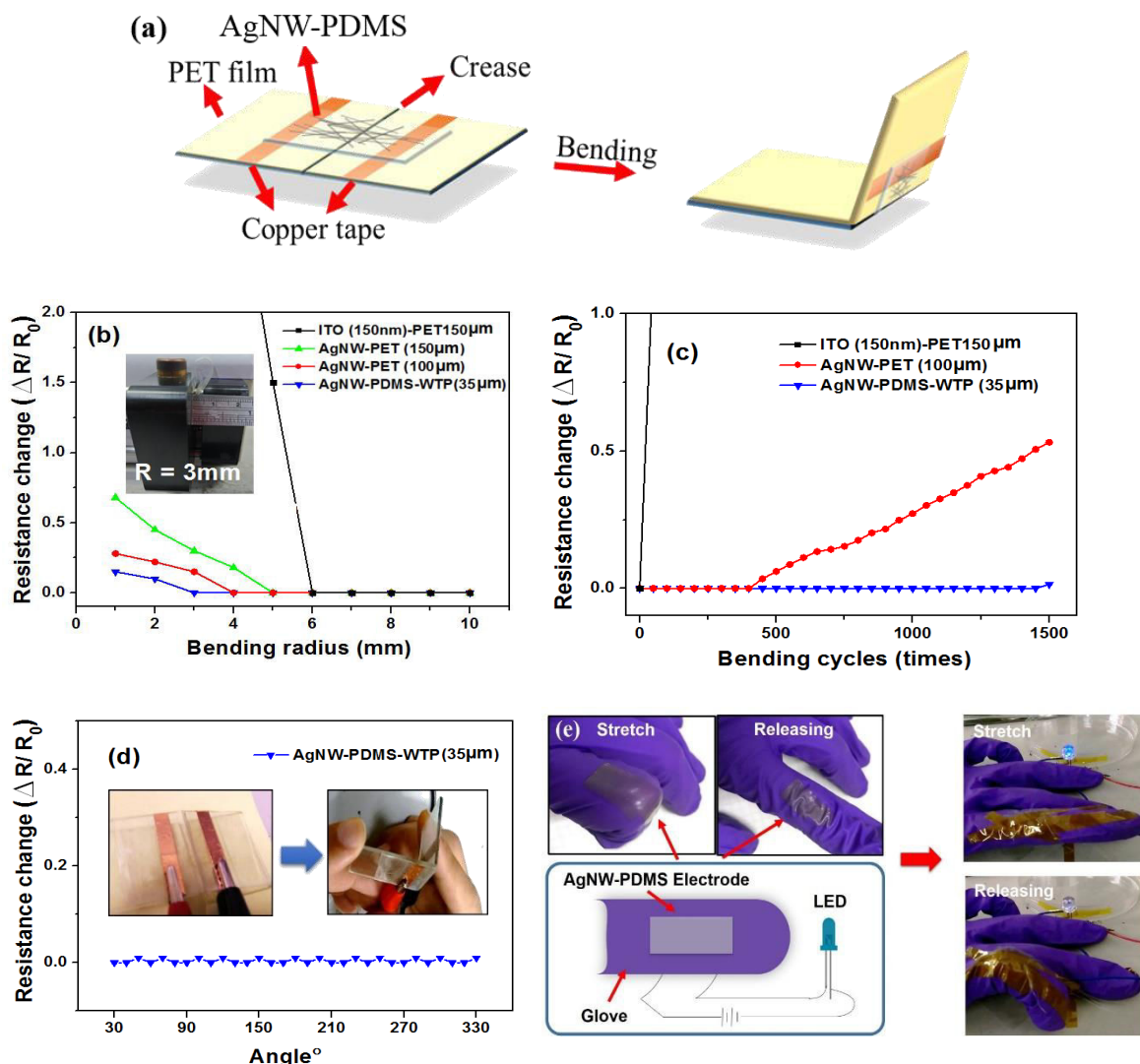
Table 1. Comparison of the sheet resistance and the optical transmittance between the reported transparent AgNW films and the AgNW-PDMS composite films.

Structure	Sheet resistance (Ω)	Transmittance (%)	References
AgNW-PVA film	69	87	24
AgNW-PET film	33	85	25
AgNW-PDMS film	35	80	34
AgNW-PDMS film	19	80	35
AgNW-PET film	20	83	36
AgNW-PDMS film	20	83	39
AgNW-PDMS film	9	82	Ours

Mechanical flexibility is another key factor of transparent electrodes for next-generation stretchable and wearable electronics. We demonstrated a custom-built process with a new bending platform and achieved ultimate flexibility, including the bending and folding capabilities of the AgNW-PDMS electrode. As shown in **Figure 4a**, the AgNW-PDMS electrode was transferred to the PET substrate through our WTP method. Sheet resistance measurements were performed at various bending angles by attaching a four-point probe at the corner of each film with copper tape. **Figure 4b** compares changes in the sheet resistance of electrodes, including ITO film (thickness 150 nm) on PET (thickness 150 μm), AgNW coating on PET substrate (thickness 150 μm and 100 μm), and AgNW embedded PDMS electrode (thickness 35 μm) with WTP method, as a function of the bending radius. (i.e., note that the thickness for AgNW films is 5 μm). The resistance change is expressed as $\Delta R/R_0$, where ΔR is the actual change in resistance after bending and R_0 is the initial value. As the AgNW-PET substrate thickness decrease from 150 μm to 100 μm , the threshold value was declined

from 5 to 4 mm, thus exhibited fairly high mechanical flexibility with a low $\Delta R/R_0$ value and also demonstrated the key factor of electrical conductivity performance is associated with the substrate thickness. By contrast, the threshold value for the ITO film on PET substrate began to crack as the bending radius approached 6 mm, resulting in a drastic increase in the $\Delta R/R_0$ value. Deposition of ITO as an additive thin film resulted in a brittle oxide layer that could easily crack from low strain. Notably, our present the WTP method was not only efficient as the bending radius approached 3 mm; it also attained an extremely low $\Delta R/R_0$ value and was far superior to those obtained in recent studies (≈ 4.8 mm).²⁰⁵ We speculated that these benefits were attributable to our design of a PVP sacrificial layer and PDMS flexible framework. Under extreme bending, the sacrificial layer avoided the AgNW network that was in direct contact with the received substrate. The flexible framework prevented looseness and detachment of the AgNWs and sliding at the interface. In addition, the AgNW-PDMS electrode exhibited excellent bending fatigue strength (**Figure 4b**). Under a radius of curvature of 4 mm, the $\Delta R/R_0$ value of the AgNW-PDMS electrode fabricated with the WTP method began to increase after only 1000 bending cycles, and it had increased by 1.5% after 1500 cycles. By contrast, the corresponding values of the ITO film on PET substrate (eight-fold after 30 bending cycles) and AgNW-PET substrate (thickness 100 μm) (two-fold after 450 bending cycles) markedly increased. Twisting is another significant requirement for testing whether TCEs can maintain their conductivity under a rigorous or deformation environment. As indicated in **Figure. 4d**, the original value of $\Delta R/R_0$ was approximately maintained under various twisting angles. Our optimized $\Delta R/R_0$ values under twisting was exhibited significantly enhanced performance compare to the recent studies.²⁰⁵ Furthermore, we customized a stretchable AgNW-PDMS electrode onto a plastic glove by using the WTP method. The 2-cm-long device was assembled with an external circuit on an LED device, (**Figure. 4e**). The LED flashed on when the voltage

source was connected to the electrode during the five stretching and releasing cycles between 0° and 90° . This phenomenon demonstrated the device's excellent conductivity, even under extreme bending conditions, as well as its suitability as an electrode for flexible electronics. In addition, we further explored practical applications and developed our stretchable electrode for the detection of human motion. **Figure 4f** illustrates the behavior of the electrode during the first eight bending and releasing cycles between 0° and 90° . When the finger bent, the resistance gradually increased from $\sim 20 \Omega$ to a maximum of $\sim 45 \Omega$. A fully reversible and rather stable change of resistance between ~ 20 and $\sim 45 \Omega$ was observed in the subsequent cycles, corresponding to the bending or releasing of the finger. Therefore, the sensor can be employed for accurate motion detection of finger joints and could be used in e-skin for robots.



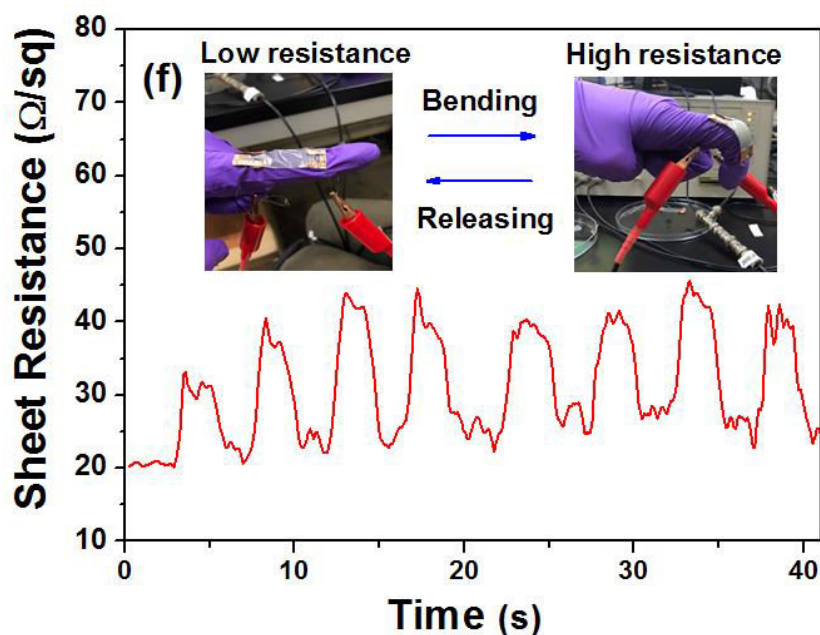
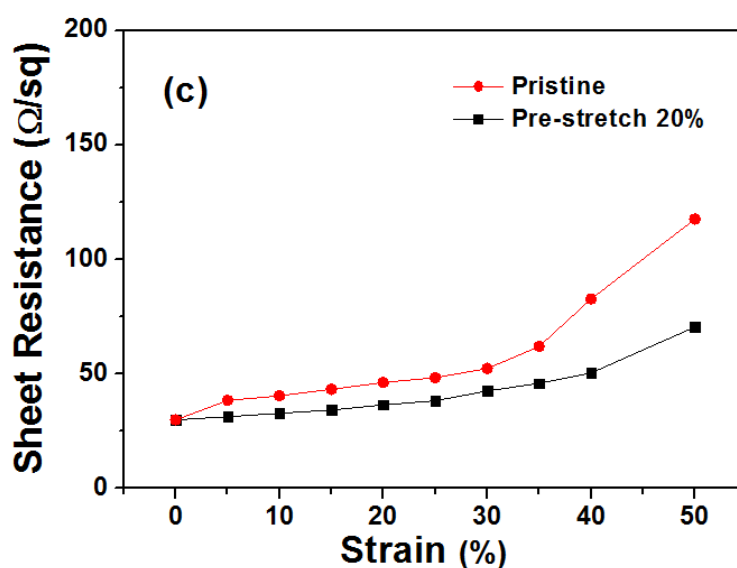
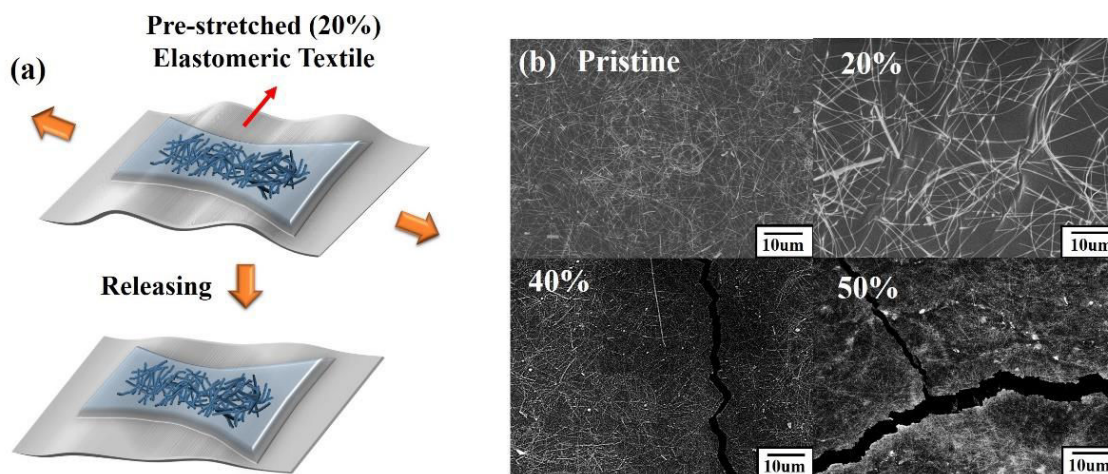


Figure 4. Application of AgNW-PDMS electrodes in semitransparent and wearable LEDs under extreme deformation. (a) Schematics of bending test. (b) Relative change in the resistances of ITO (thickness 150 nm) on PET (thickness 150 μm), AgNW on PET (thickness 150 μm and 100 μm), and the AgNW-PDMS electrode (thickness 35 μm) with the WTP method as a function of the bending radius. The inset shows a photograph of a folded AgNW-PDMS flexible transparent electrode fabricated using the WTP method with a bending radius of 300 μm set for the bending test. (c) Relative change in the resistances of ITO (thickness 150 nm) on PET (thickness 150 μm), AgNW on PET (thickness 100 μm), and the AgNW-PDMS electrode (thickness 35 μm) with the WTP method as a function of bending cycles at a bending radius of 4 mm. (d) Plot of the sheet resistance of the AgNW-PDMS electrode (thickness 35 μm) and photographic image versus bending angles between 0° and 330°. (e) Schematics of the AgNW-PDMS electrode combined with a blue LED circuit on a plastic glove. The inset shows photographs of the blue LED circuit in various folding states. (f) Detection of finger joint motion by the AgNW-PDMS electrode.

To enhance the mechanical durability of deformable AgNW-PDMS ($9 \Omega/\text{sq}$) electrodes, a strain engineering process must be developed to form a serpentine-like structure that can prevent degradation of electrical properties during plastic elongation (**Figure 5a**). The serpentine AgNW-PDMS electrode based on the WTP method was transferred on a prestretched (20%) elastomeric textile to form a buckle microstructure prior to testing.²⁰⁶⁻²⁰⁸ As indicated in **Figure 5c**, the AgNW-PDMS electrode exhibited stable conductivity when subjected to stretching of up to 40% strain without significant electrical loss corresponding to the pristine substrate (without prestretching). This excellent electrical performance was attributed to a geometrical feature of the AgNW-PDMS electrode, namely that much of the stress is relieved by the prestretched elastomeric textile regions as heavy strain is induced in a low-density AgNW network. Furthermore, individual nanowires can slide during the stretching and release of the AgNW-PDMS electrode, thereby providing excellent resistance to stretching fatigue.²⁰⁹ The field emission SEM image (**Figure 5b**) shows that the width and density of the microcracks increased with the applied strain, forming large cracks or a fine ligament network of AgNWs under higher strain. The prestretched elastomeric textile was further elongated in a specific direction to form stable contacts with AgNWs and avoid detachment from the underlying PDMS during stretching under a specific level of strain. Moreover, we demonstrated the feasibility of using our WTP-fabricated AgNW-PDMS electrode to develop a novel reversible conductive measurement for deformable electronics, as schematically illustrated in **Figure 5d-e**. To test this feasibility, we first attached our fabricated deformable AgNW-PDMS electrode onto the surface of a 300- μm thick latex balloon through the WTP method, which was then subjected to three-dimensional (3D) volume expansion and contraction. The device was expanded and contracted when suitably mounted on the balloon surface without observable mechanical delamination. As indicated in **Figure 5e**, AgNW-PDMS electrode

conductivity was measured by injection and retraction with a syringe to conduct the cycle test during volume expansion of the balloon from 5 to 30 mL. The device exhibited superior electrical properties with a low $\Delta R/R_0$ value, even when the balloon's volume expanded to 112% (30 mL), suggesting that the 3D strain on the AgNW-PDMS electrode underwent negligible resistance changes. Hence, to the best of our knowledge, the present study was the first to demonstrate an AgNW-PDMS electrode applicable to dynamic 3D surfaces for realizing real-time conductivity monitoring. Furthermore, our deformable devices have potential for extensive application in biomedical electronics for sensing and signal-processing circuits.



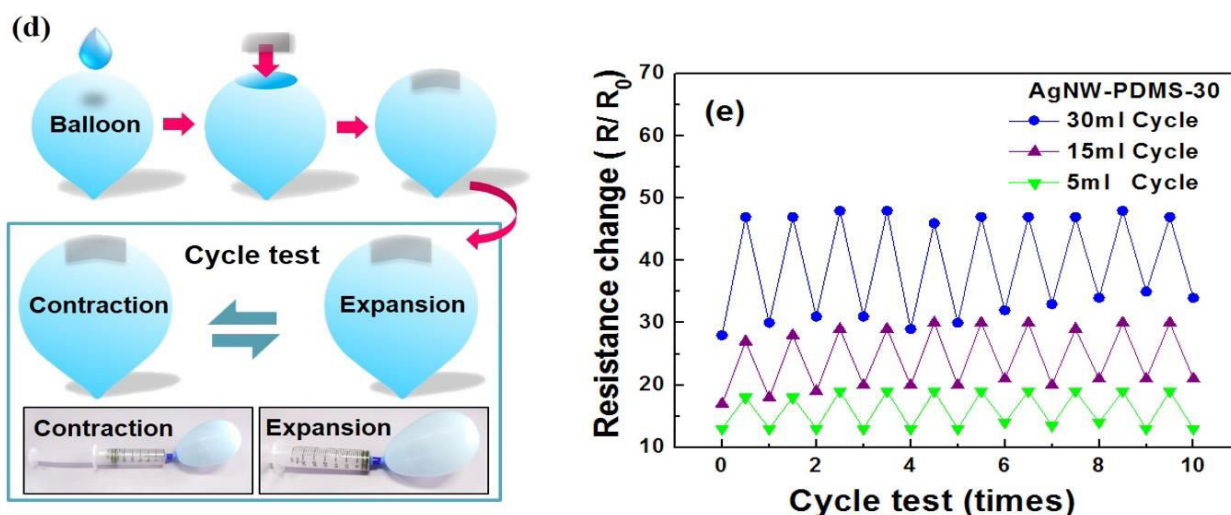


Figure 5. Demonstration of real-time conductivity monitor with the deformable AgNW-PDMS electrode. (a) Schematic of the prestretching and releasing strategy with the AgNW-PDMS electrode (prestretch: 20%) based on the WTP method. (b) SEM morphology of the AgNW-PDMS electrode under various strain stretched states from pristine to 20%, 40%, and 50%. (c) Strain-dependent electrical resistance of the AgNW-PDMS electrode with and without prestretching in various stretching tests. (d) Schematic of the deformable AgNW-PDMS electrode fabricated using the WTP method mounted on the dynamic surface of a balloon to realize the cycling test through expansion and contraction. (e) Cycle test of electrical resistance with the AgNW-PDMS electrode attached to the balloon through expansion and contraction. The insets show corresponding photographs of the expansion rate of the balloon from 112%.

3-6-3 Textile-Based WTP PLEC Devices

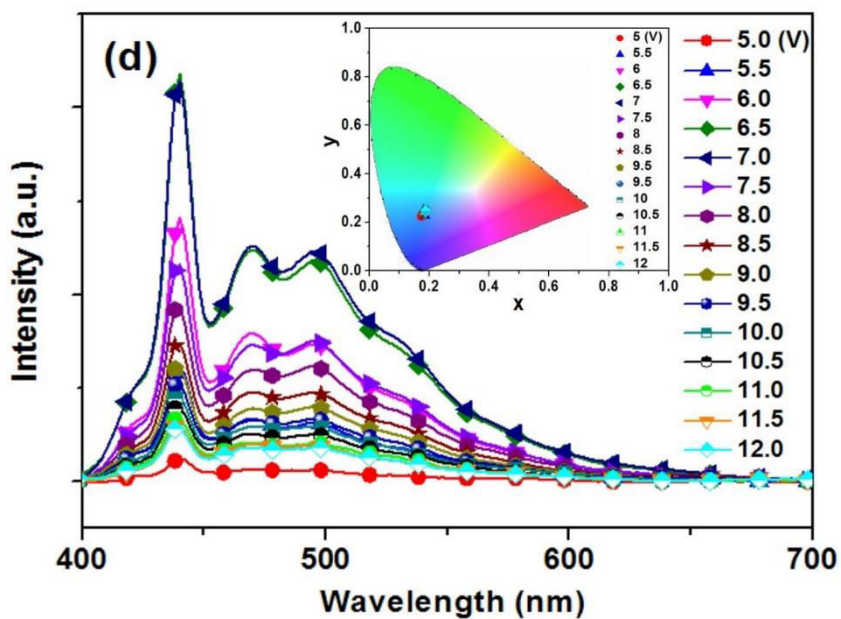
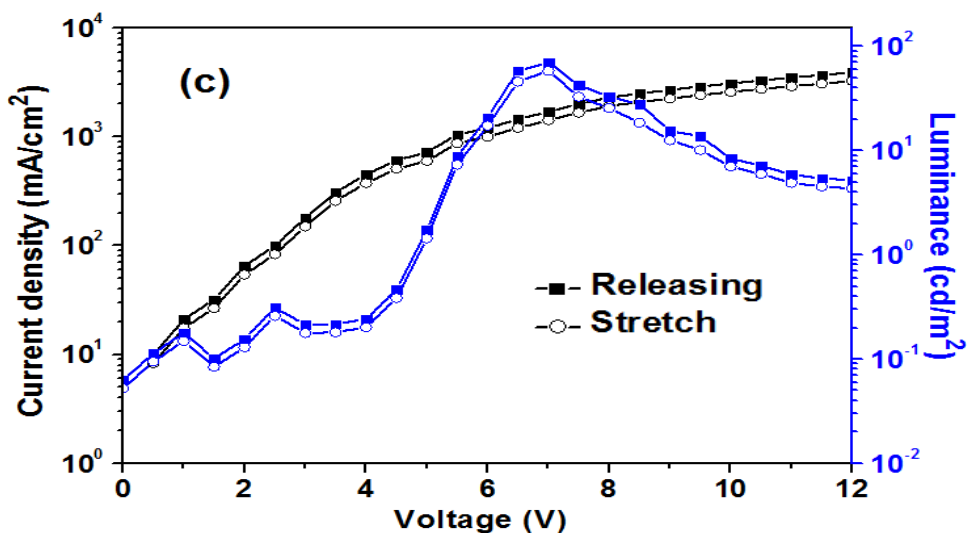
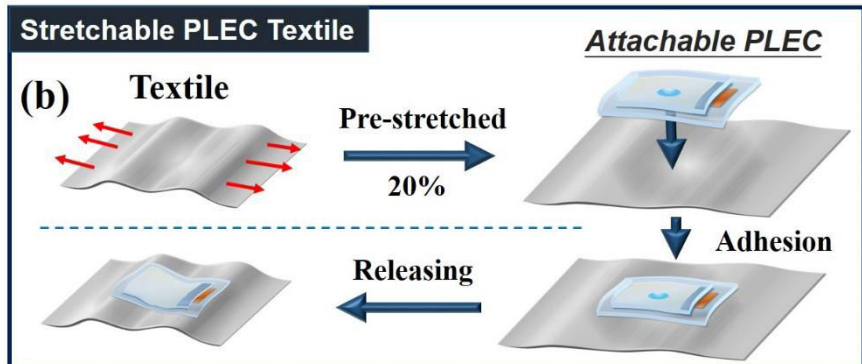
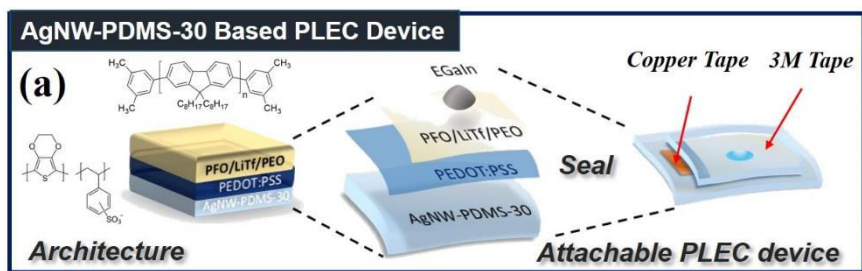
To demonstrate the potential of our AgNW-PDMS electrode for wearable electronic devices, our concept was fabricated on a simple device architecture by using PLECs instead of conventional OLEDs. The device consisted of a mixture of ionic and electronic conductors between two metal electrodes. The anode, cathode, and emissive layer supported all three processes of charge injection, charge transport, and emissive recombination because of the enhancement of charge injection that occurred in the electrodes.²¹⁰ Because of this enhancement, additional electron or hole injection, transport, and blocking layers were unnecessary. The simplicity of the PLEC architecture has previously been exploited for fabrication of intrinsically bendable and stretchable devices.²¹¹⁻²¹³ We fabricated textile-based stretchable PLECs through a roll lamination process based on a semitransparent AgNW-PDMS (9 Ω /sq) electrode (**Figure 6a**). The AgNW-PDMS electrode was first spin-coated with a thin layer of PEDOT:PSS for use as the anode. The thin PEDOT layer protects the PDMS matrix from solvent attack during subsequent coating of the electroluminescent polymer layer. Moreover, we further measured the surface roughness between the AgNW-PDMS electrode and PEDOT:PSS layer by the Atomic force microscopy (AFM). The PEDOT:PSS-AgNW-PDMS exhibit a small root mean square (RMS) value of 5.24 nm in contrast to the AgNW-PDMS with RMS value of 26.5 nm, thus representing the PEDOT:PSS layer provide a significant improvement in film roughness. (**Figure 7a-b**)

The electroluminescent polymer layer consists of a blue light-emitting polymer polyfluorene (PFO), ionic conductor polyethylene oxide (PEO), and lithium trifluoromethanesulfonate (LiTf). PFO is a particularly attractive active component in OLEDs because of its thermal and chemical stability and exceptionally high solution and solid-state fluorescence quantum yields.²¹⁴ PEO and LiTf salts are used extensively

as solid electrolytes in PLEC processes; PEO serves as a conductor to promote necessary ion conductivity; ions must be mobile during in situ electrochemical doping. LiTf salt provides additional ionic dopants with a doped polymer in the formation of a P-I-N junction. In a previous study, the cathode was a drop (diameter ≈ 2 mm) of eutectic gallium-indium (EGaIn; work function = 4.3 eV) deposited on the surface of the emitting layer and encapsulated with an adhesive elastomer [3M VHB 4905 tape (3M elastomer)]; notably, EGaIn achieved relatively high stability when exposed to air because it contains gallium oxide (Ga_2O_3), which retained its shape when the device was tilted or inverted.²¹⁵ In addition, the adhesive elastomer was initially selected based on previous reports of the fabrication of stretchable PLECs or solar cell devices.²⁰⁶⁻²⁰⁸

To integrate our PLECs into the elastomeric textile, we demonstrated the simple prestretching and releasing concept based on our WTP method (**Figure 6b**). First, the AgNW-PDMS electrode based on the WTP method was transferred onto a prestretched (20%) elastomeric textile to form a buckle microstructure prior to testing. Second, extruded drops of EGaIn were deposited on the 3M elastomer via a syringe, and then copper wires were fastened to the device and the tips of the wires were placed in the drops of EGaIn. Third, the 3M elastomer with EGaIn liquid metal was immediately attached to the top of the emitting layer for use as a top contact. With a 20% prestretch of the elastomeric textile, we optimized stretchable PLECs with a maximum tensile strain of 10% (**Figure 4c**). Periodic buckles were formed after releasing the prestretch to return the stretchable PLECs to a state corresponding to 0% tensile strain.²⁰⁶⁻²⁰⁸ **Figure 6c** shows the current density–voltage–luminance (I–V–L) characteristics of the resultant PLECs during the prestretch and release cycle between 0% and 10% tensile strain. Under 10% tensile strain, the device voltage when turned on was 5 V (1.4 cd m^{-2}); in addition, the device exhibited maximum luminance intensity of 58 cd m^{-2} (7 V) and maximum external quantum efficiencies (EQEs) of up to 0.001% compared with the

initial prestretch state (7 V, 70 cd m⁻²). We speculated that the PLECs had formed a random network of folds to accommodate the compression strain when the elastomeric textile had relaxed to its unstrained state, thereby maintaining its performance at nearly the same level as that of its prestretch state.²⁰⁶⁻²⁰⁸ In addition, our textile-based PLECs exhibited performance superior to that of a PEO-perovskite composite system on a PLEC device in a previous study.²⁰⁹ A representative electroluminescence spectrum (**Figure 6d**). Notably, electroluminescence (EL) emission maxima from PFO can broaden with bias voltages at 438, 470, and 497 nm because of variations in vibronic structures. According to the CIE 1931 standard color-matching functions, emitted blue light can be demonstrated using x,y chromaticity coordinates (0.18, 0.24) by alternating between voltages, as shown in the inset of Fig. 5d. In the present study, the PLECs were operated continuously under stretch–release cycles; demonstrative photographs of the action (**Figure 6e**), which, alongside, shows that the PLECs were able to be stretched with up to 10% tensile strain based on the stretching and releasing strategy, thereby maintaining their performance; the strategy was repeated at least three times without damage to the device. The present research promotes the potential for application of PLECs in wearable electronic devices. We believe that the developments described in this paper will contribute to real commercialization and the future of stretchable polymer light-emitting electrochemical cell devices.



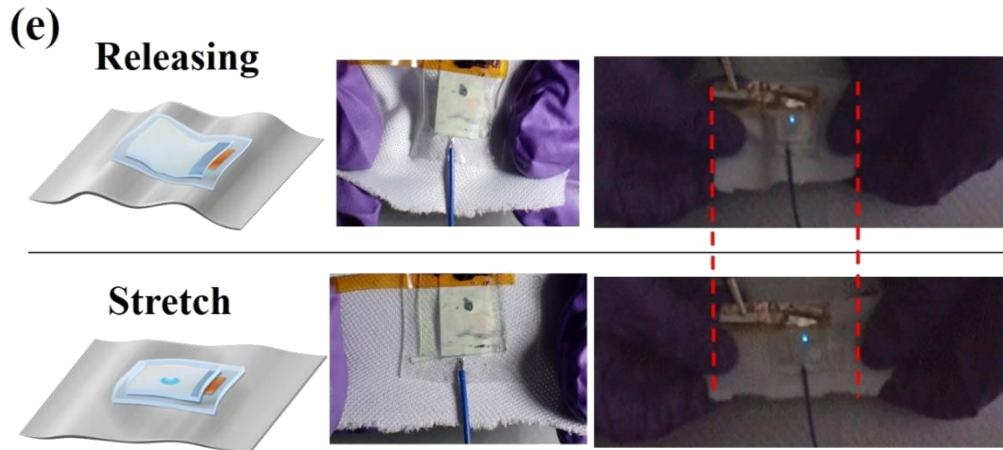


Figure 6. Schematic of the fabrication process of stretchable textile-based PLECs. (a)

Diagram of PLEC device structure based on AgNWs-PDMS electrodes with In-Ga cathodes. (b) Schematic of prestretching and releasing strategy based on the WTP method for integration on elastomeric textiles. (c) Current I–V–L responses of a PLEC device during the stretching and releasing cycle test. (d) EL spectra of the device versus various voltage bias levels. The inset contains a CIE 1931 x-y chromaticity diagram showing the brightness of PFO emission with blue color. (e) Photographs of a stretchable PLEC attached to a prestretched elastomer textile (20%); the images represent the buckle microstructure PLEC (unstrained elastomer) state being stretched to the flat PLEC (stretched elastomer) state.

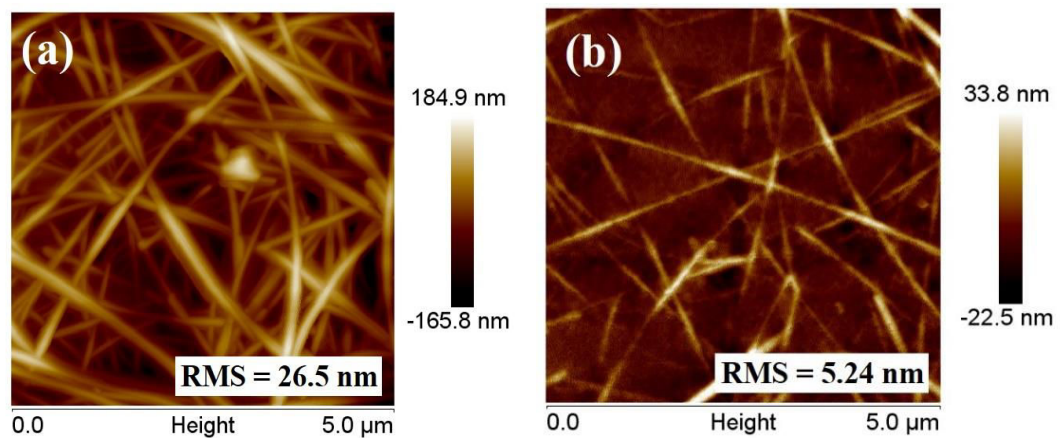


Figure 7. Tapping mode AFM images with height line profiles of the (a) AgNW-PDMS electrode, (b) PEDOT:PSS-AgNW-PDMS electrode. (5 $\mu\text{m} \times 5 \mu\text{m}$)

3-7 Conclusions

In summary, we demonstrated a WTP method for integrating AgNW electronic devices on diverse arbitrary substrates. The advantages of the WTP method are that it is facile, cost-effective, and chemical free and has nearly 100% transfer yield efficiency, regardless of transferred materials and feature geometries; these features indicate the potential of this method for large-scale production of high-performance devices on target substrates. The combination of spray coating and the WTP method provides the ability to obtain a stretchable AgNW-PDMS electrode with enhanced electrical and mechanical properties, such as high conductivity ($9 \Omega/\text{sq}$, 82% at 550 nm, $\sigma_{\text{DC}}/\sigma_{\text{Op}} \approx 200$), tensile strain (0% to 40%), flexibility (bending radius of less than 2 mm), and even superior performance compared with devices fabricated using conventional methods. Furthermore, we demonstrated that novel flexible textile-based PLECs could be accessibly fabricated using the stretchable AgNW-PDMS electrode. The prestretching in the elastomeric textile process provided the buckling microstructure in the PLECs, which permitted controllable stretching and releasing cycles and contributed to the excellent mechanical robustness of the devices. Moreover, the highest luminance intensity of the textile-based PLECs was optimized 58 cd m^{-2} at 7 V under 10% linear strain without damaging the electroluminescent properties. Thus, the innovative approach based on the WTP technique paves the way for practical applications of AgNWs on various arbitrary substrates, thereby furthering the development of the WTP technique for integration in novel textile-based PLEC systems. This research represents a major step toward the realization of flexible stretchable applications in wearable electronics.

Chapter 4

Mechanically Robust and Ultra-Sensitive Skin-Inspired Nanofiber-based Resistive Pressure Sensor Based on Fibrous Interlocked Microstructures

4-1 Introduction

The considerable development of the human skin is highly intuitive, requires the fabrication and implementation of electronic circuits and optoelectronic devices with lightweight, cost-effective, and consuming low power, as well as being able to interact with various environments, allowing us to perceive various shapes and textures by modulated different temperature or contact pressure. To date, most of researchers have been do the huge efforts to dedicate to developing versatile human-interactive devices via imitating skin-like functions including humidity, tactile, and temperature sensing capabilities, contributing to diverse applications (e.g., soft robotics, medical devices).²¹⁷⁻²¹⁹ Conventional integrated-circuit devices not only rigid and poorly deformable but also incompatibility with curvilinear and soft human bodies, restricting the practical application in developing the human-friendly interactive electronics. In contrast, the flexible and bendable wearable electronics enabled conformally mounted onto human bodies and succeed in exhibiting the sensing functionalities. In order to achieve the promising goals requires the flexible sensor platforms provided with crucial features of light weight, superior flexibility, stretchability, high sensitivity as well as rapid response.^{220, 221}

The novel strategies have been investigated extensively on the functional nanomaterials with compatibility and facile synthesis methods can capable of integrated of skin-like electronics with the assistance of sensing modules, such as pressure sensors, strain sensors, temperature sensors, etc., which inspired by the perceptive

characteristics of human skins.²²² Moreover, a diversity of functional nanomaterials have been investigated applied with the stretchable electrodes in order to maintain the high electrical and mechanical performance of skin-inspired upon the various dynamic modules through the top-down or bottom-up approaches.²²³ The top-down approach reveals that using the fabrication methods to turn the brittle and rigid inorganic materials into ultrathin films, thus demonstrating in highly flexible and conductors via the transfer-printed technology onto desired target substrates. Despite this methodology have been realized the high performance inorganic nanomaterial-based skin-inspired devices,¹⁵⁵ it is necessary to overcome the three critical issues: low stretchability, low- scale capable approach, and low mechanical stimuli stability.

4-2 Motivation

Mechanically flexible and stretchable functions are essential modules in artificial electronic skins (e-skin) electronic systems, which attracted much attention for its great potential in various applications, including health monitoring, disease diagnostics, and smart robotics.²²⁴⁻²³⁰ To develop artificial skin emulate the exquisite sensation of natural skin, it is necessary to incorporate tactile sensors with flexibility, high-sensitive, fast response, and high spatial resolution for practical emulation of the extremely complex somatosensory system with respect to low-range pressure distribution (<1 kPa). To date, several types of skin-like pressure sensors are typically based on force induced changes in capacitive,^{231,232} piezoelectric,^{233,234} triboelectric,^{235,236} and piezoresistive^{237,238} sensing mechanisms. Among them, piezoresistive sensors transduce mechanical strain into an impedance change due to their simple read-out mechanism, facile fabrication, low energy consumption, and sensitivity to both pressure and flexion.²³⁹ Typically, flexible pressure sensors can be constructed by embedding conducting fillers into soft elastomeric materials forming 3D percolating networks.²⁴⁰⁻²⁴⁴

Generally, the introduction of the microstructures with 2D polymeric surfaces is critical in the pressure sensor design in order to obtain high sensitivity, such as micropyramid,^{245,246} microdome arrays,²⁴⁷⁻²⁴⁸ microgroove shape,^{249,250} and interlocking microstructure,^{251,252} have been employed to endow the elastic materials with greatly enhanced tactile sensitivity.²⁴⁵ Despite significant device sensitivity has been achieved, conventional fabrication methods that use the organic template-assisted process suffer from long fabrication times and are inherently chemical-intensive processes that require extremely careful and exhaustive transfer techniques, which is a time-consuming, high-cost process with limited scalability. By contrast, our elastic sandwich-structured conducting nanofiber (ESSCN) skin-inspired resistive-type pressure sensors fabrication using an all-electro-spinning process alongside the fibrous interlocked-microstructures configuration (FIM) in cost-effective, compatible with large-area implementation to detect static/dynamic pressure distributions with high sensitivity, rapid response, and pragmatic spatial resolution, which has the advantage of an extended integration environment. First, the free-standing electrode can be conducted on nanofiber membranes without the additional binder agent and supporting substrate thus maximizing the use of active materials in a selective manner. Second, electrospinning is an easy, versatile, and inexpensive technique enables flexible morphology tuning, assembling various functional nanofibers, and high-throughput continuous production has motivated extensive studies on sensory applications.^{26,253-255}

Herein, we firstly demonstrated that ESSCN skin-inspired resistive-type pressure sensors through the eco-friendly, cost-effective, lithographic-free, and large-scale capable approach. The sensors with optically transparent, high sensitivity, lightweight, high durability, and ultra-flexibility are able to detect and differentiate a variety of mechanical stimuli (pressure, strain, and curvature), enabled by our stretchable electronics and a uniquely uniformly fibrous interlocked microstructures. The ESSCN

pressure sensors possess superior performance with unprecedented features including ultra-high sensitivity of 71.07 kPa^{-1} in a low-pressure regime ($<0.06 \text{ kPa}$), a fast response time ($<2 \text{ ms}$, faster than that of human fingertips ≈ 30 to 50 ms), highly repeatable and reproducible stability (>100 cycles) with excellent off/on switching behaviors in comparison with the previously reported flexible pressure sensors. **(Table 1)** In addition, the pressure sensitivity of the sensor can keep more than 50% of its original value even the tensile strain of sensor electrodes increases up to 70%, enabled exhibiting excellent performance and prolonged usage under the stretched state. Based on its superior performance, the features render our ultrathin ESSCN unique and useful for a variety of e-skin applications where conformable adherence to moving surfaces, multiple mechanical stimuli tactile sensing, and monitoring human physiological signals, further advancing e-skin devices towards mimicking the properties and capabilities of human skin.

4-3 Background and review of literatures

4-3-1 Strain and Pressure Sensors

The pressure sensor have been considerate attentions application in tactile sensors and skin-inspired electronics devices in recent years.²⁵⁶⁻²⁵⁸ Since their superior features of flexibility, deformability, durability, lightweight, and biocompatibility, the pressure sensors endow sophisticated mounted onto the human skin for monitoring of physiological health and medical diagnostics on site. The development of the high-performance skin-inspired sensors has been integrated with the engineering functional nanomaterials or hybrid micro/nanostructures, which relied on the transduction mechanisms by converting external stimuli into electrical signals.^{256, 257, 259} To date, several types of skin-like pressure sensors are typically based on force induced changes in capacitive,^{231,232} piezoelectric,^{233,234} triboelectric,^{235,236} and piezoresistive^{237,238} sensing mechanisms. Among them, piezoresistive sensors transduce mechanical strain

into an impedance change due to their simple read-out mechanism, facile fabrication, low energy consumption, and sensitivity to both pressure and flexion. Previous researchers have been focused on improving the parameters of wearable strain devices, such as sensitivity, linearity, hysteresis, gauge factor (GF), response time, and cyclic tests.²⁶⁰ However, it is difficult to accurately detect the pressure under dynamic deformation with various mechanical stimuli to achieve the high device performances. (pressure, flexible, and bending) To overcome this challenge, Someya and co-workers devoted to fabricating a bending-insensitive, ultra-flexible, and resistive-type pressure sensor with composite nanofibers as building blocks.²⁶¹ Remarkably, the sensor with the thin substrate (thickness: $<2\ \mu\text{m}$) exhibited the ultra-deformable properties as the bending radius of the sensor drops down to $80\ \mu\text{m}$. **(Figure 1a)** The promising results in precisely measuring the various distribution of the pressure on 3D surfaces and performance variation are negligibly small before and after wrapping devices around an injection needle. **(Figure 1b-d)** Zhang's and co-workers demonstrated micro-crack assisted strain sensors using AgNWs and an elastomeric PDMS platform.²⁶² The strain sensors exhibited a highly GF up to 150 000 within a large stretchability of 60% strain. **Figure 2a** shows the fabrication process of key structural element with the patterned PDMS substrate (1 mm thick), which was fabricated using a piece of steel net (80 mesh) mold to provide a regular and uniform PDMS microstructure. The promising results revealed that the GF of the strain sensor with the patterned PDMS substrate can achieved as high as $\approx 150\ 000$ within a 60% strain. Moreover, the sensor with a fast response, low creep, and an ultrahigh stability (more than 30 000 cyclic loading tests) were achieved, thereby demonstrating an appealing features of a strain sensor use for monitoring finger/wrist bending. **(Figure 2b)**

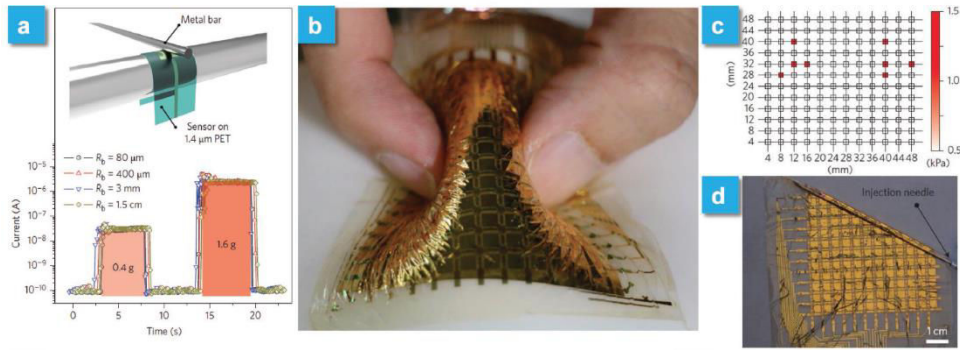


Figure 1. (a) The pressure response of the device in the bent state and response of the device fabricated on a 1.4 μm thick PET substrate. (b) Photograph of an integrated sensor array attached to the 3D surface balloon, applied with pressure by a pinching motion. (c) Measured pressure data distribution under complex bending, showing no pressure signal from deformation such as wrinkling. (d) Photograph of a sensor wrapped around an injection needle.

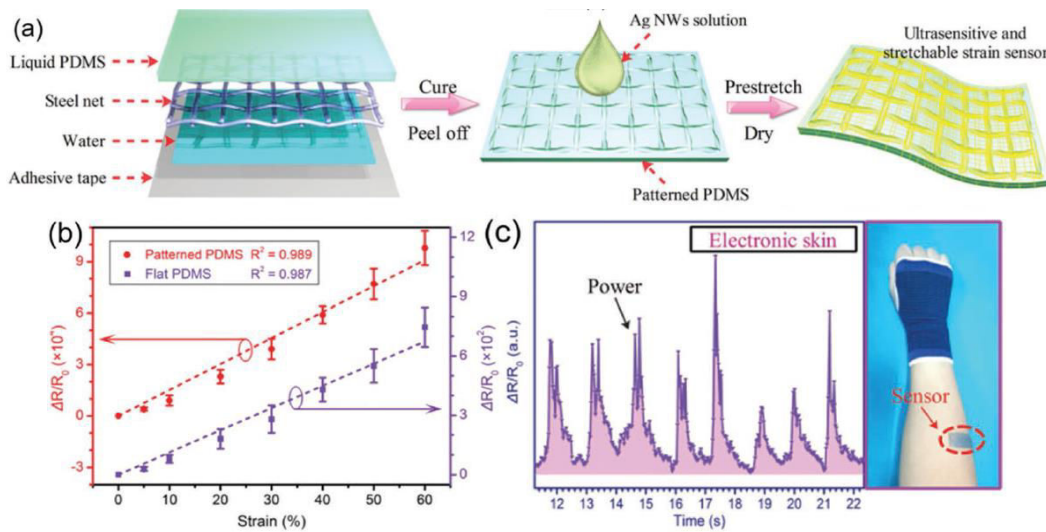


Figure 2. (a) Schematic illustration of the fabrication process for an ultrasensitive and stretchable strain sensor. (b) Relative resistance change versus strain within a 60% strain. (c) The strain sensor served as an electronic skin showing the ability to monitor the motions of the arm muscle.

4-3-2 Piezoresistive

Piezoresistive sensors transduce mechanical displacement into an electrical signal have been investigated extensively for monitoring minute structural deformations in

flexible substrate over time. Since their simple read-out mechanism have potentially sensitivity to both pressure and flexion.²³⁹ Recently, Tee and co-workers demonstrated a resistive-type pressure sensor consists of natural self-healing materials enable mimicked in artificial electronic skins.²⁶³ Lijia Pan and co-workers developed an ultrasensitive resistive pressure sensor based on an elastic, microstructured conducting polymer (EMCP), consists of interconnected hollow-sphere structures of polypyrrole (PPy) with structure-derived elasticity and a low effective elastic modulus as shown in **Figure 3**.²⁶⁴ Based on the uniquely geometry microstructured in **Figure 3** and **Figure 4**, their pressure sensor enables detect the pressure less than 1 Pa and exhibits ultra-sensitive, rapid-responding time, and excellent cycling stability, thereby demonstrated that the matrix of pressure sensors have highly potential and reliable application in human-electrics interfaces and artificial skins.

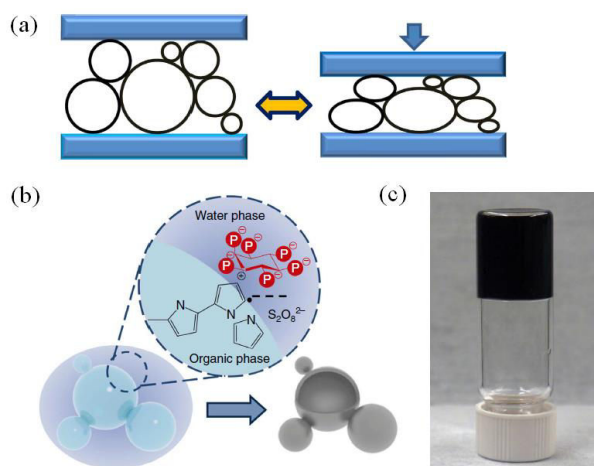


Figure 3. The novelty microstructure of EMCP material (a) Schematic of the structural elasticity of the hollow-sphere-structured PPy. (b) Schematic illustration of the interphase synthesis mechanism of PPy hydrogels with hollow-sphere microstructures. (c) Digital photograph of a PPy hydrogel.

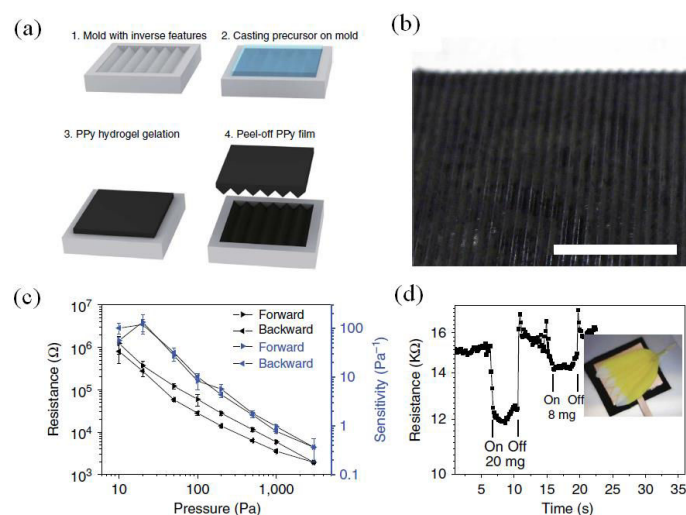


Figure 4. Fabrication and resistive pressure response of micro-patterned EMCP films. (a) Schematic illustration of the fabrication micro-patterned EMCP films. (b) Digital photo image of the micro-patterned PPy film. (c) Resistance response and pressure sensitivity of the EMCP pressure sensor, scale bar: 1 cm. The error bars represent one standard deviation. (d) Transient response to the application and removal of a 20mg weight and a flower petal (8 mg) on the micro-patterned EMCP device, the latter corresponding to a pressure of only 0.8 Pa.

4-4 Experimental section

4-4-1 Materials

Linear triblock copolymer SEBS (G1652) ($M_n = 79000 \text{ g/mol}^{-1}$, weight fraction of styrene = 30%) was purchased from Kraton, AgCF_3COO (98%), hydrazine hydrate ($\text{N}_2\text{H}_4 \cdot 4\text{H}_2\text{O}$, ~50-60%), N,N-dimethylformamide (DMF, 99.5%) and Ethanol (95.0%), Tetrahydrofuran anhydrous (THF, 99.9%) were purchased from Sigma Aldrich. Tetra-n-butylammonium perchlorate (99%) was purchased from Alfa Aesar.

4-4-2 Preparation of SEBS fiber and silver nanoparticles

SEBS was dissolved in a solvent mixture of THF/DMF (wt/wt = 4 : 1) to adjust the concentration of 12 wt %. Tetra-n-butylammonium perchlorate (4 wt% of the solute)

was added to the the polymer solution, which was electrospun onto the collector at a fixed feed rate (1 ml/hr) and voltage (14.0 kV). The nozzle-to-collector distance was 15 cm. The resulting electrospun fibre mat (SEBS fibre mat) was readily peeled away from the collector. The electrospun fibre mat was dipped in an ethanol solution of AgCF_3COO (15 wt%). The fiber mat was removed from the solution after 30 min and dried at room temperature. Hydrazine hydrate (50%) in ethanol/water mixture as solvent (vol/vol = 1:1) was dropped onto the fibre mat to reduce the absorbed precursor. After 5 min, the residual reducing agent was rinsed out several times using deionized water.

4-4-3 Design and Fabrication of the Skin-inspired ESSCN Pressure Sensor:

The same proportion of the SEBS polymer solution was electrospun onto the collector gap (3 cm in length and gap width of 1 cm) to form the SEBS dielectric layer. The feed rate was fixed at 1 ml / hr and the spinning voltage was set at 14 kV. The nozzle-to-collector distance was 15 cm. The SEBS dielectric layer was controlled with different electrospinning time (1, 2, and 3 min) designated as SEBS-1, SEBS-2 and SEBS-3, which were transferred to the SEBS/AgNPs fiber mat. The middle SEBS dielectric layer and bottom and top SEBS/AgNPs electrodes were assembled face-to-face into a resistive pressure sensor and two copper wires were glued by silver paste on each of the films as electrodes.

4-5 Characterization of the Skin-inspired ESSCN Pressure Sensor

Transmittance spectra were recorded using a Shimadzu ultraviolet–visible spectrophotometer. The Fourier transform infrared (FT-IR) spectra were recorded using a Bio-Rad 155 FT-IR spectrometer at ambient temperature in the range of 650–4000 cm^{-1} . The X-ray diffraction (XRD) patterns are recorded on an X-ray diffractometer

(D8 ADVANCE, Bruker, German) was used for elemental analysis of SEBS/AgNPs fibrous electrodes. A stress-strain curve was obtained using a universal tensile stress testing machine (Taiwan Research and Development Center Institute). The morphology and the elemental components of the samples were investigated by field-emission scanning electron microscopy (FESEM, Hitachi S-520) equipped with energy dispersive X-Ray spectroscopy (EDX) respectively, the 50 random fiber samples were selected and the diameters of SEBS dielectric nanofibers were measured by the SEM software. The resistance curves, response times, detection ranges, and mechanical stimuli of the pressure sensors were measured with a Keithley 2634B analyzer with two copper wires were glued by silver paste on each of the films as electrodes, respectively. The cyclic loading-unloading of pressure, a preselected constant pressure was repeatedly applied and released on the pressure sensor using a linear motor system. The medical tape used in the smart clothing and biomedical monitoring is a commercial elastomer transparent tape (VHB 4905, 3M), respectively. The real-time demonstration of the circuit was completed for integrated with RGB-LED garments and health-monitoring devices.

4-6 Results and discussion

The ESSCN pressure sensor with excellent durability and fast response are fabricated by employing the dielectric SEBS nanofiber with the geometry of FIM in the middle layer, sandwiched by two SEBS/AgNPs electrodes at top and bottom for packaging as shown in **Figure. 1a**. The SEBS/AgNPs composite fabrication consists of elastomeric fiber mat deposition, introduction of silver nanoparticle precursor, and nanoparticle nucleation. (See **Experimental Section**) An elastomeric SEBS block copolymer is served as a flexible framework due to its flexible, robust, and specific interaction with transition metal ions, allows the AgNPs are well dispersed, and a homogeneous random distribution is achieved.²⁴⁰ A key feature of the dielectric layer

is served as spacers that can form the geometry of FIM through electrospinning time (that is, 1, 2 and 3 mins). Hence, we have accordingly designated these spacers as SEBS-1, SEBS-2 and SEBS-3, respectively. The average thickness of the spacers in SEBS-1, SEBS-2, and SEBS-3 are 4.13 ± 0.13 , 6.21 ± 0.45 , and 12.32 ± 0.32 μm in **Figure 1b**. As expected, SEBS-1 with a lower fiber thickness yield higher optical transmittance was 91% at 550 nm in **Figure 1c and 1g**, respectively. The inset **Figure 1c** also show linearly decrease with the increasing electrospinning time, thereby demonstrating a widely dynamic range for modulating the optical transmittance in various applications. **Figure 1d and 1e** presents field-emission SEM (FE-SEM) and energy-dispersive spectroscopy (EDS) mapping images of the ES nanofiber at chemically reduced state. As shown in **Figure 1d**, the individual fiber diameter was 730 nm and bound fiber-to-fiber connections were stabilized with nanoparticles subsequent to their nucleation, thus induces orientation of silver nanoparticles along the axis of SEBS nanofibers with a diameter of 20~40 nm. An EDS elemental mapping image shows that the silver nanoparticles are densely embedded in the surface of fiber, as shown in **part e** and inset of **Figure 1e**. Notably, the Ag content within the ES nanofibers was 62.25% as estimated according to the EDS spectrum in the **Figure 1f**, which is highly revealed the silver nanoparticles are well-dispersed and formed networked percolation within nanofibers. Furthermore, the Fourier-transform infrared spectroscopy (FTIR) and X-ray diffraction (XRD) can further identify the absorption of precursors of SEBS-AgNPs before and after the chemical reduction in (**Figure 2 and Figure 3**) As shown in **Figure 2**, the two main peaks at 1130 cm^{-1} and 1182 cm^{-1} are attributed to the C-F stretching that indicates the presence of the precursor inside the fibers. **Figure 3** presents the X-ray diffraction pattern of SEBS-AgNPs are clearly presents the main peaks at (2θ) 38.10, 44.26, 64.48 and 77.39, are corresponding to the (111), (200), (220) and (311) crystal planes of the face centered cubic of AgNPs in

contrast to the pristine, resulting in identifying the nanofibers were effectively connections between each of the Ag nanoparticles. ²⁶⁵

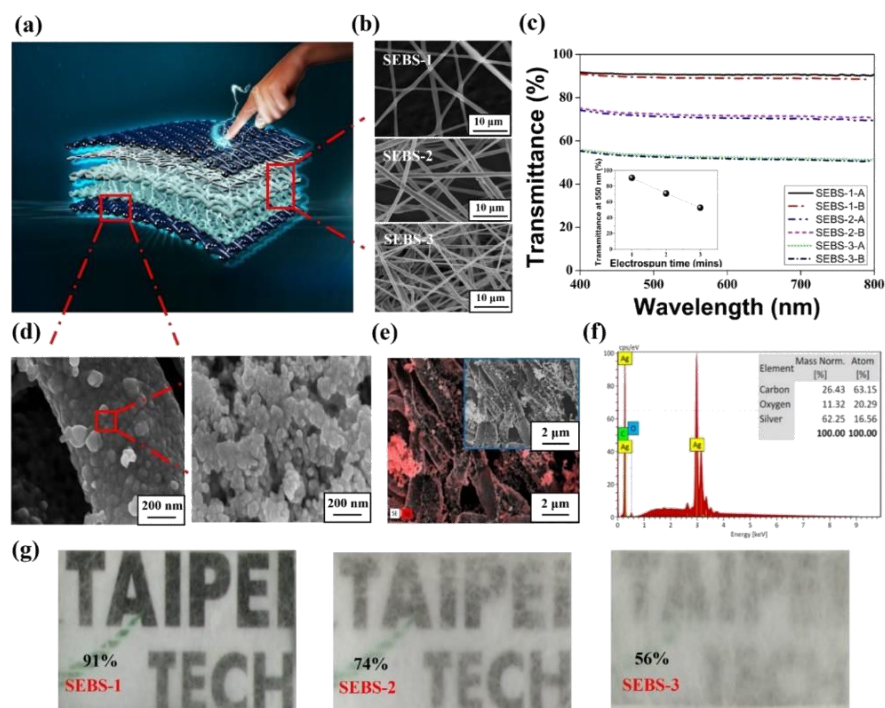


Figure 1. Schematic diagrams illustration of a skin-like ESSCN resistive pressure sensors: (a) Schematic configuration of tactile sensors with interlocked fibrous structure. (b) SEM images of intermediate SEBS composites prepared with various electrospinning time. (c) Optical transmittance curves of the SEBS composites prepared with various electrospinning time, as a function of the wavelength, respectively. The inset figures show a linear decrease of transmittance at 550 nm with the increasing electrospinning time. (d) SEM images of the conductive composite uniformly with silver nanoparticles after chemical reduction of AgCF_3COO . (e) Energy dispersive X-ray spectroscopy EDS maps of Ag within the confined are in (inset). (f) EDS spectrum recorded within the region defined in (e). (g) Photograph of various SEBS composites with corresponding transmittance values of 91%, 74% and 56%.

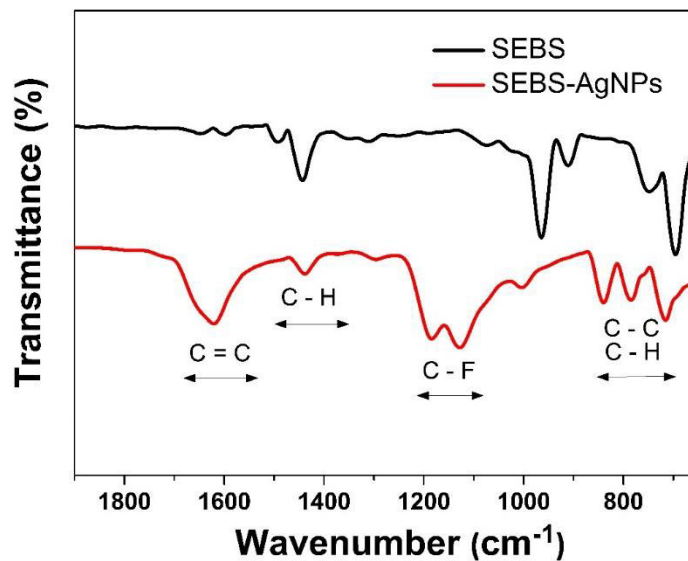


Figure 2. FTIR analysis of the SEBS composite before and after absorption of silver trifluoroacetate (STA) as Ag precursors. Black and red lines indicate results of the pure SEBS and the SEBS-AgNPs absorbing the Ag precursors, respectively. Asymmetric stretching of C-F bonds of the Ag precursors (AgCF_3COO) is appeared in the two peaks at $1,126\text{ cm}^{-1}$ and $1,184\text{ cm}^{-1}$.

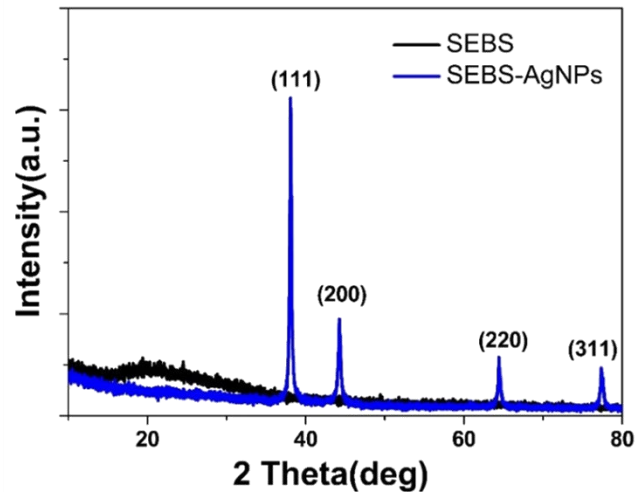


Figure 3. XRD pattern of SEBS and SEBS-AgNPs.

Intermediate intervals with the geometry of FIM are schematic illustration in **Figure 4a** enable its ability to provide a suitable platform applied to the pressure sensor. **Figure 4b** reveals that various nanofibers time interval are sophisticated dense packing and form three-dimensional with the geometry of FIM on the bottom of SEBS-AgNPs

electrode. Notably, each of nanofibrous mat interleaved between two layers of a laminate has the capability to bridge the two plies, thereby demonstrating nanointerleave not only brings to the laminate but also reinforcing strength on carrying on additional loads. Moreover, the cross-sectional SEM image in **Figure 4c** also presents the initial spacers were configured by interlocking various fiber density with a diameter range from micro to nanocontact between the top and bottom SEBS/AgNPs electrode of the sensor. Significantly, our ESSCN was uniquely designed to enable highly sensitive pressure detection. For a large pressure sensing dynamic range, the geometry of FIM with rarely fiber density was implemented to sense pressure in the low-pressure region (<0.06 kPa) while sensitivity in the higher pressure region (>0.06 kPa) was enabled using dense fiber density, thus modulating Off-on switching range for our ESSCN pressure sensor via tuning the threshold pressure and threshold resistance.

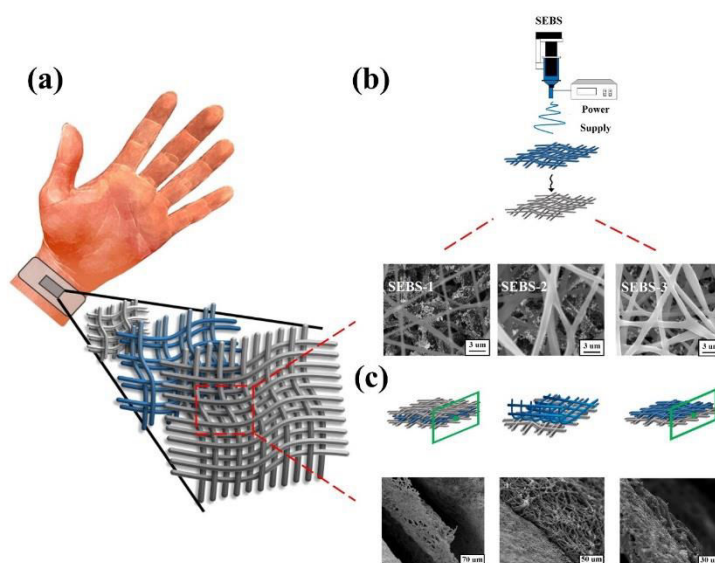


Figure 4. SEM characterization of SEBS composites: (a) Schematic illustration of integrating the fibrous electrode with a dielectric layer forming a sandwich-type composites. (b) SEM images of bottom SEBS-AgNPs electrode was covered by different fiber diameter intervals. (c) Cross-sectional schematic view of laminated composites. (d) Cross-sectional SEM images of the top and side views of a dielectric layer sandwiched by two fibrous electrodes at top and bottom.

Figure 5a-c shows the pressure response (that is, press, blue line; release, red line) based on fibrous interlocked-microstructures corresponding to SEBS-1, SEBS-2, and SEBS-3, respectively. The resulting square pressure-sensitive was 1.5 cm² in size. Slightly higher resistances were observed with SEBS-1 for the first cycle, the subsequent cycles were reproducible. Based on our design, when no pressure is applied, the sensor is non-conductive and prevent the current flowing due to the AgNPs are not involved in percolation. Upon increasing the pressure, the initial AgNPs are contacted with each other and lead to increased electric current. As expected, SEBS-1 with a lower coverage of fibers yield higher efficiency to achieve the conductivity. Notably, all the SEBS-1, SEBS-2 and SEBS-3 exhibited changes in resistance of up to seven orders of magnitude by applying pressure between 0 and 0.18 kPa, 0 and 6 kPa, and 0 and 26 kPa, respectively. Moreover, **Figure 5d** revealed that the threshold of the resistance switching of SEBS-1, SEBS-2 and SEBS-3 was gradually increased as a function of the coverage of fibers, showing onset detection of pressures at 0.07, 0.75, 10.31 kPa. (Second forward). **Figure 5e** showed high durability and stability of our ESSCN devices with no hysteresis as demonstrated by multiple cycle tests (100 cycles). All of SEBS-1 to SEBS-3 exhibited the excellent reproducibility and durability with negligible variations in the 100 loading and unloading tests by applying pressure between 0.16 to 0.176 kPa, 5.77 to 6.11 kPa, and 22.02 to 25.69 kPa, thereby demonstrating our ESSCN pressure sensors has both long-term stability and reliability. Furthermore, the minimum press response and response time characteristic of ESSCN sensors is the key factor in the study of the tactile application. The investigation of the detection limit of our SEBS-1 with dynamic pressure inputs have been applied in **Figure 5f**. Remarkably, the response time is under the resolution limit of our measurement system (<2 ms) in contrast to SEBS-3 (<10 ms) in (**Figure 6**), which exhibited an ultra-fast response and far faster than human fingertips (\approx 30 to 50 ms),

showing its excellent sensitivity is fit for the application of nanoforce sensing like “tactile” condition, respectively; these values represent a significant improvement in response time compared with previous reports. (**Table 1**) Therefore, the facile and tunable design of our SEBS-1 is ideal for human interactive system, which will be discussed and demonstrated in the integration section.

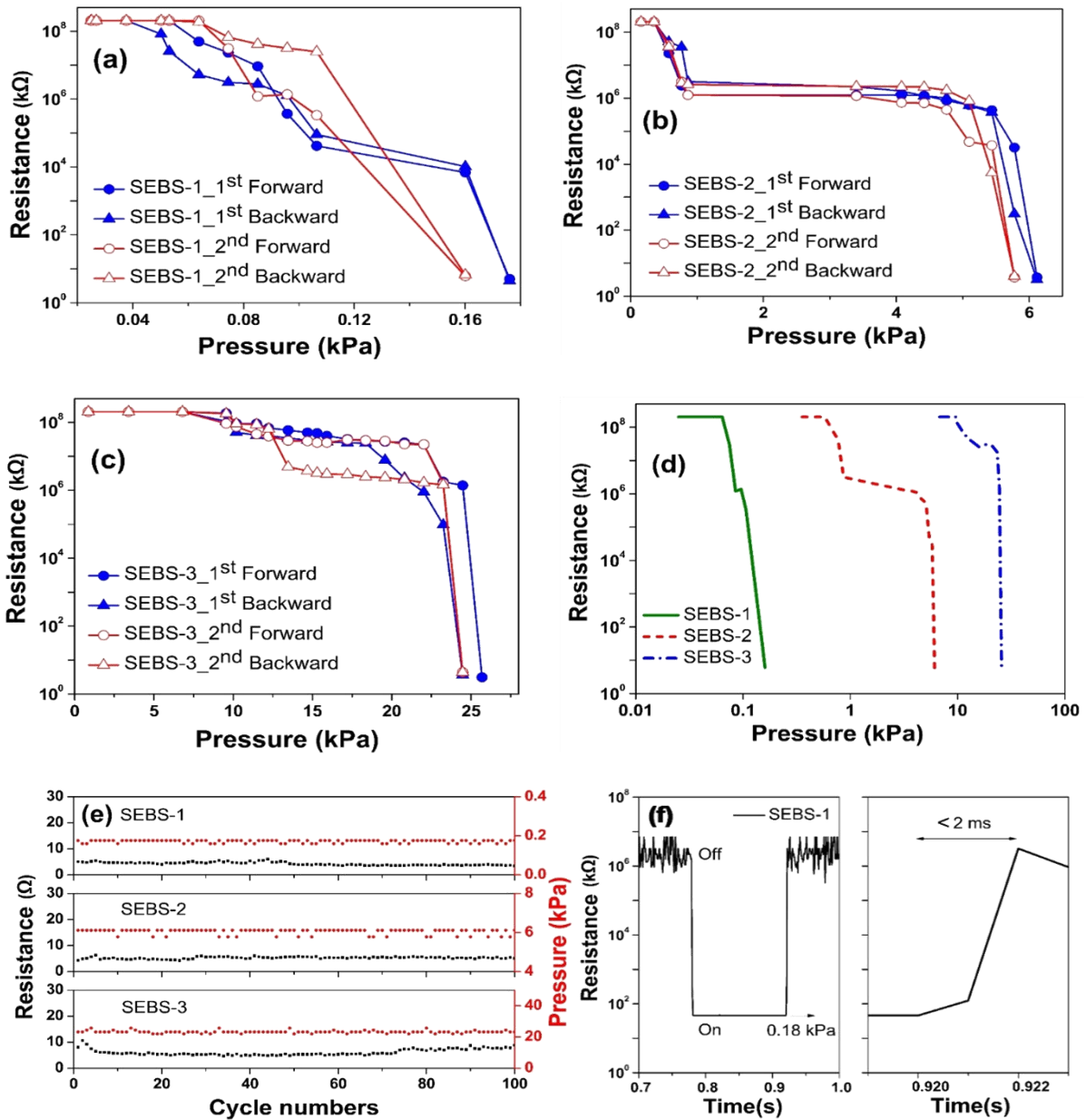


Figure 5. Pressure-sensing performance, durability and time-resolved responses:

The pressure response for four consecutive measurements of (a) SEBS-1, (b) SEBS-2 and (c) SEBS-3. (d) The comparison of the resistance response and the threshold of resistance switching range of SEBS (second forward). (e) The stability test of the pressure sensor under a varied certain pressure range (0.16 to 0.176 kPa; 5.77 to 6.11 kPa; 22.02 to 25.69 kPa) over 100 loading-unloading cycles. (f) Response time of the SEBS-1 pressure sensor with an applied pressure of 0.18 kPa and exhibited instant response time within 2 ms. (the right figure shows the magnified curve of the left one)

Table 1. The Comparison of this work and previous flexible pressure sensors

Type of Devices	Materials [Ⓢ]	Sensitivity [Ⓢ]	Response time [Ⓢ]	References [Ⓢ]
Piezoelectric [Ⓢ]	PZT [Ⓢ]	2 $\mu\text{A}\cdot\text{Pa}^{-1}$ [Ⓢ]	0.1 [Ⓢ]	[1] [Ⓢ]
Piezoelectric [Ⓢ]	ZnO nanorod [Ⓢ]	2.1 $\mu\text{S}\cdot\text{kPa}^{-1}$ [Ⓢ]	150 [Ⓢ]	[2] [Ⓢ]
Piezoelectric [Ⓢ]	PVDF [Ⓢ]	0.2 $\text{V}\cdot\text{kPa}^{-1}$ [Ⓢ]	- [Ⓢ]	[3] [Ⓢ]
Piezoelectric [Ⓢ]	P(VDF-TrFE) Nanofiber [Ⓢ]	0.41 $\text{V}\cdot\text{Pa}^{-1}$ [Ⓢ]	- [Ⓢ]	[4] [Ⓢ]
OFET [Ⓢ]	Microstructured PDMS [Ⓢ]	0.55 kPa^{-1} [Ⓢ]	<10 [Ⓢ]	[5] [Ⓢ]
OFET [Ⓢ]	Microstructured PDMS [Ⓢ]	8.4 kPa^{-1} [Ⓢ]	<10 [Ⓢ]	[6] [Ⓢ]
Capacitance	Porous PDMS	1.5 kPa^{-1}	-	[7] [Ⓢ]
Capacitance	AgNWs/PVDFNM	4.2 kPa^{-1}	<26	[8] [Ⓢ]
Capacitance	AgNW/ moulded PDMS	3.8 kPa^{-1}	<150	[9] [Ⓢ]
Capacitance	Microhair structured/PDMS	0.58 kPa^{-1}	<30	[10] [Ⓢ]
Capacitance	Ag/PDMS	1.45 MPa^{-1}	100	[11] [Ⓢ]
Capacitance	SBS/AgNPs fibers	0.21 kPa^{-1}	<10	[12] [Ⓢ]
Piezoresistive	Au NWs/tissue paper	1.14 kPa^{-1}	<17	[13] [Ⓢ]
Piezoresistive	CNT/Microstructured PDMS	15.1 kPa^{-1}	40	[14] [Ⓢ]
Piezoresistive	Cu NWs/PVA	0.036 kPa^{-1}	-	[15] [Ⓢ]
Piezoresistive	PEDOT:PSS/PUD-Micropyramid	10.32 kPa^{-1}	-	[16] [Ⓢ]
Piezoresistive	SWNTs/Microstructured PDMS	1.8 kPa^{-1}	<10	[17] [Ⓢ]
Piezoresistive	Hierarchically-Graphene/PDMS	8.5 kPa^{-1}	40	[18] [Ⓢ]
Piezoresistive	CSilkNM/PDMS	34.47 kPa^{-1}	<16.7	[19] [Ⓢ]
Piezoresistive	SEBS/AgNPs	71.07 kPa^{-1}	<2	This work.

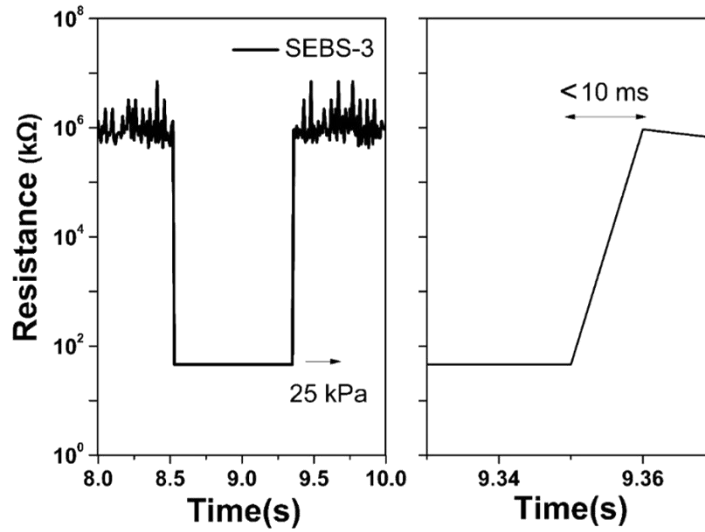


Figure 6. Response time of the SEBS-3 pressure sensor with an applied pressure of 25 kPa and exhibited instant response time within 10 ms. (the right figure shows the magnified curve of the left one)

Mechanical flexibility is another key factor of pressure sensor for next-generation stretchable and wearable electronics. **Figure 7a, 7c, and 7e** illustrated the shape deformation of the sensors unit with various mechanical stimuli (pressure, strain, and curvature) applied on the electronic skins. To estimate the pressure sensitivity of the sensors, the relative whole resistance change ($\Delta R/R_0$) of the sensor unit was calculated on the basis of measured values and plotted as the function of applied loading force (F) as shown in **Figure 7b**. The pressure sensitivity S can be defined as the slope of the curve in **Figure 7b** ($S = \delta(\Delta R/R_0)/\delta F$). As shown in **Figure 7b** (that is, press, cycle line; release, triangle line), there are three different kinds of stages observed in the response curve of SEBS-1. The sensor exhibited ultra-high sensitivity of up to 71.07 kPa^{-1} in the low-pressure region ($< 0.06 \text{ kPa}$, Stage I), which is significantly higher than that measured in the high-pressure region ($> 0.06 \text{ kPa}$, Stage II). The results show high linearity of $R^2 = 0.98$, indicating a very high reproducibility of our sensors. Notably, as the pressure is applied with a small loading force, the current increases instantaneously due to the nanofibers are ultrathin and easily deformable. A sharp slope is observed in

this period, since the deformation accumulation of ultrathin nanofibers causing a rapid increase in the contact area, resulting in providing a large sheet resistance to reduce the resistance markedly. In stage II (0.063-0.095 kPa), where the nanofibers is being deformed, the average sensitivity was 7.38 kPa^{-1} , requiring higher pressure to further deform the nanofibers. In stage III ($> 0.095 \text{ kPa}$), the sensitivity further reduced to 0.01 kPa^{-1} as ESSCN membrane has a highly compact structure, requiring large loading force to close the conductive AgNPs in the ESSCN. In comparison, the SEBS-3 has a relatively smaller pressure sensitivity of 0.18 kPa^{-1} and 0.02 kPa^{-1} in the low and high pressure range as shown in **(Figure 8)**. Another advantage of our ESSCN electronics is the mechanical robustness against bending and stretching forces are schematic illustrated in **Figure 7d and 7f**. The bending stability of the sensor was measured by our previous custom-built with a new bending platform and achieved ultimate flexibility and bending capabilities of the ESSCN electronics.²⁴⁵ **Figure 7d** shows the curve of resistive change ($\Delta R/R_0$) versus pressure of the sensor were measured before bending and after 100-cycle bending with 3-mm bending radius. The resistive change of the 100-cycle bending results at each pressure show no appreciable degradation in comparison with the as-prepared sensor. The pressure sensor with the geometry of FIM is robust and stable to the repeated loading/unloading and bending cycles based on the above results.

Figure 7f shows the plots of relative resistance change ($\Delta R/R_0$) of the sensor under different tensile strain as a function of loading force. It can be observed that the corresponding sensitivities ($S = \delta (\Delta R/R_0) / \delta F$) at stage I decreased to 130% and 115% under 30% and 50% of tensile strain and increased to 81% while the tensile strain at 70% in comparison with original sensor, respectively, and the sensitivities at stage II almost keep the same value compared to the original value except for the 70% of tensile strain in **(Figure 9)**. Furthermore, the SEM images of the intermediate SEBS-1 and

SEBS-3 dielectric layers before (inset) and after under 70% of tensile strain are shown in (**Figure 10**). In comparison to the initial SEBS composites, the fiber interval and interfacial strength between the fiber and the top SEBS AgNPs electrodes are obviously undergo mechanical deformation during 70% of tensile strain, thus enabling increased contact areas between the top and bottom electrodes while established more AgNPs conductive paths and increased the electronic transport efficiency, resulting in the resistance decrease of the composites upon stretching. Moreover, these significant improved sensors responses at high strain mainly arise from severe separation among intermediate SEBS blocks, such as a break of contacts, contact area, and spacing variation upon stretching. Meanwhile, the distance between the two electrode decreases due to poisson effect, resulting in an increase in electrical conductivity,²⁴² thereby demonstrated our ESSCN sensor enabled with a desirable combination of high sensitivity and broad sensing range. On the other hand, the incorporation of AgNPs can elevated the mechanical performance of SEBS composite, the stress-strain curves are plotted in (**Figure 11**). The tensile strength and elastic modulus for SEBS-AgNPs membrane increased to 2.18 MPa and 0.24 MPa in comparison with 0.51 MPa and 0.05 MPa for the pristine SEBS, and also show no appreciable degradation occurs in the elongation at break, thereby demonstrating the rigid AgNPs could be employed as conductive bridges to construct effective percolation network, not only greatly improve both tensile strength and elastic modules but also endowing the enhancement of the stiffness of SEBS composites with certain electrical conductivity under high strains.²⁶⁵ Conventional stretchable pressure sensors have focused on sensing with multiple force properties rather than investigate the relationship between the pressures versus under stretched state.²⁴⁵ By contrast, our ESSCN pressure sensor can be applied on arbitrary curved and moving surface and keep more than 50% of its original pressure sensitivity. Furthermore, along with decreasing the thickness of PDMS will further increase the

response speed due to minimizing the viscoelastic behavior of polymer chains based on previous theory.²⁴⁸ In comparison to recent researches with high-performance flexible pressure sensors in (**Table 1**), our unique ESSCN electronics endow a sandwich-type composites with superior electrical performance in critical aspects evaluating pressure sensors such as sensitivity, response time, and detection limit, promising potentially useful in emulating human skin for a variety of touch sensor-based applications.

To demonstrate the potential of our ESSCN pressure sensors application in wearable electronic devices, our innovative concept in **Figure 12a** presents the ESSCN electronics (1 cm × 0.5 cm) was integrated into the RGB-LED wristband and garments for realizing the diverse compelling applications. As illustrated in Figure 5b, we constructed a simple circuit consisting of RGB-LED wristband by connecting a copper wire with ESSCN electronics. The Off-on switching range of the RGB-LED wristband luminance is modulated by the applied pressure, while the predominant color of the light converts from red to blue, reflecting a decrease in voltage of the pressure sensor resulted from the decreased electrical resistance subjected to larger compressive strain. Significantly, our ESSCN electronics with economical, lightweight, and adjustable pressure switch property intuitively display laminated on the skin and garment by changing the intensity and/or colors of the RGB-LED, thereby showing feasibility comprising health-monitoring sensors as demonstrated in **Figure 12b**.

In modern medical practice, the jugular venous pulse (JVP) waveform is a powerful diagnostic tool for assessing cardiac function, and provides more valuable information for non-invasive medical diagnosis. However, conventional methods require the expensive and complexed system such as cardiac MRI, or echocardiography.²⁶⁶ By contrast, we present an innovative concept for real-time monitoring of JVP pulse signals was performed on the neck based on our ESSCN electronics as demonstrated in (**Figure 12c**). **Figure 12d** presents real-time relative resistance curve of ESSCN

electronics over the JVP pulse signals. The ESSCN electronics endow provide high resolution to intuitively display clinical information of JVP pulse signals due to the ultra-sensitive (71.07 kPa^{-1}) and fast response time ($<2 \text{ ms}$). In general, a typical biphasic waveform of JVP contains important clinical messages which can be derived from three upward and two downward deflections certain characteristic points through the cardiac mechanism.²⁶⁶ As indicated in **Figure 12e**, the three upward deflections consists of “A”(atrial contraction), “C”(right ventricular contraction), “V” (atrial venous filling); while the two downward consists of “X”(the atrium relaxes) and “Y”(opening of the tricuspid valve), which are associated with the previous literature data.²⁶⁶ Such promising results suggest that the ESSCN pressure sensor can delicately collect physical signals, implying its potential to serve as a noninvasive, biocompatible, wearable, and real-time health-monitoring device for disease diagnosis.

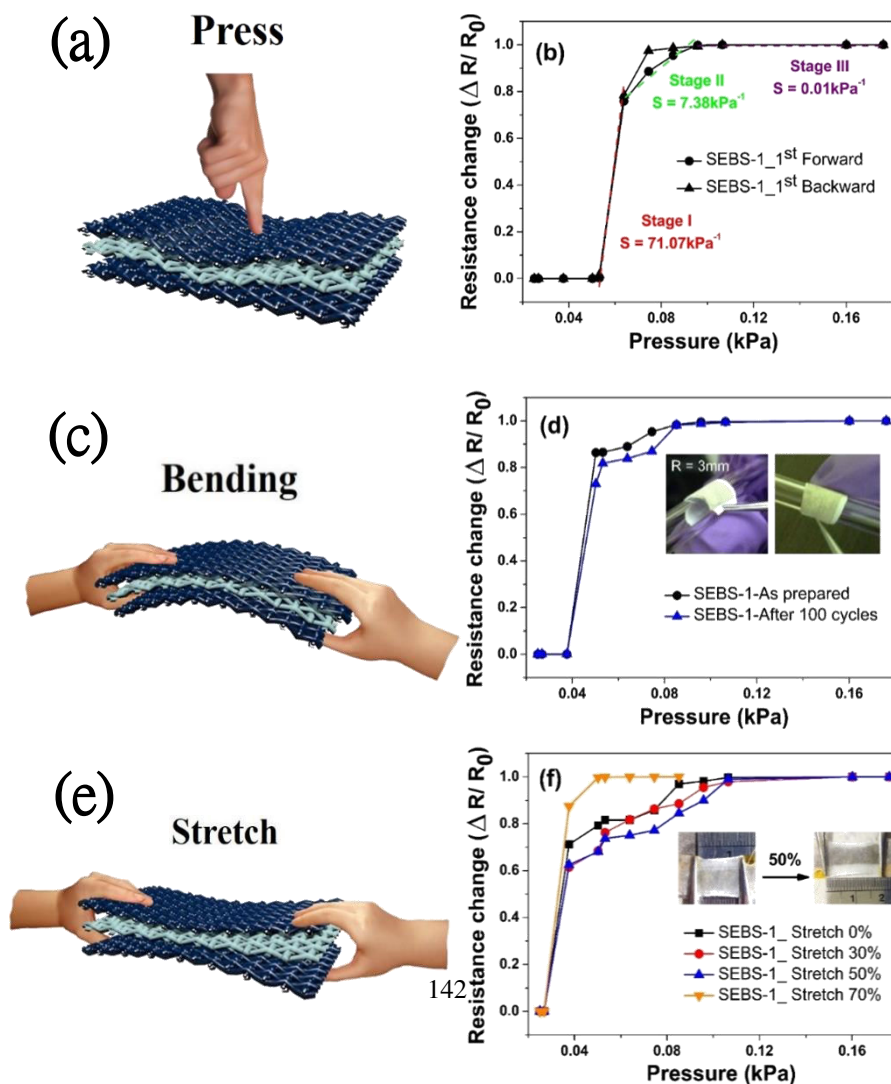


Figure 7. Detection of various static mechanical stimuli: (a, c, e) Schematic illustration of the shape deformation of the SEBS-1 pressure sensor under press, stretching, and bending. (b, d, f) The plots of relative resistance change ($\Delta R/R_0$) of the sensors as a function of loading force under pressures, bending curvatures, and tensile strains, respectively.

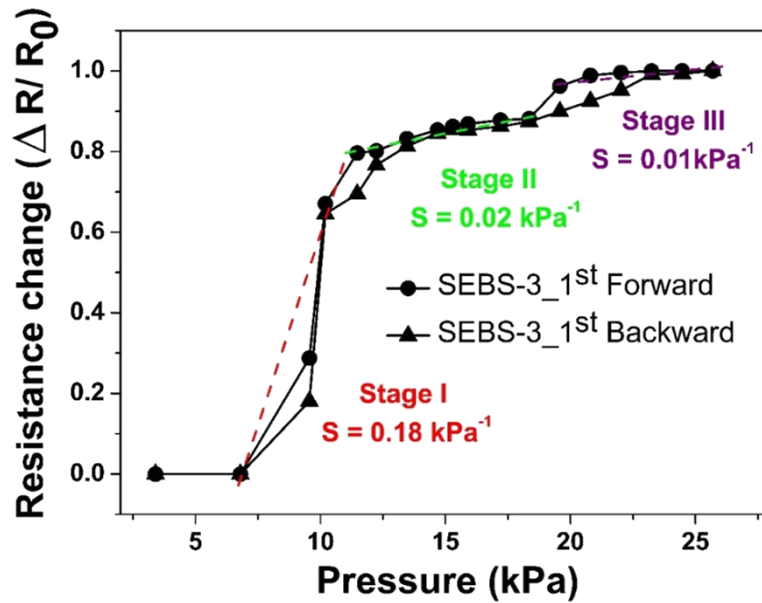


Figure 8. The plots of relative resistance change ($\Delta R/R_0$) of the SEBS-3 pressure sensor as a function of loading force under pressures.

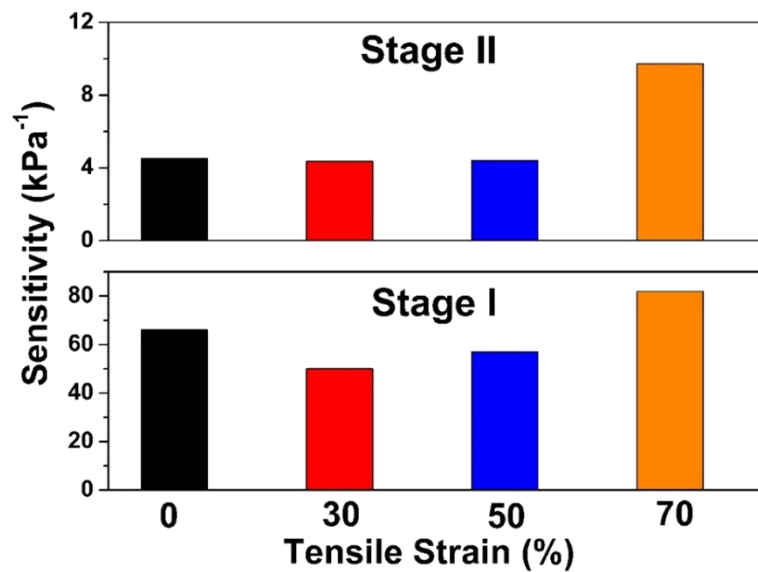


Figure 9. The sensitivities of the sensor under various tensile strain at stage I and stage II, which was obtained from the slopes of the curves in **Figure 7f**.

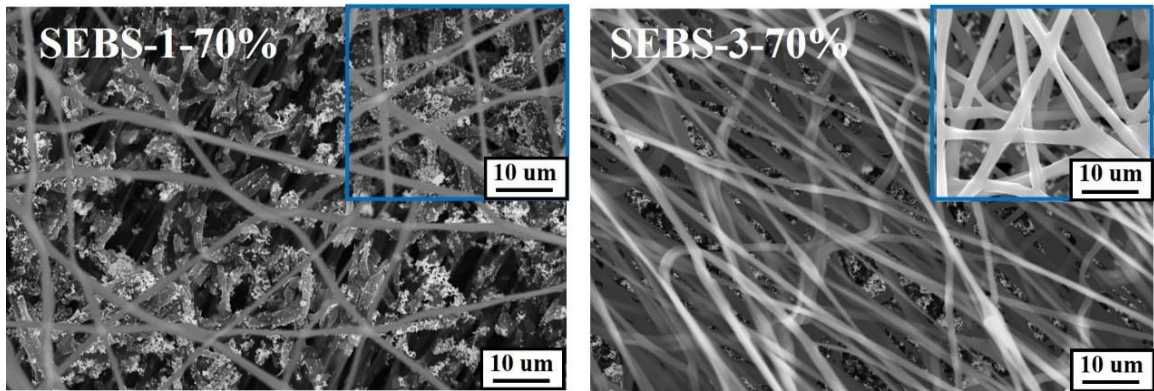


Figure 10. SEM image of the SEBS-1 and SEBS-3 composites before stretching (inset) and after 70% of the tensile strain.

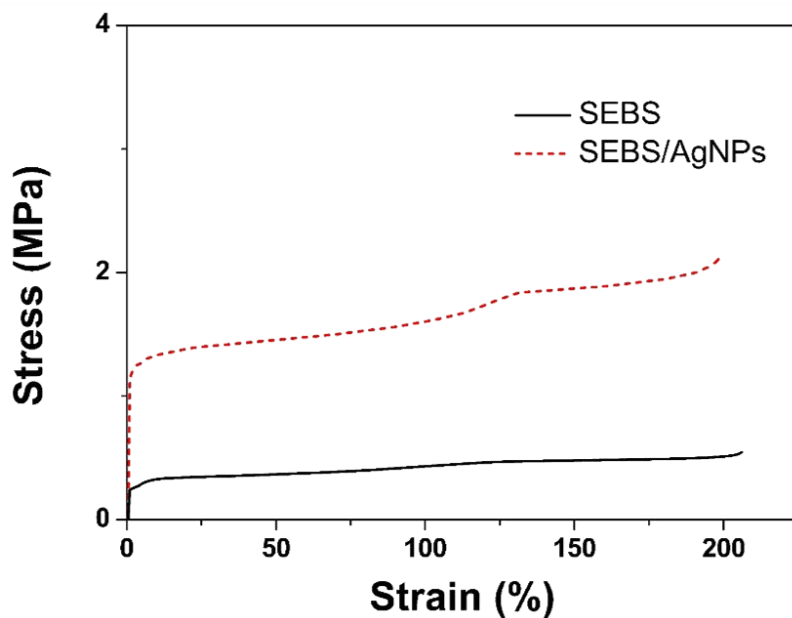


Figure 11. Stress-strain curves of SEBS and SEBS-AgNPs composites.

4-7 Conclusions

In summary, we firstly demonstrated a novel skin-inspired highly stretchable and nano-deformable ultrasensitive pressure sensor based on natural resistive-type SEBS nanofiber membranes through the eco-friendly, facile, cost-effective, lithographic-free, and large-area capable approach. The ESSCN with uniquely uniformly fibrous interlocked-microstructures capable of sensing, differentiating, and simultaneously

capturing various tactile stimulation information induced by normal pressure, lateral strain, and bending. Furthermore, our newly-designed fibrous-based ESSCN electronics possess numerous remarkable features and advantageous merits, including an ultrahigh sensitivity for a broad pressure range (71.07 kPa^{-1} for 0.2-60 Pa and 7.38 kPa^{-1} for 63-95 kPa⁻¹), a rapid response time (<2 ms), and an excellent durability and stability over (>100 cycles), thereby exhibiting unprecedented features and superior performance in contrast with previously reported pressure sensors. Additionally, our ESSCN electronics configuration was observed to demonstrate a wide resistance value range, and, more importantly, the threshold of resistance switching range and its sensitivity could be varied in terms of its thickness by modulating the electrospinning time to achieve specific requirements for various applications. Based on remarkable performance and the superior conformal contact of the sensor onto an uneven surface, the circuit of RGB-LED garments and high-fidelity human physiological signal (jugular venous pulses) can be monitored in real-time. We foresee that our skin-inspired ESSCN pressure sensors, which is fabricated from a natural rubber material through a cost-effective, lightweight, large-area expandability, and possesses combined features simultaneous multi-stimulus sensing, enable potentially facile integration into wearable artificial skins for human health monitoring, medical diagnostics, and tactile sensors.

Chapter 5 • References and Notes.

1. Hamilton, J. W.; Kaltreider, R. C.; Bajenova, O. V.; Innat, M. A.; McCaffrey, J.; Turpie, B. W.; Rowell, E. E.; Oh, J.; Nemeth, M. J.; Pesce, C. A.; Lariviere, J. P. *Environ. Health* **1998**, *106*, 1005-1015.
2. Vallee, B. L.; Ulmer, D. D. *Annu. Rev. Biochem.* **1972**, *41*, 91-128.
3. Partanen, T.; Heikkila, P.; Hernberg, S.; Kauppinen, T.; Moneta, G.; Ojajarvi, A. *Scand. J. Work. Environ. Health* **1991**, *17*, 231-239.
4. W. S. Wan Ngah, M. A. *Bioresource. Technol.* **2008**, *99*, 3935-3948.
5. U.S. Environmental Protection Agency. Risk Assessment, Management and Communication of Drinking Water Contamination; US EPA 625/4-89/024, EPA: Washington, DC, **1989**.
6. M. Ghaedi, F. Ahmadi, A. Shokrollahi, *J. Hazard. Mater.* **2007**, *142*, 272-278.
7. H. Karami, M. F. Mousavi, Y. Yamini, M. Shamsipur, *Anal. Chim. Acta* **2004**, *509*, 89-97.
8. E. Marguí, P. Kregsamer, M. Hidalgo, J. Tapias, I. Queralt, C. Strelí, *Talanta* **2010**, *82*, 821-827.
9. Z. Chen, M. Megharaj, R. Naidu, *Talanta* **2007**, *72*, 394-400.
10. Rurack, K.; Resch-Genger, U. *Chem. Soc. Rev.* **2002**, *31*, 116-127.
11. Yang, Y. K.; Yook, K. J.; Tae, J. *J. Am. Chem. Soc.* **2005**, *127*, 16760-16761.
12. Amendola, V.; Fabbri, L.; Foti, F.; Licchelli, M.; Mangano, C.; Pallavicini, P.; Poggi, A.; Sacchi, D.; Taglietti, A. *Coord. Chem. Rev.* **2006**, *250*, 273-299.
13. Boening, D. W. *Chemosphere* **2000**, *40*, 1335-1351.
14. Milaeva, E. R. *Journal of Inorganic Biochemistry* **2006**, *100*, 905-915.
15. Liu, B.; Tian, H. *Chem. Commun.* **2005**, *25*, 3156-3158.
16. Leng, B.; Zou, L.; Jiang, J.; Tian, H. *Sens. Actuators, B* **2009**, *140*, 162-169.
17. Zou, Q.; Tian, H. *Sens. Actuators, B* **2010**, *149*, 20-27.
18. Lua, Z. J.; Wang, P. N.; Zhang, Y.; Chen, J. Y.; Zhen, S.; Leng, B.; Tian, H. *Anal. Chim. Acta* **2007**, *597*, 306-312.
19. Wang, W.; Wen, Y.; Zhang, Y.; Fei, X.; Li, Y.; Yang, Q.; Xu, X. *Dalton Trans.* **2013**, *42*, 1827-1833.
20. Liu, C.; Xu, J.; Yang, F.; Zhou, W.; Li, Z.; Wei, M.; Yu, M. *Sens. Actuators, B* **2015**, *212*, 364-370.
21. Patrick, L. G. F.; Whiting, A. *Dyes Pigm.* **2002**, *55*, 123-132.
22. Fan, J.; Lin, C.; Li, H.; Zhan, P.; Wang, J.; Cui, S.; Hu, M.; Cheng, G.; Peng, X. *Dyes Pigm.* **2013**, *99*, 620-676.
23. Hu, Z. Q.; Li, M.; Liu, M. D.; Zhuang, W. M.; Li, G. K. A. *Dyes Pigm.* **2013**, *96*,

71-75.

24. Shi, X. L.; Mao, G. J.; Zhang, X. B.; Liu, H. W.; Gong, Y. J.; Wu, Y. X.; Zhou, L. Y.; Zhang, J.; Tan, W. *Talanta* **2014**, *130*, 356-362.
25. Babel, A.; Li, D.; Xia, Y.; Jenekhe, S. A. *Macromolecules* **2005**, *38*, 4705-4711.
26. Kuo, C. C.; Lin, C. H.; Chen, W. C. *Macromolecules* **2007**, *40*, 6959-6966.
27. Kuo, C. C.; Tung, Y. C.; Lin, C. H.; Chen, W. C. *Macromol. Rapid Commun.* **2008**, *29*, 1711-1715.
28. Chen, Y. Y.; Kuo, C. C.; Chen, B. Y.; Chiu, P. C.; Tsai, P. C. *J. Polym. Sci., Part B: Polym. Phys.* **2015**, *53*, 262-269.
29. Kuo, C. C.; Tung, Y. C.; Chen, W. C. *Macromol. Rapid Commun.* **2010**, *31*, 65-70.
30. Chiu, Y. C.; Kuo, C. C.; Hsu, J. C.; Chen, W. C. *ACS Appl. Mater. Interfaces* **2010**, *2*, 3340-3347.
31. Chiu, Y. C.; Chen, Y.; Kuo, C. C.; Tung, S. H.; Kakuchi, T.; Chen, W. C. *ACS Appl. Mater. Interfaces* **2012**, *4*, 3387-3395.
32. Chen, L. N.; Chiu, Y. C.; Hung, J. J.; Kuo, C. C.; Chen, W. C. *Macromol. Chem. Phys.* **2014**, *215*, 286-294.
33. Wang, W.; Yang, Q.; Sun, L.; Wang, H.; Zhang, C.; Fei, X.; Sun, M.; Li, Y. *J. Hazard. Mater.* **2011**, *194*, 185-192.
34. Chen, L. N.; Kuo, C. C.; Chiu, Y. C.; Chen, W. C. *RSC Adv.* **2014**, *4*, 45345-45353.
35. Chen, B. Y.; Kuo, C. C.; Huang, Y. S.; Lu, S. T.; Liang, F. C.; Jiang, D. H. *ACS Appl. Mater. Interfaces* **2015**, *7*, 2797-2808.
36. Cho, C. J.; Lu, S. T.; Kuo, C. C.; Liang, F. C.; Chen, B. Y.; Chu, C. C. *React. Funct. Polym.* **2016**, *108*, 137-147.
37. Hung, C. C.; Kuo, C. C.; Weng, N. K.; Wu, W. C.; Chen, B. Y.; Cho, C. J.; Hsu, I. J.; Chiu, Y. C.; Chen, C. C. *Polym. J. (Tokyo, Jpn.)* **2016**, *48*, 439-449.
38. Chen, J.; Zeng, F.; Wu, S.; Su, J.; Tong, Z. *Small* **2009**, *5*, 970-978.
39. Hu, Z. Q.; Lin, C. S.; Wang, X. M.; Ding, L.; Cui, C. L.; Liu, S. F.; Lu, H. Y. *Chem. Commun.* **2010**, *46*, 3765-3767.
40. Wan, X.; Liu, S. *J. Mater. Chem.* **2011**, *21*, 10321-10329.
41. Wang, J.; Li, H.; Long, L.; Xiao, G.; Xie, D. *J. Lumin.* **2012**, *132*, 2456-2461.
42. D. Maity, T. Govindaraju, *Inorg. Chem.* **2011**, *50*, 11282-11284.
43. Q. Zhao, F.Y. Li, C.H. Huang, *Chem. Soc. Rev.* **2010**, *39*, 3007-3030.
44. Y.J. Na, W.Y. Choi, G.R. You, C. Kim, *Sens. Actuators B* **2016**, *223*, 234-240.
45. T. Gunnlaugsson, H.D.P. Ali, M. Glynn, P.E. Kruger, G.M. Hussey, F.M. Pfeffer, C.M.D. dos Santos, J. Tierney, *J. Fluoresc.* **2005**, *15*, 287-299.
46. M.Y. Berezin, S. Achilefu, *Chem. Rev.* **2010**, *110*, 2641-2684.
47. Z.-X. Han, X.-B. Zhang, Z. Li, Y.-J. Gong, X.-Y. Wu, Z. Jin, C.-M. He, L.-X. Jian, J. Zhang, G.-L. Shen, R.-Q. Yu, *Anal. Chem.* **2010**, *82*, 3108-3113.

48. C.Y. Li, Y. Zhou, Y.F. Li, C.X. Zou, X.F. Kong, *Sens. Actuators B* **2013**, *186*, 360-366.
49. Y. Zhang, Y. Fang, N.Z. Xu, M.Q. Zhang, G.Z. Wu, C. Yao, *Chin. Chem. Lett.* **2016** *26*, 1673-1678.
50. V. Guzsvány, H. Nakajima, N. Soh, K. Nakano, I. Švancara, K. Vytřas, L. Bjelica, T. Imato, *Electroanal.* **2011**, *23*, 1593-1596.
51. G. Aragay, J. Pons, A. Merkoçi, *Chem. Rev.* **2011**, *111*, 3433-3458.
52. Kim, J. S., Quang, D. T. *Chem. Rev.*, **2007**, *107*, 3780-3799
53. C. S. Lim, J. N. Miller, J.W. Bridges, *Anal. Chim. Acta* **1980**, *114*, 183-189.
54. Ono, A.; Togashi, H. *Angew. Chem., Int. Ed.* **2004**, *43*, 4300-4302.
55. Kim, H. N., Lee, M. H., Kim, H. J., Kim, J. S., Yoon, J. *J. Chem. Soc. Rev.*, **2008**, *37*, 1465-1472.
56. Y.-K. Yang, K.-J. Yook and J. Tae, *J. Am. Chem. Soc.*, **2005**, *127*, 16760-16761.
57. Chen, J.; Zeng, F.; Wu, S.; Su, J.; Tong, Z. *Small* **2009**, *5*, 970-978.
58. Xu, M.; Wu, S.; Zeng, F.; Yu, C. *Langmuir* **2010**, *26*, 4529-4534.
59. Li, C.; Liu, S. *Chem. Commun.* **2012**, *48*, 3262-3278.
60. Ma, B.; Wu, S.; Zeng, F.; Luo, Y.; Zhao, J.; Tong, Z. *Nanotechnology* **2010**, *21*, 195501-195512.
61. Wan, X.; Liu, S. *J. Mater. Chem.* **2011**, *21*, 10321-10329.
62. Lee, M. H., Kim, H. J., Yoon, S., Park, N., Kim, J. S. *Org. Lett.*, **2008**, *10*, 213-216.
63. A. Yarin, S. Koombhongse and D. Reneker, *J. Appl. Phys.*, **2001**, *90*, 4836-4846.
64. B. J. Haupt, T. J. Senden and E. M. Sevick, *Langmuir*, **2002**, *18*, 2174-2182.
65. S. Mei, X. Feng and Z. Jin, *Macromolecules*, **2011**, *44*, 1615-1620.
66. K. M. Forward and G. C. Rutledge, *Chem. Eng. J.*, **2012**, *183*, 492-503.
67. W. Wang, Q. Yang, L. Sun, H. Wang, C. Zhang, X. Fei, M. Sun, Y. Li, *J. Hazard. Mater. Part A*. **2011**, *194*, 185-192.
68. Li, C.; Zhang, Y.; Hu, J.; Cheng, J.; Liu, S. *Angew. Chem., Int. Ed.* **2010**, *49*, 5120-5124.
69. Gregg, S. J.; Sing, K. S. W. Adsorption, Surface Area and Porosity: Academic Press: New York, **1982**.
70. Huang, Y. S.; Kuo, C. C.; Shu, Y. C.; Jang, S. C.; Tsen, W. C.; Chuang, F. S.; Chen, C. C. *Macromol. Chem. Phys.* **2014**, *215*, 879-887.
71. Huang, Y. S.; Kuo, C. C.; Huang, C. C.; Jang, S. C.; Tsen, W. C.; Chuang, F. S.; Chen, B. Y.; Chen, J. J.; Chow, J. D.; Shu, Y. C. *RSC Adv.* **2015**, *5*, 88857-88865.
72. Manimala, J. C.; Anslyn, E. V. *Eur. J. Org. Chem.* **2002**, 3909-3922.
73. Kim, K. S.; Qian, L. *Tetrahedron Lett.* **1993**, *34*, 7677-7680.
74. Batey, R. A.; Powell, D. A. *Org. Lett.* **2000**, *2*, 3237-3240.
75. Megelski, S.; Stephents, J. S.; Chase, D. B.; Rabolt, J. F. *Macromolecules* **2002**,

- 35, 8456-8466.
76. Chen, H. C.; Wang, C. T.; Liu, C. L.; Liu, Y. C.; Chen, W. C. *J. Polym. Sci., Part B: Polym. Phys.* **2009**, *47*, 463-470.
 77. Wang, C. T.; Kuo, C. C.; Chen, H. C.; Chen, W. C. *Nanotechnology* **2009**, *20*, 375604-375614.
 78. Smith, T.; Guild, J. The C.I.E. *Trans. Opt. Soc.* **1931**, *33*, 73-134.
 79. Poynton, C. A Guided Tour of Color Space: John Wiley & Sons: New York, **1997**, 1-14.
 80. Jiao, G. S.; Loudet, A.; Lee, H. B.; Kalinin, S.; Johansson, L. B. A.; Burgess, K. . *Tetrahedron* **2003**, *59*, 3109-3116.
 81. Chang, D.; Zhao, W.; Yang, H.; Huang, Z.; Liu, X.; Han, A. *Tetrahedron Lett.* **2016**, *57*, 2655-2659.
 82. Degirmenci, A.; Algi, F. *Dyes Pigm.* **2017**, *140*, 92-99.
 83. Wang, X.; Drew, C.; Lee, S. H.; Senecal, K. J.; Kumar, J.; Samuelson, L. *Nano Lett.* **2002**, *2*, 1273-1275.
 84. Reddy, C. S.; Zak, A.; Zussman, E. *J. Mater. Chem.* **2011**, *21*, 16086-16093.
 85. Meier W: *ChSRv* **2000**, *29*, 295-303.
 86. Sun P, Zhang Y, Shi L, Gan Z: *Macromol Biosci* **2010**, *10*, 621-631.
 87. Torchilin V: *Adv Drug Deliv Rev* **2011**, *63*, 131-135.
 88. Peng, F. B.; Lu, L. Y.; Sun, H. L.; Wang, Y. Q.; Liu, J. Q.; Jiang, Z. Y. *Chem. Mater.* **2005**, *17*, 6790-6796.
 89. Kariduraganavar, M. Y.; Varghese, J. G.; Choudhari, S. K.; Olley, R. H. *Ind. Eng. Chem. Res.* **2009**, *48*, 4002-4010.
 90. Ferguson CJ, Hughes RJ, Pham BTT, Hawkett BS, Gilbert RG, Serelis AK, Such CH: *Macromolecules* **2002**, *35*, 9243-9245.
 91. Du JZ, Sun TM, Song WJ, Wu J, Wang J: *Angew Chem Int Ed Engl* **2010**, *49*, 3621-3626.
 92. Lefaux CJ, Zimmerlin JA, Dobrynin AV, Mather PT. *J Polym Sci Part B: Polym Phys* **2004**, *42*, 3654-3666.
 93. Liu TY, Hu SH, Liu K, Liu DM, Chen SY, *J Control Release* **2008**, *126*, 228-236.
 94. Heskins M, Guillet JE, *J MACROMOL SCI A-CHEM* **1968**, *2*, 1441-1455.
 95. Balamurugan SS, Bantchev GB, Yang Y, McCarley RL *Angew Chem* **2005**, *117*, 4950-4954.
 96. Caruso F: *Chem Eur J* **2000**, *6*, 413-419.
 97. Chiang WH, Huang WC, Chang CW, Shen MY, Shih ZF, Huang YF, Lin SC, Chiu HC, *J Control Release* **2013**, *168*, 280-288.
 98. Hu SH, Liao BJ, Chiang CS, Chen PJ, Chen IW, Chen SY, *Adv Mater* **2012**, *24*, 3627-3632.

99. Huang H-Y, Hu S-H, Chian C-S, Chen S-Y, Lai H-Y, Chen Y-Y, *J. Mater. Chem.*, **2012**, *22*, 8566-8573.
100. Liu T-Y, Hu S-H, Liu D-M, Chen S-Y, Chen I.W, *Nano Today* **2009**, *4*, 52-65.
101. Liu T-Y, Hu S-H, Liu K-H, Shaiu R-S, Liu D-M, Chen S-Y, *Langmuir* **2008**, *24*, 13306-13311.
102. Liu T-Y, Liu K-H, Liu D-M, Chen S-Y, Chen I.W., *Adv Funct Mater* **2009**, *19*, 616-623.
103. Ruhland TM, Reichstein PM, Majewski AP, Walther A, Muller AH. *J Colloid Interface Sci* **2012**, *374*, 45-53.
104. Gil, E.S.; Hudson, S.M. *Prog. Polym. Sci.* **2004**, *29*, 1173-1222.
105. Chen, S.; Jiang, L.; Dan, Y. *J. Appl. Polym. Sci.* **2011**, *121*, 3322-3331.
106. Yang, X.; Jiang, Wei.; Liu, L.; Chen, B.; Wu, S.; Sun, D.; Li, F. *J. Magn. Magn. Mater.* **2012**, *324*, 2249-2257.
107. Si, S.; Kotal, A.; Mandal, T.K.; Giri, S.; Nakamura, H.; Kohara, T. *Chem. Mater.* **2004**, *16*, 3489-3496.
108. Zhao, C.; Jiang, Z.; Zhao, J.; Cao, K.; Zhang, Q.; Pan, F. *Ind. Eng. Chem. Res.* **2014**, *53*, 1606-1616.
109. Jiang, X.; Zhai, S.; Jiang, X.; Lu, G.; Huang, X. *Polymer* **2014**, *55*, 3703-3712.
110. Liu, F.; Ni, Q.Q.; Murakami, Y. *Text. Res. J.* **2013**, *83*, 510-518.
111. Xu, L.; Liu, N.; Cao, Y.; Lu, F.; Chen, Y.; Zhang, X.; Feng, L.; Wei, L. *ACS Appl. Mater. Interfaces* **2014**, *6*, 13324-13329.
112. Jinming Hu and Shiyong Liu, *Macromolecules* **2010**, *43*, 8315-8330
113. Uchiyama, S.; Kawai, N.; de Silva, A. P.; Iwai, K. *J. Am. Chem. Soc.* **2004**, *126*, 3032-3033.
114. Hu, J. M.; Li, C. H.; Liu, S. Y. *Langmuir* **2010**, *26*, 724-729.
115. Li, C. H.; Liu, S. Y. *J. Mater. Chem.*, **2010**, *20*, 10716-10723.
116. Qiao, R. R.; Yang, C. H.; Gao, M. Y. *J. Mater. Chem.* **2009**, *19*, 6274-6293.
117. Dudek, G.; Turczyn, R.; Strzelewicz, A.; Krasowska, M.; Rybak, A.; Grzywna, Z. *J. Sep. Purif. Technol.* **2013**, *109*, 55-63.
118. Hasanabadi, N.; Ghaffarian, S. R.; Hasani-Sadrabadi, M. M. *Solid State Ionics* **2013**, *232*, 58-67.
119. Yathindranath, V.; Rebbouh, L.; Moore, D. F.; Miller, D. W.; Lierop, J. V.; Hegmann, T. *Adv. Funct. Mater.* **2011**, *21*, 1457-1464.
120. Reddy, L. H.; Arias, J. L.; Nicolas, J.; Couvreur, P. *Chem. Rev.* **2012**, *112*, 5818.
121. C. Sanson, O. Diou, J. Th_ evenot, E. Ibarboure, A. Soum, A. Brulet, S. Miraux, E. Thiaudiere, S. Tan, A. Brisson, V. Dupuis, O. Sandre and S. b. Lecommandoux, *ACS Nano*, **2011**, *5*, 1122-1140.

122. Huang, H.-Y., Hu, S.-H., Chian, C.-S., Chen, S.-Y., Lai, H.-Y., Chen, Y.-Y., *J. Mater. Chem.*, **2012**, *22*, 8566-8573
123. Zhang, W.; Zhang, W.; Zhou, N.; Cheng, Z.; Zhu, J.; Zhu, X. *Polymer* **2008**, *49*, 4569-4575.
124. Manimala, J.C.; Anslyn, E.V. *J. Org. Chem.* **2002**, *23*, 3909-3922.
125. Kim, K.S.; Qian, L. *Tetrahedron Lett.* **1993**, *34*, 7677-7680.
126. Batey, R.A.; Powell, D.A. *Org. Lett.* **2000**, *2*, 3237-3240.
127. Zhang, X.; Niu, Y.; Meng, X.; Li, Y.; Zhao, J. *CrystEngComm* **2013**, *15*, 8166-8172.
128. P. C. Hsu, S. Wang, H. Wu, V. K. Narasimhan, D. Kong, H. R. Lee, Y. Cui, *Nat. Commun.*, **2013**, *4*, 2522-2529.
129. J. Liang, L. Li, K. Tong, Z. Ren, W. Hu, X. Niu, Y. Chen, Q. Pei, *ACS Nano* **2014**, *8*, 1590-1600.
130. H. Guo, N. Lin, Y. Chen, Z. Wang, Q. Xie, T. Zheng, N. Gao, S. Li, J. Kang, D. Cai, D. L. Peng, *Sci. Rep.* **2013**, *8*, 421-425.
131. S. Iijima, *Nature*, **1991**, *354*, 56-58.
132. K. S. Novoselov, A. K. Geim, S. V. Morozov, D. Jiang, Y. Zhang, S. V. Dubonos, I. V. Grigorieva, A. A. Firsov, *Science*, **2004**, *306*, 666-669.
133. J. Y. Lee, S. T. Connor, Y. Cui, P. Peumans, *Nano Letters*, **2008**, *8*, 689-692.
134. Y. Xia, G. M. Whitesides, *Annu. Rev. Mater. Sci.* **1998**, *28*, 153-184.
135. J. A. Rogers, R. G. Nuzzo, *Mater. Today* **2005**, *8*, 50-56.
136. E. Menard, M. A. Meitl, Y. Sun, J.-U. Park, D. J. Shir, Y.-S. Nam, S. Jeon, J. A. Rogers, *Chem. Rev.* **2007**, *107*, 1117-1160.
137. Q. Cao, J. A. Rogers, *Adv. Mater.* **2009**, *21*, 29-53.
138. T. Dürkop, S. A. Getty, E. Cobas, M. S. Fuhrer, *Nano Lett.* **2004**, *4*, 35-39.
139. T. W. Kelley, P. F. Baude, C. Gerlach, D. E. Ender, D. Muires, M. A. Haase, D. E. Vogel, S. D. Theiss, *Chem. Rev.* **2004**, *16*, 4413-4422.
140. J. M. J. Frechet, *Science* **1994**, *263*, 1710-1715.
141. J. Yeom, M. A. Shannon, *Adv. Funct. Mater.* **2010**, *20*, 289-295.
142. S.-I. Park, Y. Xiong, R.-H. Kim, P. Elvikis, M. Meitl, D.-H. Kim, J. Wu, J. Yoon, C.-J. Yu, Z. Liu, Y. Huang, K.-C. Hwang, P. Ferreira, X. Li, K. Choquette, J. A. Rogers, *Science* **2009**, *325*, 977-981.
143. J.-H. Choi, K.-H. Kim, S.-J. Choi, H. H. Lee, *Nanotechnology* **2006**, *17*, 2246-2249.
144. J. Yoon, A. J. Baca, S.-I. Park, P. Elvikis, J. B. Geddes III, L. Li, R. H. Kim, J. Xiao, S. Wang, T.-H. Kim, M. J. Motala, B. Y. Ahn, E. B. Duoss, J. A. Lewis, R. G. Nuzzo, P. M. Ferreira, Y. Huang, A. Rockett, J. A. Rogers, *Nat. Mater.* **2008**, *7*, 907-915.

145. A. J. Baca , K. J. Yu , J. Xiao , S. Wang , J. Yoon , J. H. Ryu , D. Stevenson , R. G. Nuzzo , A. A. Rockett , Y. Huang , J. A. Rogers , *Energy Environ. Sci.* **2010**, *3* , 208-211.
146. D.-H. Kim , Y.-S. Kim , J. Wu , Z. Liu , J. Song , H.-S. Kim , Y. Y. Huang , K.-C. Hwang , J. A. Rogers , *Adv. Mater.* **2009**, *21*, 3703-3707.
147. J.-H. Ahn , H.-S. Kim , K. J. Lee , S. Jeon , S. J. Kang , Y. Sun , R. G. Nuzzo , J. A. Rogers , *Science* **2006** , *314* , 1754-1757.
148. S. Kim , J. Wu , A. Carlson , S. H. Jin , A. Kovalsky , P. Glass , Z. Liu , N. Ahmed , S. L. Elgan , W. Chen , P. M. Ferreira , M. Sitti , Y. Huang , J. A. Rogers , *Proc. Natl. Acad. Sci. U.S.A.* **2010** , *107* , 17095-17100.
149. D. Chanda , K. Shigeta , S. Gupta , T. Can, A. Carlson , A. Mihi , A. J. Baca , G. R. Bogart , P. Braun , J. A. Rogers , *Nat. Nanotechnol.* **2011** , *6* , 402-407.
150. Q. Cao , H.-S. Kim , N. Pimparkar , J. P. Kulkarni , C. Wang , M. Shim , K. Roy , M. A. Alam , J. A. Rogers , *Nature* **2008** , *454* , 495-500.
151. A. Kumar and C. Zhou, *ACS Nano* **2010**, *4*, 11-14.
152. Y. Kim, T. I. Ryu, K.-H. Ok, M.-G. Kwak, S. Park, N.-G. Park, C.-J. Han, B.-S. Kim, M.-J. Ko, H.-J. Son and J.-W. Kim, *Adv. Funct. Mater.* **2015**, *25*, 4580-4589.
153. D. S. Hecht and L. Hu, G. Irvin, *Adv. Mater.* **2011**, *23*, 1482.
154. L. Hu, H. Wu and Y. Cui, *MRS Bull.* **2011**, *36*, 760-765.
155. D.-H. Kim, N. Lu, R. Ma, Y.-S. Kim, R.-H. Kim, S. Wang, J. Wu, S. M. Won, H. Tao, A. Islam, K. J. Yu, T.-I. Kim, R. Chowdhury, M. Ying, L. Xu, M. Li, H.-J. Chung, H. Keum, M. McCormick, P. Liu, Y.-W. Zhang, F. G. Omenetto, Y. Huang, T. Coleman and J. A. Rogers, *Science* **2011**, *333*, 838-843.
156. D. Son, J. Lee, S. Qiao, R. Ghaffari, J. Kim, J. E. Lee, C. Song, S. J. Kim, D. J. Lee, S. W. Jun, S. Yang, M. Park, J. Shin, K. Do, M. Lee, K. Kang, C. S. Hwang, N. Lu, T. Hyeon and D.-H. Kim, *Nat. Nanotechnol.* **2014**, *9*, 397-404.
157. J. Jiu, T. Araki, J. Wang, M. Nogi, T. Sugahara, S. Nagao, H. Koga, K. Suganuma, E. Nakazawa, M. Hara, H. Uchidab and K. Shinozakic, *J. Mater. Chem. A* **2014**, *2*, 6326-6330.
158. H. Kang, S. Jung, S. Jeong, G. Kim and K. Lee, *Nat. Commun.* **2015**, *6*, 6503-6510.
159. M.-S. Lee, K. Lee, S.-Y. Kim, H. Lee, J. Park, K.-H. Choi, H.-K. Kim, D.-G. Kim, D.-Y. Lee, S.-W. Nam and J.-U. Park, *Nano Lett.* **2013**, *13*, 2814-2821.
160. L. Hu, H.-S. Kim, J.-Y. Lee, P. Peumans and Y. Cui, *ACS Nano* **2010**, *4*, 2955-2963.
161. S. Choi, S. I. Han, D. Jung, H. J. Hwang, C. Lim, S. Bae, O. K. Park, C. M. Tschabrunn, M. Lee, S. Y. Bae, J. W. Yu, J. H. Ryu, S.-W. Lee, K. Park, P. M. Kang, W. B. Lee, R. Nezafat, T. Hyeon and D.-H. Kim, *Nat. Nanotechnol.* **2018**, *13*,

- 1048-1058.
162. M. Layani, A. Kamyshny and S. Magdassi, *Nanoscale* **2014**, *6*, 5581-5591.
163. D. Langley, G. Giusti, G. Mayousse, C. Celle, D. Bellet and J.-P. Simonato, *Nanotechnology* **2013**, *24*, 452001-452021.
164. C. Yan, W. Kang, J. Wang, M. Cui, X. Wang, C. Y. Foo, K. J. Chee and P. S. Lee, *ACS Nano* **2014**, *8*, 316-322.
165. H.-C. Liu, Y.-C. Lai, C.-C. Lai, B.-H. Wu, H.-W. Zan, P. Yu, Y.-L. Chueh and C.-C. Tsai, *ACS Appl. Mater. Interfaces* **2015**, *7*, 232-240.
166. D.-S. Leem, A. Edwards, M. Faist, J. Nelson, D. D. C. Bradley and J. C.D. Mello, *Adv. Mater.* **2011**, *23*, 4371-4375.
167. H. Lee, D. Lee, Y. Ahn, E.-W. Lee, L. S. Park and Y. Lee. *Nanoscale* **2014**, *6*, 8565-8570.
168. J. Lee, P. Lee, H. B. Lee, S. Hong, I. Lee, J. Yeo, S. S. Lee, T.-S. Kim, D. Lee and S. H. Ko *Adv. Funct. Mater.* **2013**, *23*, 4171-4176.
169. Y. Joo, J. Byun, N. Seong, J. Ha, H. Kim, S. Kim, T. Kim, H. Ima, D. Kima and Y. Hong, *Nanoscale* **2015**, *7*, 6208-6215.
170. J. Song, H. Jiang, Y. Huang and J. A. Rogers, *Sci. Technol. A* **2009**, *27*, 1107-1125.
171. C. Yan, J. Wang, X. Wang, W. Kang, M. Cui, C.Y. Foo and P. S. Lee, *Adv. Mater.* **2013**, *26*, 943-950.
172. F. Xu and Y. Zhu, *Adv. Mater.* **2012**, *24*, 5117-5122.
173. S. De, T. M. Higgins, P. E. Lyons, E. M. Doherty, P. N. Nirmalraj, W. J. Blau, J. J. Boland and J. N. Coleman, *ACS Nano* **2009**, *3* , 1767-1774.
174. B.X.-Y. Zeng, Q.-K. Zhang, R.-M. Yu and C.Z. Lu, *Adv. Mater.* **2010**, *22*, 4484-4488.
175. A. R. Madaria, A. Kumar and C. Zhou, *Nanotechnology* **2011**, *22*, 245201-245208.
176. A. R. Madaria, A. Kumar, F. N. Ishikawa and C. Zhou, *Nano Res* **2010**, *3*, 564-573.
177. M. K. Choil, J. Yang, K. Kang, D. C. Kim, C. Choil, C. Park, S. J. Kim, S. I. Chae, T.-H. Kim, J. H. Kim, T. Hyeon and D.-H. Kim, *Nat. Commun.* **2015**, *6*, 7149-8149.
178. B. C. Yu, C. Masarapu, J. JRong, B. Wei and H. Jiang, *Adv. Mater.* **2009**, *21*, 4793-4797.
179. J. Darren, D.J. Lipomi, B.C.-K. Tee, M. Vosgueritchian and Z. Bao, *Adv. Mater.* **2011**, *23*, 1771-1775.
180. M. A. Meitl, Y. Zhou, A. Gaur, S. Jeon, M. L. Usrey, M. S. Strano, J. A. Rogers, *Nano Lett.* **2004**, *4*, 1643-1647.
181. T. Kraus, L. Malaquin, H. Schmid, W. Riess, N. D. Spencer, H. Wolf, *Nat. Nanotechnol.* **2007**, *2*, 570-576.

182. S. Y. Park , T. Kwon , H. H. Lee , *Adv. Mater.* **2006** , *18* , 1861-1866.
183. J.-H. Choi , K.-H. Kim , S.-J. Choi , H. H. Lee , *Nanotechnology* **2006** , *17* , 2246-2249.
184. J. K. Kim , J. W. Park , H. Yang , M. Choi , J. H. Choi , K. Y. Suh , *Nanotechnology* **2006** , *17* , 940-946.
185. Z. Wang , J. Zhang , R. Xing , J. Yuan , D. Yan , Y. Han , *J. Am. Chem. Soc.* **2003** , *125* , 15278-15279
186. A. C. Ford , J. C. Ho , Y.-L. Chueh , Y.-C. Tseng , Z. Y. Fan , J. Guo , J. Bokor , A. Javey , *Nano Lett.* **2009** , *9* , 360-365.
187. A. Javey , S. Nam , R. S. Friedman , H. Yan , C. M. Lieber , *Nano Lett.* **2007** , *7* , 773-777.
188. Y. Huang , X. Duan , C. Lieber , *Small* **2005** , *1* , 142-147.
189. O. L. Muskens , S. L. Diederhofen , B. C. Kaas , R. E. Algra , E. P. A. M. Bakkers , J. G. Rivas , A. Lagendijk , *Nano Lett.* **2009** , *9* , 930-934.
190. Z. Y. Fan , J. G. Lu , *Appl. Phys. Lett.* **2005** , *86* , 123510-123514.
191. D. H. Zhang , Z. Liu , C. Li , T. Tang , X. Liu , S. Han , B. Lei , C. Zhou , *Nano Lett.* **2004** , *4* , 1919-1924.
192. K. Heo , C.-J. Kim , M.-H. Jo , S. Hong , *J. Mater. Chem.* **2009** , *19* , 901-908.
193. W. Lu , C. M. Lieber , *J. Phys. D: Appl. Phys.* **2006** , *39* , R387-R406.
194. H. J. Fan , P. Wener , M. Zacharias , *Small* **2006** , *2* , 700-704.
195. Y. Cui , M. T. Björk , J. A. Liddle , C. Sönnichsen , B. Boussert , A. P. Alivisatos , *Nano Lett.* **2004** , *4* , 1093-1101.
196. S. De , P. E. Lyons , P. N. Nirmalraj , S. Sorel , J. J. Boland , E. M. Doherty , P. J. King , W. J. Blau , V. Scardaci , J. Joimel and J. N. Coleman , *ACS Nano* **2009** , *3* , 714-720.
197. S. H. Tan , N.-T. Nguyen , Y.C. Chua and T. G. Kang , *Biomicrofluidics* **2010** , *4* , 032204-032208.
198. J. Y. Lee , S. T. Connor , Y. Cui and P. Peumans , *Nano Lett.* **2008** , *8* , 689-692.
199. W. Xu , Q. Xu , Q. Huang , R. Tan , W. Shen and W. Song , *J. Mater. Sci. Technol.* **2016** , *32* , 158-161.
200. T. Akter and W. S. Kim , *ACS Appl. Mater. Interfaces* **2012** , *4* , 1855-1859.
201. T. Araki , J. Jiu , M. Nogi , H. Koga , S. Nagao , T. Sugahara and K. Suganuma , *Nano Research* **2014** , *7* , 236-245.
202. S.-E. Park , S. Kim , D.-Y. Lee , E. Kim and J. Hwang , *J. Mater. Chem. A* **2013** , *1* , 14286-14293.
203. V. Scardaci , R. Coull , P. E. Lyons , D. Rickard and J. N. Coleman , *small* **2011** , *7* , 2621-2628.
204. M. Dressel and G. Gruner , *Electrodynamics of Solids: Optical Properties of Electrons in Matter* , Cambridge University Press , Cambridge , UK , **2002**.

205. H.-S. Liu, B.-C. Pan and G.-S Liou, *Nanoscale* **2017**, *9*, 2633-2639.
206. M. Kaltenbrunner, M. S. White, E. D. Głowacki, T. Sekitani, T. Someya, N. S. Sariciftci and S. Bauer, *Nat. Commun.* **2012**, *3*, 770-777.
207. J. A. Rogers, T. Someya and Y. Huang, *Science* **2010**, *327*, 1603-1607.
208. D.-H. Kim, J. Xiao, J. Song, Y. Huang and J. A. Rogers, *Adv. Mater.* **2010**, *22*, 2108-2124.
209. J. Liang, L. Li, K. Tong, Z. Ren, W. Hu, X. Niu, Y. Chen and Q. Pei, *ACS Nano* **2014**, *8*, 1590-1600.
210. J. Wang and P. S. Lee, *Nanophotonics* **2017**, *6*, 435-451.
211. Z. Yu, X. Niu, Z. Liu and Q. Pei, *Adv. Mater.* **2011**, *23*, 3989-3994.
212. J. Liang, L. Li, X. Niu, Z. Yu and Q. Pei, *Nat. Photonics* **2013**, *7*, 817-824.
213. A. Sandström, H. F. Dam, F. C. Krebs and L. Edman, *Nat. Commun.* **2012**, *3*, 1002-1007.
214. B. G. Klärner, J.-I. Lee, M. H. Davey and R. D. Miller, *Adv. Mater.* **1999**, *11*, 115-119.
215. M. D. Dickey, *Adv. Mater.* **2017**, 1606425-1606434.
216. J. Li, S. G. R. Bade, X. Shan and Z. Yu, *Adv. Mater.* **2015**, *27*, 5196-5202.
217. Y. Lee, J. Park, S. Cho, Y. E. Shin, H. Lee, J. Kim, J. Myoung, S. Cho, S. Kang, C. Baig, H. Ko, *ACS Nano* **2018**, *12*, 4045-4054.
218. T. Q. Trung, N. E. Lee, *Adv. Mater.* **2016**, *28*, 4338-4372.
219. S. Wang, J. Y. Oh, J. Xu, H. Tran, Z. Bao, *Acc. Chem. Res.* **2018**, *51*, 1033-1045.
220. T. Cheng, Y. Zhang, W. Y. Lai, W. Huang, *Adv. Mater.* **2015**, *27*, 3349-3376.
221. T. H. Chang, K. Li, H. Yang, P. Y. Chen, *Adv. Mater.* **2018**, *30*, 1802418-1802431.
222. X. Wang, L. Dong, H. Zhang, R. Yu, C. Pan, Z. L. Wang, *Adv. Sci.* **2015**, *2*, 1500169-1500180.
223. Son, D.; Lee, J.; Qiao, S.; Ghaffari, R.; Kim, J.; Lee, J. E.; Song, C.; Kim, S. J.; Lee, D. J.; Jun, W.; Yang, S.; Park, M.; Shin, J.; Do, K.; Lee, M.; Kang, K.; Hwang, C. S.; Lu, N.; Hyeon, T.; Kim, D.-H. *Nat. Nanotechnol.* **2014**, *9*, 397-404.
224. D. Son, Z. Bao, *ACS Nano* **2018**, *12*, 11731-11739.
225. C. Larson, B. Peele, S. Li, S. Robinson, M. Totaro, L. Beccai, B. Mazzolai, R. Shepherd, *Science* **2016**, *351*, 1071-1074.
226. D.-H. Kim, N. Lu, R. Ma, Y.-S. Kim, R.-H. Kim, S. Wang, J. Wu, S. M. Won, H. Tao, A. Islam, *Science* **2011**, *333*, 838-843.
227. K. Takei, T. Takahashi, J. C. Ho, H. Ko, A. G. Gillies, P. W. Leu, R. S. Fearing, A. Javey, *Nat. Mater.* **2010**, *9*, 821-826.
228. C.nh. Pang, J. H. Koo, A. Nguyen, J. M. Caves, M.-G. Kim, A. Chortos, K. Kim, P. J. Wang, J. B.-H. Tok, Z. Bao, *Adv. Mater.* **2014**, *27*, 634-640
229. R. Feiner, L. Engel, S. Fleischer, M. Malki, I. Gall, A. Shapira, Y. S.-D., T. Dvir,

- Nat. Mater.* **2016**, *15*, 679-685.
230. T. Yamada, Y. Hayamizu, Y. Yamamoto, Y. Yomogida, A. I.-N, D. N. Futaba, K. Hata, *Nat. Nanotechnol.* **2011**, *6*, 296-301.
231. B. You, C. J. Han, Y. Kim, B. K. Ju, J. W. Kim, *J. Mater. Chem. A* **2016**, *4*, 10435-10443.
232. S. Jun, C. J. Han, Y. Kim, B. K. Ju, J. W. Kim, *J. Mater. Chem. A* **2017**, *5*, 3221-3229.
233. J.-W. Jeong, W.-H. Yeo, A. Akhtar, J. J. S. Norton, Y.-J. Kwack, S. Li, S.-Y. Jung, Y. Su, W. Lee, J. Xia, H. Cheng, Y. Huang, W.-S. Choi, T. Bretl, J. A. Rogers, *Adv. Mat.* **2013**, *25*, 6839-6846.
234. Y. Yang, H. Zhang, Z.-H. Lin, Y. S. Zhou, Q. Jing, Y. Su, J. Yang, J. Chen, C. Hu, Z. L. Wang, *ACS Nano* **2013**, *7*, 9213-9222.
235. F.-R. Fan, L. Lin, G. Zhu, W. Wu, R. Zhang, Z. L. Wang, *Nano Lett.* **2012**, *12*, 3109-3114.
236. C. Pan, L. Dong, G. Zhu, S. Niu, R. Yu, Q. Yang, Y. Liu, Z. L. Wang, *Nat. Photonics* **2013**, *7*, 752-758.
237. Q. Liu, J. Chen, Y. Li, G. Shi, *ACS Nano* **2016**, *10*, 7901-7906.
238. J. Zhong, Q. Zhong, Q. Hu, N. Wu, W. Li, B. Wang, B. Hu, J. Zhou, *Adv. Funct. Mater.* **2015**, *25*, 1798-1803.
239. C. Pang, G.-Y. Lee, T.-i. Kim, S. M. Kim, H. N. Kim, S.-H Ahn, K.-Y. Suh, *Nat. Mater.* **2012**, *11*, 795-801.
240. M. Vural, A. M. Behrens, O. B. Ayyub, J. J. Ayoub, P. Kofinas, *ACS Nano*. **2015**, *9*, 336-342.
241. Y. Tang, S. Gong, Y. Chen, L. W. Yap, W. L. Cheng, *ACS Nano* **2014**, *8*, 5707-5714.
242. F.-C. Liang, Y.-W. Chang, C.-C. Kuo, C.-J. Cho, D.-H. Jiang, F.-C. Jhuang, S.-P. Rweia, R. Borsali, *Nanoscale* **2019**, *11*, 1520-1530.
243. M. Park, J. Im, M. Shin, Y. Min, J. Park, H. Cho, S. Park, M. B. Shim, S. Jeon, D. Y. Chung, J. Bae, U. Jeong, K. Kim, *Nat. Nanotechnol.* **2012**, *7*, 803-809.
244. J. Lee, H. Kwon, J. Seo, S. Shin, J. H. Koo, C. Pang, S. Son, J. H. Kim, Y. H. Jang, D. E. Kim, T. Lee, *Adv. Mater.* **2015**, *27*, 2433-2439.
245. C.-L. Choong, M.-B. Shim, B.-S Lee, S. Jeon, D.-S Ko, T.-H. Kang, J. Bae, S. H. Lee, K.-E. Byun, J. Im, Y. J. Jeong, C. E. Park, J.-J. Park, U.-I. Chung, *Adv. Mater.* **2014**, *26*, 3451-3458.
246. H.-H. Chou, A. Nguyen, A. Chortos, J. W.F. To, C. Lu, J. Me, T. Kurosawa, W.-G. Bae, J. B.-H. Tok, Z. Bao, *Nat. Commun.* **2015**, *6*, 8011-8021.
247. G. Y. Bae, S. W. Pak, D. Kim, G. Lee, D. H. Kim, Y. Chung, K. Cho, *Adv. Mater.* **2016**, *28*, 5300-5306.

248. S. C. B. Mannsfeld, B. C-K. Tee, R. M. Stoltenberg, C. V. H-H. Chen, S. Barman, B. V. O. Muir, A. N. Sokolov, C. Reese, Z. Bao, *Nature Materials* **2010**, *9*, 859-864.
249. F. R. Fan, L. Lin, G. Zhu, W. Wu, R. Zhang, Z. L. Wang, *Nano. Lett.* **2012**, *12*, 3109-3114.
250. L. Pan, A. Chortos, G. Yu, Y. Wang, S. Isaacson, R. Allen, Y. Shi, R. Dauskardt, Z. N. Bao, *Nat. Commun.* **2014**, *5*, 3002-3010.
251. J. Park, Y. Lee, J. Hong, Y. Lee, M. Ha, Y. Jung, H. Lim, S. Y. Kim, H. Ko, *Acs Nano*. **2014**, *8*, 12020-12029.
252. J. Park, J. Kim, J. Hong, H. Lee, Y. Lee, S. Cho, S.-W. Kim, J. J. Kim, S. Y. Kim, H. Ko, *NPG Asia Materials* **2018**, *10*, 163-176.
253. F.-C. Liang, C.-C. Kuo, B.-Y. Chen, C.-J. Cho, C.-C. Hung, W.-C. Chen, R. Borsali, *ACS Appl. Mater. Interfaces* **2017**, *9*, 16381-16396.
254. Y.-C. Chiu, Y. Chen, C.-C. Kuo, S.-H. Tung, T. Kakuchi, W.-C. Chen, *ACS Appl. Mater. Interfaces* **2012**, *4*, 3387-3395.
255. J.-Y. Chen, C.-C. Kuo, C.-S. Lai, W.-C. Chen, H.-L. Chen, *Macromolecules* **2011**, *44*, 2883-2892.
256. X. Fan, N. Wang, F. Yan, J. Wang, W. Song, Z. Ge, *Adv. Mater. Technol.* **2018**, *3*, 1800628-1800653.
257. S. Chen, R. Wu, P. Li, Q. Li, Y. Gao, B. Qian, F. Xuan, *ACS Appl. Mater. Interfaces* **2018**, *10*, 37760-37766.
258. X. Fang, J. Tan, Y. Gao, Y. Lu, F. Xuan, *Nanoscale* **2017**, *9*, 17948-17956.
259. L. Li, H. Xiang, Y. Xiong, H. Zhao, Y. Bai, S. Wang, F. Sun, M. Hao, L. Liu, T. Li, Z. Peng, J. Xu, T. Zhang, *Adv. Sci.* **2018**, *5*, 1800558-1800567
260. M. Amjadi, K.-U. Kyung, I. Park, M. Sitti, *Adv. Funct. Mater.* **2016**, *26*, 1678-1698.
261. S. Lee, A. Reuveny, J. Reeder, S. Lee, H. Jin, Q. Liu, T. Yokota, T. Sekitani, T. Isoyama, Y. Abe, Z. Suo, T. Someya, *Nat. Nanotechnol.* **2016**, *11*, 472-478.
262. X. Q. Liao, Z. Zhang, Z. Kang, F. F. Gao, Q. L. Liao, Y. Zhang, *Mater. Horiz.* **2017**, *4*, 502-510.
263. Tee, B. C. K., Wang, C., Allen, R. Bao, Z., *Nat. Nanotechnol.* **2012**, *7*, 825-832.
264. L. Pan, A. Chortos, G. Yu, Y. Wang, S. Isaacson, R. Allen, Y. Shi, R. Dauskardt, Z. Bao., *Nature Communications* **2014**, *5*, 3002-3010.
265. S. Zhao, J. Li, D. Cao, Y. Gao, W. Huang, G. Zhang, R. Sun, C.-P. Wong, *J. Mater. Chem. C*, **2016**, *4*, 6666-6674.
266. C. Pang, J. H. Koo, A. Nguyen, J. M. Caves, M.-G. Kim, A. Chortos, K. Kim, P. J. Wang, J. B.-H. Tok, Z. Bao, *Adv. Mater.* **2015**, *27*, 634-640.

Chapter 6 、 Publications

Ten Selected Publications (Five First Authors)

1. Loganathan Veeramuthu^a, Wan-Ling Li^a, **Fang-Cheng Liang**^a, Chia-Jung Cho, Chi-Ching Kuo,* Wei-Cheng Chen, Ja-Hon Linc , Wen-Ya Lee, Chih-Te Wang, Wen-Yinn Lin, Syang-Peng Rwei, “Smart garment energy generators fabricated using stretchable electrospun nanofibers“ **Reactive and Functional Polymers**, 142, 96-103 (2019) (SCI) (IF: **3.21**, Journal Rank (Biochemistry, Genetics and Molecular Biology, Biochemistry): (2017, CiteScore Rank 118/402=**2.93%**). **contributed equally to this work**
2. Ming-Yi Huang, Loganathan Veeramuthu, Chi-Ching Kuo* , Yi-Chun Liao, Dai-Hua Jiang, **Fang-Cheng Liang**, Zhen-Li Yan, Redouane Borsali, Chu-Chen Chueh* ”Improving Performance of Cs-based Perovskite Light-Emitting Diodes by dual additives consisting of Polar Polymer and n-Type Small Molecule” **Organic Electronics**, 67, 294-301 (2019) (IF: **3.44**, Journal Rank (Electrical and Electronic Engineering): (2017, CiteScore Rank 85/644=**13.2%**) (cooperate with France) **Universite Grenoble Alpes, France-CNRS**
3. **Fang-Cheng Liang**, You-Wei Chang, Chi-Ching Kuo,* , Chia-Jung Cho, Dai-Hua Jiang, Fu-Cheng Jhuang, Syang-Peng Rwei, and Redouane Borsali “Mechanically Robust Silver Nanowire–Polydimethylsiloxane Electrode Based on Facile Transfer Printing Techniques for Wearable Displays” **Nanoscale**, 11, 1520-1530 (2019) (SCI) (IF: **7.57**, Journal Rank (Materials Science, General Material science) (2017, CiteScore Rank 21/248=**6.39%**) (cooperate with France) **Universite Grenoble Alpes, France-CNRS**
4. Bo-Yu Chen, Yen-Chen Lung, Chi-Ching Kuo* , **Fang-Cheng Liang**, Tien-Liang Tsai, Dai-Hua Jiang, Toshifumi Satoh, ”Novel Multifunctional Luminescent Electrospun Fluorescent Nanofiber Chemosensor-Filters and Their Versatile Sensing of pH, Temperature, and Metal Ions” **Polymers**, 10, 1259-1275 (2018) (SCI) (IF: **3.3**, Journal Rank (Polymer Science): (2017, CiteScore Rank 63/359=**17.55%**)
5. **Fang-Cheng Liang**, Yi-Hsing Huang, Chi-Ching Kuo,* , Chia-Jung Cho, Syang-Peng Rwei, Qun Jia, Yuansheng Ding, Yougen Chen,* , and Redouane Borsali “Thermally deposited silk fibroin as the gate dielectric layer in organic thin film transistors based on conjugated polymer” **Reactive and Functional Polymers**, 131, 368-377 (2018) (SCI) (IF: **3.07**, Journal Rank (Biochemistry, Genetics and Molecular Biology, Biochemistry) (2017, CiteScore Rank 118/402=**2.93%**) (cooperate with France) **Universite Grenoble Alpes, France-CNRS**
6. **Fang-Cheng Liang**, Chi-Ching Kuo,*Bo-Yu Chen, Chia-Jung Cho, Chih-Chien

- Hung, Wen-Chang Chen, Redouane Borsali. “RGB-Switchable Porous Electrospun Nanofiber Chemosensor-filter Prepared from Multifunctional Copolymers and Their Versatile Sensing for pH and Heavy Metal” **ACS Appl. Mater. Interfaces**, 9, 16381-16396 (2017) (SCI) (IF: 8.09, Journal Rank (Materials Science, General Material science) (2017, CiteScore Rank 24/438=5.48%) (cooperate with France) **Universite Grenoble Alpes, France-CNRS**
7. **Fang-Cheng Liang**, Yi-Ling Luo, Chi-Ching Kuo , Bo-Yu Chen , Chia-Jung Cho, Fan-Jie Lin, Yang-Yen Yu, and Redouane Borsali “Novel Magnet and Thermoresponsive Chemosensory Electrospinning Fluorescent Nanofibers and Their Sensing Capability for Metal Ions” **Polymers**, 9, 136 (2017) (SCI) (IF: 3.3, Journal Rank (Polymer Science): (2017, CiteScore Rank 63/359=17.55%) (cooperate with France) **Universite Grenoble Alpes, France-CNRS**
 8. Bo-Yu Chen, Chi-Ching Kuo, Chia-Jung Cho, **Fang-Cheng Liang** and Ru-Jong Jeng “Novel Fluorescent Chemosensory Filter Membranes Composed of Electrospun Nanofibers with Ultra-Selective and Reversible pH and Hg²⁺ Sensing Characteristics” **Dyes and Pigments**, 143 129-142 (2017) (SCI) (IF: 3.76, Journal Rank (Chemical Engineering, Process Chemistry and Technology) (2017, CiteScore Rank 10/53=18.86%)
 9. Chia-Jung Cho, Shih-Tung Lu, Chi-Ching Kuo,* **Fang-Cheng Liang**, Bo-Yu Chen, Chien-Chia Chu “Pyrene or rhodamine derivative modified surfaces of electrospun nanofibrous chemosensors for colorimetric and fluorescent determination of Cu²⁺, Hg²⁺, and pH” **Reactive and Functional Polymers**, 108, 137-147 (2016) (SCI) (IF: 3.15, Journal Rank (Biochemistry, Genetics and Molecular Biology, Biochemistry): (2017, CiteScore Rank 118/402=2.93%)
 10. Bo-Yu Chen, Chi-Ching Kuo,* Yun-Shao Huang, Shih-Tung Lu, **Fang-Cheng Liang**, and Dai-Hua Jiang, “Novel Highly Selective and Reversible Chemosensors Based on Dual-Ratiometric Fluorescent Electrospun Nanofibers with pH- and Fe³⁺-Modulated Multicolor Fluorescence Emission” **ACS Appl. Mater. Interfaces**, 7, 2797–2808 (2015) (SCI) (IF: 7.14, Journal Rank (Materials Science, General Material science) (2017, CiteScore Rank 24/438=5.48%)

Two Selected Patents:

1. 金屬離子感測化合物包含其多重感測共聚物及其纖維，郭霽慶，陳伯瑜，**梁芳誠**，發明專利，台灣，專利申請字號：TW105123231 (I607972)
2. 水轉印導電貼附膜之製造方法及其製造之水轉印導電貼附膜，以及使用該水轉印導電貼附膜之穿戴式元件、發光元件及穿戴式發光裝置，郭霽慶，**梁芳誠**，張祐維，發明專利，台灣，專利申請字號：108124501 (申請中)